University of Alberta

Laboratory determination of seismic anisotropy in sedimentary rock from the Western Canadian Sedimentary Basin

by

Darrel B. Hemsing ©

A thesis submitted to the Faculty of Graduate Studies and Research
in partial fulfillment of the requirements for the degree of

Master of Science
in
Geophysics

Department of Physics

Edmonton, Alberta
Fall, 2007

Library and Archives Canada

Published Heritage Branch

395 Wellington Street
Ottawa ON K1A 0N4
Canada

Bibliothèque et Archives Canada

Direction du Patrimoine de l'édition

395, rue Wellington
Ottawa ON K1A 0N4
Canada

Your file Votre référence
ISBN: 978-0-494-33255-9
Our file Notre référence
ISBN: 978-0-494-33255-9

NOTICE:
The author has granted a non-exclusive license allowing Library and Archives Canada to reproduce, publish, archive, preserve, conserve, communicate to the public by telecommunication or on the Internet, loan, distribute and sell theses worldwide, for commercial or non-commercial purposes, in microform, paper, electronic and/or any other formats.

The author retains copyright ownership and moral rights in this thesis. Neither the thesis nor substantial extracts from it may be printed or otherwise reproduced without the author's permission.

AVIS:
L'auteur a accordé une licence non exclusive permettant à la Bibliothèque et Archives Canada de reproduire, publier, archiver, sauvegarder, conserver, transmettre au public par télécommunication ou par l'Internet, prêter, distribuer et vendre des thèses partout dans le monde, à des fins commerciales ou autres, sur support microforme, papier, électronique et/ou autres formats.

L'auteur conserve la propriété du droit d'auteur et des droits moraux qui protège cette thèse. Ni la thèse ni des extraits substantiels de celle-ci ne doivent être imprimés ou autrement reproduits sans son autorisation.

In compliance with the Canadian Privacy Act some supporting forms may have been removed from this thesis.

While these forms may be included in the document page count, their removal does not represent any loss of content from the thesis.

Conformément à la loi canadienne sur la protection de la vie privée, quelques formulaires secondaires ont été enlevés de cette thèse.

Bien que ces formulaires aient inclus dans la pagination, il n'y aura aucun contenu manquant.

Canada

Abstract

Seismic anisotropy is the variation of wave speed through different directions in a material. Preferential alignment of minerals, layering, and preferred orientation of porosity all cause seismic anisotropy to be observed in many crustal rocks. Shale, in particular, exhibits a relatively large degree of anisotropy. Taking anisotropy into account will improve the quality of seismic images, helping to correctly locate 3-D targets and avoid potentially costly mispositions. In this thesis, core samples from Alberta, Canada are tested for anisotropy using a conventional ultrasonic pulse transmission method. Although attempts were made to sample clay rich shales, petrographical characterization revealed that several different types of rocks were tested, including sandstones, shales, carbonates, and an anhydrite sample. Under the assumption of transverse isotropy velocities, elastic constants, and anisotropic parameters are found. The largest anisotropy is found in a shale which exhibited preferred orientation of clay minerals.

Acknowledgements

I would like to thank Doug Schmitt for his supervision during my time here. I would also like to thank Len Tober for all the technical assistance he provided in the lab. Dean Rokosh assisted with collection of the samples, Diane Caird performed X-ray diffraction, George Braybrook assisted with the scanning electron microscope, Don Resultay made thin sections, and conversations with Heather Kaminsky helped clarify the whole rock analysis results.

I would also like to thank Renee for her support and encouragement in both academic and personal endeavors. She kept me grounded throughout my time here, and made the entire experience much more enjoyable.

This work was funded in part by a Discovery grant to Dr. Schmitt from the National Science and Engineering Research Council of Canada, and by the Alberta Energy Research Institute as part of COURSE project 1514.

Table of Contents

Chapter 1: Introduction....1

Chapter 2: Background....4

2.1 Theory....4

2.1.1 Elasticity....5

2.1.2 Anisotropy Notation....12

2.2 Shales....14

2.2.1 Shale Mineralogy....15

2.2.2 Porosity & Permeability....16

2.3 Anisotropy....18

2.3.1 Layering....18

2.3.2 Preferred Orientation of Clay Minerals....21

2.3.3 Aligned Microcracks & Pores....23

2.4 Ultrasonic Elastic Constant Measurement Techniques....24

2.4.1 Pulse Transmission....24

2.4.2 Pulse Reflection....31

2.4.3 Resonant Ultrasound Spectroscopy (RUS)....33

2.5 Summary....36

Chapter 3: Experimental Procedure....37

3.1 Transducers....37

3.2 Sample Preparation....41

3.3 Data Acquisition....44

3.4 Waveforms & Calibration....48
3.5 Analysis of Errors in Velocity....55
3.6 Summary....57
Chapter 4: Characterization....58
4.1 Introduction....58
4.2 Density & Porosity....65
4.2.1 Grain Density....65
4.2.2 Bulk Density & Porosity....67
4.2.3 Pore Structure....69
4.3 Mineralogical Content....76
4.3.1 X-Ray Diffraction (XRD)....76
4.3.2 Whole Rock Analysis....77
4.4 Texture....82
4.4.1 Scanning Electron Microscope (SEM)....82
4.4.2 Thin Sections....93
4.5 Summary....103
Chapter 5: Results & Discussion....105
5.1 Velocities....105
5.1.1 Consolidation Tests....106
5.1.2 Sandstone Velocities....107
5.1.3 Carbonate Velocities....110
5.1.4 Shale and Anhydrite Velocities....112
5.1.1 Empirical Velocity-Pressure Relation....114

5.2 Sources of Anisotropy....119
5.2.1 Sandstone Anisotropy....122
5.2.2 Carbonate Anisotropy....124
5.2.3 Shale and Anhydrite Anisotropy....126
5.2.4 Comparison With Seismics in the Region....129
5.3 Elastic Constants....130
5.3.1 Calculation of C_{13} from V_{SV}....135
5.4 V_P/V_S Ratios....138
5.5 Discussion & Summary....146
Chapter 6: Conclusion....149
6.1 Motivation for this Work....149
6.2 Summary....149
6.3 Contributions of this Work....151
6.4 Future Work....152
6.5 Concluding Remarks....153
References....155
Appendix: Experimental Data....169
A.1 Mannville Shale 1 (SSA010)....169
A.2 Mannville Shale 2 (SSA011)....175
A.3 Mount Head Carbonate (SSA019)....181
A.4 Wabamun Carbonate (SSA025)....187
A.5 2nd White Specks Sandstone (SSA034)....193
A.6 Big Valley Anhydrite (SSA035)....198

A.7 Bow Island Sandstone (SSA037).....203

List of Tables

2.1 Measures of anisotropy of various shales from the literature.....14

3.1 Peak pressure and pressure step sizes of each sample.....47

3.2 Calibration times (μs) for each buffer set.....49

4.1 Geological parameters.....60

4.2 Grain densities of the samples as well as selected minerals.....67

4.3 Bulk density and porosity.....68

4.4 Pore-size distributions of the samples.....75

4.5 Minerals identified from X-ray diffraction.....77

4.6 Whole rock major element analysis for all samples in the SSA series.....80

5.1 Best fit parameters fit to the carbonate sample velocities.....116

5.2 Anisotropic parameters of the samples at low, mid, and peak pressure.....120

5.3 Elastic constants of the samples at low, mid, and peak pressure.....134

5.4 Bulk and shear modulus of selected minerals.....135

5.5 The difference in C_{13} calculations using Equation 2.18 and Equation 5.2....136

A.1 Geological parameters of the Mannville shale 1.....169

A.2 Properties of the cores of the Mannville shale 1.....169

A.3 Velocities of the Mannville shale 1.....169

A.4 Elastic constants and anisotropic parameters of the Mannville shale 1.....172

A.5 Geological parameters of the Mannville shale 2.....175

A.6 Properties of the cores of the Mannville shale 2.....175

A.7 Velocities of the Mannville shale 2.....176

A.8 Elastic constants and anisotropic parameters of the Mannville shale 2.....178

A.9 Geological parameters of the Mount Head carbonate.....181

A.10 Properties of the cores of the Mount Head carbonate.....181

A.11 Velocities of the Mount Head carbonate.....182

A.12 Elastic constants and anisotropic parameters of the Mount Head carbonate.....184

A.13 Geological parameters of the Wabamun carbonate.....187

A.14 Properties of the cores of the Wabamun carbonate.....187

A.15 Velocities of the Wabamun carbonate.....188

A.16 Elastic constants and anisotropic parameters of the Wabamun carbonate.....190

A.17 Geological parameters of the 2nd White Specks sandstone.....193

A.18 Properties of the cores of the 2nd White Specks sandstone.....193

A.19 Velocities of the 2nd White Specks sandstone.....194

A.20 Elastic constants and anisotropic parameters of the 2nd White Specks sandstone.....196

A.21 Geological parameters of the Big Valley carbonate.....198

A.22 Properties of the cores of the 2nd White Specks sandstone.....198

A.23 Velocities of the Big Valley anhydrite.....199

A.24 Elastic constants and anisotropic parameters of the Big Valley anhydrite.....201

A.25 Geological parameters of the Bow Island sandstone.....203

A.26 Properties of the cores of the Bow Island sandstone.....203

A.27 Velocities of the Bow Island sandstone.....204

A.28 Elastic constants and anisotropic parameters of the Bow Island sandstone.....206

List of Figures

2.1 The symmetry of a transversely isotropic medium....8

2.2 Plane waves versus group waves....10

2.3 The basic premise of a pulse transmission experiment....25

2.4 The propagation direction and polarization of waves measured in the multi-core method in transversely isotropic rocks....27

2.5 The experimental configuration of Kebaili & Schmitt (1997) and Mah & Schmitt (2001a, 2001b)....28

2.6 The single core method developed by Wang (2002a) for use on transversely isotropic materials....29

2.7 The basic premise of a pulse reflection experiment....32

2.8 A resonant ultrasound spectroscopy experimental setup at ultrasonic frequencies....34

2.9 Amplitude versus frequency spectrum from a resonant ultrasound spectroscopy experiment....35

3.1 The steps necessary to build the transducers....40

3.2 Photograph of the finished transducers....41

3.3 Before and after photos of a prepared sample....44

3.4 A schematic of the experimental setup....47

3.5 Examples of waveforms traveling through the buffers and through a sample....49

3.6 Waveform suites of the buffers....51

3.7 Waveform suites of the Mannville shale 1.....52

3.8 P-waveform suites of the Mount Head carbonate.....53

3.9 The initial signal and amplitude spectrum through the buffers.....54

3.10 The initial signal and amplitude spectrum through the Mannville shale 1....55

4.1 Sample locations.....61

4.2 Photographs of the samples.....62

4.3 Natural radioactivity and P-wave sonic log data.....64

4.4 Cumulative and incremental intrusion curves from mercury porosimetry for the samples.....72

4.5 Scanning electron microscope images for each sample in the plane parallel to bedding.....86

4.6 Scanning electron microscope images for each sample in the plane perpendicular to bedding.....90

4.7 Thin section images for each sample in the plane parallel to bedding.... 96

4.8 Thin section images for each sample in the plane perpendicular to bedding.....100

5.1 Results of consolidation tests on the 2nd White Specks sandstone.....107

5.2 Velocities of the Bow Island sandstone.....108

5.3 Velocities of the Mound Head carbonate.....111

5.4 Velocities of the Mannville shale 1.....114

5.5 Empirical fits of the velocities of the Mound Head carbonate.....117

5.6 Empirical fits of the velocities of the Wabamun carbonate.....118

5.7 Anisotropic parameters of the Bow Island sandstone.....123

5.8 Anisotropic parameters of the Mount Head carbonate.....126

5.9 Anisotropic parameters of the Mannville shale 1.....128

5.10 Elastic constants of the Bow Island sandstone.....131

5.11 Elastic constants of the Mount Head carbonate.....133

5.12 C_{13} for the Mount Head carbonate calculated using Equations 2.18 and 5.2.....138

5.13 V_P/V_S ratios for all of the samples.....141

5.14 V_P versus V_S for the shale and sandstone samples with the mudrock line defined by Castagna et al. (1985).....146

A.1 Waveform suites for the Mannville shale 1.....171

A.2 Velocities of the Mannville shale 1.....172

A.3 Elastic constants of the Mannville shale 1.....174

A.4 Anisotropic parameters of the Mannville shale 1.....175

A.5 Waveform suites for the Mannville shale 2.....177

A.6 Velocities of the Mannville shale 2.....178

A.7 Elastic constants of the Mannville shale 2.....180

A.8 Anisotropic parameters of the Mannville shale 2.....181

A.9 Waveform suites for the Mount Head carbonate.....183

A.10 Velocities of the Mount Head carbonate.....184

A.11 Elastic constants of the Mount Head carbonate.....186

A.12 Anisotropic parameters of the Mount Head carbonate.....187

A.13 Waveform suites for the Wabamun carbonate.....189

A.14 Velocities of the Wabamun carbonate.....190

A.15 Elastic constants of the Wabamun carbonate.....192

A.16 Anisotropic parameters of the Wabamun carbonate.....193

A.17 Waveform suites for the 2nd White Specks sandstone.....195

A.18 Velocities of the 2nd White Specks sandstone.....196

A.19 Elastic constants of the 2nd White Specks sandstone.....197

A.20 Anisotropic parameters of the 2nd White Specks sandstone.....198

A.21 Waveform suites for the Big Valley anhydrite.....200

A.22 Velocities of the Big Valley anhydrite.....201

A.23 Elastic constants of the Big Valley anhydrite.....202

A.24 Anisotropic parameters of the Big Valley anhydrite.....203

A.25 Waveform suites for the Bow Island sandstone.....205

A.26 Velocities of the Bow Island sandstone.....206

A.27 Elastic constants of the Bow Island sandstone.....207

A.28 Anisotropic parameters of the Bow Island sandstone.....208

Chapter 1

Introduction

Seismic anisotropy is the variation of wave speed with propagation direction in a material. This phenomenon is very prevalent and exists to some degree in most geological structures. It is caused by factors such as layering, or preferred orientation of minerals or pores. Essentially, any texture gives rise to anisotropy. Shales display particularly severe amounts of seismic anisotropy, where the velocity parallel to bedding can be up to 40% faster than the velocity perpendicular to bedding.

Beyond its academic interest, anisotropy[1] is economically important due to its influence on seismic images which are used to locate targets in the subsurface. Shales typically make up more than 50% of the volume of a sedimentary basin where oil and gas deposits are found; and this fact makes studying anisotropy an important endeavor. Seismic processing techniques rely on measures of the anisotropy in order to properly image the Earth. If anisotropy is not taken into account, poor images of the subsurface will be obtained and targets may be missed by several hundred meters (Isaac & Lawton, 1999).

Laboratory measurements are an essential aspect in the study of seismic anisotropy. Not only is it a method to investigate the anisotropy of rocks on a small scale, it can also aid in the processing and interpretation of larger scale field studies. Knowledge of the anisotropy is needed by those attempting to develop seismic models of the Earth. There

[1] In this thesis the term 'anisotropy' will refer to seismic anisotropy.

is a dearth of velocity measurements on core samples from Alberta, particularly in studies of anisotropy. This work is motivated by the need to add to the database of anisotropy measurements on core from Alberta. The anisotropy of several samples from southwestern Alberta is found as a function of pressure. Also, an attempt is made to understand the source of anisotropy through in depth petrographical characterization.

A short review of elastic anisotropy is given in Chapter 2. In particular, the relations between phase velocities measured in the laboratory and the elastic constants in transversely isotropic media are given. A review of the sources of anisotropy is given, as well as traits of typical shales. At the end of the chapter, several ultrasonic methods of determining anisotropy will be discussed.

Chapter 3 describes the pulse transmission experiments used to measure velocities of the samples. The method used to build stacked P- and S-wave transducers and the procedure used for measurements is given in detail. This chapter provides examples of waveforms and the method used to determine velocities from them, as well as a determination of error on the velocities.

In Chapter 4 the samples are characterized petrographically. The bulk properties of the samples are determined through density and porosity measurements. The pore structures of the samples are explored through mercury porosimetry. Mineralogy is found through X-ray diffraction and whole rock analysis techniques. Texture of the samples, including mineral orientation and layering, is observed through scanning electron microscope and thin sections.

The changes of velocity and elastic constants with pressure are presented and discussed in Chapter 5. Also, the changes of anisotropy and V_P/V_S with pressure are also shown. The major controls on these variables are discussed in this chapter.

Chapter 6 is the final chapter in this thesis and gives an overview of the work accomplished, the primary contributions of this work, and directions for future work.

Chapter 2

Background

Shales and other clay-rich sediments comprise up to 75 percent of the clastic fill in sedimentary basins (Jones & Wang, 1981). Since these shales overlie basins which may contain oil and gas reservoirs it is economically important to understand the properties of these sediments. Shales have long been observed to be seismically anisotropic (e.g., Banik, 1984), that is wave speeds change with direction, and this presents a problem in conventional seismic processing. If anisotropy is not properly taken into account poor images of the subsurface will be obtained (e.g., Banik, 1984; Isaac & Lawton, 1999; Vestrum et al., 1999; Gray et al., 2001). Laboratory investigation of anisotropy provides important information that leads to a better understanding of rock properties in situ. Seismic anisotropy and its dependence on pressure will be studied ultrasonically in this thesis using the pulse transmission method. The causes of anisotropy, usually ignored in most studies, and other properties of the rocks will also be considered.

2.1 Theory

In this section, a brief overview of elastic anisotropy is provided, primarily in order to show that phase velocities depend on the elastic constants of a material. In particular, the relation between elastic stiffness and phase velocity in transversely isotropic media

will be explored. Also, Thomsen's anisotropy parameters will be introduced as a method of reporting anisotropy.

2.1.1 Elasticity

A brief review of anisotropy and the relation between elastic constants and phase velocities is provided here. For a more in depth analysis the reader is referred to Musgrave (1970) or Auld (1973).

In an elastic medium, stress and strain are related by Hooke's law:

$$\sigma_{ij} = C_{ijkl}\varepsilon_{kl} \tag{2.1}$$

where the stress σ is the second-rank stress tensor, the strain ε is the second-rank strain tensor, and $i, j, k, l = 1, 2, 3$ indicating one of three orthogonal axes and there is summation over repeated indices. C is a fourth-rank tensor of elastic stiffnesses with $3^4 = 81$ elements. The strain is defined in terms of derivatives of the displacement vectors as:

$$\varepsilon_{kl} = \frac{1}{2}\left(\frac{\partial u_i}{\partial x_j} + \frac{\partial u_j}{\partial x_i}\right) \tag{2.2}$$

where u_i is the displacement in the x_i direction.

Not all of the elastic stiffness elements are independent. Symmetry of the stress and strain tensors, as well as internal energy arguments lead to the equalities $C_{ijkl} = C_{jikl} = C_{jilk} = C_{ijlk}$ and $C_{ijkl} = C_{klij}$, which reduces the number of independent elements to 21. It is convenient here to introduce Voigt notation where the four indices i, j, k, and l, are replaced by two indices I and J. Hooke's law now appears as:

$$\begin{bmatrix}\sigma_1\\ \sigma_2\\ \sigma_3\\ \sigma_4\\ \sigma_5\\ \sigma_6\end{bmatrix} = \begin{bmatrix}C_{11} & C_{12} & C_{13} & C_{14} & C_{15} & C_{16}\\ C_{12} & C_{22} & C_{23} & C_{24} & C_{25} & C_{26}\\ C_{13} & C_{23} & C_{33} & C_{34} & C_{35} & C_{36}\\ C_{14} & C_{24} & C_{34} & C_{44} & C_{45} & C_{46}\\ C_{15} & C_{25} & C_{35} & C_{45} & C_{55} & C_{56}\\ C_{16} & C_{26} & C_{36} & C_{46} & C_{56} & C_{66}\end{bmatrix}\begin{bmatrix}\varepsilon_1\\ \varepsilon_2\\ \varepsilon_3\\ \varepsilon_4\\ \varepsilon_5\\ \varepsilon_6\end{bmatrix} \tag{2.3}$$

where *I (J)* = 1, 2, 3, 4, 5, 6 when *i,j (l,k)* = 11, 22, 33, 23 or 32, 13 or 31, 12 or 21, respectively. σ and ε are now represented as 6 X 1 vectors and the elastic stiffness are represented as a symmetric 6 X 6 matrix provided that:

$$\begin{bmatrix}\varepsilon_1\\ \varepsilon_2\\ \varepsilon_3\\ \varepsilon_4\\ \varepsilon_5\\ \varepsilon_6\end{bmatrix} = \begin{bmatrix}\varepsilon_{11}\\ \varepsilon_{22}\\ \varepsilon_{33}\\ 2\varepsilon_{23}\\ 2\varepsilon_{13}\\ 2\varepsilon_{12}\end{bmatrix} \tag{2.4}$$

The 21 independent elastic constants seen in Equation 2.3 is the largest number of elastic constants that any material can have, seen in media of triclinic symmetry. Materials of higher symmetry contain fewer independent elastic constants. In the familiar isotropic case, the elastic stiffness matrix has only 2 independent parameters, C_{33} and C_{44}, often referred to in terms of the bulk modulus (K) and shear modulus (μ), or the Lamé parameters λ and μ:

$$C_{IJ} = \begin{bmatrix} C_{33} & C_{33}-2C_{44} & C_{33}-2C_{44} & 0 & 0 & 0\\ C_{33}-2C_{44} & C_{33} & C_{33}-2C_{44} & 0 & 0 & 0\\ C_{33}-2C_{44} & C_{33}-2C_{44} & C_{33} & 0 & 0 & 0\\ 0 & 0 & 0 & C_{44} & 0 & 0\\ 0 & 0 & 0 & 0 & C_{44} & 0\\ 0 & 0 & 0 & 0 & 0 & C_{44}\end{bmatrix} \tag{2.5}$$

where $C_{33} = \lambda + 2\mu = K + 4/3\mu$, and $C_{44} = \mu$.

Some other important symmetries in rocks are transversely isotropic (TI), and orthogonal, which have 5 and 9 independent elastic constants, respectively. Shales are often considered to be elastically TI (e.g., Vernik & Nur, 1992; Johnston & Christensen, 1995), which means that velocities measured within the symmetry plane will be constant, while velocities measured perpendicular to this plane will be different (Figure 2.1). The velocities in Figure 2.1 are labeled as P- or S-wave with vertically polarized S-waves labeled as SV and horizontally polarized S-waves labeled as SH. In a TI medium the S-wave propagating parallel to the symmetry axis does not split and thus does not need a polarization label. The number refers to the propagation direction relative to the symmetry axis. For example, $V_{SH,90}$ refers to the S-wave propagating and polarized 90° to the symmetry axis. $V_{P,0}$ is different from $V_{P,90}$, and $V_{S,0}$ is different from $V_{SH,90}$, however in a TI material $V_{S,0}$ is the same as $V_{SV,90}$. Samples examined in this thesis are presumed to be TI with the bedding plane as the symmetry plane. In a material of TI symmetry the elastic tensor has 5 independent elastic constants:

$$C_{IJ} = \begin{bmatrix} C_{11} & C_{11}-2C_{66} & C_{13} & 0 & 0 & 0 \\ C_{11}-2C_{66} & C_{11} & C_{13} & 0 & 0 & 0 \\ C_{13} & C_{13} & C_{33} & 0 & 0 & 0 \\ 0 & 0 & 0 & C_{44} & 0 & 0 \\ 0 & 0 & 0 & 0 & C_{44} & 0 \\ 0 & 0 & 0 & 0 & 0 & C_{66} \end{bmatrix} \qquad (2.6)$$

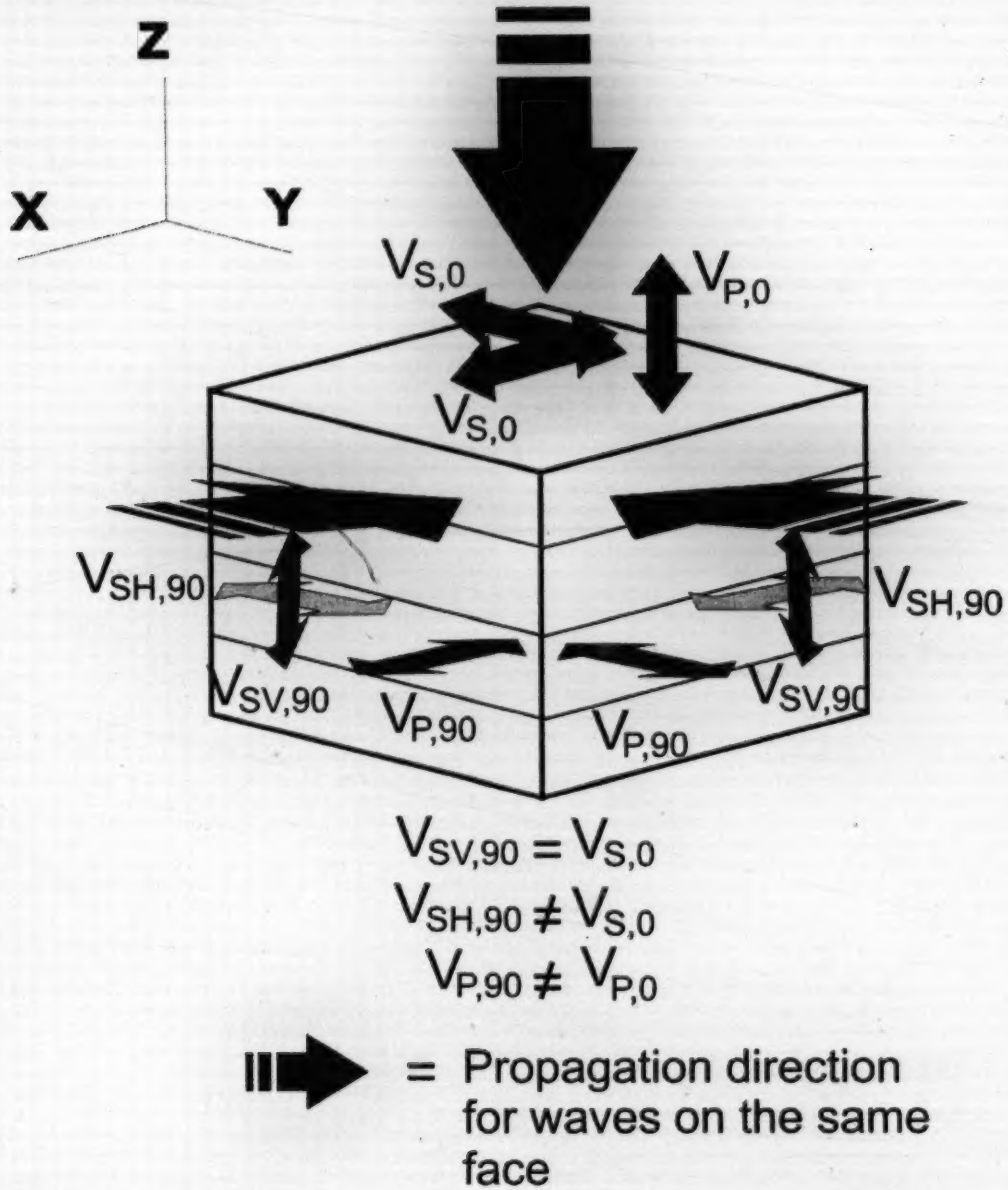

Figure 2.1 – The symmetry of a TI medium. Elastic properties are symmetric about the Z-axis. Waves are propagating into the face of the cube that they are located on. Waves of the same colour propagate with the same speed. The vertically polarized S-wave propagating 90° from the symmetry axis propagates at the same speed at the S-wave traveling parallel to the symmetry axis. See text for more details.

In geophysical investigations, however, it is not the elastic constants that are directly important but the wave speeds that are observed. These wave-speeds are critical to imaging in the subsurface. Specifically, we will consider the relation between elastic constants and phase velocity. In an isotropic material, the group (ray) and the phase (plane wave) velocity are the same and relate to the elastic moduli via:

$$V_P = \sqrt{\frac{K + \frac{4}{3}\mu}{\rho}} = \sqrt{\frac{\lambda + 2\mu}{\rho}} = \sqrt{\frac{C_{33}}{\rho}} \tag{2.7}$$

$$V_S = \sqrt{\frac{\mu}{\rho}} = \sqrt{\frac{C_{44}}{\rho}} \tag{2.8}$$

When dealing with anisotropic media, however, the distinction between group and phase velocities is an important one. Phase velocity is the velocity of the mono-frequency plane wave, while group velocity is the velocity of energy propagation along a ray path. Alternatively, phase velocity is the component of group velocity in the direction of the wave normal. Figure 2.2 demonstrates the difference. A point source at O produces a wavefront W in an anisotropic medium which is shown at time t. At point G, the group velocity is the distance the wavefront has traveled from the origin divided by the time (x/t). The plane wave P associated with point G is tangent to W at this point. If a plane wave is viewed at point G then the distance traveled since time t = 0 is X, thus the phase velocity at this point is X/t. In an isotropic medium the wavefront W is circular and the group velocity equals the phase velocity at all points. However, in an anisotropic medium this is not necessarily true. Without careful consideration in experiments, it can

be difficult to determine whether group or phase velocities, or something in between, are being measured.

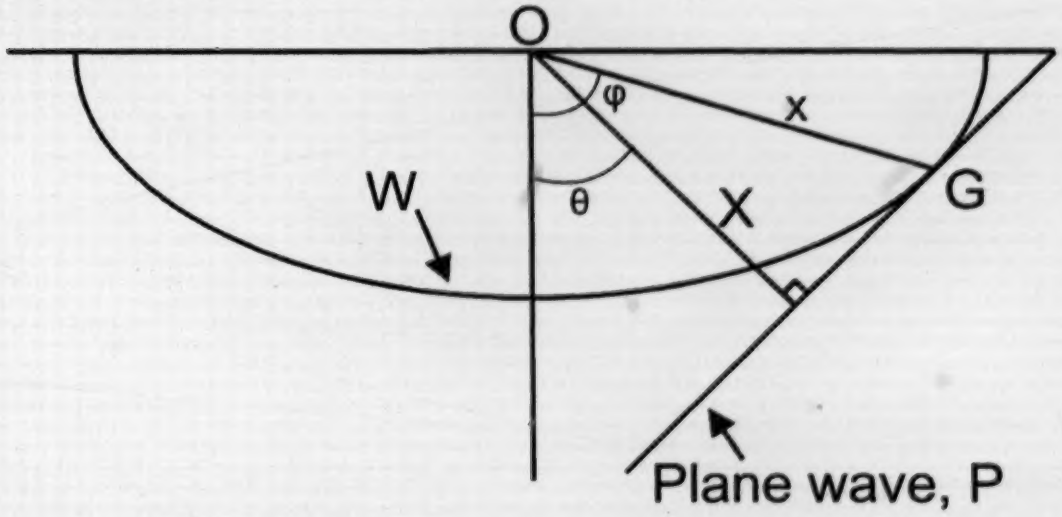

Figure 2.2 - A point source at O produces a wavefront W seen at time t. The group velocity is x/t while the phase velocity is X/t.

With this distinction in mind, we consider the equation of motion in an anisotropic elastic medium (Musgrave, 1970) in order to relate velocity and elastic constants:

$$(C_{ijkl}n_j n_l - \rho v^2 \delta_{ik})p_k = 0 \qquad (2.9)$$

where n_j, n_l are components of the wavefront normal, ρ is the density, v is the phase velocity, δ is the Kronecker delta function, and p is a unit displacement vector. The well known Christoffel[1] matrix is defined as $\Gamma_{ik} = C_{ijkl}n_j n_l$ and Equation 2.9 is more commonly written as:

[1] Elwin Christoffel (1829-1900) was a German mathematician and physicist. He worked in various fields including potential theory, conformal maps, invariant theory, tensor analysis, and geodesy.

$$(\Gamma_{ik} - \rho v^2 \delta_{ik}) p_k = 0 \qquad (2.10)$$

which is known as the Christoffel equation. This eigenvalue problem will yield three phase velocities with mutually orthogonal polarizations, one P and two S, for any direction **n**. Generally, these waves are not polarized perfectly with respect to the propagation direction and thus are often referred to as quasi P- (qP) and quasi S-waves (qS). In a medium of TI symmetry the phase velocities are given by (Thomsen, 1986):

$$V_P(\theta) = \left\{ \frac{C_{11}\sin^2(\theta) + C_{33}\cos^2(\theta) + C_{44} + \sqrt{M}}{2\rho} \right\}^{1/2} \qquad (2.11)$$

$$V_{SV}(\theta) = \left\{ \frac{C_{11}\sin^2(\theta) + C_{33}\cos^2(\theta) + C_{44} - \sqrt{M}}{2\rho} \right\}^{1/2} \qquad (2.12)$$

$$V_{SH}(\theta) = \left(\frac{C_{66}\sin^2(\theta) + C_{44}\cos^2(\theta)}{\rho} \right)^{1/2} \qquad (2.13)$$

where

$$M = \left\{ (C_{11} - C_{44})\sin^2(\theta) - (C_{33} - C_{44})\cos^2(\theta) \right\}^2 + (C_{13} + C_{44})^2 \sin^2(2\theta),$$

ρ is the envelope density of the sample, P or S indicates a longitudinal or shear wave, respectively, and θ indicates the angle between the propagation direction of the wave and the rotational axis of symmetry of the TI medium (Figure 2.2). The five necessary elastic constants are found using Equations 2.11 - 2.13 from five velocities, $V_P(90)$, $V_P(0)$, $V_P(45)$, $V_{SH}(90)$, and $V_{SV}(0) = V_{SH}(0) = V_{SV}(90)$.

$$C_{11} = \rho V_{P,90}^2 \tag{2.14}$$

$$C_{33} = \rho V_{P,0}^2 \tag{2.15}$$

$$C_{44} = \rho V_{S,0}^2 \tag{2.16}$$

$$C_{66} = \rho V_{SH,90}^2 \tag{2.17}$$

$$C_{13} = -C_{44} + \left[\frac{\left(4\rho V_{P,45}^2 - C_{11} - C_{33} - 2C_{44}\right)^2 - \left(C_{11} - C_{33}\right)^2}{4} \right]^{1/2} \tag{2.18}$$

These formulae are important because velocities, rather than elastic constants, are directly observed. They allow the determination of the five TI elastic constants from the available data.

2.1.2 Anisotropy Notation

Obtaining appropriate anisotropy values and finding a way to denote them can be a complicated problem in seismic processing (e.g., Thomsen, 1986; Alkhalifah & Tsvankin, 1995; Tsvankin, 1996). Although directly comparing vertically and horizontally traveling waves is convenient in laboratory experiments, the most common method of describing TI anisotropy is through the so-called 'Thomsen' parameters.

Although there are several ways to determine anisotropy in TI media, the simplest measure is to directly compare the P- or S-wave velocities traveling perpendicular and parallel to bedding:

$$A = \frac{V_{par} - V_{perp}}{V_{par}} \tag{2.19}$$

where V_{par} and V_{perp} are the velocities parallel and perpendicular to bedding, respectively. Anisotropies (A) of shales have been observed up to nearly 40% (Johnston & Christensen, 1995). This measure of anisotropy, however, does not provide enough information nor is it easily found in the field where measurements parallel to bedding cannot be made from the surface. Using the elastic constants, Thomsen (1986) developed three parameters that also quantified the anisotropy of the TI materials, provided that the anisotropy is 'weak':

$$\varepsilon = \frac{C_{11} - C_{33}}{2C_{33}} \tag{2.20}$$

$$\gamma = \frac{C_{66} - C_{44}}{2C_{44}} \tag{2.21}$$

$$\delta = \frac{(C_{13} + C_{44})^2 - (C_{33} - C_{44})^2}{2C_{33}(C_{33} - C_{44})} \tag{2.22}$$

ε is a measure of the P-wave anisotropy and γ is a measure of the SH-wave anisotropy. δ is a more complicated expression that may be viewed as a measure of the anellipticity of the P-wave curve (Cholach & Schmitt, 2006). Alternatively, in seismic processing it is related to the short-spread NMO[2] velocities in TI media. Table 2.1 shows that typical values of the anisotropic parameters in shale vary, although the anisotropy of both P- and S-waves is usually significant.

[2] Normal moveout (NMO) is the effect of arrival time differences due to separation for varying source-receiver offsets in reflection seismology. There is a delay in arrival time for far offsets. Off of a flat reflector, a plot of arrival times versus offset will have a hyperbolic shape for offsets near the source.

	Sample	Effective pressure (MPa)	Anisotropy (A) P	S	ε	γ	δ
Dewhurst & Siggins (2006)	Muderong Shale	60[a]	17%[b]	29%[b]	0.21	0.47	0.47
Wang (2002)	Africa Shale	30.35[a]	13%[b]	17%[b]	0.166	0.229	-0.007
	North Sea Shale	27.59[a]	8%[b]	10%[b]	0.097	0.113	0.096
Hornby (1998)	Jurassic Shale	40	17%[b]	23%[b]	0.23	0.36	0.11
Johnston & Christensen (1995)	Chattanooga Shale	50	31%	35%	0.55	0.71[b]	0.16
	New Albany Shale	50	22%	21%	0.31	0.31[b]	0.13
Vernik & Nur (1992)	Williston Basin Shale	70	21%[b]	26%[b]	0.29	0.42	0.18

Table 2.1: Measures of anisotropy of various shales from the literature. [a] Effective pressure = Confining pressure - Pore pressure. [b] Calculated from data available in the paper.

2.2 Shales

Fine-grained sediments, less than approximately 63 μm, make up ~50% of all sedimentary rock. The term 'shale' is used as a broad group name for all fine-grained siliciclastic rocks; however, it is also commonly used in a more limited sense to refer to laminated clayey rocks (Boggs, 2003). Here we will use the term shale in a broad group sense, though emphasis will be placed on laminated, clay-rich rocks. Although detailed nomenclature systems have been developed based on texture, mineralogical composition, fissility, and structure, shales are often referred to informally by properties such as colour (e.g., black shale), organic content (e.g., carbonaceous shale), major chemical constituents (e.g., calcerous shale), or by time period of deposition (e.g., Devonian shale). Other common names for shales include mudrocks, siltstone, and lutite.

The study of shales is complex. Despite the abundance of shales, there is a relative lack of research as compared to sandstones owing, in part, to their fine grain size and the lack of interest in these rocks as reservoir materials. Methods to determine the properties of shales are different, and often more complex, than those of other rocks. Thin sections are a less useful method of examination of shales since their fine grain size makes the analysis difficult. Mineralogy and chemical analysis of shales is usually determined by methods such as powder X-ray diffraction, scanning electron microscopy, and X-ray fluorescence. Even with these methods, determining individual clay mineralogy can be particularly difficult (Boggs, 2003). Due to very small sizes, grain sizes in shale cannot be determined by sieving; rather, they are usually determined by particle settling velocity when put in solution. To complicate matters, clay minerals have small aspect ratios and do not settle in the same way that rounder particles do. Factors such as these have slowed the research of shales.

The definition of shale encompasses a broad range of rocks and methods to investigate them are relatively complicated. Factors such as fissility and fine grain size further make the study and understanding of shales complex. This section will provide an overview of the mineralogy and various properties of shales.

2.2.1 Shale Mineralogy

Although shales contain many different constituent minerals, the two primary types are clay minerals and framework silicates, the latter usually being quartz (Pettijohn, 1975). Typical shales have quartz content in the range of 30-40 percent and clay content that frequently exceeds 50 percent, though these values may vary widely. Common clay minerals found in shale are kaolinite, smectite, illite, muscovite, chlorite, corrensite,

vermiculite, sepiolite, and attapulgite (Potter et al., 1980; Boggs, 2003). The framework silicate is most often quartz and occasionally feldspar or zeolites. Other constituents found in shales, generally in lesser amounts, include carbonates such as calcite and dolomite, oxides and hydroxides such as hematite, sulfur minerals, organic materials such as kerogen, and various other minor constituents such as glass or heavy minerals (Pettijohn, 1975; Potter et al., 1980).

2.2.2 Porosity & Permeability

Shales exhibit a wide range of porosity values. Porosities from nearly 0%, (Johnston & Christensen, 1995) up to 35% (Potter et al, 1980; Wang, 2002b), and many intermediate porosities (e.g., Hornby, 1998; Domnesteanu et al., 2002; Wang, 2002) have been studied. The pore space in shales is typically very small. It is not uncommon for the modal pore size to be on the order of a few tens of nanometers (e.g., Katsube et al., 1991; Domnesteanu et al., 2002; Connell-Madore & Katsube, 2006; Dewhurst & Siggins, 2006). The pore sizes also generally decrease with increasing depth (Connell-Madore & Katsube, 2006) and induration.

Despite frequently having high porosities, shales tend to have very low permeabilities. One reason for this is the fact that clay minerals have high aspect ratios and due to gravimetric stress are often aligned parallel to bedding. The thin clay platelets frequently overlap one another which creates unconnected porosity and a very tortuous path for fluids; a situation that makes it difficult for fluid to flow (e.g., Maltman, 1994; Kwon et al., 2001). The permeability of shales decreases further when a stress is applied due to the corresponding decrease in porosity (Dewhurst, 1998, 1999).

Another parameter that is important in determining the permeability and transport properties of a material is specific surface area. The specific surface area is a measure of the surface area of all pore space within a sample over a given volume (e.g., m^2/cm^3) or over a given weight (e.g., m^2/g). If the grain size (D) and porosity (φ) of a sample are known, the specific surface area can be calculated using a derivative of the Carman-Kozeny equations (Salem, 2001):

$$S_S = \frac{6(1-\varphi)}{D} \tag{2.23}$$

Due to the small size of clay particles, S_S is quite large for shales. Even a small amount of clay can greatly increase S_S (e.g., Hammecker & Jeannette, 1994). Typical values are seen in the work of Domnesteanu et al. (2002), who found a surface area of 14 m^2/g, and Dewhurst & Siggins (2006), who found a large S_S of 30 m^2/g in a sample of Muderong shale. In cases where the clay fraction is very large, S_S can exceed 60 m^2/g (Dewhurst et al., 1999).

Porosity-permeability data suffers uncertainty and scatter due to the variations in tortuosity caused by overlapping platelets, even in similar samples (Katsube et al., 1991; Kwon et al., 2001). The low permeability of shales is important as they often serve as a nearly impermeable barrier to fluid flow. Despite the low, and difficult to measure, permeability of shales, there have been numerous laboratory studies on the subject. A relatively large shale permeability is seen in the work of Domnesteanu et al. (2002), who tested North Sea shale with 14.62% porosity and found a permeability of 0.02 mD (1.97×10^{-17} m^2). Shale permeabilities typically fall in the 10^{-22} - 10^{-19} m^2 range (Katsube et al., 1991; Neuzil, 1994; Kwon et al., 2001, 2004).

2.3 Anisotropy

There are three primary sources of anisotropy in shales.

1) Layering of materials will cause anisotropy of TI symmetry. Even if the layers are composed of isotropic materials, the effective medium will be anisotropic.

2) Preferred orientation of clay minerals is another mechanism of anisotropy. Clay mineral orientation is often considered to be a main contributor to the anisotropy in many shales.

3) The third major source of anisotropy in shales is the preferred orientation of cracks and pores.

These three sources of anisotropy will be discussed in this section.

2.3.1 Layering

Sedimentary basins are often composed of finely layered material. Layering causes anisotropy, even if the layers themselves are isotropic. A media composed of horizontal layers will appear as TI provided that the seismic wavelength is long in relation to the layer thickness (e.g., Backus, 1962; Melia & Carlson, 1984; Hovem, 1992). This is important since we can view a TI material as having hexagonal symmetry[3], which yields a better understanding of the relationship between velocities and elastic stiffnesses.

[3] It is useful to note for those readers familiar with optical mineralogy that the elastic anisotropy of a hexagonal material is exactly the same as a transversely isotropic medium, that is, both have an axis of rotational symmetry. Optically, however, this material will display six fold symmetry when observed down the c-axis.

Elastic waves traveling in finely layered media were first studied theoretically by early authors (e.g., Postma, 1955; Backus, 1962) who showed that, in the long-wavelength approximation, layered media behave as TI. Backus (1962) dealt with the issue in a general manner, showing that if a material is composed of TI layers, each having an elastic stiffness tensor of the form

$$\begin{bmatrix} a & b & f & 0 & 0 & 0 \\ b & a & f & 0 & 0 & 0 \\ f & f & c & 0 & 0 & 0 \\ 0 & 0 & 0 & d & 0 & 0 \\ 0 & 0 & 0 & 0 & d & 0 \\ 0 & 0 & 0 & 0 & 0 & m \end{bmatrix}$$

then, in the long-wavelength approximation, the material would appear as a transversely isotropic material where the effective medium elastic constants (capital letters) may be calculated from the individual layer elastic constants as (Melia & Carlson, 1984):

$$\begin{aligned} A &= \left\langle a - f^2 c^{-1} \right\rangle + \left\langle c^{-1} \right\rangle^{-1} \left\langle f c^{-1} \right\rangle^2 \\ B &= \left\langle b - f^2 c^{-1} \right\rangle + \left\langle c^{-1} \right\rangle^{-1} \left\langle f c^{-1} \right\rangle^2 \\ C &= \left\langle c^{-1} \right\rangle^{-1} \\ F &= \left\langle c^{-1} \right\rangle^{-1} \left\langle f c^{-1} \right\rangle \\ D &= \left\langle d^{-1} \right\rangle^{-1} \\ M &= \left\langle m \right\rangle \end{aligned} \qquad (2.24)$$

where the brackets $\langle\ \rangle$ indicate an average of the properties, weighted by their proportions. For instance, if the medium is composed of layers of two TI materials with

proportions Δ_1 and Δ_2 ($\Delta_1 + \Delta_2 = 1$) and with the elastic constants of the materials denoted by the subscripts 1 and 2, then:

$$A = \left\{\Delta_1\left(a_1 - \frac{f_1^2}{c_1}\right) + \Delta_2\left(a_2 - \frac{f_2^2}{c_2}\right)\right\} + \left\{\frac{\Delta_1}{c_1} + \frac{\Delta_2}{c_2}\right\}^{-1}\left\{\frac{\Delta_1 f_1}{c_1} + \frac{\Delta_2 f_2}{c_2}\right\}^2 \text{ and}$$

$$C = \left\{\frac{\Delta_1}{c_1} + \frac{\Delta_2}{c_2}\right\}^{-1}$$

The remainder of the elastic constants may be calculated similarly. If the individual layers are isotropic, the effective medium is still TI, however, the number of independent elastic constants for each layer is reduced from five to two.

This theory has been tested in laboratory experiments using materials constructed of isotropic layers. Of note, Melia & Carlson (1984) measured P-waves in a medium composed of isotropic layers of epoxy and glass and the layer thickness of each material was varied. Marion et al. (1994) measured P-waves perpendicular to bedding in layers of steel and plastic disks to investigate the frequency dependence on the long-wavelength approximation. In both cases, the layered media were found to be seismically TI. There have also been numerical experiments investigating this phenomenon (e.g., Carcione et al., 1991; Hovem, 1992; Liu and Schmitt, 2006). All of these experiments, in part, attempt to define the ratio of seismic wavelength (λ) to layer thickness (a) that constitutes 'long' in the long-wavelength approximation. The results indicate that the ratio λ/a depends on the layer materials and should be at least 5-10 in order for the long-wavelength approximation to be valid. In addition to theoretical, controlled laboratory, and numerical experiments, anisotropy has been attributed to layering in many laboratory experiments on geological samples (e.g., Lo et al., 1986; Johnston & Christensen, 1994,

1995; Hornby, 1998; Mah, 2005) and in field studies (e.g., Uhrig & Van Melle, 1955; Kebaili & Schmitt, 1996).

2.3.2 Preferred Orientation of Clay Minerals

Shales contain a large portion of clay minerals. As the shales are compacted in the sedimentary basin, the plate-like clay minerals are rotated due to stress. The minerals are rotated and lie perpendicular to the maximum compressive stress; in the case of a non-dipping basin this stress is vertical due to gravitational loading. This produces a fabric in which a large portion of the clay minerals are oriented horizontally, parallel to the bedding plane (e.g., Maltman, 1994; Kim et al., 1999). Since clays minerals are elastically anisotropic (e.g., Sayers, 1994; Katahara, 1996; Wang et al., 2001; Sayers, 2005; Cholach & Schmitt, 2006) this preferred orientation results in anisotropy, whose symmetry is often TI (e.g., Kaarsberg, 1959; Johnston & Christensen, 1995; Sayers, 2005).

There have been numerous instances in the laboratory where anisotropy has been directly related to preferred orientation of clay minerals. Kaarsberg (1959) performed some of the earliest experiments on preferred orientation of clay in shales. Kaarsberg (1959) measured sound velocities through Cretaceous and Devonian shales and found the preferred orientation of the clay illite through X-ray diffraction. It was found that as the bulk density of the shales increased, attributed to compaction at greater depths, the sound velocities also increased. The anisotropy also increased with increasing density. The increase in anisotropy with compaction was explained by an increase in the preferred orientation of illite. This was confirmed by X-ray diffraction measurements.

Johnston and Christensen (1995) used a similar X-ray diffraction method to relate preferred orientation of clay minerals to seismic anisotropy in a suite of shales. Electron microprobe backscatter images were used to obtain images of the texture which revealed large amounts of preferred orientation. At pressures of 100 MPa, anisotropies of up to 35% were attributed prominently to the orientation of clay. They also found that anisotropy increased with increasing degrees of orientation.

Jones & Wang (1981) measured the anisotropy of two shale cores from the Williston Basin. Velocity measurements indicated a TI symmetry in the samples. Using both velocity data and electron micrographs they attributed the anisotropy to clay minerals oriented parallel to the bedding plane. The core obtained from a greater depth had a larger amount of orientation and a higher anisotropy.

Lo et al. (1986) examined a Chicopee shale under isotropic pressure and determined that the velocity anisotropy was caused by bedding and the preferred orientation of clay minerals. Rai & Hanson (1988) performed experiments on shales and sandstones using both isotropic as well as uniaxial stress. The shale samples did not exhibit any stress induced anisotropy leading to the conclusion that the anisotropy was due to a preferred orientation of clay minerals rather than anisotropy from cracks, as was the case in the sandstones.

Recently, Wenk and coworkers have developed a technique to quantitatively find the orientation of minerals (Lonardelli et al., 2005; Wenk et al., 2007; Lonardelli et al., 2007). X-ray synchrotron diffraction is used to find the orientation distributions (OD) of minerals such as kaolinite or illite. The single crystal properties of each mineral are then averaged over the OD's to provide the elasticity of the entire rock. Initial tests on an

illite-rich sample revealed a quasi-TI symmetry (Wenk et al., 2007). This method gives a quantitative measure on the anisotropy contributed by preferred orientation of minerals and could be useful in differentiating sources of anisotropy.

2.3.3 Aligned Microcracks & Pores

Aligned microcracks, pores, or fractures are another source of anisotropy as has been seen in numerous laboratory experiments, particularly at low pressure. Vernik & Nur (1992) performed velocity experiments on shales and found anisotropy due to layering, preferred orientation of minerals, and microcracks. The anisotropy in the sample decreased as the pressure increased, indicating the closure of microcracks. The microcracks appearing in the mature shales were hypothesized to have been created due to hydrocarbon generation and migration. One core in this data set was further quantified by Vernik (1993), who found a total porosity of 0.87% and a porosity due to cracks of 0.14%. Calculations were made to differentiate the intrinsic anisotropy from the crack-induced anisotropy. At a pressure of 5 MPa, the anisotropy parameters ε, γ, and δ are 0.32, 0.22, and 0.16, respectively, due to the intrinsic anisotropy and 0.65, 0.36, and 0.40, respectively, for the total anisotropy. This illustrates the significant effect that aligned microcracks can have on anisotropy, even if the porosity due to cracks is very small.

Johnston & Christensen (1995) found similar, though less dramatic, results when performing velocity tests on shales. Microcracks oriented parallel to bedding increased the amount of seismic anisotropy. However, when the confining pressure was increased, the amount of anisotropy decreased, indicating the closure of microcracks.

2.4 Ultrasonic Elastic Constant Measurement Techniques

There are several different ways to ultrasonically measure elastic constants in rock samples. These experimental methods offer a view of the samples from a different frequency range than traditional field data and allow them to be examined in a controlled setting. The pulse transmission method is the most popular method of ultrasonic measurements. It involves measuring the travel time of a wave traveling directly through the sample and then calculating the velocities and elastic constants using formulae such as those given above in Section 2.1.1. Pulse reflection experiments are similar to pulse transmission experiments except that reflected waves are measured instead of transmitted waves. Resonant ultrasound spectroscopy measures the samples natural resonances to determine the elastic stiffnesses. The pulse transmission, pulse echo, and resonant ultrasound spectroscopy methods will be reviewed in this section.

2.4.1 Pulse Transmission

The pulse transmission method is the most common method used to determine the elastic constants of geologic materials (e.g., Hughes & Cross, 1951; Hughes & Jones, 1951; Wyllie et al., 1956, 1958; Birch, 1961, 1962; Podio et al., 1968; Timur, 1977; Christensen & Wang, 1985; Sondergeld & Rai, 1986; Rai & Hanson, 1988; Marion et al., 1992; Vernik & Liu, 1997; Dey-Barsukov et al., 2000; Mah & Schmitt, 2001; Wang, 2002b). This method involves measuring the travel time of an ultrasonic wave propagating through a sample. Velocities are found from the travel times and elastic constants are then calculated from the velocities. Depending on the elastic symmetry of the sample, measurements taken in several well-chosen directions can yield the entire suite of non-trivial elastic constants. Some of the more common symmetries studied are

isotropic, hexagonal, and orthorhombic which need 2, 5, and 9 velocities, respectively, to obtain the elastic stiffnesses as noted above in Section 2.1.1.

The most common pulse-transmission method typically uses waves near 1 MHz frequencies on samples a few centimeters in dimension. Using piezoelectric ceramics, ultrasonic transducers are placed on either side of the sample in order to generate and record either P- or S-waves (Figure 2.3). A voltage is applied to the transmitting transducer, which sends a single-frequency pulse through the sample, while the transducer on the opposite end of the sample supplies a voltage in response to the arrival of the wave. The travel time through the sample is then picked from the resulting waveform, and this together with knowledge of the length of the samples is used to calculate the velocity.

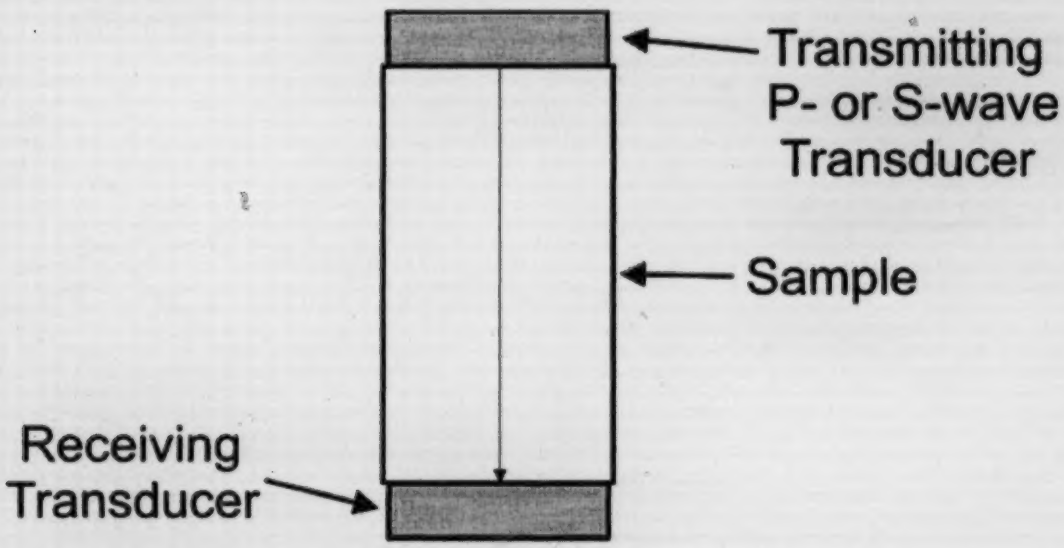

Figure 2.3 - The basic premise of a pulse-transmission experiment. A transmitting transducer sends a wave through the sample where it is recorded by a receiving transducer.

As discussed earlier, there is a difference between the group (ray) and phase (plane wave front) velocities in anisotropic media. As such, it is important to ask what is actually being measured in laboratory experiments. Some experiments, such as those using small receivers and a laser as a point source, measure group velocities (e.g., Aussel & Monchalin, 1989; Every & Sachse, 1990; Castagnède et al., 1991). However, for experimental setups devised similar to Figure 2.3, it has been shown that phase, rather than group, velocities are measured provided that the transducers are a large fraction relative to the sample length over which the wave propagates (e.g., Dellinger & Vernik, 1994; Johnston & Christensen, 1994; Hornby, 1998). This allows elastic constants to be directly measured from the phase velocities obtained in the method outlined in Section 2.1.1. As mentioned previously, there is typically an assumption of symmetry which reduces the number of independent elastic constants as well as the number of velocities needed to determine them. Various anisotropic symmetries, including hexagonal (e.g., Lo et al., 1986; Vernik & Nur, 1992; Wang, 2002b), and orthorhombic (e.g., Cheadle et al., 1991; Kebaili & Schmitt, 1997; Takanashi et al., 2001; Mah and Schmitt, 2001) have been studied using the pulse-transmission method.

Shales are typically considered to have a TI, or hexagonal, symmetry with a symmetry axis perpendicular to bedding. The most common method of finding elastic constants in a material of TI symmetry is as follows: three cores are taken from a larger sample, one in each of the directions parallel and perpendicular to bedding, and one in an off-axis direction, usually 45° from bedding. P-waves are measured on all three of these cores, while the S-wave and SH-wave are found in the cores parallel and perpendicular to the symmetry axis, respectively (Figure 2.4). These five velocities are used to compute

the five elastic constants that fully describe the material. Multi-core methods have been used by many authors to study anisotropy (e.g., Hughes & Cross, 1951; Birch, 1960, 1961; Podio et al., 1968; Jones & Wang, 1981; Lo et al., 1986; Vernik & Nur, 1992; Johnston & Christensen, 1995; Vernik & Liu, 1997; Hornby, 1998; Cholach et al, 2005).

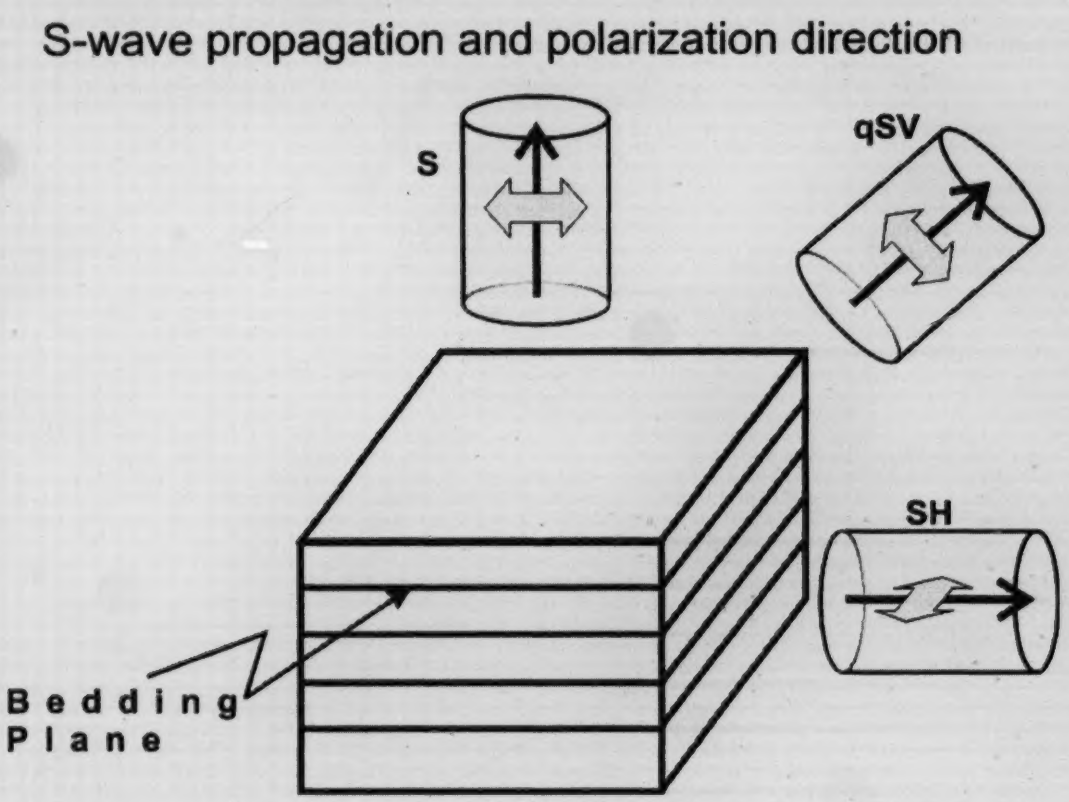

Figure 2.4 - The propagation direction and polarization of waves measured in the multi-core method in TI rocks. The SH-wave is found in the core cut parallel to bedding while the qSV-wave is found in the core cut 45° to bedding. The polarization of the S-wave traveling perpendicular to bedding is irrelevant because of symmetry. P-waves are found on all cores.

There are, however, disadvantages to the multi-core method. For example, it can be difficult to properly core a sample exactly in the directions desired. Further, there is a risk that the coring will sample different heterogeneities of the material and give erroneous results. To overcome these limitations, variations on the multi-core technique have also been used. Rather than using multiple cores, experiments have been devised using a multi-faced cube (e.g., Markham, 1957; Rai & Hanson, 1988; Mah & Schmitt, 2003; Mah, 2005). This technique has the benefit that heterogeneity issues are avoided since all of the waves are propagating through the same medium. Kebaili & Schmitt (1997) and Mah & Schmitt (2001a, 2001b) used blocks of acrylic and phenolic to develop laboratory methods that simulate walk-away VSP. Near point-source transducers, on the order of 2-3 mm, are placed along orthogonal surfaces of the sample (Figure 2.5). The Radon transform is applied to the resulting travel time versus offset plots and phase velocities are calculated. Since the signal from one source transducer reaches many receivers at different locations, this method has the distinct benefit that velocities through a range of angles may be sampled without further machining of the testing material.

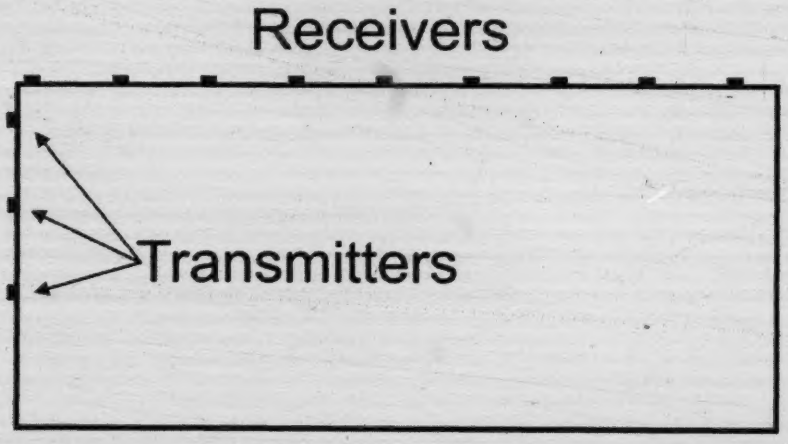

Figure 2.5 – The experimental configuration for experiments done by Kebaili & Schmitt (1997) and Mah & Schmitt (2001a, 2001b).

Wang (2002a) developed an alternative pulse transmission variant where all necessary velocities are measured on a single core taken parallel to the bedding plane (Figure 2.6). As usual, transducers are placed on the ends of the core to measure the velocities parallel to bedding. In order to obtain the velocities perpendicular and 45° to bedding, ultrasonic transducers are built into a rubber jacket that surrounds the core. Dewhurst & Siggins (2006) used a similar single-plug method on a sample of Muderong shale. Nihei et al. (2006) also used a method similar to Wang (2002a) and advanced it by rotating the sample while inside the jacket to obtain velocity measurements at numerous off-axis angles and acquire a better measurement of the C_{13} elastic constant.

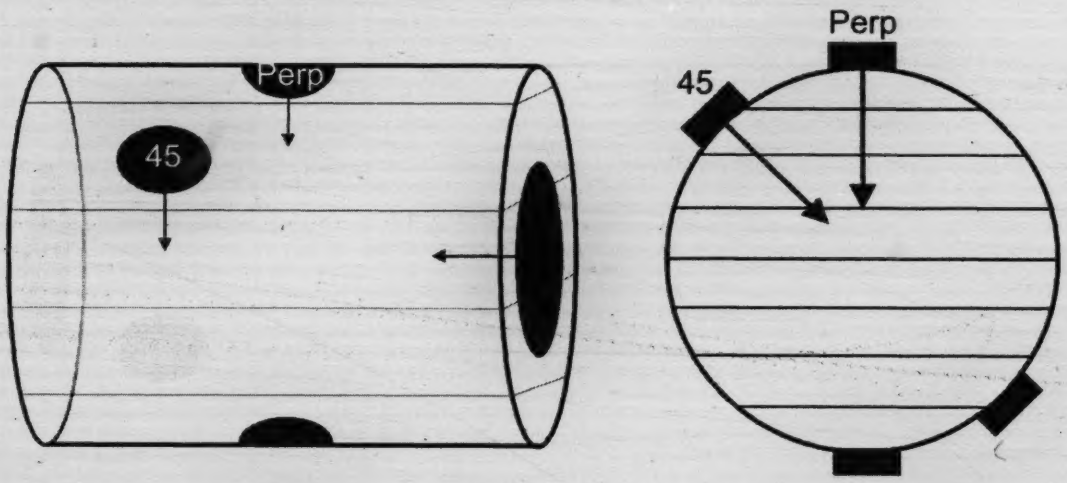

Figure 2.6 - The single-core method developed by Wang (2002a) for use on TI materials. A core is cut parallel to bedding and transducers are affixed to either end to measure the velocity parallel to bedding. Transducers used to measure velocities perpendicular and 45° to bedding are fit into a rubber jacket that is placed around the sample.

The elastic constants C_{11}, C_{33}, C_{44}, and C_{66} are well defined due to simple calculations and low error in the velocity measurements. More uncertainty, however, is associated with the elastic constant C_{13} due to its more complicated formula (Equation 2.18) that allows for the buildup of uncertainty from the propagation of errors. There is also a side-slip of energy as waves propagate in off-axis directions (e.g., Johnston & Christensen, 1995), which can make the signal weaker than those found along principle axes.

The general method of attaining more accurate values of difficult-to-find elastic constants is by obtaining velocity measurements in more than one off-axis angle. The elastic constants are then adjusted until they best match the velocities (e.g., Every & Sachse, 1990; Castagnède et al., 1991; Chu et al., 1994; Reverdy & Audoin, 2001; Isawa et al., 2002). Other than Nihei et al. (2006) mentioned above, there have been several attempts at this in the geophysical literature. Of note is the work of Johnston & Christensen (1995), who obtained cores in 10-15° increments and constructed phase velocity surfaces from both the off-axis measurements as well as the calculated C_{13}. The C_{13} constant was adjusted iteratively until a best-fit was found between the observed and calculated velocity surfaces.

The pulse-transmission method allows the user to change many parameters and analyze their effects on seismic velocity, elasticity, and anisotropy. Pressure (e.g., Johnston & Christensen, 1995; Takanashi et al., 2001), pore fluid (e.g., Wyllie et al., 1956, 1958; King, 1966; Wang, 2002b), temperature (e.g., Hughes & Cross, 1951; Timur, 1977; Johnston, 1987), and many other variables are commonly manipulated in the course of these experiments.

2.4.2 Pulse Reflection

A popular technique for studies of attenuation, the pulse reflection procedure is also used to measure the velocities and elastic constants of materials. This method is similar to the pulse transmission technique in the fact that it involves ultrasonic waves traveling through the sample of interest. However, pulse transmission measures velocities of direct waves traveling through the material whereas pulse reflection, as its name implies, measures reflections of ultrasonic waves. Like pulse transmission, in order to analyze sample of lower than isotropic symmetry it is common practice to obtain cores in multiple directions. Once the phase velocities are obtained, the necessary elastic constants may be calculated.

The pulse reflection process was outlined by Winkler & Plona (1982). As seen in Figure 2.7, a rock sample is placed between two buffers, often lucite. On one buffer there is an ultrasonic transducer which emits a pulse, either broadband or centered on a single frequency. This wave will propagate through the sample and reflect off of various boundaries, most notably at the interfaces between the buffers and sample. The reflected pulses are received by the same transducer that transmitted them. Provided that the experiment has been properly devised such that none of the required reflections interfere, the reflections from the top and the bottom of the sample can be identified and studied individually. In order to determine the ultrasonic velocity through the sample, these waves may be examined in two ways. If the pulse emitted from the transducer is centered on a single-frequency, then a specific, well defined peak/trough in each reflection is examined (e.g., Best & McCann, 1995; Assefa et al., 2003). The difference in the two-way traveltime between the two reflections gives the velocity:

$$V = \frac{2L}{\delta t} \tag{2.25}$$

where L is the sample length and δt is the two-way travel time. If the pulse emitted from the transducer is broadband, then velocity is determined as a function of frequency. The phase spectrum of each reflection is unwrapped and the phase velocity may be found from the phase difference as (Winkler & Plona, 1982):

$$V(\omega) = \frac{\omega 2L}{\phi} \tag{2.26}$$

where ω is the frequency, L is the sample length, and φ is the phase difference between the two reflections.

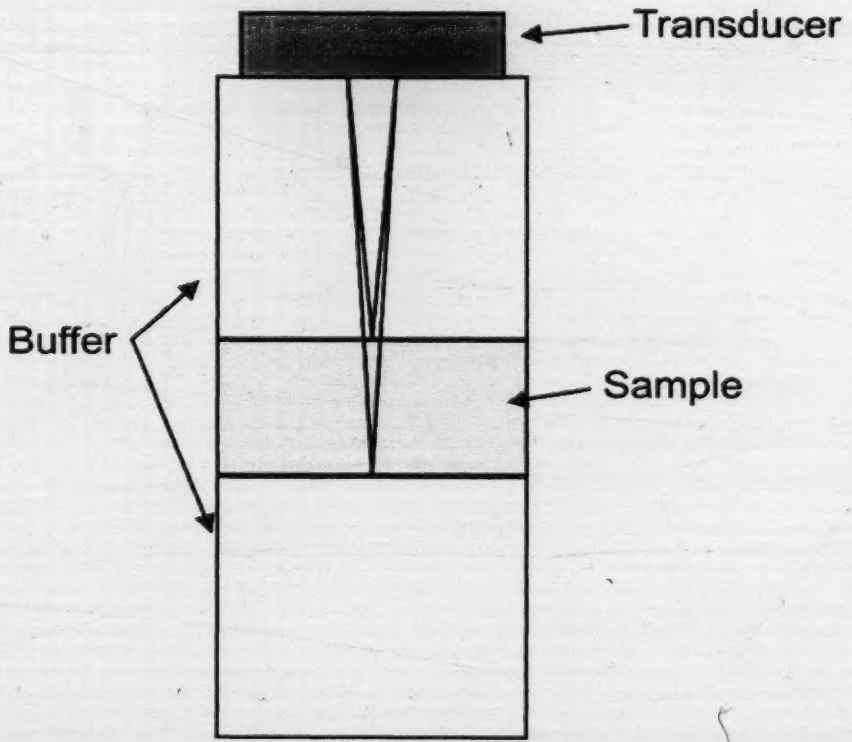

Figure 2.7 - The basic premise of a pulse reflection experiment. A pulse is reflected from the top and bottom of the sample. The difference in times is used to calculate the velocity.

The pulse reflection method has been used extensively on sandstones (e.g., Green & Wang, 1994; Jones et al., 1998; Khaksar et al., 1999) and limestones (e.g., Assefa et al., 2003). Recent attempts have been made to use this technique on clay-rich sandstones (Klimentos & McCann, 1990; Klimentos, 1991; Best & McCann, 1995) and shales (Domnesteanu et al., 2002).

2.4.3 Resonant Ultrasound Spectroscopy (RUS)

Resonant ultrasound spectroscopy (RUS) is another method to determine the elastic constants of materials. RUS differs significantly from pulse-transmission and pulse-reflection techniques. In RUS experiments the elastic constants are determined without the need for phase velocities, and perhaps the simplest comparison might be to the organ pipe frequency problems encountered in standing wave problems in all introductory physics texts. The premise of RUS is to excite a sample through a continuous range of frequencies and find its natural resonances. The resonant frequencies of the sample depend both on the elastic constants of the material, the dimensions, and the sample geometry. This data may then be inverted to find the elastic moduli of the sample. A major benefit of the RUS method is that the entire suite of elastic constants may, in principle, be found from a single sample and a single measurement set consisting of sweeping through a series of frequencies.

For ultrasonic frequencies a typical RUS setup has the corners of a small sample, on the order of a few millimeters, held lightly between two piezoelectric transducers capable of producing a large range of frequencies (Figure 2.8). This frequency range is on the order of 0.1-10 MHz, obtained by swept frequency AC or a broadband pulse that

covers the frequency range (Maeva et al., 2004). More information may be garnered from transducers that cover a wider frequency range. One transducer sends the signal and, depending on the setup, either transducer can receive the signal. An example of an amplitude versus frequency spectrum, which shows the resonances of a cylindrical core of granite, is seen in Figure 2.9. The sample size can range from the millimeter scale for high frequency experiments (e.g., Migliori & Darling, 1996) up to the meter scale for lower frequency experiments (e.g., Winkler, 1979).

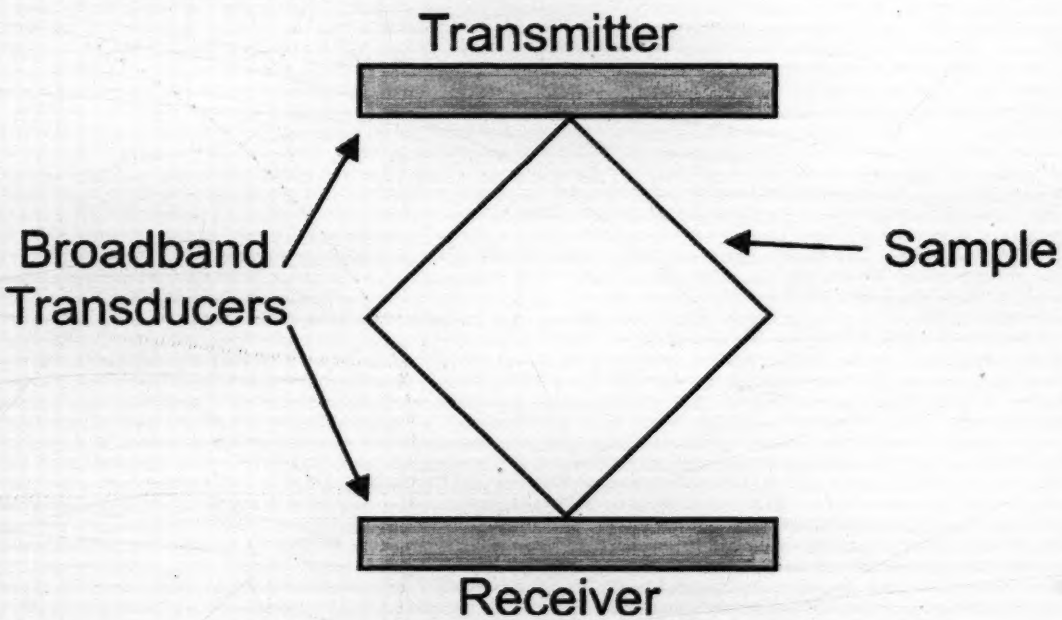

Figure 2.8 - A RUS experimental setup at ultrasonic frequencies. The sample, a few millimeters in size, is held lightly between two broadband transducers. Resonance modes are found in order to determine the elastic constants.

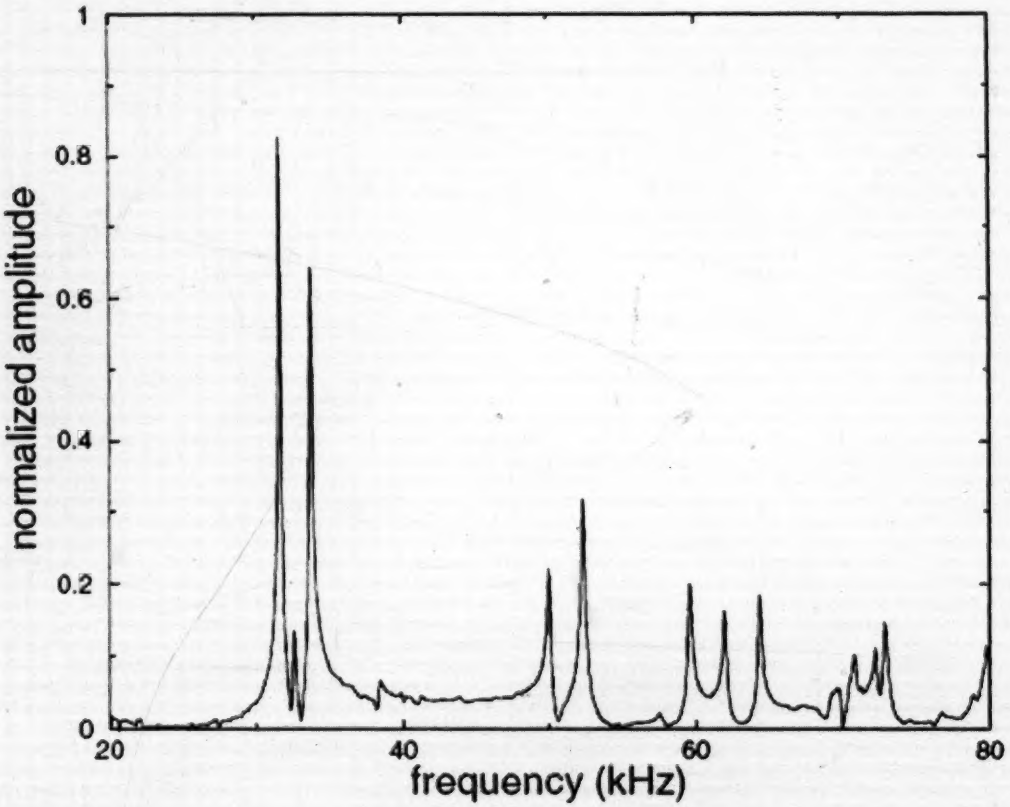

Figure 2.9 - Amplitude versus frequency spectrum of a cylindrical granite core (2.527 cm diameter and 7.15 cm long). Figure from Zadler et al. (2004) with permission to use granted by Blackwell Publishing.

When an RUS experiment is designed, there are several critical factors that must be considered. The first is the sample shape. Resonance modes are different for every shape and it is important to know what these modes are (Leisure and Willis, 1997). Typically parallelpipeds or spheres are used, although cylinders are also employed. Another important factor that needs to be accounted for are the resonant frequencies of the transducers themselves (Migliori et al., 1993). If appropriate transducers are not used

then the normal modes of the transducers may obscure the data, making interpretation more difficult. RUS is often used on metal samples when material can easily be machined into appropriate shapes (Migliori et al., 1993; Chu et al., 1996; Koopman et al., 2002; Leisure et al., 2004), but resonant techniques are gaining more popularity in geophysical experiments (e.g., Ulrich et al., 2002; Zadler et al., 2004). However, a major practical problem with the use of such resonant techniques on rock is that it may be difficult or impossible to include the effects of confining pressure on the material. This is crucial as the wave speeds for rocks, most of which have a highly nonlinear stress-strain relationship at low confining pressures, measured at room pressure will have little correspondence to wave speeds at depth in the earth.

2.5 Summary

A brief overview of elastic anisotropy was given in this chapter to show that the phase velocities of a material depend on the elastic constants. Thomsen's (1986) anisotropic parameters were introduced, which approximately define the anisotropy of TI materials. A short review of the properties of shales and the common causes of anisotropy were given. Common ultrasonic laboratory methods of determining elastic coefficients in materials were also presented. This introduction leads to the next chapter in which the methodologies of making anisotropic measurements and calculating the elastic constants of the resulting materials are discussed.

Chapter 3

Experimental Procedure

The main contribution of this thesis is the measurement of elastic anisotropy in a number of sedimentary rock samples. This is achieved using an ultrasonic pulse transmission method, the basic principles of which were discussed in Section 2.4.1. Briefly, ultrasonic transducers are placed on either end of a sample in order to produce and receive waves. A travel time is then picked from this wave and the velocity through the sample can be calculated. In a medium of TI symmetry, P- and S-wave velocities taken in just three directions can provide the entire suite of elastic constants.

Details of the pulse transmission method used to measure ultrasonic velocities are given in this chapter. In order to simultaneously measure P- and S-waves, a method of stacking piezoelectric ceramics is developed. Methods used to prepare and measure samples will also be given. Examples of waveforms, the procedure to pick travel times, calibration of the signal, and errors in velocities will be discussed in order to prepare the reader for the full results in later chapters.

3.1 Transducers

The transmitting and receiving transducers are the key elements in the ultrasonic measurements. The construction of the transducers employed is described in this section.

Ultrasonic transducers are placed on either end of a core in order to generate and record P- and S-waves (Figure 2.3). Ceramics made from lead zirconate titanate (PZT)

were used as a main component of the transducers in these experiments. PZT is a piezoelectric ceramic which changes shape in response to an applied voltage, and correspondingly a change in shape generates a voltage. The polarization of the ceramic will determine the vibration mode and whether a P-wave or an S-wave is produced. An axially polarized ceramic will cause axial compression/expansion and consequently generate a longitudinal (P-) wave. Correspondingly, a lateral polarization will yield a transverse (S-) wave. In these experiments, the P-wave crystals were circular disks with a diameter of 20 mm and a thickness of 1.97 mm while the S-wave crystals were square plates with side lengths of 17 mm and a thickness of 1.00 mm. Both were labeled by the manufacturer as having resonant frequencies centered on 1 MHz and were made of material PZT-5H from Omega Piezo Technologies Inc.

Originally, attempts were made to place small P- and S-wave transducers side by side in order to measure the different waves at the same time. On 2.54 cm diameter cores however, this brought about the issue of signal strength in soft and layered materials. Also of concern was the matter of phase and group velocities in anisotropic media, as discussed in Chapter 2. These concerns necessitated the development of a new technique. To allow simultaneous measurements of P- and S-waves on the 2.54 cm diameter cores a method of stacking the P-wave ceramic on top of the S-wave ceramic was developed. Methods of stacking transducers have been used in the past (e.g., van Steveninck, 1967). Using conductive epoxy (HSW Pure Silver Conductive Epoxy), the P-wave transducer was placed on the S-wave transducer, separated by a piece of copper foil which acts as an electrode. This arrangement was then affixed onto an aluminum buffer using conductive epoxy (Figure 3.1). The aluminum buffers were 2.54 cm in diameter, with a length of

2.54 cm. The P- and S-wave ceramics were then coated with a thin layer of nonconducting epoxy and allowed to dry. As a final step in preparing the transducers, a damping material of urethane rubber (Flexane®80 Liquid) and iron filings was poured on top of the ceramics (Figure 3.2).

The thin layer of epoxy around the ceramics is very important in order to prevent conduction. The first iteration of the transducers did not have this layer and during testing the signal would deteriorate with increasing pressure. The iron filings in the damping material were causing a small amount of conduction between the positive and negative sides of the ceramics. The conduction would increase as increasing pressure caused more contact between iron pieces. Once the epoxy layer was added to the arrangement this problem disappeared. This method of stacking the P- and S-wave piezoelectric ceramics allows for the largest ceramics, and hence the largest amplitude waves, to be used without pressurizing the sample more than once. Large amplitude waves may be an important factor when working with highly attenuative samples. A total of 6 transducers were made to allow for the measurement of 3 cores simultaneously.

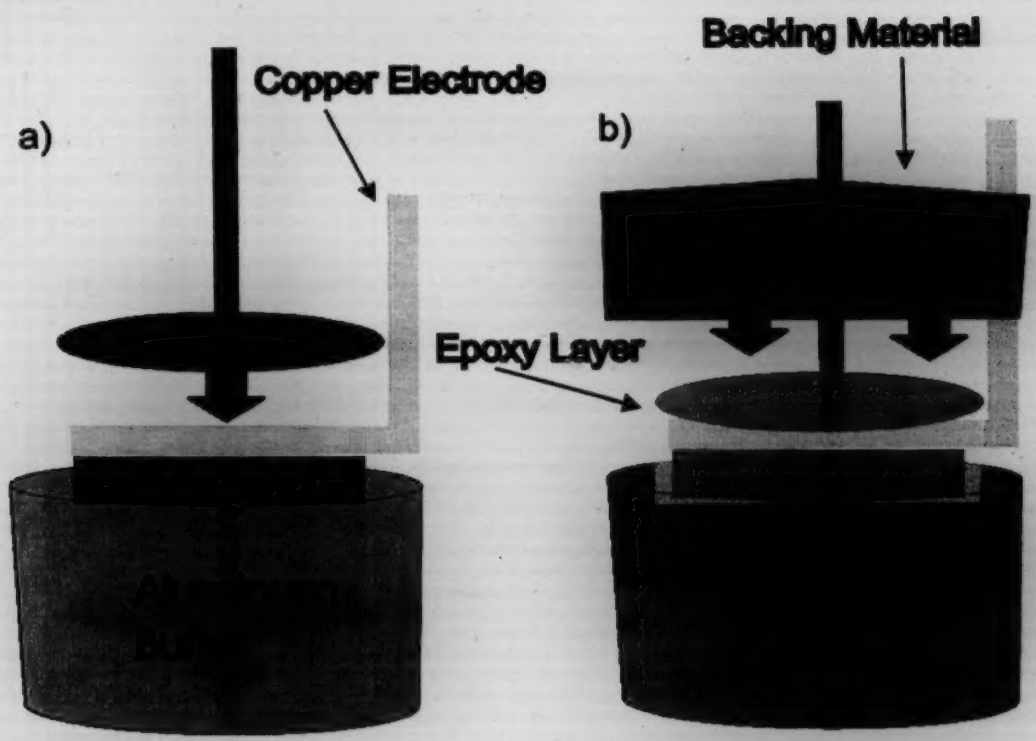

Figure 3.1 - The steps necessary to build the transducers. a) First the P-wave transducer is stacked onto the S-wave transducer with a copper electrode between them. b) The ceramics are then coated with a thin layer of epoxy. The entire back of the aluminum buffer is then coated with a damping material of urethane rubber and iron filings.

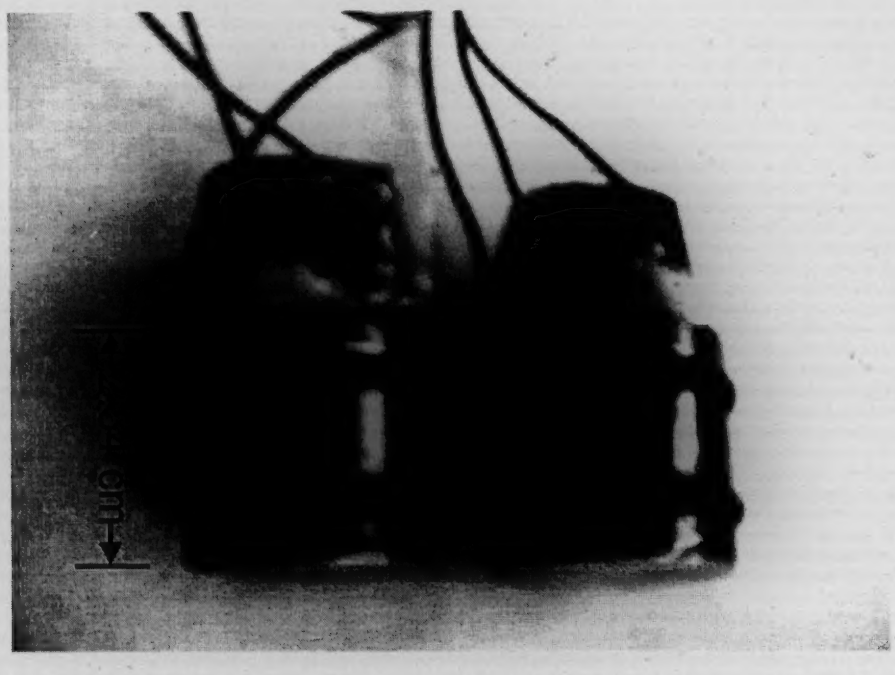

Figure 3.2 - Photograph of the finished transducers. The piezoelectric ceramics are buried in the urethane rubber on the top of the aluminum buffers as shown in Figure 3.1.

3.2 Sample Preparation

This project involved determining elastic parameters in TI samples. This requires obtaining P- and S-wave velocities in three directions; perpendicular to bedding, 45° to bedding, and parallel to bedding. Seven samples from five wells in Southern Alberta were measured using the 'three plug' method (Section 2.4.1) in order to determine their elastic constants. Three cores were taken from each sample, one in each of the required directions as shown in Figure 2.4. Elastic constants were calculated from the velocities using Equations 2.14 - 2.18.

Coring was done dry in order to prevent excess water from being absorbed into the clay minerals and changing the intrinsic properties of the rocks. Coring was done at

low speed and with the coarsest of the diamond bits available in our laboratory, and care was taken to prevent the samples from becoming too hot. Typically, a few seconds of coring was followed by 1-2 minutes of rest, in order to allow the sample to cool. This method also seemed to improve the recovery rate of usable core. Cores proved quite difficult to obtain in some of the samples. Several samples were ruined in the course of coring due to their friable nature. Coring was attempted on approximately eleven or twelve samples and usable cores were obtained in all three directions on only seven samples. Coring in the direction perpendicular to bedding was particularly difficult; rather than produce usable core, the more friable samples would fracture into small disks a few millimeters long. After coring, the ends of the samples were made roughly parallel using a disk sander. Again, in order to prevent the samples from heating excessively this was done at low speed, with plenty of time to allow the sample to cool. The final step to achieving parallelism was to sand the cores by hand using abrasive paper until they were measured to be better than 0.1 mm using a dial gauge. Despite the gentle treatment of the samples, most of the cores were chipped on the edges at the ends of the cores. Finished cores were 2.54 cm in diameter and were 2.1 - 5.7 cm in length. No method was found to adequately core the more friable samples. It seems that the three plug method is inappropriate for these types of samples and a different method must be used. Although not applied here, some possible techniques that could be used are the multi-faced cube method (e.g., Rai & Hanson, 1988), the τ-p method (e.g., Kebaili & Schmitt, 1997), or the single plug method (Wang, 2002a). These techniques are briefly reviewed in Chapter 2.

After sanding, the three cores were dried at 80-85° C for a minimum of 48 hours. When the samples were dried, they were removed from the oven and weighed

immediately before the final preparation and measurement. A thin (0.08 mm) piece of lead foil was attached to the ends of the core in order to improve contact between the ends of the core and the aluminum buffers during measurements. Each core was then placed into securely fitting reinforced Tygon™ tubing and a transducer was placed on each end (Figure 3.3). The transducers were carefully aligned to ensure proper polarization of the shear wave ceramics. The first sample in this data set was measured using Tygon™ tubing that was not reinforced. After the sample was removed from the pressure vessel it appeared, from a slight discolouration, that the sample had leaked. The discolouration was only superficial because when the sample was sanded lightly the sample was normally coloured. It is not believed that this affected the velocities in a significant way. The exact cause of this leak was not discovered, although every sample measured subsequently was jacketed with reinforced Tygon™ and the problem never reoccurred.

P-wave transmissions were measured on all 3 cores while the SH- and qSV-waves were measured in the parallel and 45° to bedding directions, respectively (Figure 2.4). The S-wave traveling perpendicular to bedding was also measured. In TI media, the particular polarization of this shear wave is immaterial. After the transducers had been aligned, metal ties were tightened around the Tygon to improve the seal and prevent leakage of the surrounding hydraulic fluid. If hydraulic fluid leaks into the sample, it intrudes into the pore space and changes the properties of the sample. Since the oil cannot be fully removed, caution must be taken that the sample does not leak. The final step in the preparation was connecting the transducers to the pulse generator and oscilloscope, and placing them inside the pressure vessel.

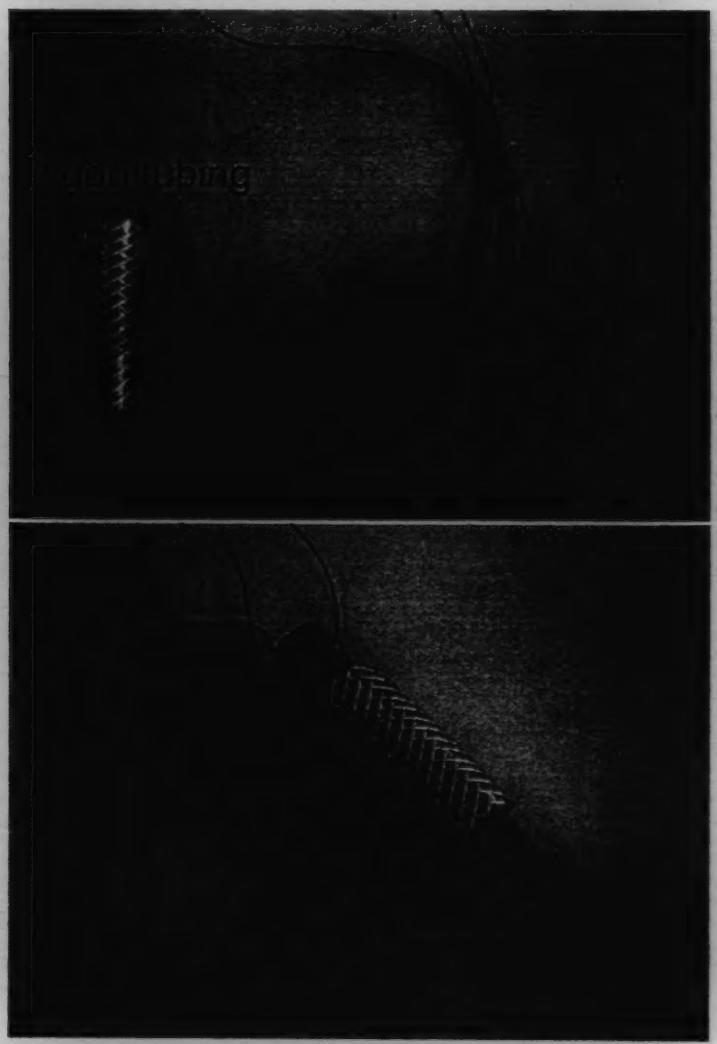

Figure 3.3 – Before and after photos of a prepared sample with the various components labeled. Reference is a dime (diameter 18.03 mm).

3.3 Data Acquisition

The data acquisition system consisted of a pressure vessel, a pulse generator, and a digital oscilloscope (Figure 3.4). Using an air pump the pressure vessel is capable of reaching pressures of up to 200 MPa in steps as small as 0.25 MPa by adjusting with a

hand driven pump. A hydraulic fluid (76 Unax AW 22) was used as the confining fluid. A cylindrical cavity 10 cm in diameter and approximately 40 cm deep in the pressure vessel was large enough to fit all three cores, allowing simultaneous velocity measurements for all directions. The pulse generator (Panametrics, model 5800 PR) was used to pulse the piezoelectric transducers with a fast-rising, 200 V square wave. The resulting wave propagated through the sample and was recorded by a digital oscilloscope (Gagescope, model 400-586-203). The oscilloscope recorded the signal in time intervals of 10 ns and gave the final waveform as a stack of 256 traces to minimize random noise.

Measurements were taken in 2.5 MPa or 5.0 MPa increments both during pressurization and depressurization. The depth from which the sample was taken controlled the peak pressure. The peak pressure for each sample depended on the density of the sample and the depth from which it was taken. The peak pressure was calculated from:

$$P = \rho g h \qquad (3.1)$$

where ρ is the density of the sample, g is acceleration due to gravity (9.81 m/s^2), and h is the depth from which the sample was retrieved. This is a very rough estimate of what the in situ pressure would be for each sample. It assumes that material between the surface and the sample is of the same density as the sample. Further, there is no correction for any pore fluid pressure that may be present in situ. It should be noted that at the time of these calculations precise determination of the densities had not been made. Instead, the density was calculated by measuring the dimensions and weight of the sample cores. Since many of the cores had chips in them this brings about a slight discrepancy if calculating the peak pressure with the bulk densities given in Chapter 4. Using this

method, the peak pressure for the samples fell in the range 22.5 – 85.0 MPa. Step size and peak pressure for each sample is shown in Table 3.1.

Twenty-five minutes were taken between each measurement to allow temperature – pressure conditions in the pressure vessel to equilibrate, and to allow any cracks or pores in the sample to open or close. During this time, the waveforms would slowly change. In the first few seconds after the pressure change the first arrival would quickly become faster or slower, then it would slowly adjust towards the equilibrated value. Typically, the signal became stronger with pressure due to better contact. Christensen & Wang (1985) tested Berea sandstone and noted that equilibration was usually attained in less than twelve hours in their sample. One of the samples in this work (Mannville shale 1 [SSA010], Figure 5.4) was inadvertently left under pressure overnight while measuring. The time between measurements was approximately 20 hours. For the next several data points, the P-wave velocities in the directions perpendicular and 45° to bedding were approximately 1.2% higher than expected. The P-wave parallel to bedding and the S-wave perpendicular to bedding also appeared approximately 0.3% higher than expected, although this is well within regular errors and difficult to ascertain. The remaining S-waves showed no discernable increase. The extra increase in velocities is due to increased grain contact and decreased porosity that did not occur within the twenty-five minutes usually allotted for equilibration.

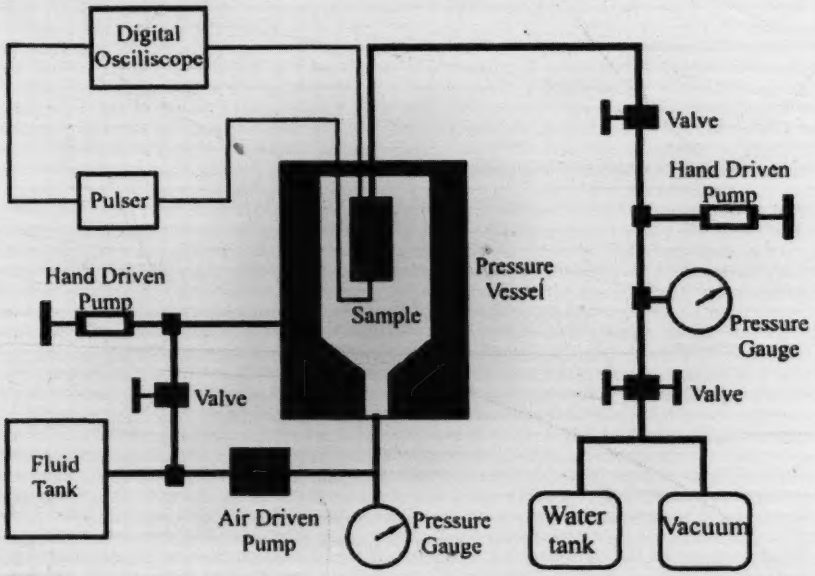

Figure 3.4 - A schematic of the experimental setup. The sample was placed in the pressure vessel and pulsed with the pulser. The oscilloscope read the signal. Pressure was provided from an air driven pump and fine tuned with a hand driven pump. The pore pressure equipment was not used in this set of experiments. Figure modified after He (2006).

Sample	Step size (MPa)	Peak pressure (MPa)
Mannville shale 1 (SSA010)	5.0	75.0
Mannville shale 2 (SSA011)	5.0	75.0
Mount Head carbonate (SSA019)	5.0	85.0
Wabamun carbonate (SSA025)	5.0	85.0
2nd White Specks sandstone (SSA034)	2.5	22.5
Big Valley anhydrite (SSA035)	5.0	45.0
Bow Island sandstone (SSA037)	2.5	25.0

Table 3.1 - Peak pressure and pressure step sizes of each sample.

3.4 Waveforms & Calibration

Calibration involved measuring the delay through the aluminum buffers so travel times obtained in later experiments could be adjusted. This calibration is necessary as each transducer constructed will have a slightly different delay time. Further, the response of the transducers is pressure dependent and this effect must be corrected for in order to eliminate the error that would otherwise be introduced. To account for this, the buffers were measured end-to-end under pressure. Measurements were found for pressures up to 90.0 MPa. Care was taken to use the same buffer pairs that were used in calibration for all other experiments. Travel times of the resulting signals were picked at the first extremum. A typical record is shown in Figure 3.5, with the first arrival marked by arrows. Figure 3.5a shows the waveform through end-to-end buffers while Figure 3.5b shows the signal at the same pressure traveling through the finished sample. The buffer travel time is subtracted from the total travel time, leaving only the time through the sample. This method provides a more accurate travel time than attempting to pick the first break of the signal, since the extremum is much more reliably picked. The fact that the travel time through the sample is obtained by subtracting the travel time of the buffers removes any errors from not picking the first break and makes the results shown here comparable to other studies. The length of the sample is then divided by the travel time to provide the velocity through the sample.

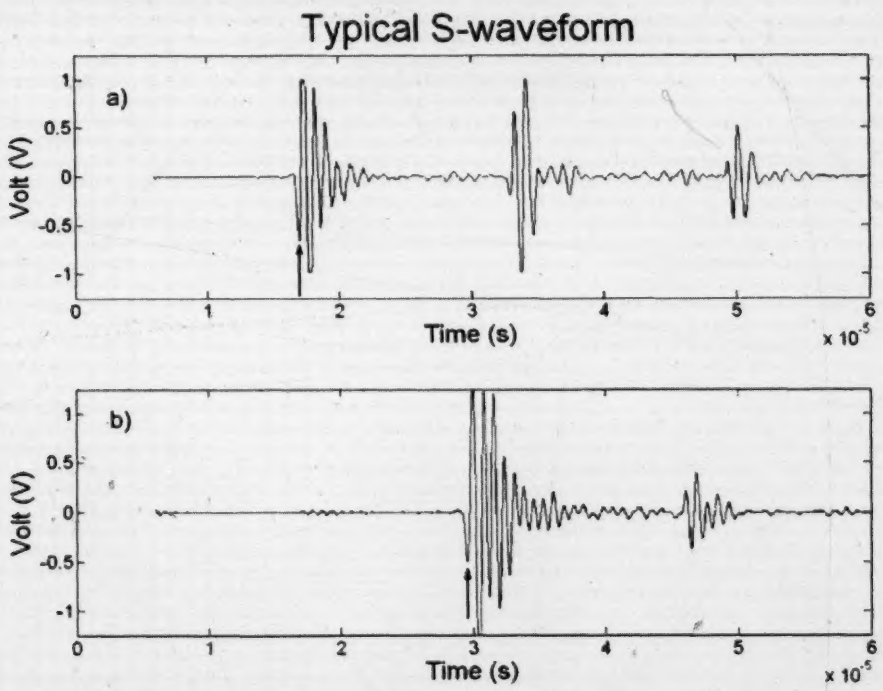

Figure 3.5 - The signal through a) the buffers and b) the buffers and sample. The travel time is picked at the first extremum, marked by arrows. To obtain the travel time through the sample, the time in a) is subtracted from the time in b).

The travel times of the buffers had a small amount of scatter and hysteresis (<0.02 μs), except for a few outliers. When preliminary data was corrected using these calibration curves it was clear that the outliers were not appropriate corrections. Since the calibration data appeared to depend linearly on pressure and had negligible hysteresis it was fit with a straight line. The final calibration data is shown in Table 3.2.

Pressure (MPa)	Buffer Set P12	P34	P56	S12	S34	S56
5.0	9.076	9.397	9.209	17.058	16.982	17.037
10.0	9.069	9.389	9.196	17.053	16.977	17.030
15.0	9.062	9.381	9.183	17.048	16.972	17.024
20.0	9.055	9.372	9.170	17.043	16.967	17.017

Pressure (MPa)	Buffer Set P12	P34	P56	S12	S34	S56
25.0	9.048	9.364	9.157	17.039	16.961	17.010
30.0	9.041	9.356	9.144	17.034	16.956	17.004
35.0	9.034	9.348	9.131	17.029	16.951	16.997
40.0	9.027	9.340	9.118	17.024	16.946	16.990
45.0	9.021	9.332	9.106	17.019	16.940	16.983
50.0	9.014	9.323	9.093	17.014	16.935	16.977
55.0	9.007	9.315	9.080	17.009	16.930	16.970
60.0	9.000	9.307	9.067	17.005	16.924	16.963
65.0	8.993	9.299	9.054	17.000	16.919	16.957
70.0	8.986	9.291	9.041	16.995	16.914	16.950
75.0	8.979	9.283	9.028	16.990	16.909	16.943
80.0	8.973	9.275	9.015	16.985	16.903	16.936
85.0	8.966	9.266	9.002	16.980	16.898	16.930
90.0	8.959	9.258	8.989	16.976	16.893	16.923

Table 3.2 - Calibration times (μs) for each buffer set.

As mentioned previously, waveforms were collected as confining pressure was increasing as well as decreasing. This data can be plotted together to provide a 'suite' of normalized waveforms over the pressure range. The suite of waveforms from the buffers is shown in Figure 3.6. Since the signal is only passing through aluminum there is very little dependence on pressure over this range. Figure 3.7 shows these suites for all P- and S-waves measured on the Mannville shale 1. The delay of the buffers is removed and the dependence of travel times through the sample on the confining pressure can be observed. Although there is an effect, the travel times of the Mannville shale 1 do not change significantly with confining pressure. This indicates a lack of closing microcracks or pores in the sample, but these issues will be discussed in more detail later. The character of the observed waveforms for other samples has a more dramatic dependence on pressure. Figure 3.8, for example, shows P-waveforms obtained on the Mount Head carbonate. As the pressure increases to 85.0 MPa the waves arrive significantly earlier. This indicates that as the pressure is increased, there is some type of porosity closing

which increases velocity. These mechanisms will be discussed in more detail in Chapter 5. Note in the waveform suites that differences in travel times between waves traveling parallel and perpendicular to bedding cannot be interpreted as anisotropy since measurements were performed on cores of different lengths.

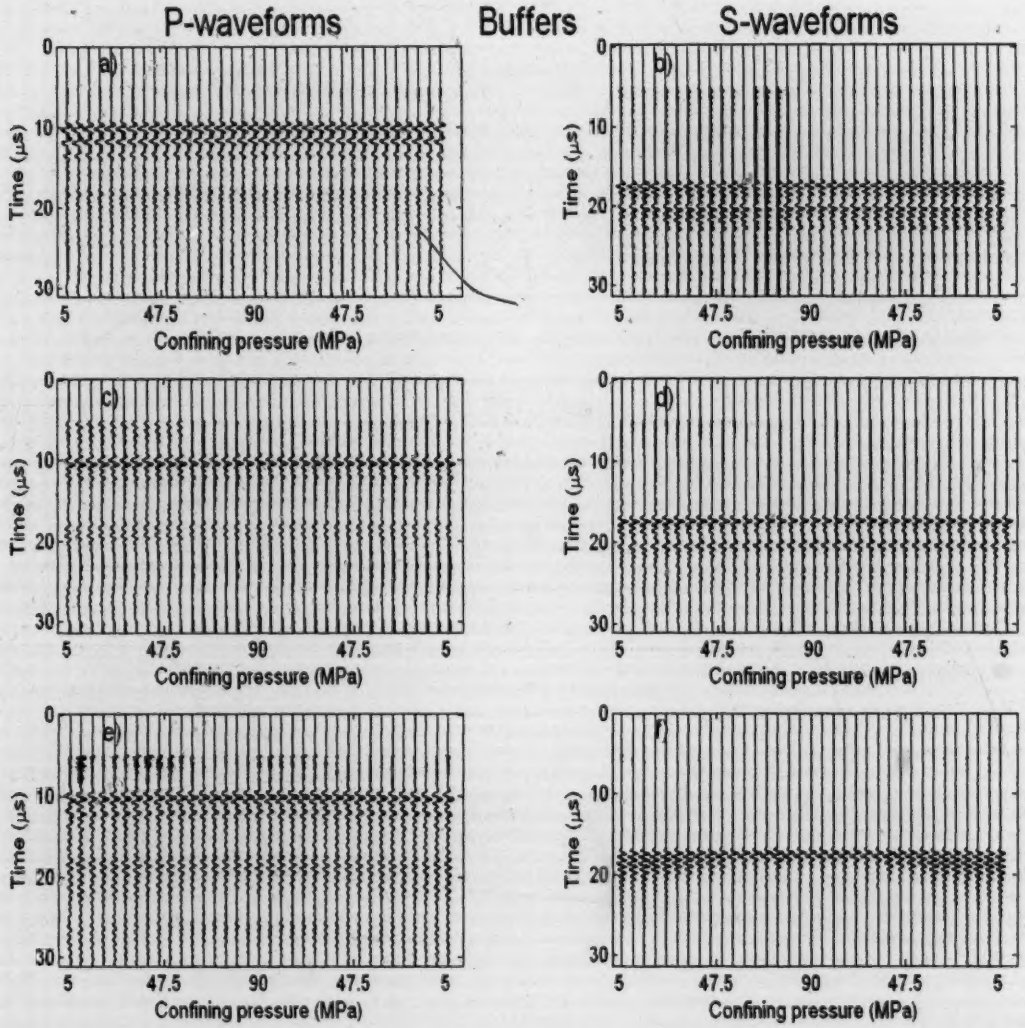

Figure 3.6 – Waveform suites of the buffers. a) and b) show the P- and S-waves, respectively, in the 12 buffer set. c) and d) show the waveforms in the 34 set, and e) and f) show the waveforms in the 56 set. There is almost no pressure dependence.

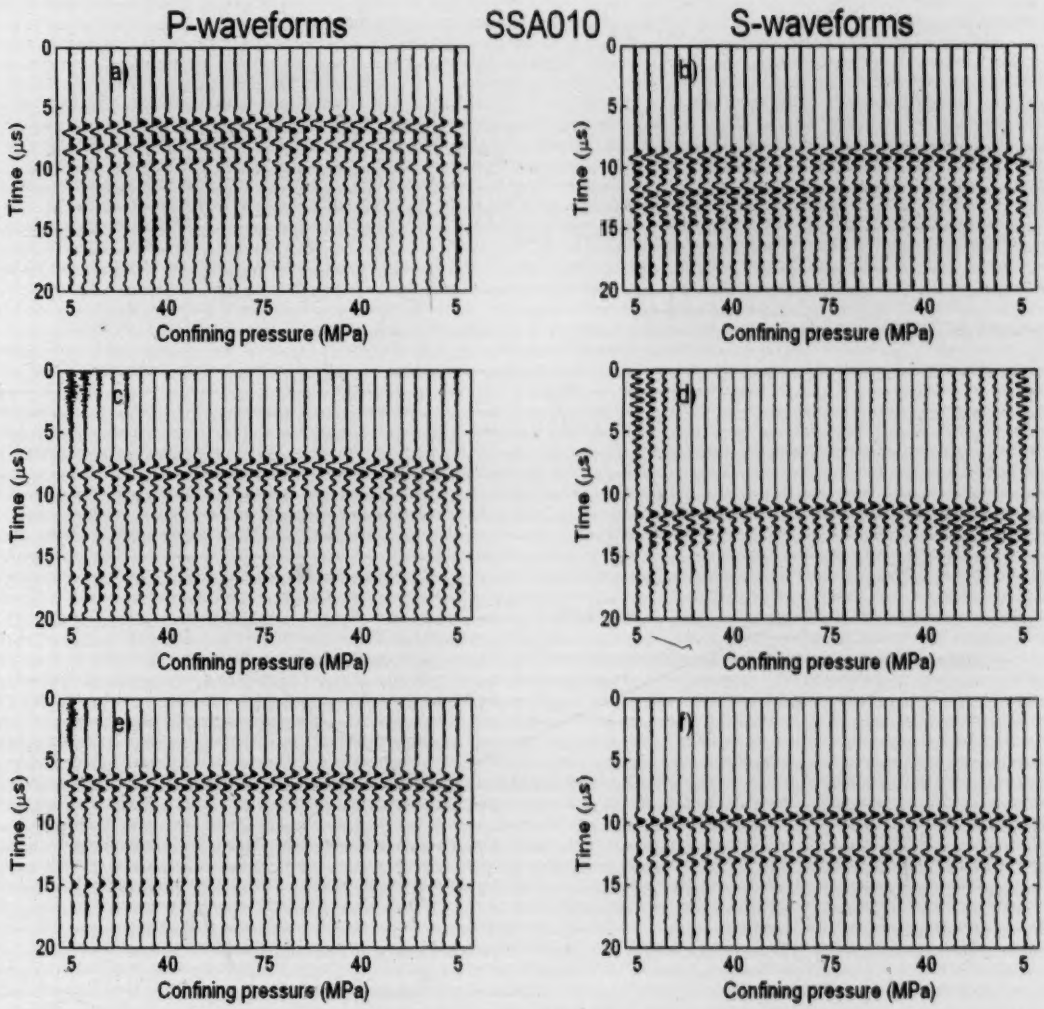

Figure 3.7 – Complete suite of waveforms obtained for the Mannville shale 1. a) and b) show the P- and S-waves, respectively, traveling perpendicular to bedding. c) and d) show the waveforms traveling 45 to bedding, and e) and f) show the waveforms parallel to bedding.

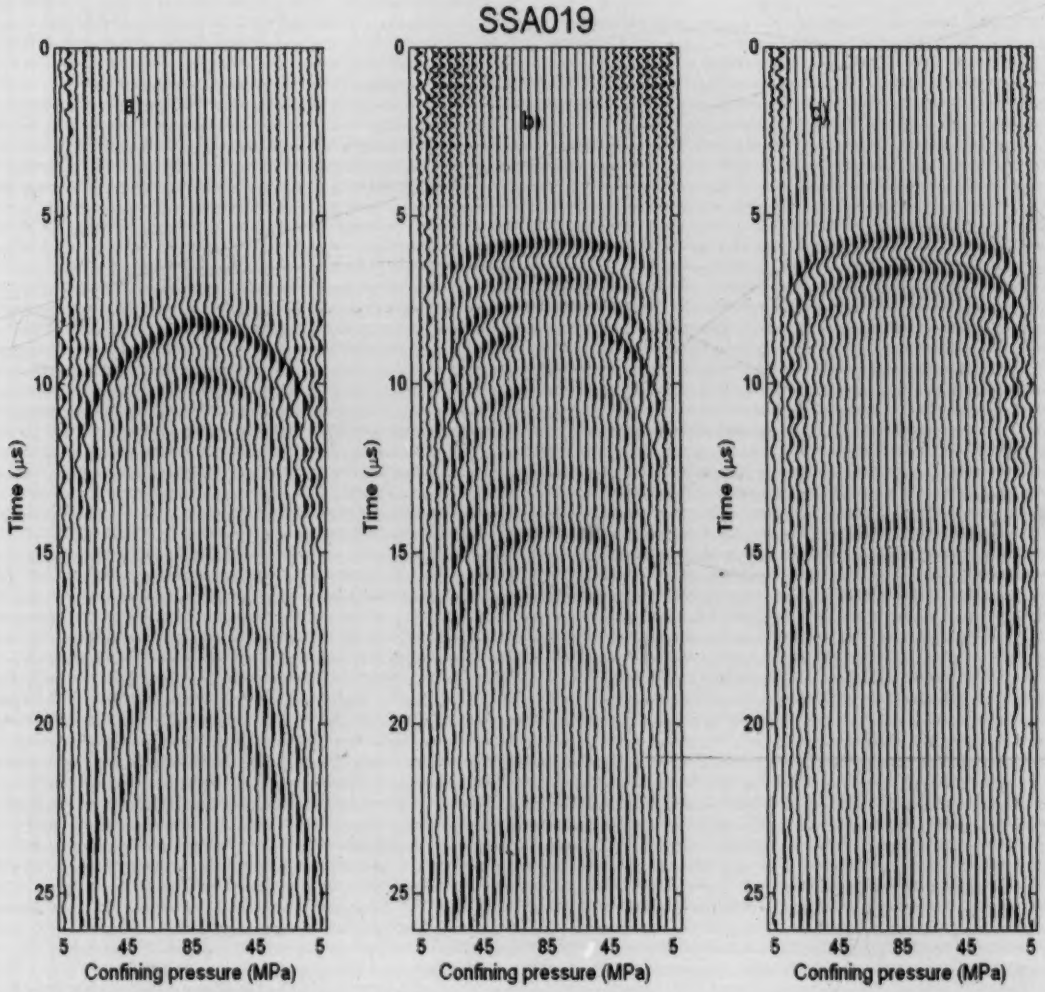

Figure 3.8 - P-waves measured in the directions a) parallel, b) 45°, and c) perpendicular to bedding in the Mount Head carbonate. This sample shows a strong dependence on travel time with pressure.

In order to ensure that the transducers are in the correct frequency range to measure the signal properly, the first arrival and the amplitude spectrum of the signal are shown in Figure 3.9 and Figure 3.10. Figure 3.9 shows the signal through only the aluminum buffers at 75.0 MPa. The piezoelectric ceramics were labeled as having a peak

frequency of 1 MHz and this central frequency has shifted only slightly. Figure 3.10 shows the initial signal and amplitude spectrum through the Mannville shale 1 at 75.0 MPa. This is fairly representative of the other samples, however there is sometimes a slightly larger shift of peak frequency, this likely depends on the details of the final composition of each individual transducer. Like the buffer-to-buffer configuration, the central frequency is near 1 MHz. The small shift in peak frequency of the signal is partially brought about due to the backing material used in making the transducers. These plots show that reasonable 'broadband' waveforms were produced by the transducers with good energy provided over the ranges of at least 0.5 MHz to 1.5 MHz for both transducers.

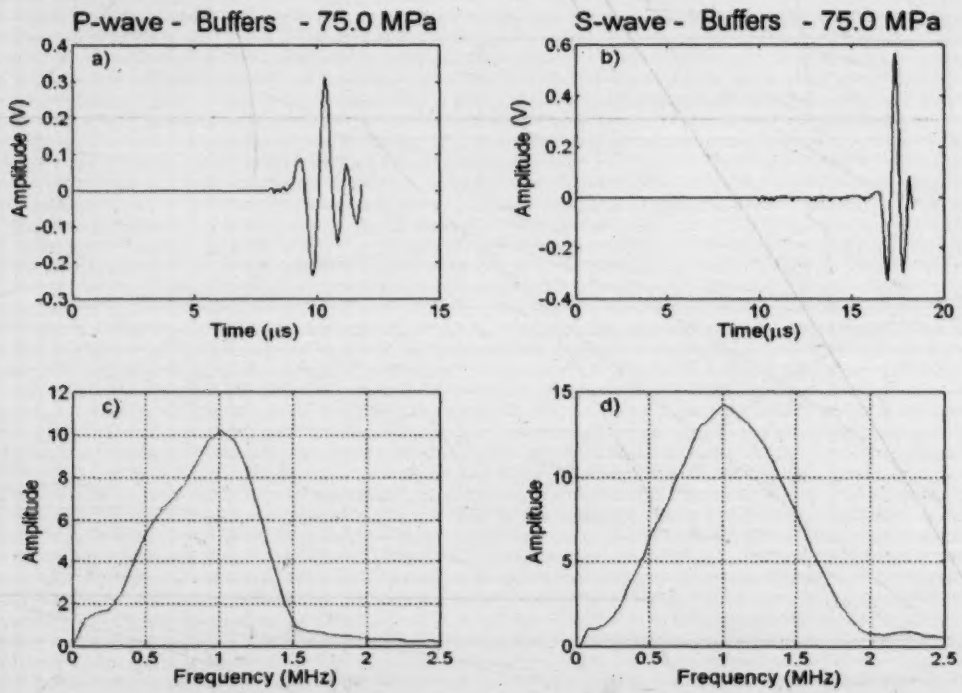

Figure 3.9 – a) The initial signal and c) amplitude spectrum of P-waves through the buffers. The same is shown for S-waves in b) and d). The peak frequency is around 1 MHz in both the P- and S-waves.

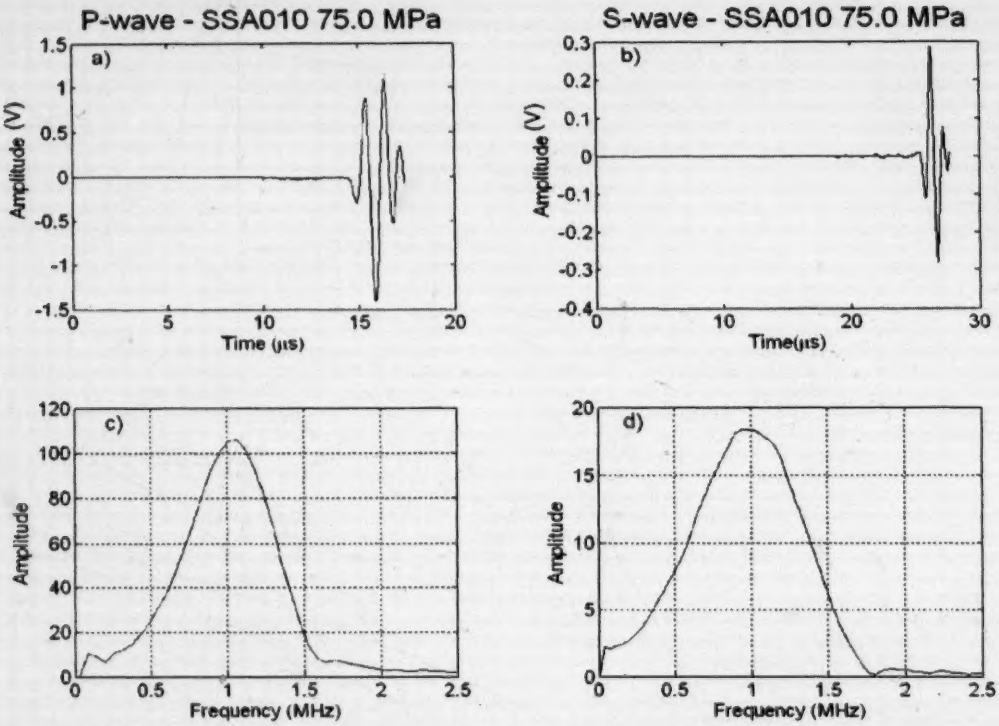

Figure 3.10 - a) The initial signal and c) amplitude spectrum of P-waves through the Mannville shale 1. The same is shown for S-waves in b) and d). The peak frequency is near 1 MHz.

3.5 Analysis of Errors in Velocity

Despite the careful calibration, there are still errors that are unavoidable. There are three main sources of error in the final sample travel times. These sources are:

1) Travel time picking error: 0.05 μs maximum for low pressures (point is excluded otherwise). This error is generally 0.02 μs or less, particularly for high pressures.
2) Parallelism error: A total error of no more than 0.1 mm in the sample length.
3) Buffer calibration error: Considered to be less than 0.02 μs.

There is also the concern of the sample shortening under pressure. If this is not taken into account the velocities will appear higher than they actually are. Sample compression is not expected to be of great concern; estimates are on the order of 0.1-0.2% over the entire pressure range for most samples, and less than 0.1% for those samples not subjected to higher pressures. Nonetheless, due to the possible shortening of samples, the velocities given here are upper bounds.

One of the shortest samples in these experiments is the 2nd White Specks sandstone that was cored parallel to bedding. Calculating error on this sample will give us a maximum error. The velocity of the sample is found as:

$$V = l/t \tag{3.2}$$

where l is the length of the sample and t is the travel time through the sample.

Propagation of error gives the error of the velocity as:

$$\delta V = V\sqrt{\left(\frac{\delta l}{l}\right)^2 + \left(\frac{\delta t}{t}\right)^2} \tag{3.3}$$

where δ denotes the error of the particular parameter.

The length of the perpendicular to bedding core of the 2nd White Specks sandstone is 0.02359 m, and the P- and S-wave velocities at the lowest pressure (22.5 MPa) are 3597 m/s and 2718 m/s respectively. In both cases the maximum error in length is 0.0002 m and the maximum error in time is 0.05 μs + 0.02 μs = 0.07 μs. Evaluating Equation 3.2 gives:

$$\frac{\delta V_P}{V_P} = \sqrt{\left(\frac{\delta l}{l}\right)^2 + \left(\frac{\delta t}{t}\right)^2} = \sqrt{\left(\frac{0.0001}{0.02359}\right)^2 + \left(\frac{0.07*10^{-6}}{6.56*10^{-6}}\right)^2} = 1.1\%$$

$$\frac{\delta V_S}{V_S} = \sqrt{\left(\frac{\delta l}{l}\right)^2 + \left(\frac{\delta t}{t}\right)^2} = \sqrt{\left(\frac{0.0001}{0.02359}\right)^2 + \left(\frac{0.07 * 10^{-6}}{8.68 * 10^{-6}}\right)^2} = 0.9\%$$

This worst-case scenario gives a 1.1% error in the P-wave velocity and a 0.9% error in the S-wave velocity. Since error in picking the time is generally less than 0.05 μs and the length of the core is generally longer than 2.359 cm, the error in the measured velocities is generally less than 1%, and is more typically expected to be around 0.5% - 0.7%.

3.6 Summary

This chapter gave details of the experimental method used to obtain data reported in Chapter 5. Detailed information on how to build transducers using stacked P- and S-wave ceramics, as well as how to prepare the samples and acquire data was provided. Examples of waveforms were introduced and the method of picking travel times from them was described. The amplitude spectra of the resulting waves were examined and it was determined that although subtle, the waves have deviated slightly from 1 MHz. Velocity error was calculated resulting in a maximum error of 1.1% for P-waves and 0.9% for S-waves.

Chapter 4

Characterization

This chapter will review the methods used to characterize the samples. A helium pycnometer is used to determine density and porosity while a mercury porosimeter is used to examine the pore structure. Whole rock analysis and X-ray diffraction are used to determine the minerals present in the sample, while scanning electron microscope images and thin sections are used to describe the texture.

4.1 Introduction

Core samples were obtained from the Energy and Utilities Board (EUB) core repository facility in Calgary for this project. These samples were chosen by Dr. Dean Rokosh on the basis of the examination of well logs prior to sampling. A total of thirty-two cores were collected whose origins were from various locations in Alberta. In this work, a total of seven samples from five wells and six different formations have been studied, all from SW Alberta (Figure 4.1, Table 4.1). These cores can be considered a representative collection from some of the major formations in SW Alberta.

Most of the samples were slightly friable which caused some fracturing during coring; however, usable cores were eventually obtained in all directions. There are several different types of rocks and they come from a variety of depths. Aside from the fact that they are generally fine grained and layered, there are no unifying themes between the individual samples. This highlights the difficulties that can be encountered

in attempting to obtain appropriate materials, even for a trained geologist, as the original goal was to sample clay rich shales.

Sample SSA010 is from the Mannville formation and is one of two samples that best represent a clay-rich shale. This sample comes from a depth of 3021.0 m, is dark grey, and is approximately 30% clay, most of which is smectite and illite (Heather Kaminsky, personal communication). SSA010 is very finely layered and appears homogenous laterally. Photos of all of the samples are seen in Figure 4.2.

SSA011 is the second sample that is most representative of a clay-rich shale. This sample is from the same well and formation as SSA010, although the depth that this core was retrieved from is slightly deeper at 3078.9 m. SSA011 is dark grey and layered and seems slightly more heterogeneous than SSA010.

SSA034 is largely quartz with small amounts of clays and other minerals. This sample is from the 2nd White Specks formation and was cored from a depth of 970.0 m. SSA034 is a medium gray with dark gray layers. The size of the layers varies widely; some layers are as small as 1 mm, although usually larger, some layers are up to 1.5 cm. This sample is fairly heterogeneous, layers often become thicker or thinner laterally.

SSA037 is similar to SSA034 in terms of mineral content. SSA037 is mostly quartz, with a small amount of other minerals. This sample is a light gray and very finely layered. The layers are typically less than 1 mm, and the sample appears to be laterally homogeneous. This sample is from the Bow Island formation and was sampled from a depth of 1044.7 m.

SSA019 is from the Mount Head formation and contains mainly dolomite and quartz, with very low levels of clay. It is a light colour and appears very homogenous

with no layering or other noticeable features. This sample was not friable and cored easily.

SSA025 is another sample whose dominant constituent mineral is dolomite, and also has very low levels of clay. This sample is from the Wabamun formation, taken from a depth of 3643.9 m. SSA025 is dark gray with very fine layering. This sample seems to be laterally homogenous.

SSA035 contains mainly anhydrite and lesser amounts of dolomite. Visually, it is alternating layers of light and medium gray, and somewhat heterogeneous. The layers are generally quite thick, often approaching 1 cm. This sample is from the Big Valley formation and from a depth of 1837.5 m.

In order to more easily identify the samples they will no longer be referred to by number. Rather, they will be referred to by the formation name and type of sample. The new names are given in Table 4.1.

Sample[a]	Location	Elevation of Kelly Bushing (m)	Depth below Kelly Bushing (m)	Depth below sea level (m)
Mannville shale 1 (SSA010)	6-11-14-29W4	1328.2	3021.0	1692.8
Mannville shale 2 (SSA011)	6-11-14-29W4	1328.2	3078.9	1750.7
Mount Head carbonate (SSA019)	14-12-16-2W5	1322.5	3620.0	2297.5
Wabamun carbonate (SSA025)	7-20-6-3W5	1578.8	3643.9	2065.1
2nd White Specks sandstone (SSA034)	6-16-6-22W4	975.2	970.0	-5.2

Sample[a]	Location	Elevation of Kelly Bushing (m)	Depth below Kelly Bushing (m)	Depth below sea level (m)
Big Valley anhydrite (SSA035)	6-16-6-22W4	975.2	1837.5	862.3
Bow Island sandstone (SSA037)	6-34-10-22W4	943.1	1044.7	101.6

Table 4.1 - Geological parameters. [a] Formations are based on the provided well log interpretations.

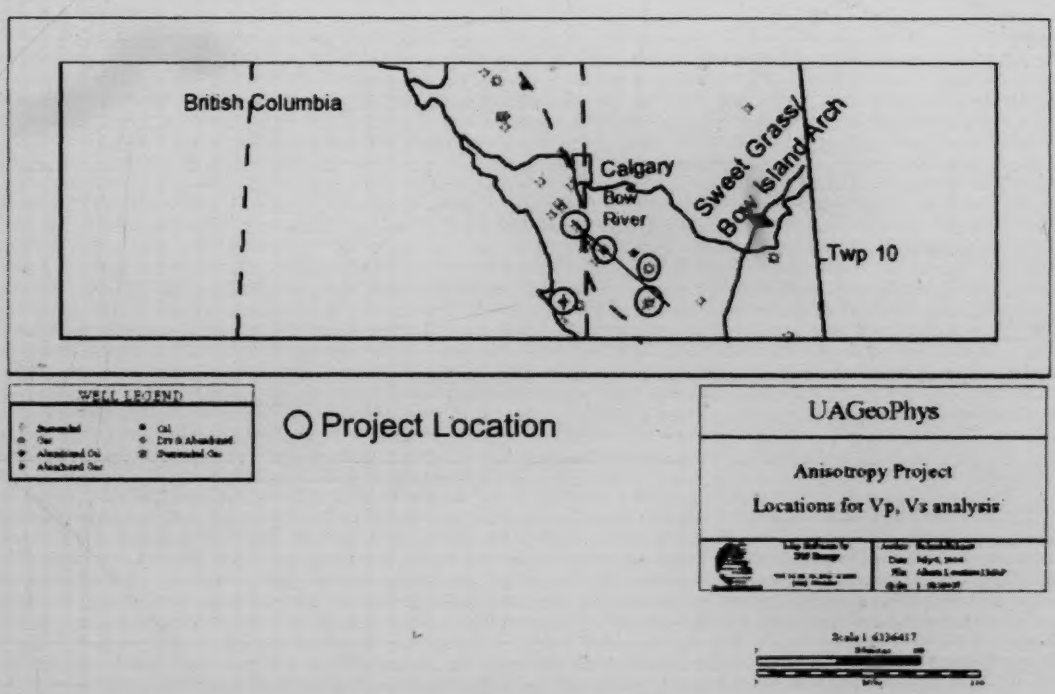

Figure 4.1 - Sample locations. Seven samples were studied from these five wells. The line is the line along which the logs in Figure 4.3 are plotted.

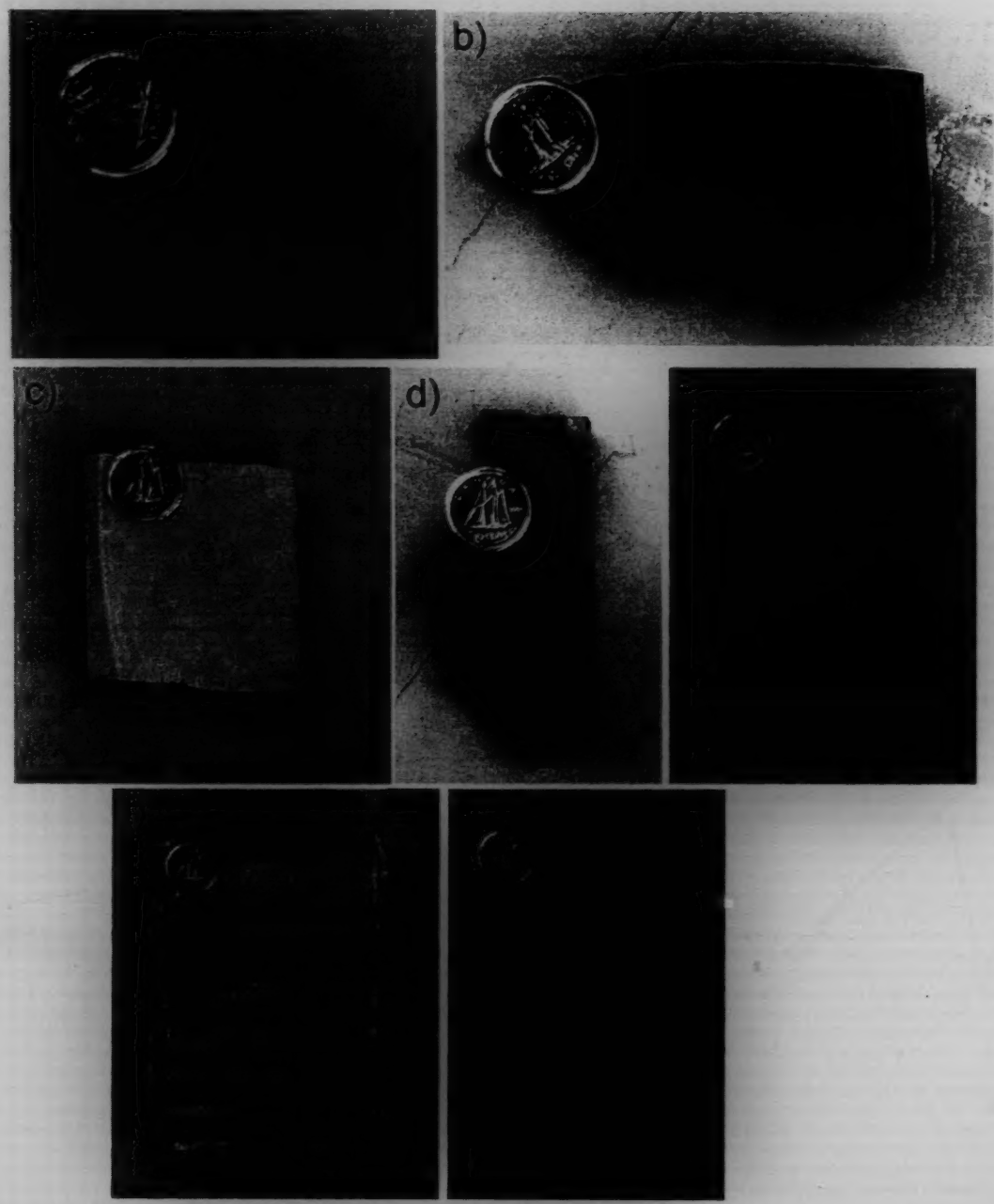

Figure 4.2 - Photographs of a) Mannville shale 1 (SSA010), b) Mannville shale 2 (SSA011), c) Mount Head carbonate (SSA019), d) Wabamun carbonate (SSA025), e) 2nd White Specks sandstone (SSA034), f) Big Valley anhydrite (SSA035) and g) Bow

Island sandstone (SSA037) in the plane perpendicular to bedding. Bedding is horizontal and the assumed symmetry axis is vertical. Reference is a dime (diameter 18.03 mm).

Available well logs for the samples are plotted in Figure 4.3. They are projected onto the line shown in Figure 4.1, where the normal from that line intersects the project locations. The formations which the samples originated from are indicated. The depths and names of the formations came from interpretations provided with the logs. Natural radioactivity and P-wave sonic logs are shown. The Bow Island sandstone log file did not contain P-wave sonic information.

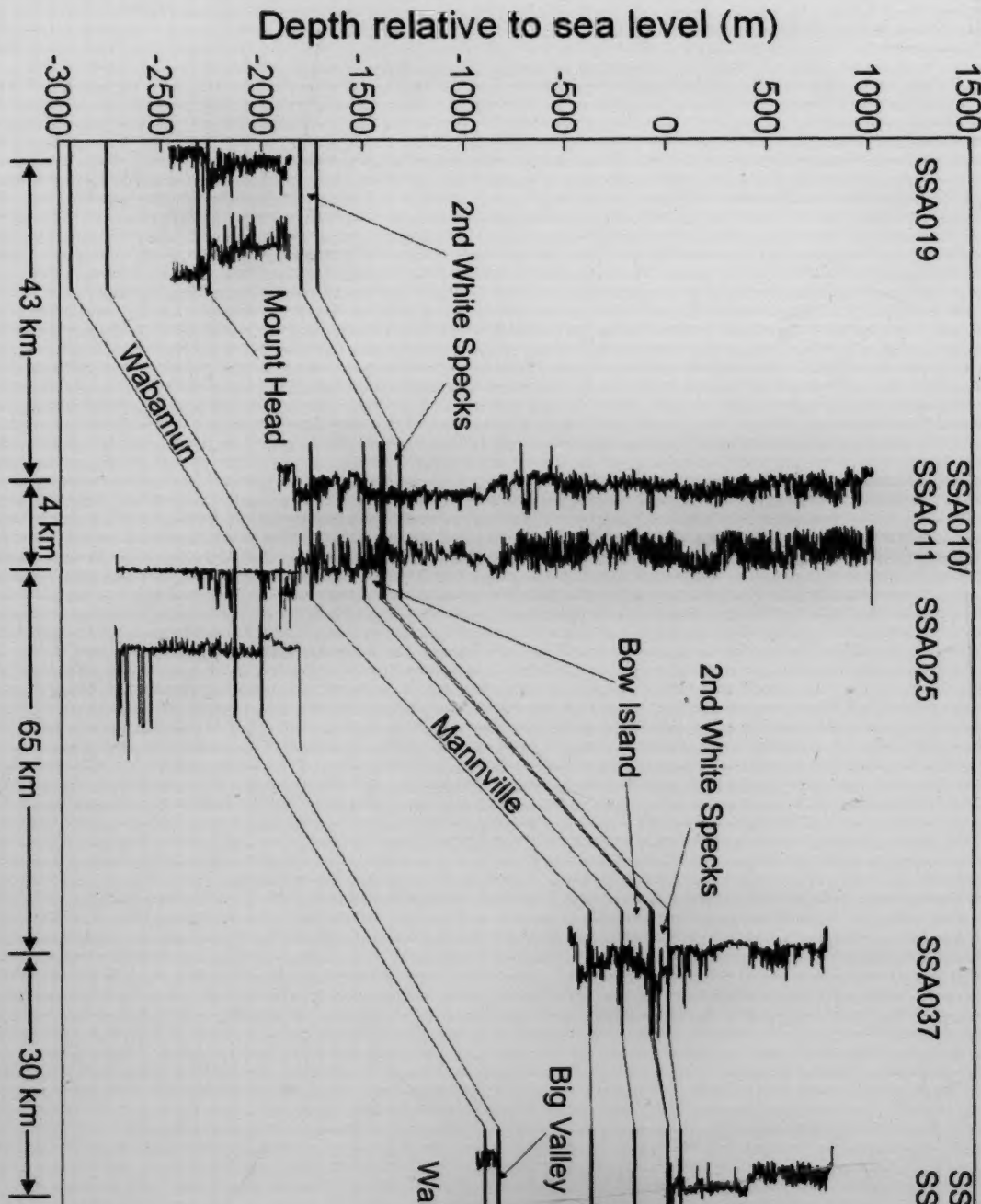
Depth relative to sea level (m)
1500
1000
500
0
-500
-1000
-1500
-2000
-2500
-3000
SSA019
SSA010/
SSA011
SSA025
SSA037
SSA034/
SSA035
2nd White Specks
Mount Head
Wabamun
Bow Island
Mannville
2nd White Specks
Big Valley
Wabamun
43 km
4 km
65 km
30 km

Figure 4.3 – Natural radioactivity (left log, blue) and P-wave sonic velocity (right log, green) for each sample. The Bow Island sandstone (SSA037) does not have a sonic log. Each sample is placed where the normal of the line in Figure 4.1 intersects.

4.2 Density & Porosity

Helium porosimetry and another medium displacement method are used to determine the grain and bulk densities and the porosities of the samples. The methods and results are described and examined in this section. Mercury porosimetry is used to examine the pore size distributions.

4.2.1 Grain Density

Grain density is the density of only the solid mineral constituents of the rock. That is, the density of the sample minus any volume contributed from pores, microcracks, or voids between grains. The grain density was determined using a helium pycnometer (Micromeritics model MVP-6DC) at the University of Alberta. The pycnometer determines the volume of the solid portion of a sample using the intrusion of helium at a known temperature and pressure relative to a calibration volume. There are two chambers in the pycnometer. The sample is placed in the second chamber. The first chamber is flooded with He gas at a known temperature and is allowed to equilibrate in pressure. Once this pressure is recorded (P_1), a valve is opened allowing the He to flow into a second reference chamber. The final pressure is then recorded (P_2). This final pressure depends on the total volume accessible to the He gas between the two chambers, that is, the total volume of the chambers minus that of the sample. Using the perfect gas law:

$$PV = nRT \tag{4.1}$$

where P is pressure, V is volume, n is the number of moles of gas, R is the gas constant, and T is the temperature. The final solid volume may then be calculated via:

$$V_S = V_C - V_R\left(\frac{P_1}{P_2} - 1\right) \tag{4.2}$$

where V_C is the volume of the second chamber, V_R is the volume of the first reference chamber, P_1 is the pressure when helium is only in the first chamber, and P_2 is the pressure after the helium has been allowed to flow into the second chamber.

Since helium can intrude into the pores and void spaces of the rock grain volume, rather than envelope volume, is determined. The grain density is simply:

$$\rho_G = \frac{m}{V_S} \tag{4.3}$$

where m is the mass of the dried sample. The grain densities measured for the samples are shown in Table 4.2. For convenience, the densities of selected minerals are included for comparison. Samples were dried and weighed immediately prior to measuring. The scale used to measure the samples was accurate to 0.01 grams.

The samples appear to be in two distinct groups where the two shale and 2 sandstone samples have grain densities of 2.633 g/cm^3 ± 0.017 g/cm^3, while the two carbonates and the anhydrite have grain densities of 2.850 g/cm^3 ± 0.038 g/cm^3. The group of samples with lower grain densities have a large amount of quartz, while the samples with higher grain densities have a large amount of heavier minerals, namely dolomite and anhydrite, which have higher densities than that of quartz.

Sample	Mass (g)	Grain Volume (cm^3)	Grain Density (g/cm^3)
Mannville shale 1 (SSA010)	36.76	13.97	2.63
Mannville shale 2 (SSA011)	53.34	20.19	2.64
Mount Head carbonate (SSA019)	8.98	3.19	2.81
Wabamun carbonate (SSA025)	53.04	18.79	2.82
2nd White Specks sandstone (SSA034)	28.64	10.95	2.62
Big Valley anhydrite (SSA035)	37.42	12.96	2.89
Bow Island sandstone (SSA037)	7.71	2.91	2.65
Quartz			2.65[a]
Dolomite			2.87[b]
Anhydrite			2.98[c]
Calcite			2.71[d]
Kaolinite			2.44[e]
Illite			2.71[e]
Smectite			2.39[e]

Table 4.2 - Grain densities of the samples and of selected common minerals. [a] Koga et al., 1958. [b] Nur & Simmons, 1969. [c] Schwerdtner et al., 1965. [d] Peselnick & Robie, 1963. [e] Wang et al., 2001.

4.2.2 Bulk Density & Porosity

The bulk (or envelope) density of the sample includes any volume from pores or cracks. Bulk density was measured using a Micromeritics Geopyc (1360) at the University of Alberta. The geopyc determines volume through displacement of a surrounding material (Dryflo™). The material is a mixture of particles of varying sizes and a small amount of graphite lubricant such that the mixture acts as a fluid and ensures determination of the volume with a high degree of accuracy. This material is placed into a glass tube of known diameter and packed until the force reaches a preset value. When the force reaches the maximum value the depth of the plunger is recorded. The sample is then carefully added and the same procedure is carried out. The sample volume is the difference of volumes between the two runs. The tests of samples shown in this thesis were performed in glass tubes of 38.1 mm diameter and to a maximum force of 90 N.

After determining the bulk volume of the samples, the bulk density may be determined (Table 4.3). Bulk density is a measure of the sample including the pore space while grain density is a measure of the sample without the pore space. Also shown in Table 4.3 is the porosity. Porosity may be determined from a comparison of the grain density and the bulk density:

$$\phi = \frac{\rho_g - \rho_b}{\rho_g} \tag{4.4}$$

where φ is the porosity, ρ_g is the grain density, and ρ_b is the bulk density of the sample. Several of the bulk densities exceed the grain densities. They are all within 0% porosity within error and thus indicate a very low porosity. Four of the samples have porosities less than 1.1%. The 2nd White Specks and Bow Island sandstones are larger grained quartz samples and have porosities of 5.3% and 11.7%, respectively. The Mount Head carbonate has the largest porosity at 20.1%.

Sample	Mass (g)	Bulk Volume (cm^3)	Bulk Density (g/cm^3)	Porosity φ (%)
Mannville shale 1 (SSA010)	22.03	8.4692	2.60	1.1 ± 1.5
Mannville shale 2 (SSA011)	53.29	19.802	2.69	<< 1
Mount Head carbonate (SSA019)	19.09	8.4931	2.25	20.1 ± 1.9
Wabamun carbonate (SSA025)	24.30	8.5955	2.83	0 ± 1.3
2nd White Specks sandstone (SSA034)	23.01	9.2851	2.48	5.3 ± 2.9
Big Valley anhydrite (SSA035)	30.79	10.5149	2.93	<< 1
Bow Island sandstone (SSA037)	31.02	13.2696	2.34	11.7 ± 0.5

Table 4.3 - Bulk density and porosity.

4.2.3 Pore Structure

Porosity by itself tells little about the types or sizes of the pores. The pore dimensions of the samples are analyzed using a mercury porosimeter (Micromeritics Autopore IV) at the University of Alberta. The porosimeter operates by injecting mercury into the pore space of the sample. The sample is immersed in mercury and the pressure is increased to a maximum of 413 MPa. As the pressure is increased mercury is injected into the samples. Each pressure is associated with a particular pore size; low pressures corresponding to larger pores and higher pressures correlating to smaller pore spaces. The Washburn equation (Washburn, 1921) provides the relationship between pressure and the pore size as:

$$D = \frac{-4\gamma\cos(\psi)}{P} \tag{4.5}$$

where D is the pore throat diameter, P is the pressure, γ is the surface tension of the intruding fluid, and ψ is the contact angle of the intruding fluid. The surface tension and contact angle of mercury are 0.4835 N/m (at 25° C; Nicholas et al., 1961) and 140°, respectively. This means that at a pressure of 413 MPa, the smallest pore size that will be intruded is ~ 3.5 nm.

The cumulative volume of mercury, V_{Hg}, injected into the sample is recorded as a function of pressure, P. This allows us to observe the total amount of mercury injected into the sample and at which pressure the contribution is the greatest. The derivative of the cumulative volume

$$\partial V_{Hg} = \frac{dV_{Hg}}{dP}\Delta P \tag{4.6}$$

gives the incremental intrusion for each pressure/pore throat diameter. This is an important measure as it reveals the general distribution of pore sizes in the sample. The porosity that the porosimeter intrudes is not necessarily the entire porosity. Any occluded porosity will not be reached. As well, any porosity with a diameter smaller than ~3.5 nm diameter cannot be reached by the maximum pressure of 413 MPa available on this instrument.

There are several different characteristics exhibited in the porosimetry data. One example can be seen in the cumulative intrusion and incremental intrusion curves for the Mannville shale 1 (Figure 4.4). This figure shows that the Mannville shale 1 has a bimodal distribution; peaks occur at 0.0137 MPa (pore size of 0.1 mm) and at 172.25 MPa (~ 8 nm). Other samples show only a single major porosity size. The Mount Head carbonate, for instance, shows a sharp increase in the incremental intrusion at a pressure of 0.77 MPa (1.9 μm). This indicates that the sample's porosity is largely contained within a small range of pore sizes. Table 4.4 gives the pore size distributions of all the samples; that is, how much porosity is found within a certain pore size range. The total porosity in each sample as determined from mercury porosimetry is also given. The porosities roughly agree with those found using helium porosimetry; the largest difference is 1.9%, found in both the Mannville shale 1 and the 2nd White Specks sandstone. The mean difference between the methods is 1.2%, and most individual porosities found from Hg porosimetry are within the errors of those found using previous methods.

The most significant amount of intrusion of the most clay-rich sample, the Mannville shale 1, occurs between the pore sizes of 5.4 – 10.8 nm. These values are

small, although it is typical for the dominant pore size in shales to be on the order of a few tens of nanometers. The Mannville shale 2 shows much the same trend, approximately 70% of the small amount of porosity in this sample is contained in pores less than 50 nm. The Wabamun carbonate is a low porosity dolomite sample where most of the porosity comes from cracks and grain boundaries between tightly packed dolomite grains. The modal pore size in this sample is 11 nm. The 2nd White Specks sandstone also has very small pores; most of the porosity in the sample is contained in pores smaller than 50 nm. The Big Valley anhydrite is virtually nonporous and shows almost no intrusion. The Mount Head carbonate and the Bow Island sandstone show larger pores, and higher porosity, than the rest of the samples. The Mount Head carbonate has significant porosity from pores 1-2 μm in size, and the majority of pores in the Bow Island sandstone are 0.3 – 1 μm in size.

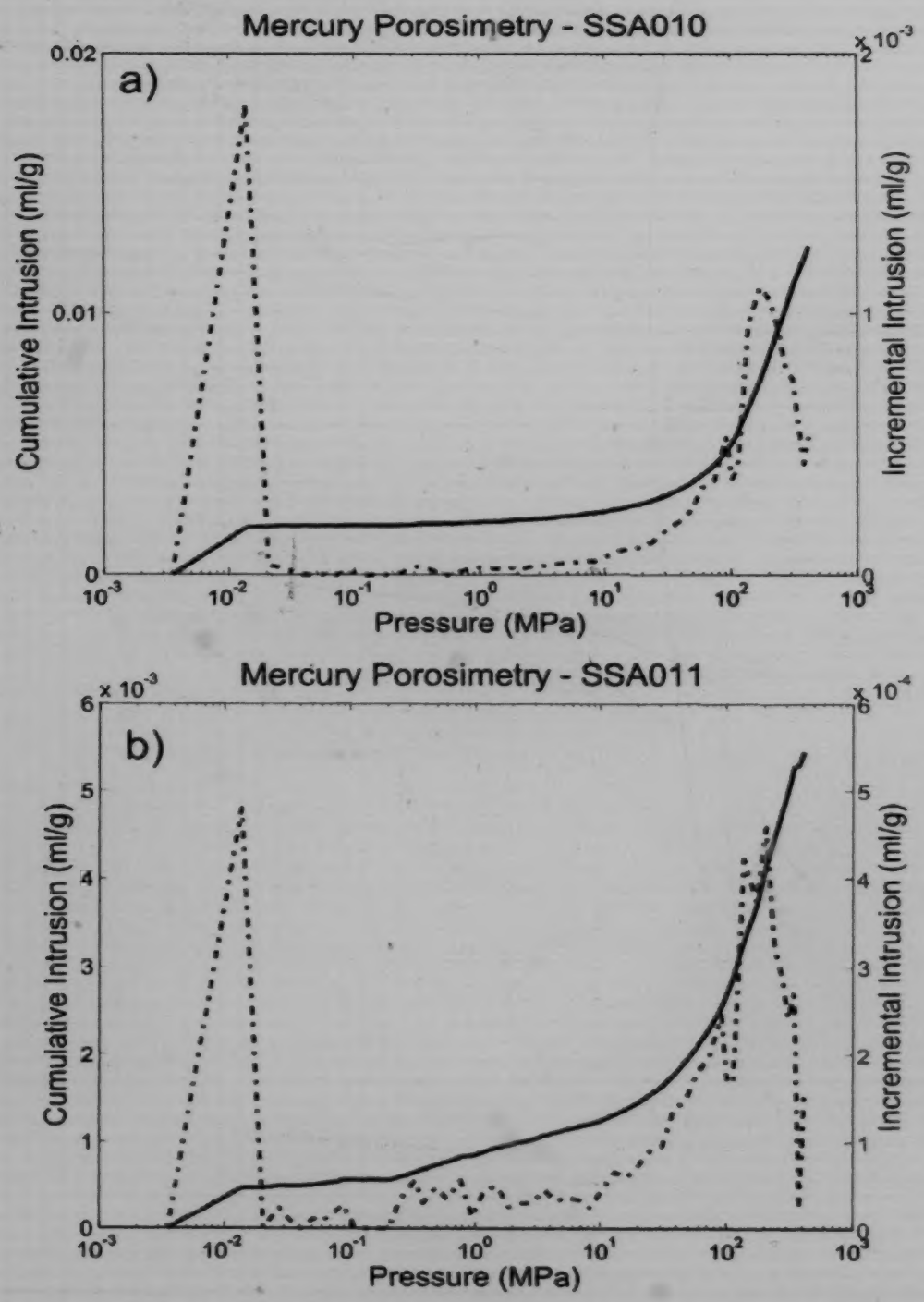

Figure 4.4 - Cumulative and incremental intrusion curves for the a) Mannville shale 1 (SSA010) and b) Mannville shale 2 (SSA011).

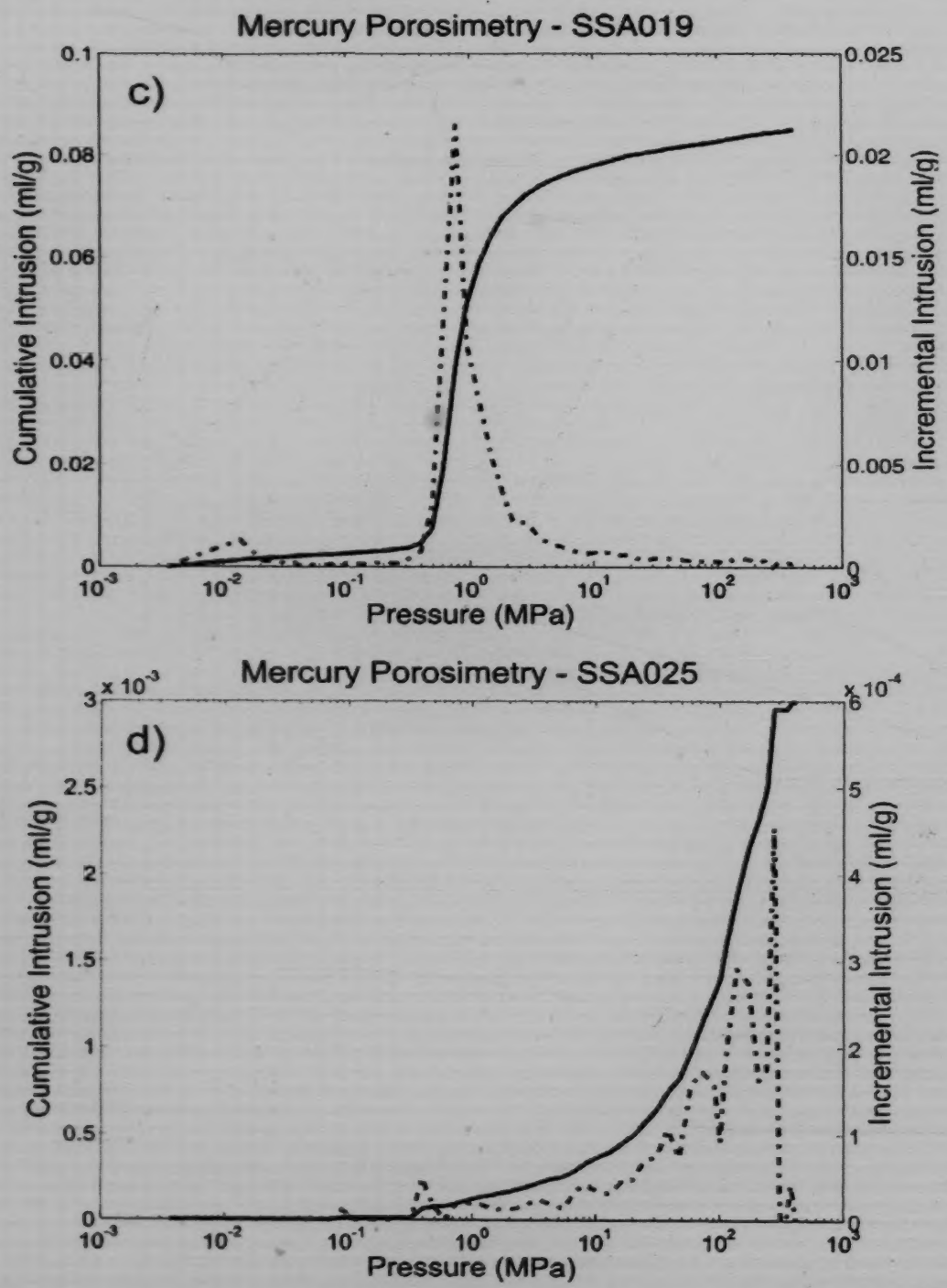

Figure 4.4 *(continued)* - Cumulative and incremental intrusion curves for the c) Mount Head carbonate (SSA019) and b) Wabamun carbonate (SSA025).

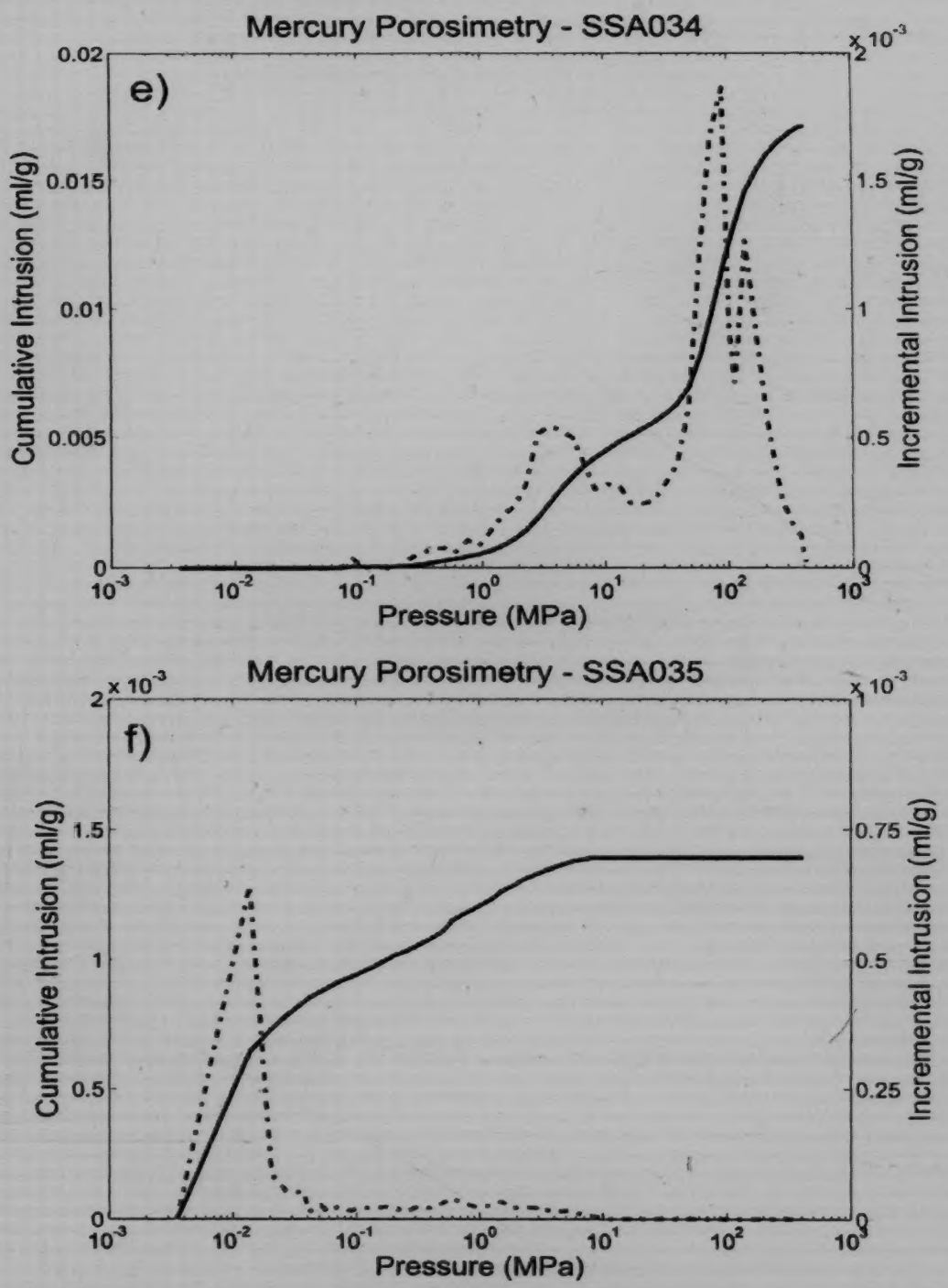

Figure 4.4 *(continued)* - Cumulative and incremental intrusion curves for the e) 2nd White Specks sandstone (SSA034) and f) Big Valley anhydrite (SSA035).

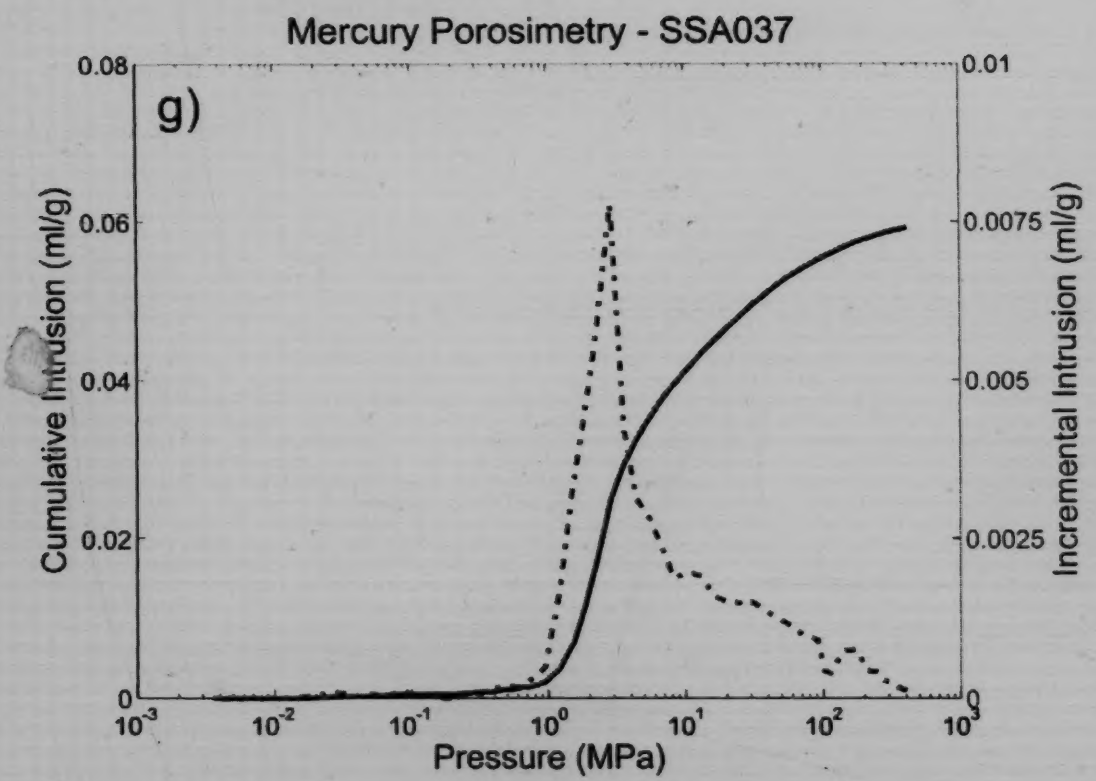

Figure 4.4 *(continued)* – Cumulative and incremental intrusion curves for the g) Bow Island sandstone (SSA037).

Pore-size range (nm)	Pressure (MPa)	SSA010	SSA011	SSA019	SSA025	SSA034	SSA035	SSA037
3.5 – 5.4	413 – 275	0.54	0.15	0.13	0.01	0.11	0.00	0.15
5.4 – 10.8	275 – 138	0.92	0.32	0.24	0.25	0.45	0.00	0.42
10.8 -	138 -	0.54	0.22	0.27	0.17	1.03	0.00	0.55
20.3 -	73 -	0.27	0.15	0.34	0.12	0.84	0.00	1.05
47.9 -	31 -	0.12	0.07	0.46	0.06	0.23	0.00	1.36
113 -	13 -	0.06	0.04	0.67	0.03	0.29	0.00	1.81
270 -	5.5 -	0.04	0.03	1.33	0.02	0.45	0.02	4.00
659 -	2.3 -	0.02	0.03	4.39	0.01	0.20	0.03	3.41
1573 -	0.94 -	0.01	0.03	10.75	0.01	0.07	0.04	0.26
3745 -	0.40 -	0.02	0.03	0.35	0.01	0.04	0.02	0.07
8603 -	0.17 -	0.00	0.01	0.14	0.00	0.01	0.02	0.04
20548 -	0.07 -	0.00	0.01	0.09	0.00	0.00	0.02	0.04

Pore-size range (nm)	Pressure (MPa)	SSA010	SSA011	SSA019	SSA025	SSA034	SSA035	SSA037
39193 -	0.04 -	0.44	0.11	0.47	0.00	0.00	0.24	0.04
Hg Porosity	(%)	3.0	1.2	19.6	0.7	3.7	0.4	13.2

Table 4.4 - Pore size distributions. Each entry in a column represents how much porosity (%) is found in each pore size range. The total porosity found from Hg porosimetry is seen in the bottom row, and is the sum of the column above.

4.3 Mineralogical Content

Powder X-ray diffraction is used to identify the minerals of the samples. Whole rock analysis is used to determine the proportions of oxides present by weight. The results of both tests show that there is a wide variety of minerals present.

4.3.1 X-Ray Diffraction (XRD)

X-ray diffraction (XRD) is used here as a method of gaining semi-quantitative information about the types of minerals present in the samples. In a powder XRD experiment the sample is ground into a fine powder and then bombarded with X-rays. The intensity (number of x-ray counts) of the diffracted and reflected x-rays is found as a function of angle (2θ). Each mineral has a unique spectrum and the spectrum from a sample allows the mineral composition to be determined. A precise measure of the amount of each mineral present is not available from this test, although a qualitative amount is obtainable. Each of the seven samples analyzed in this thesis were ground into a fine powder for powder XRD tests. Tests were carried out in the Earth and Atmospheric Science department at the University of Alberta using a Rigaku Geigerflex Power Diffractometer operated by Diane Caird.

The samples varied widely in composition. The two Mannville samples were largely quartz with significant amounts of clay and were the most typical shale samples in the group. The 2nd White Specks and Bow Island sandstones were mostly quartz and had clays and other minerals in lesser amounts. The main constituent mineral in the Mount Head and Wabamun carbonates was dolomite. Quartz was present in both samples, however, levels in the Wabamun sample were quite small. No clay minerals were detected. The Big Valley anhydrite contained mainly anhydrite and dolomite with no clays minerals discernable. Full results are shown in Table 4.5.

Sample	Minerals
Mannville shale 1 (SSA010)	Quartz, Smectite, Albite, Clinochlore
Mannville shale 2 (SSA011)	Quartz, Dolomite, Kaolinite, Illite, Calcite
Mount Head carbonate (SSA019)	Dolomite, Quartz
Wabamun carbonate (SSA025)	Dolomite, Quartz
2nd White Specks sandstone (SSA034)	Quartz, Calcite, Illite, Kaolinite, Anorthite
Big Valley anhydrite (SSA035)	Quartz, Dolomite, Anhydrite, Fluorite
Bow Island sandstone (SSA037)	Quartz, Kaolinite, Muscovite, Anorthite

Table 4.5 - Minerals identified from XRD.

4.3.2 Whole Rock Analysis

The whole rock analysis was performed by SGS Minerals Services in Lakefield, Ontario, Canada. Wavelength dispersive X-ray fluorescence (WDXRF) was used to determine various oxide contents. This method uses a beam of X-rays to excite the sample and then measures X-rays fluoresced from the sample. A diffracting crystal is placed between the sample and detector in order to decompose the X-ray signal into a number of wavelengths which depend, in part, on the atomic layer spacing of the crystal. Each of the different wavelength X-rays propagate at a particular angle. Detectors placed at appropriate places within the spectrometer can measure the different X-rays, which

allows for determination of the composition. Using this method the whole rock suite (SiO_2, Al_2O_3, Fe_2O_3, MgO, CaO, Na_2O, K_2O, TiO_2, P_2O_5, MnO, Cr_2O_3, V_2O_5) was quantitatively determined. This method may also be used to determine the quantity of Ni and Co, the rare Earth oxides (La_2O_3, Ce_2O_3, Nd_2O_3, Pr_2O_3, Sm_2O_3), and other major oxide elements (BaO, SrO, ZrO_2, HfO_2, Y_2O_3, Nb_2O_5, ThO_2, U_2O_8). The samples were prepared for WDXRF by first crushing and pulverizing the sample to pass through a 150 mesh (106 μm). A homogenous glass disk was formed using 0.2 - 0.5 g of the sample with 7 g of a 50/50 mix of lithium tetraborate/lithium metaborate. The loss on ignition (LOI) was determined gravimetrically at 1000°C. LOI is used as a rough measure of organic content and carbonate content in sediments (e.g., Heiri et al., 2001).

Results of the whole rock analysis for all samples in the SSA series are shown in Table 4.6. Each element is given as a weight percent and determined to a tolerance of 0.01%, except for MgO and Na_2O, which were resolved to a tolerance of 0.05%. In conjunction with controlled XRD experiments, XRF data may be used as a part of determining specific clay fractions in rocks. Although a detailed analysis is not done here some qualitative clay data is available. High percentages of Al_2O_3 and K_2O are indicative of clays (Boggs, 2003). Typical shales have SiO_2, Al_2O_3, and K_2O levels of approximately 57 – 68 %, 16 – 19 %, and 2.5 – 5.0 %, respectively. These values, particularly those of SiO_2, may vary considerably depending on the mineralogy of the sample. Magnesium, sodium, iron, calcium and other trace elements may also be present in clays, however, they are generally present in smaller amounts and are less useful as indicators.

Similar to XRD analysis, the XRF data implies that the carbonate and anhydrite samples have very small amounts of clay; Al_2O_3 and K_2O in all three samples were <1%. Both Al_2O_3 and K_2O levels in the Mannville shale 1 are much higher than any of the other samples in the measured set at 15.4% and 2.26%, respectively. These values are low in the ranges given for shales and it is probably the case that clay content in this sample is less than in a typical shale (~50%). The Mannville shale 2 has the next largest amount of clay in the samples measured and has Al_2O_3 and K_2O values of 9.44% and 1.07%, respectively. The 2nd White Specks and Bow Island sandstones are mostly quartz and have similar Al_2O_3 and K_2O levels of roughly 5% and 1%, respectively.

SSA035 (Big Valley anhydrite) has only a sum of 69.2% in Table 4.6. This is not a mistake in the WRA procedure, it is because a main constituent in this sample is anhydrite ($Ca(SO_4)$). Upon inquiry, we were informed that sulfur was noted to be in the sample, however, the package that was purchased did not include sulfur measurements and was not reported to us.

Sample	SiO_2 %	Al_2O_3 %	Fe_2O_3 %	MgO %	CaO %	Na_2O %	K_2O %	TiO_2 %	P_2O_5 %	MnO %	Cr_2O_3 %	V_2O_5 %	LOI %	Sum %
SSA008	49.1	10.7	4.37	1.71	12.2	0.51	2.28	0.51	0.20	0.02	0.02	0.05	14.8	96.4
SSA010	65.3	15.4	6.56	2.23	0.63	1.96	2.26	0.79	0.19	0.05	0.03	0.03	4.00	99.4
SSA011	69.2	9.44	4.27	1.70	3.14	0.42	1.07	0.72	0.28	0.02	<0.01	0.02	7.64	97.9
SSA012	48.4	9.99	4.59	1.66	10.5	0.56	2.25	0.46	0.19	0.01	0.02	0.04	18.5	97.1
SSA013	53.3	9.68	8.94	1.61	8.10	0.77	2.15	0.46	0.36	0.06	<0.01	0.02	12.0	97.4
SSA016	29.0	5.38	1.81	0.92	30.0	0.44	1.06	0.20	0.17	0.03	0.01	0.02	28.3	97.3
SSA017	61.6	14.9	5.87	1.29	0.69	0.58	2.89	0.83	0.18	0.02	0.02	0.04	9.58	98.5
SSA019	9.08	0.13	0.08	18.7	27.9	0.07	0.03	<0.01	0.09	<0.01	<0.01	<0.01	42.6	98.6
SSA020	8.06	0.77	0.21	18.2	28.2	0.08	0.44	0.04	0.02	<0.01	<0.01	<0.01	42.4	98.4
SSA023	75.8	13.3	0.67	0.62	0.50	<0.05	1.53	0.88	0.04	<0.01	0.01	0.05	4.83	98.3
SSA025	4.64	0.42	0.14	19.7	29.2	0.08	0.17	0.02	0.01	<0.01	<0.01	<0.01	44.3	98.6
SSA027	64.6	10.2	2.90	2.16	5.03	0.47	2.13	0.53	0.20	<0.01	0.01	0.04	10.7	99.0
SSA029	19.5	1.18	0.44	16.4	25.0	0.11	0.70	0.10	0.01	0.01	<0.01	<0.01	36.4	99.9
SSA031	70.7	13.2	2.65	1.18	0.43	0.62	2.59	0.76	0.20	0.01	0.02	0.03	5.78	98.2
SSA032	25.4	8.88	2.98	12.6	17.4	0.10	3.17	0.39	0.05	0.04	<0.01	<0.01	27.8	98.9
SSA034	85.5	4.30	1.38	0.56	1.79	0.49	0.83	0.21	0.60	<0.01	<0.01	<0.01	2.43	98.1
SSA035	5.32	0.67	0.28	8.91	34.3	<0.05	0.35	0.03	0.01	<0.01	<0.01	<0.01	19.7	69.2

Sample	SiO_2 %	Al_2O_3 %	Fe_2O_3 %	MgO %	CaO %	Na_2O %	K_2O %	TiO_2 %	P_2O_5 %	MnO %	Cr_2O_3 %	V_2O_5 %	LOI %	Sum %
SSA036	61.9	15.3	5.76	1.43	0.59	0.78	3.03	0.73	0.22	0.02	0.01	0.04	8.74	98.6
SSA037	84.2	5.26	1.68	0.76	1.59	0.57	1.03	0.30	0.19	0.03	<0.01	0.01	3.33	98.9
SSA038	81.1	8.16	2.60	0.75	0.51	0.94	1.57	0.38	0.15	<0.01	<0.01	<0.01	2.88	99.0
SSA039	62.3	14.5	4.78	1.55	1.42	0.59	2.95	0.71	0.21	<0.01	0.01	0.02	8.98	98.1
SSA040	58.4	9.17	4.75	2.99	6.57	0.47	2.12	0.50	0.20	0.02	<0.01	0.02	11.9	97.1
SSA041	66.4	9.28	4.18	1.97	2.60	0.68	2.04	0.45	0.50	0.03	0.01	0.03	9.74	97.9
SSA042	66.5	10.9	3.64	2.38	2.93	0.53	2.24	0.55	0.15	<0.01	0.01	0.01	7.18	97.0

Table 4.6 - Whole rock major element analysis for all samples in the SSA series. All elements are given as a weight percent and determined to a tolerance of 0.01%, except for MgO and Na_2O, which were resolved to a tolerance of 0.05%.

4.4 Texture

Scanning electron microscope and thin sections are used to examine the textural properties of the samples. Layering and other larger scale effects are seen in thin sections. The scanning electron microscope is able to probe at a higher magnification and can better image fine pore-scale structure. Grain sizes of coarse grained samples may be determined from thin sections, however, SEM must be used for more fine grained samples.

4.4.1 Scanning Electron Microscope (SEM)

The scanning electron microscope (SEM) is generally used to image the surface of materials at a magnification much higher than optical microscopes. Electrons, rather than light, are used to produce this image. In a vacuum, an electron gun is used to emit electrons towards the sample. A magnetic field is used to focus the emitted electrons onto a very precise area of the sample. Some of these electrons will be involved in inelastic collisions, where a secondary electron is emitted from the sample. The SEM detects and counts the secondary electrons as they scatter from the sample. Scanning coils are used to move the electron beam and scan the sample, and the final image is produced by combining each point. Sample preparation included covering with a gold coating to improve conductivity. An acceleration voltage of 20 kV was used.

Using equipment in the Earth and Atmospheric Science department at the University of Alberta, SEM images were taken in the planes approximately parallel and perpendicular to bedding. For final preparation the samples were then covered by a gold coating and placed in vacuum. Each sample had a total viewable surface area on the

order of 0.5-1.0 cm^2. The purpose of performing scanning electron microscopy on these samples was to investigate the nature of the rocks. Factors that would influence seismic anisotropy, such as preferred orientation of minerals, were of particular importance. Other interesting features such as fractures and grain packing, those which affect bulk properties, were also examined. Images of the samples in the planes parallel and perpendicular to bedding are seen in Figure 4.5 and Figure 4.6, respectively.

The Mannville shale 1 was the only sample examined in this thesis that exhibited preferred orientation of minerals under SEM analysis. While images in the plane parallel (Figure 4.5a) to bedding revealed an abundance of quartz and smectite, no mineral orientation was seen. The orientation of smectite was seen in the plane perpendicular to bedding, roughly left to right in Figure 4.6a. This is expected in a shale. The minerals become oriented perpendicular to the maximum compressive stress, which is typically vertical. This leaves the clay minerals oriented parallel to bedding. From these images it is also obvious that there is very little pore space, and most of the existing pore space is very small; less than approximately 1 μm. Unfortunately, the spatial resolution of even these SEM images does not allow us to see features on the order of a few nanometers, a scale at which mercury porosimetry indicates makes up the majority of the pore space.

The Mannville shale 2 is abundant with quartz and smectite. Locally around quartz grains the smectite tends to be oriented around the edges of the larger quartz grains. Away from quartz grains the clay shows no orientation. Some minerals identified in the X-ray diffraction were not seen in SEM analysis (albite and clinochlore). This is not to say that the X-ray diffraction is incorrect, rather that the sample is heterogeneous enough that some minerals are not located in this small section of sample. The

composition of this sample is largely the same as the Mannville shale 1, however there are differences. As noted, there is a lack of orientation in this sample, and there seems to be less clay overall.

The Mount Head carbonate is a largely dolomite sample with a significant amount of quartz cement. The dolomite grains are loosely packed and this produces significant porosity (~20%). The sample is very fine grained. The dolomite grains are about 25 μm, and most of the quartz grains are < 2.5 μm, and many are < 1 μm. There is a small amount of unidentified clay in the Mount Head carbonate. These string-like minerals are not abundant enough to significantly affect the bulk properties of the sample.

The Wabamun carbonate is composed mostly of tightly packed dolomite. There is very little porosity in this sample, however pore space can be identified from unidentified clay found growing wherever the existing porosity is on the mineral surfaces. Like the Mount Head carbonate, this clay is not abundant enough to affect the bulk properties. The sample is, in general, fine grained. Most of the dolomite grains are < 50 – 60 μm, although thin sections will show that some exceed 100 μm.

Images of the 2nd White Specks sandstone show large amounts of quartz with a small amount of illite and other minerals. There are localized pockets of oriented clay minerals, found along fractures or around quartz grains, however these appear random at larger scales and will probably have only a small effect on anisotropy. The quartz in the sample is generally well rounded and is not typically fine grained (>100 μm) and size is more easily determined via thin sections.

The Bow Island sandstone is much like the 2nd White Specks sandstone. It is largely quartz with some muscovite overgrowth and a smaller amount of kaolinite.

Although both of the sandstone samples have clay, neither has a considerable amount, nor is there any observable preferred orientation of the clays.

The Big Valley anhydrite is a sample that is largely anhydrite and dolomite. This sample has large layers and this is an issue as small pieces are necessary for SEM. Depending on the layer either dolomite or anhydrite is observed. Figure 4.6f shows a boundary between layers. On the top is anhydrite and on the bottom is mainly a mix of dolomite and anhydrite. In both layers the anhydrite and the dolomite the grains are very tightly packed together and there is very little porosity.

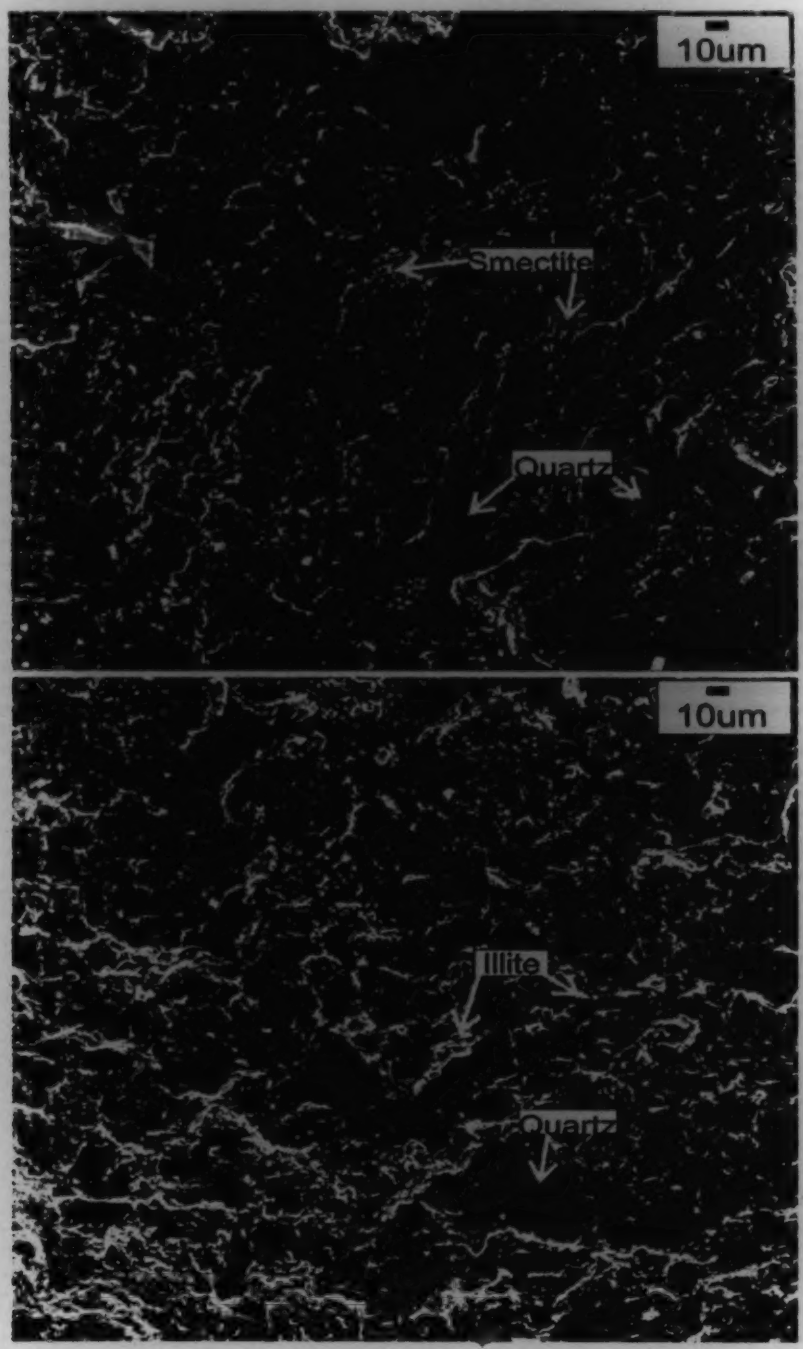

Figure 4.5 – SEM images in the plane parallel to bedding of a) the Mannville shale 1 (SSA010, 355 x 355 μm^2 viewing area) and b) the Mannville shale 2 (SSA011, 355 x 355 μm^2 viewing area).

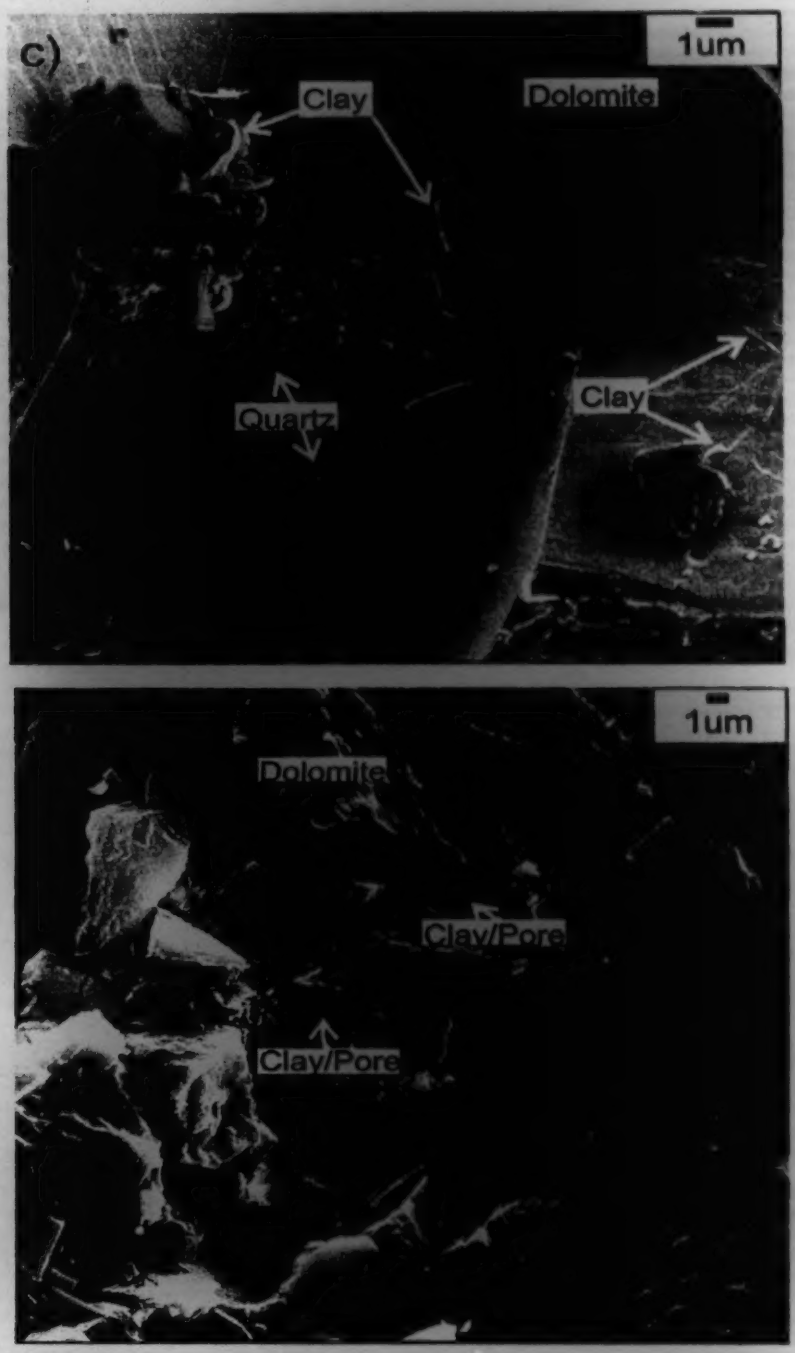

Figure 4.5 *(continued)* – SEM images in the plane parallel to bedding of c) the Mount Head carbonate (SSA019, 21 x 21 μm^2 viewing area) and d) the Wabamun carbonate (SSA025, 36 x 36 μm^2 viewing area).

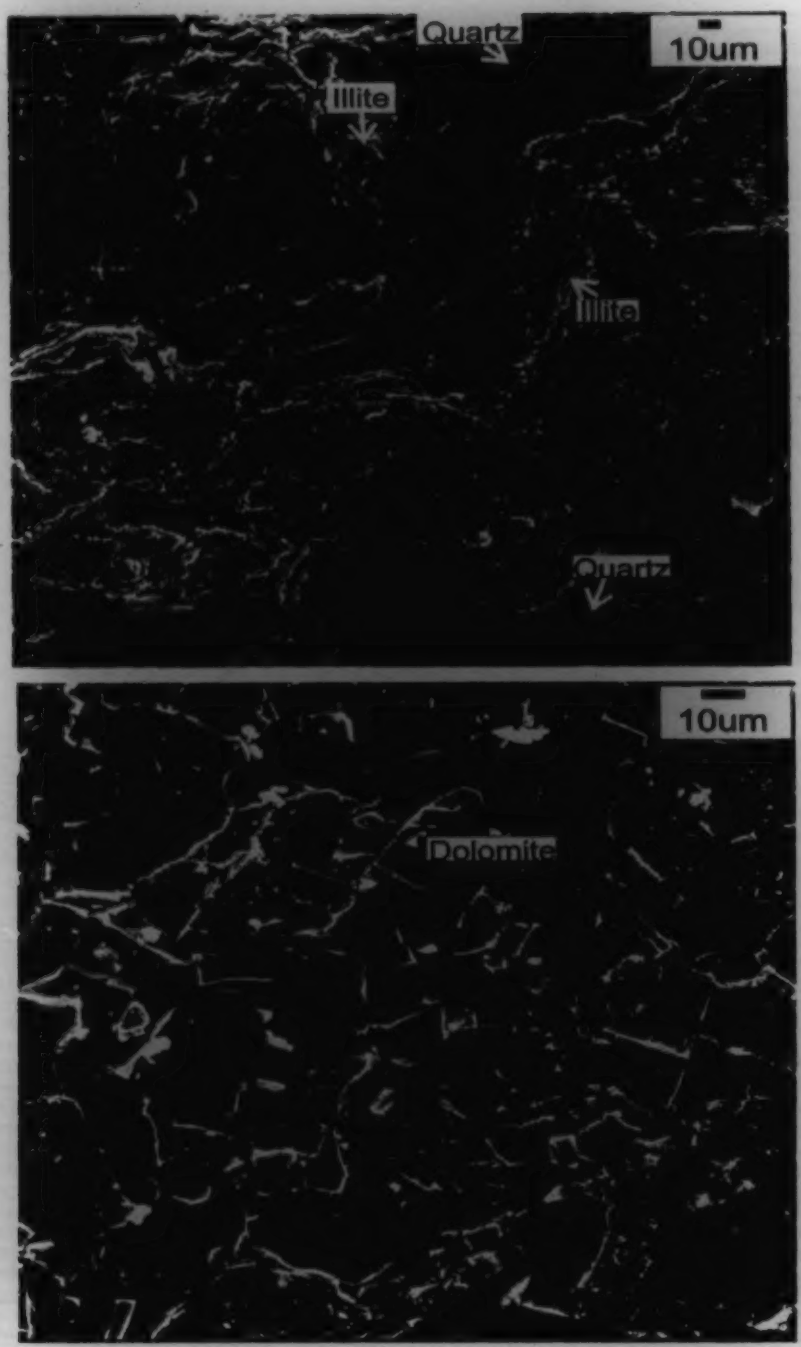

Figure 4.5 *(continued)* – SEM images in the plane parallel to bedding of e) the 2nd White Specks sandstone (SSA034, 355 x 355 μm^2 viewing area) and d) the Big Valley anhydrite (SSA035, 182 x 182 μm^2 viewing area).

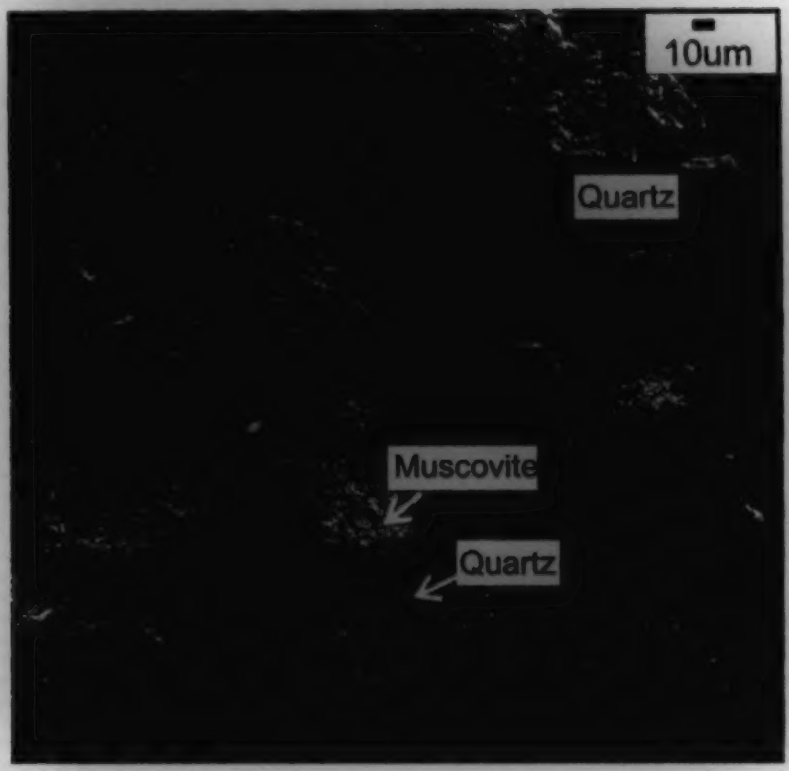

Figure 4.5 *(continued)* - SEM image in the plane parallel to bedding of g) the Bow Island sandstone (SSA037, 355 x 355 μm^2 viewing area).

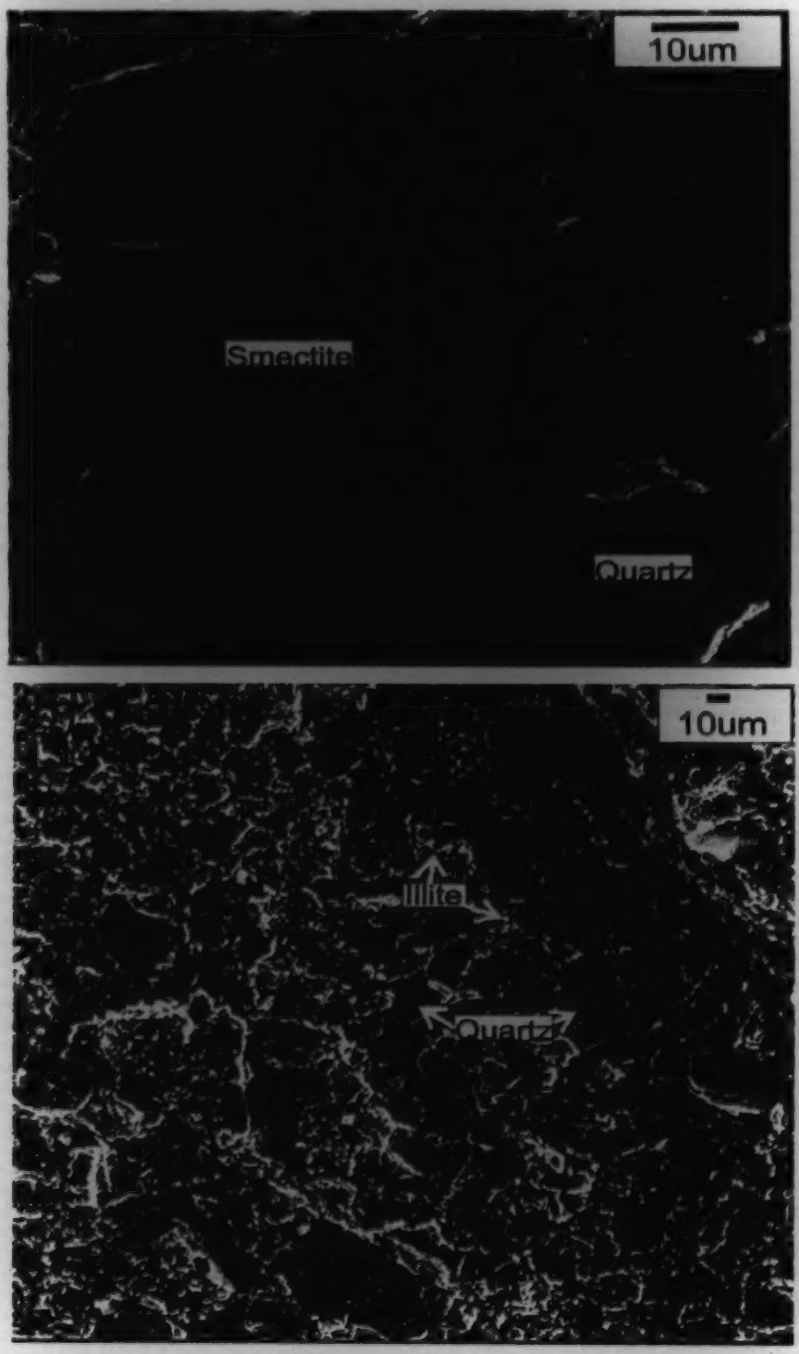

Figure 4.6 – SEM images in the plane perpendicular to bedding of a) the Mannville shale 1 (SSA010, 90 x 90 μm^2 viewing area) and b) the Mannville shale 2 (SSA011, 355 x 355 μm^2 viewing area).

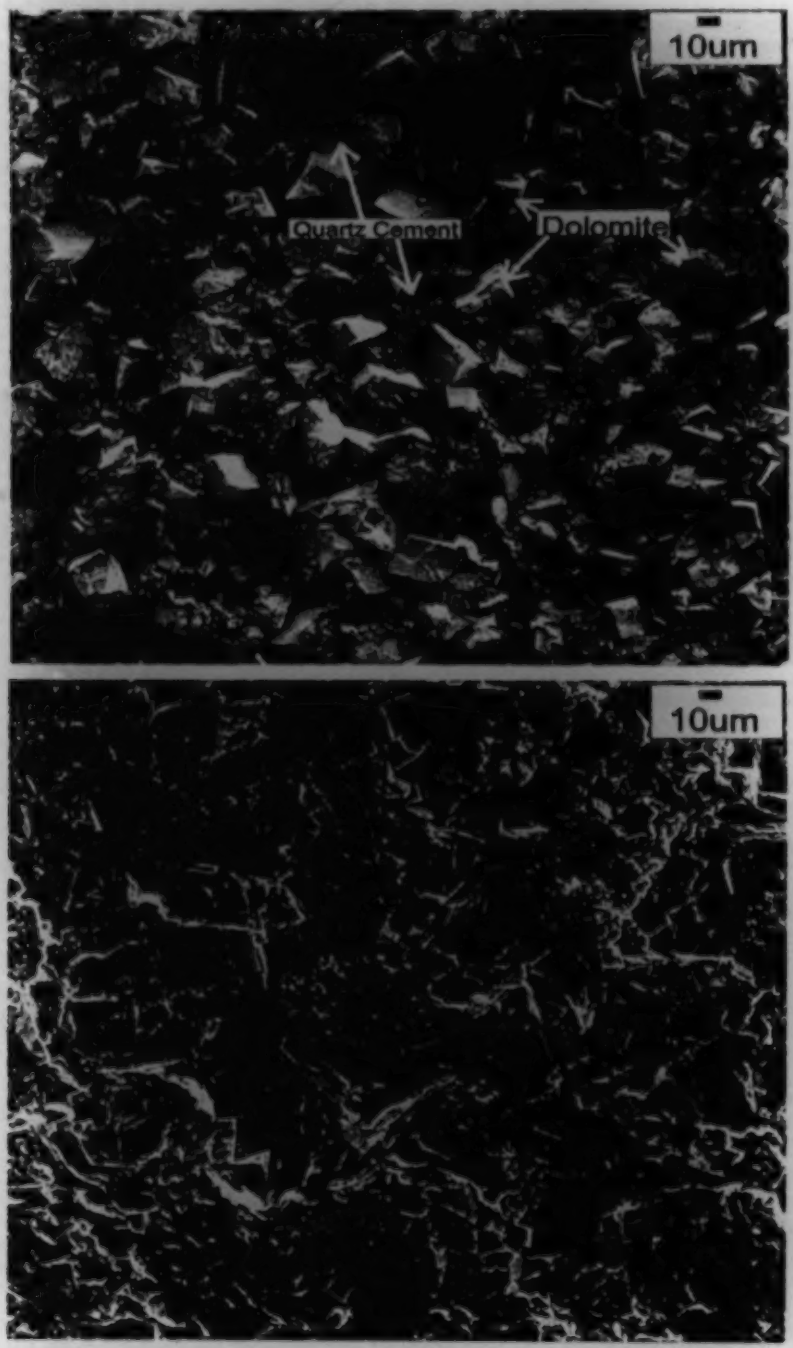

Figure 4.6 *(continued)* – SEM images in the plane perpendicular to bedding of c) the Mount Head carbonate (SSA019, 355 x 355 μm^2 viewing area) and d) the Wabamun carbonate (SSA025, 355 x 355 μm^2 viewing area).

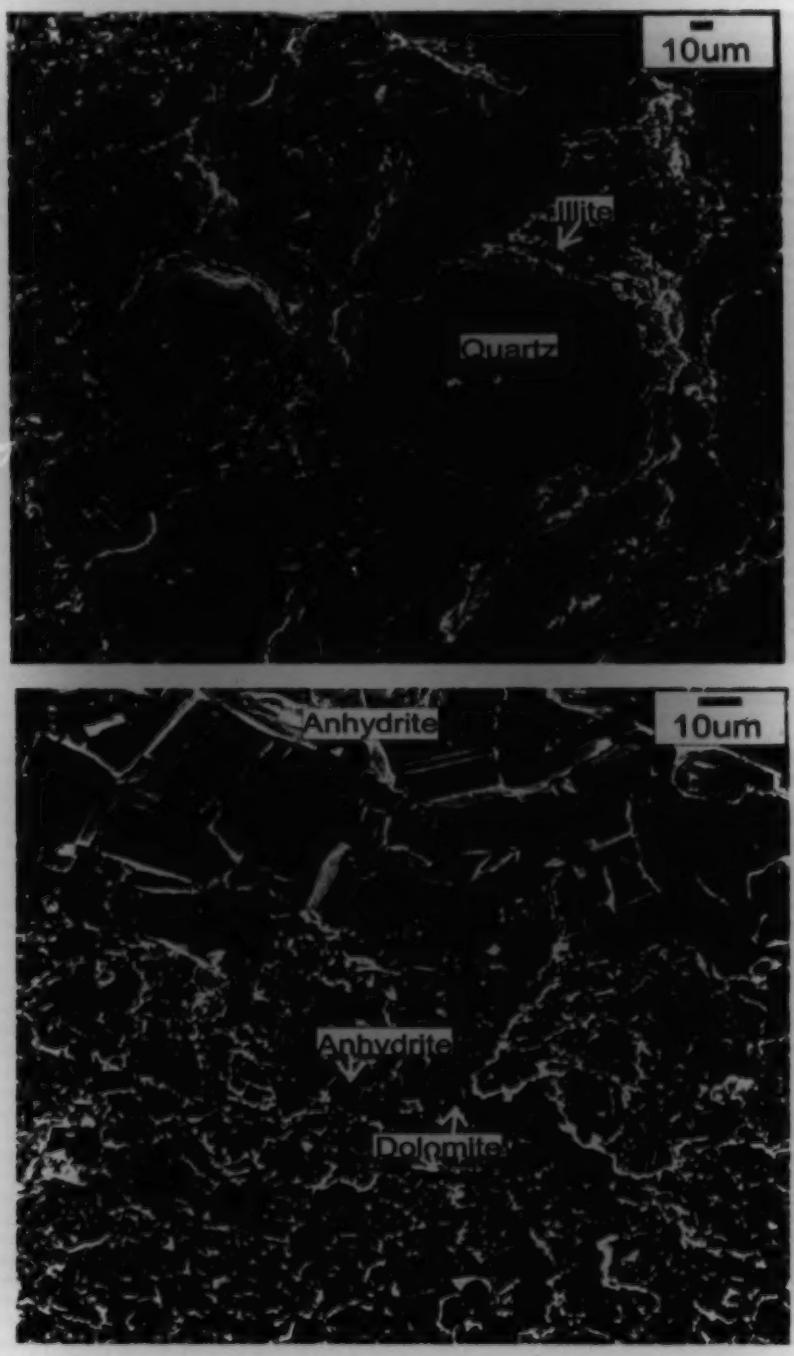

Figure 4.6 *(continued)* – SEM images in the plane perpendicular to bedding of e) the 2nd White Specks sandstone (SSA034, 355 x 355 μm^2 viewing area) and d) the Big Valley anhydrite (SSA035, 182 x 182 μm^2 viewing area).

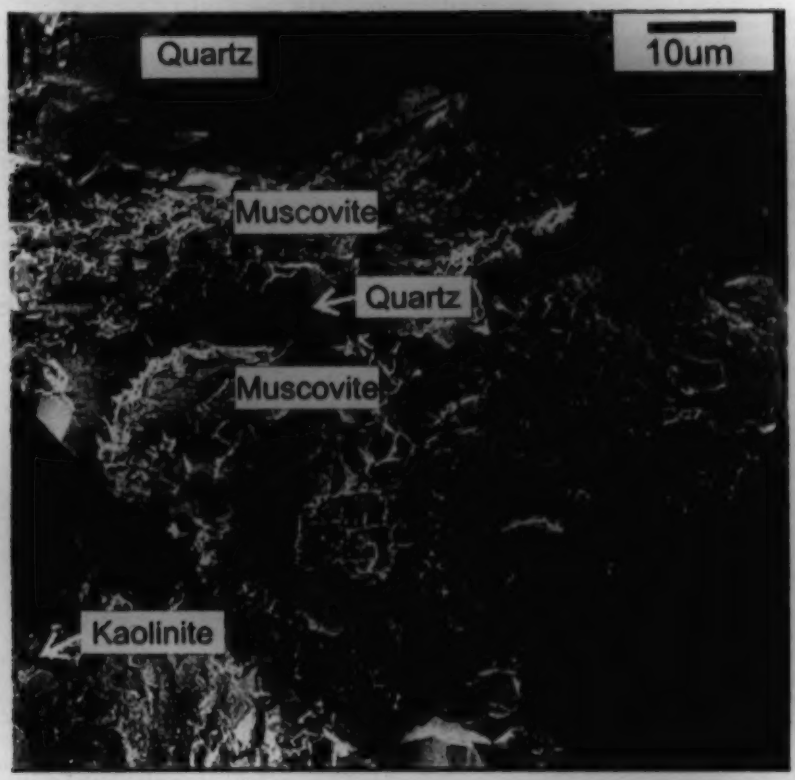

Figure 4.6 *(continued)* - SEM images in the plane perpendicular to bedding of g) the Bow Island sandstone (SSA037, 90 x 90 μm^2 viewing area).

The samples are all very different. The Mannville shale 1 is the only sample in this group that showed any discernible preferred orientation of minerals that would add to the anisotropy of the sample. Differences in the structures were seen. For example, both shales contained large amounts of clay and fine-grained quartz. The sandstones also contained quartz, however the grains were larger and more pore space is seen.

4.4.2 Thin Sections

Thin sections were made at the Thin Section laboratory in the Earth and Atmospheric Sciences department at the University of Alberta by Don Resultay. Two

thin sections were made from each sample; one in each direction perpendicular and parallel to the bedding plane. Most of the samples are fine grained and detailed analysis through thin sections is difficult. Properties such as layer thickness and grain size are determined using both thin sections and SEM. With the exception of the Mount Head carbonate, all of the samples are layered to some extent. The thin sections were examined under a microscope using cross polarized light at various magnifications of 40x, 100x, and 200x. These images are seen in the planes parallel (Figure 4.7) and perpendicular (Figure 4.8) to bedding. A blue epoxy was used when making these thin sections in order to observe any porosity that is present.

In the plane parallel to bedding the Mannville shale 1 has no distinct texture. The sample is relatively fine grained; the quartz grains are 50 – 100 μm. Thin sections cut perpendicular to bedding reveals thin layers (~0.2 mm – 1.0 mm) running parallel to bedding. These layers are likely a source of anisotropy. The Mannville shale 2 is similar to the Mannville shale 1 in terms of mineralogical content. Thin sections show the sample as fine grained with no distinct texture, in the plane parallel to bedding. A thin section cut perpendicular to bedding shows thin layers (~0.3 mm – 0.7 mm) running parallel to bedding (Figure 4.8).

Thin sections of the Mount Head carbonate show dolomite grains approximately 25 μm in size. Thin sections cut perpendicular to bedding show a large amount of porosity and a generally homogenous sample with no apparent layering. The dolomite is noted to be fine grained through thin sections, using SEM images the quartz in this sample is seen to be very fine grained, most of the grains are smaller than 2.5 μm and many are smaller than 1 μm. There is no texture evident from thin sections.

The Wabamun carbonate is typically fine-grained, generally less than 50 – 60 μm, although some grains exceed 100 μm. In the plane perpendicular to bedding there is no texture evident. Thin sections cut perpendicular to bedding show thin layers (~ 0.2 – 1.0 mm), which add to the anisotropy (Figure 4.8).

Thin sections of the 2nd White Specks sandstone show that the sample is not, in general, fine-grained. Most of the quartz grains are several hundred microns in width. There is no layering evident in the thin sections, however the sample is layered. The layers are sometimes as small as 1 mm, although usually larger.

The Bow Island sandstone is similar to the other sandstone in the fact that they are both largely quartz with small amounts of clay. The sample shows fine layers and relatively large quartz grains, although not as large as the 2nd White Specks sandstone. Typically the large quartz grains are 200 – 300 μm. Some of the layers are up to 1 mm thick, however, most of the layers are smaller, often 0.3 – 0.5 mm.

Thin sections show that the Big Valley anhydrite is fairly fine grained. A thin section cut perpendicular to bedding shows a transition between an anhydrite layer and a dolomite/anhydrite layer. The layers are at least a few millimeters thick.

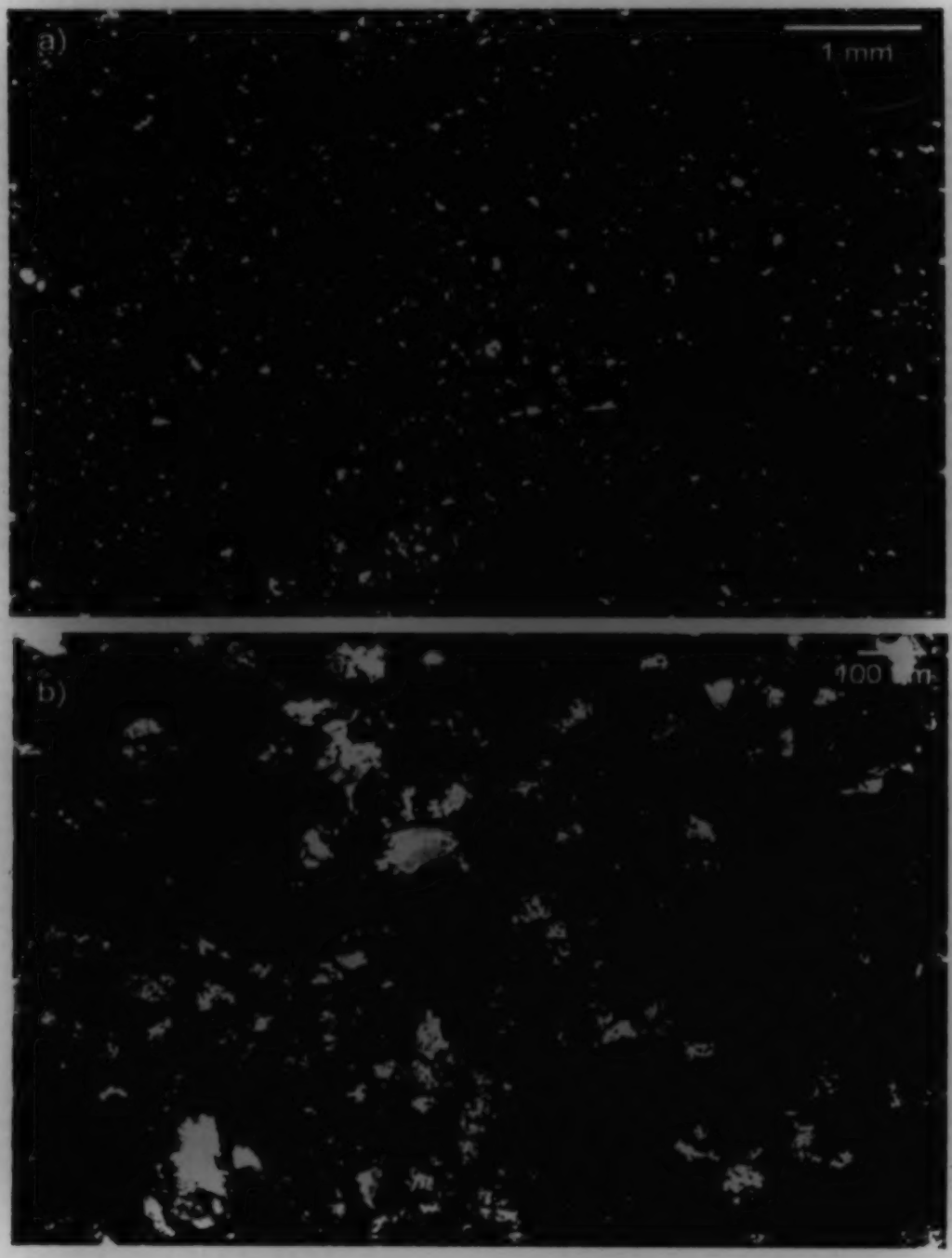

Figure 4.7 – Thin sections taken under cross polarized light in the plane parallel to bedding of a) the Mannville shale 1 (SSA010, 6.9 x 5.2 mm^2) and b) the Mannville shale 2 (SSA011, 1.4 x 1.0 mm^2).

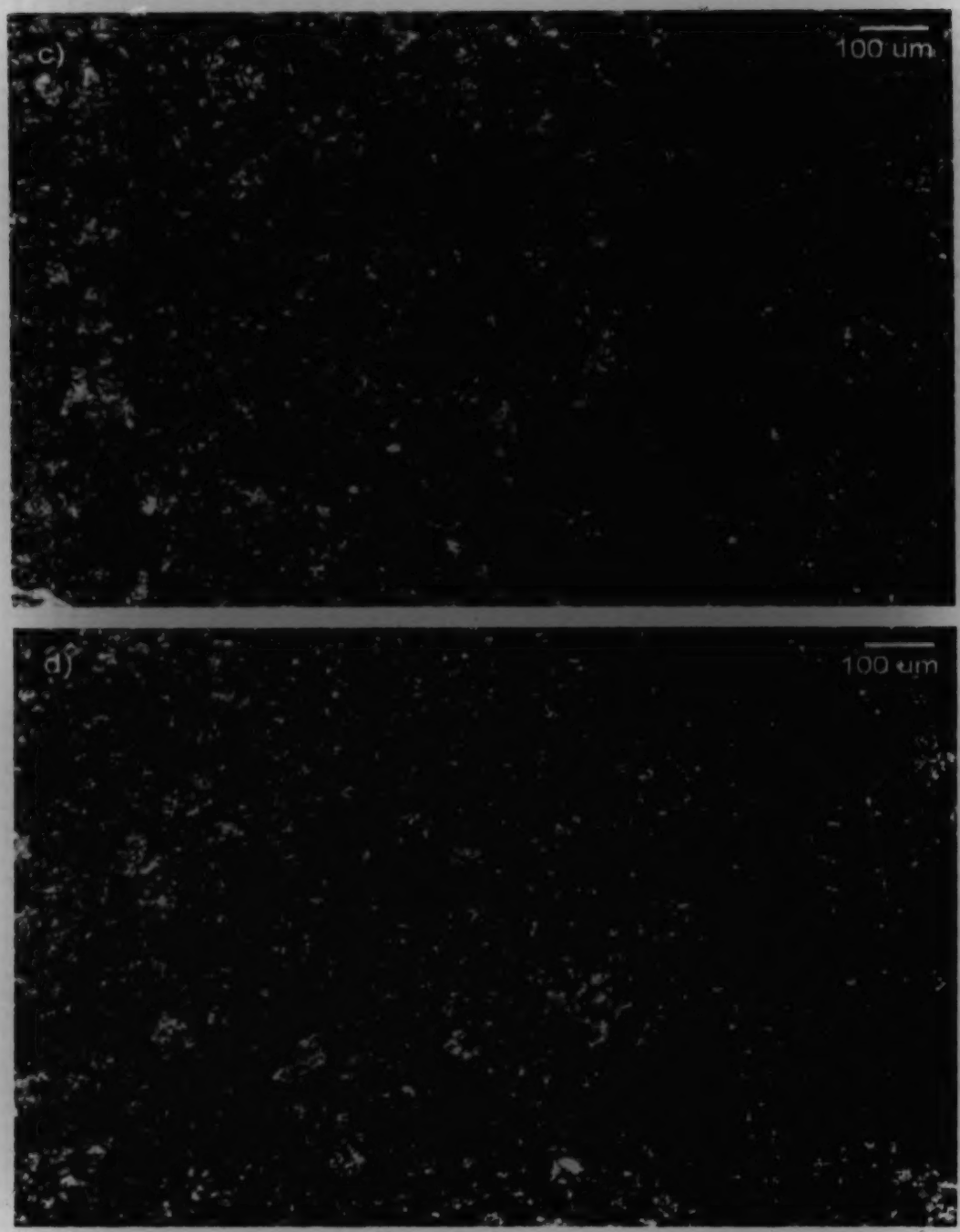

Figure 4.7 *(continued)* – Thin sections (1.4 x 1.0 mm^2) taken under cross polarized light in the plane parallel to bedding of c) the Mount Head carbonate (SSA019) and d) the Wabamun carbonate (SSA025).

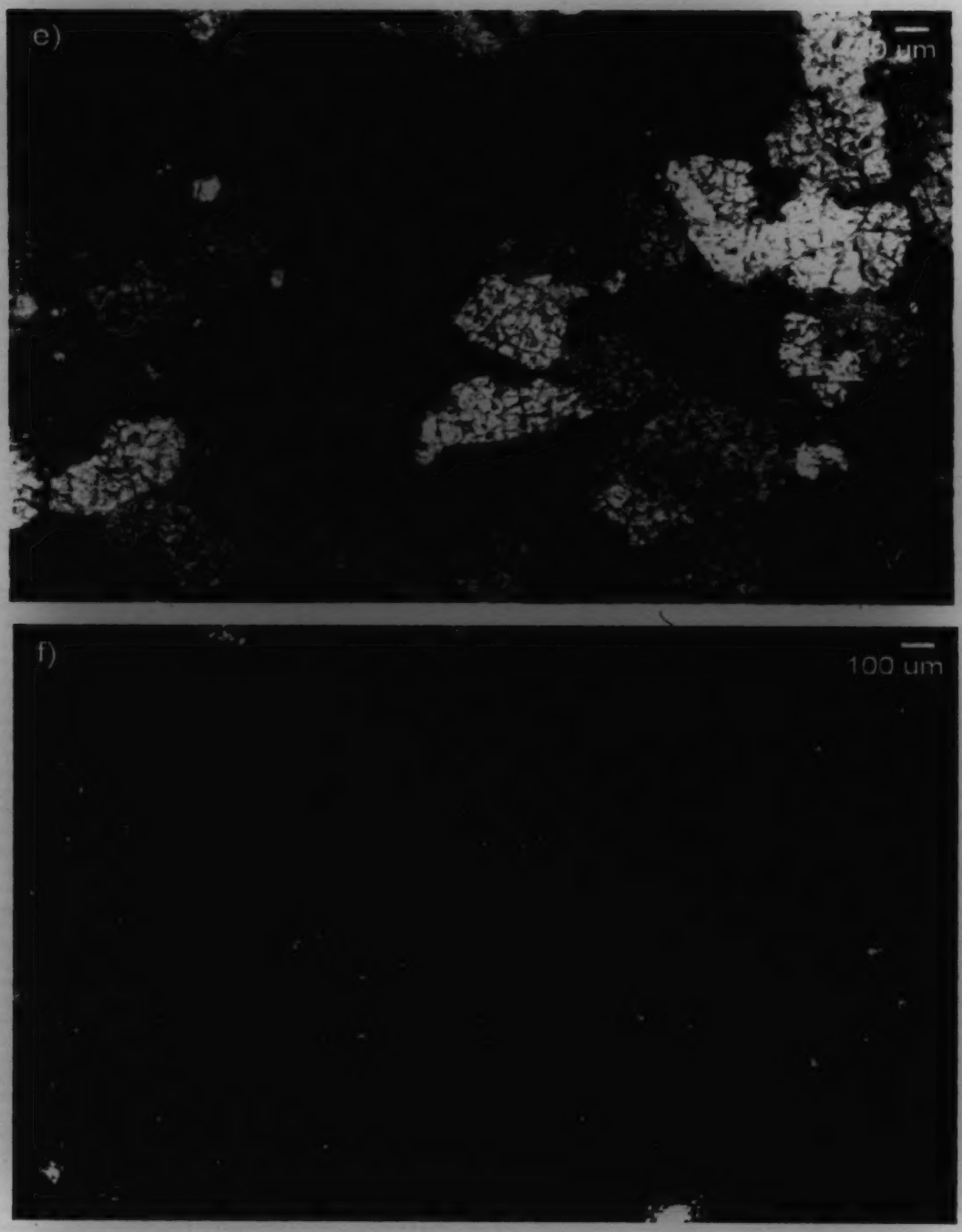

Figure 4.7 *(continued)* – Thin sections (2.7 x 2.1 mm^2) taken under cross polarized light in the plane parallel to bedding of e) the 2nd White Specks sandstone (SSA034) and d) the Big Valley anhydrite (SSA035).

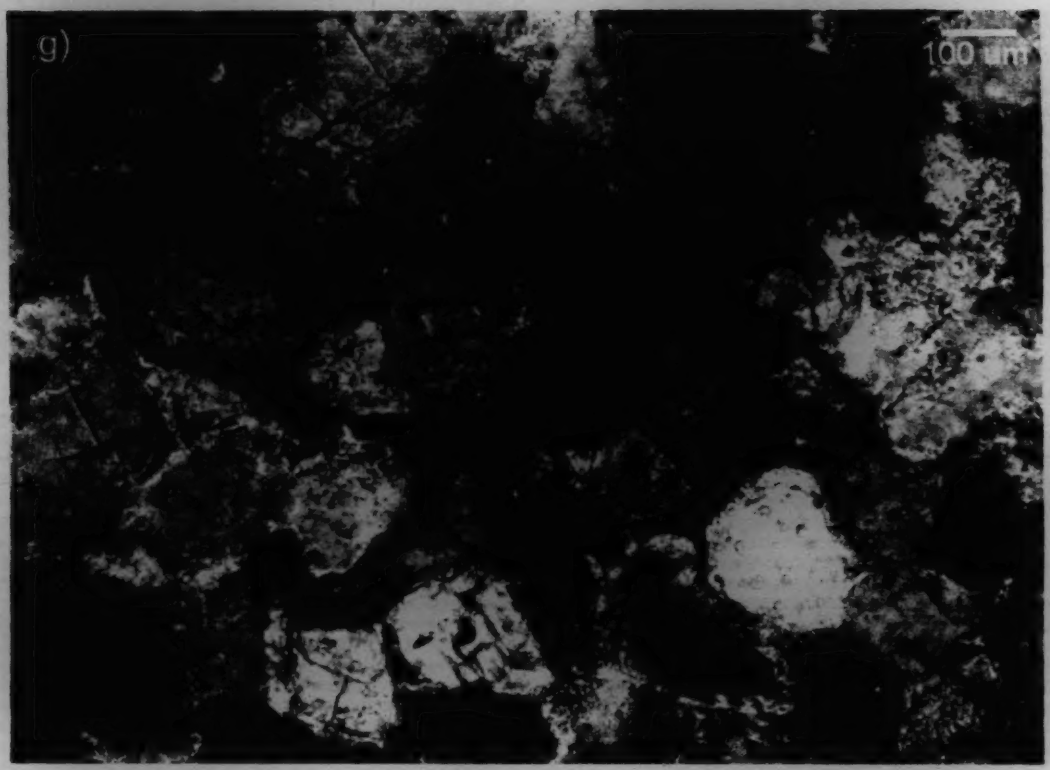

Figure 4.7 *(continued)* - Thin sections (1.4 x 1.0 mm^2) taken under cross polarized light in the plane parallel to bedding of g) the Bow Island sandstone (SSA037).

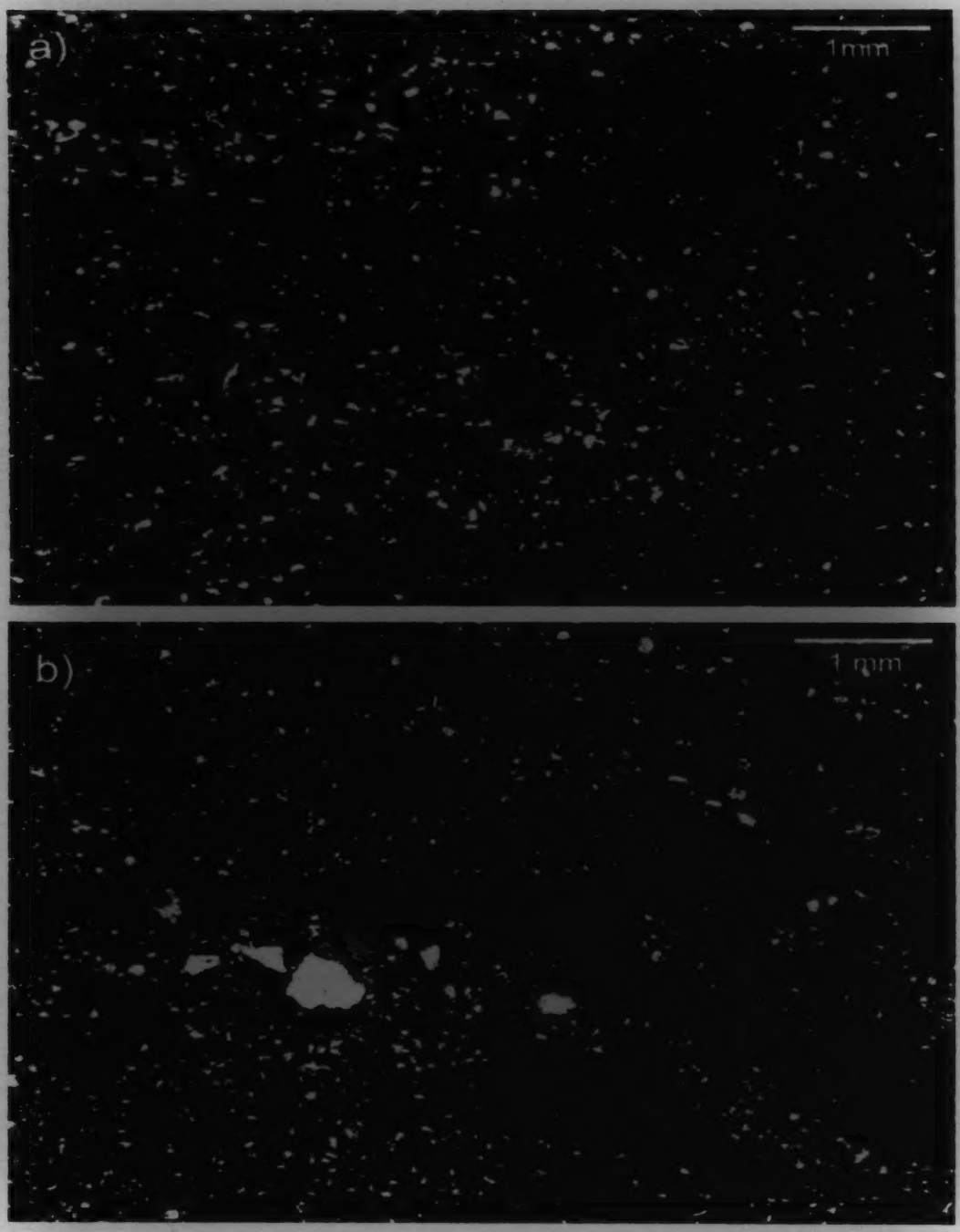

Figure 4.8 – Thin sections (6.9 x 5.2 mm^2) taken under cross polarized light in the plane perpendicular to bedding of a) the Mannville shale 1 (SSA010) and b) the Mannville shale 2 (SSA011).

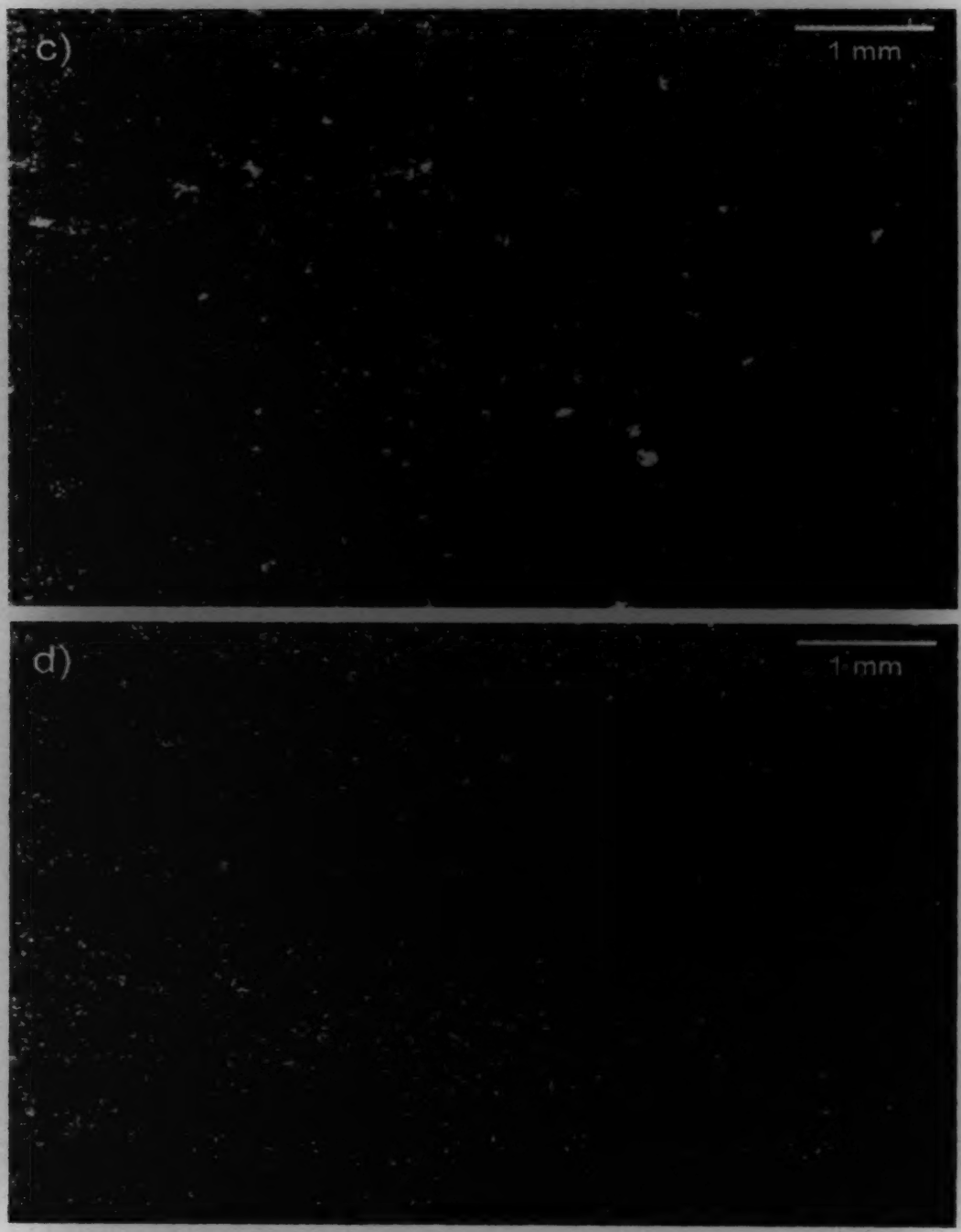

Figure 4.8 *(continued)* – Thin sections (6.9 x 5.2 mm^2) taken under cross polarized light in the plane perpendicular to bedding of c) the Mount Head carbonate (SSA019) and d) the Wabamun carbonate (SSA025).

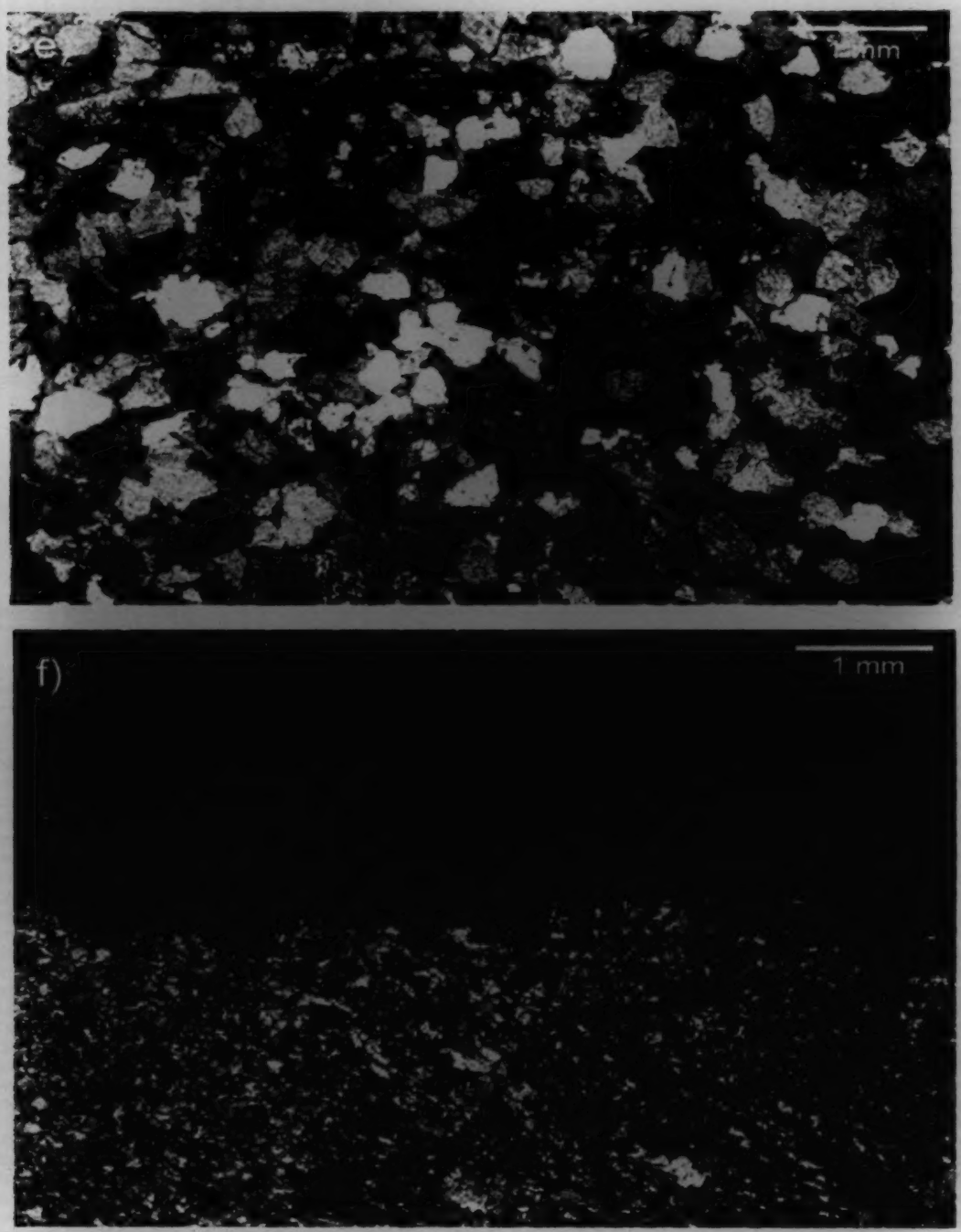

Figure 4.8 *(continued)* – Thin sections (6.9 x 5.2 mm^2) taken under cross polarized light in the plane perpendicular to bedding of e) the 2nd White Specks sandstone (SSA034) and d) the Big Valley anhydrite (SSA035).

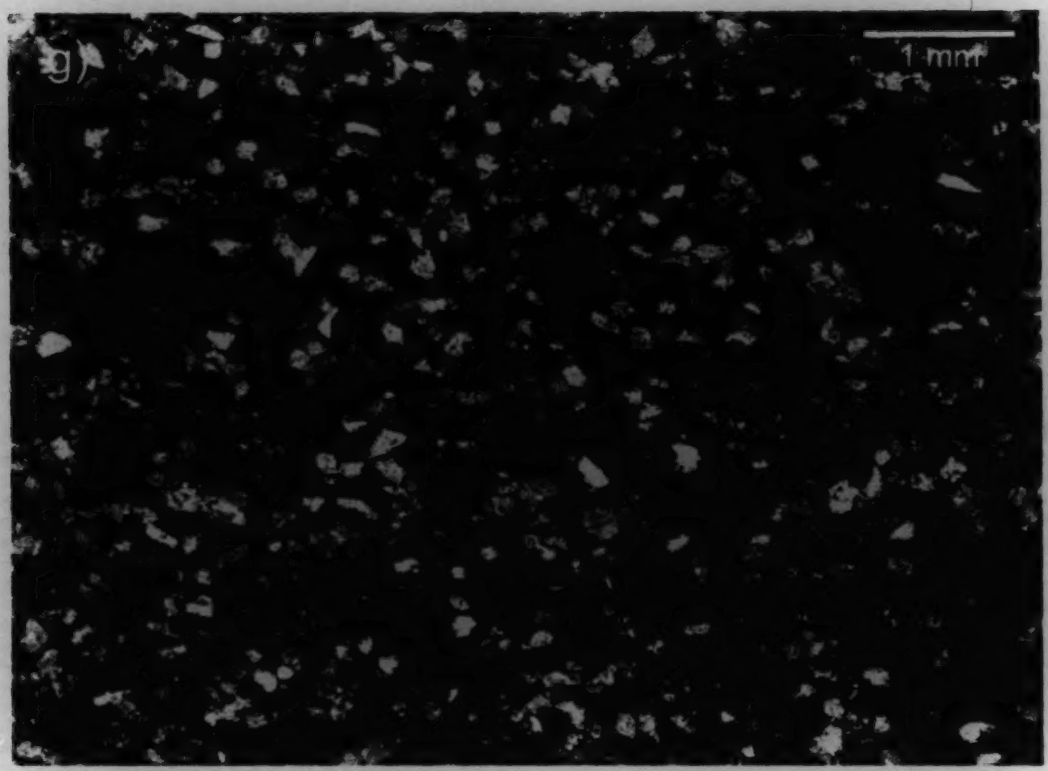

Figure 4.8 *(continued)* - Thin sections (6.9 x 5.2 mm^2) taken under cross polarized light in the plane perpendicular to bedding of g) the Bow Island sandstone (SSA037).

4.5 Summary

The samples studied in this thesis are examined petrographically. XRD and XRF reveal that there are several different types of compositions. The two Mannville shale samples are the only two samples with significant clay content. The two sandstone samples have small amounts of clay, while the main constituents in the two carbonate and anhydrite samples are non-siliceous. Mercury porosimetry reveals that the pore structures are also very different. For instance, most of the porosity in the shales comes from pores only a few nanometers in diameter, while pores in the Mount Head carbonate are on the order of about a micron. Thin sections and SEM images revealed the structure

of the samples and show that the Mannville shale 1 is the only sample to exhibit any discernable preferred orientation of clay minerals, although all of the samples except the Mount Head carbonate are layered.

Chapter 5

Results & Discussion

Ultrasonic P- and S-wave waveforms are found as a function of confining pressure on seven sedimentary samples of varying composition using a standard pulse transmission method described in Chapter 3. The behaviour of velocities, elastic constants, and anisotropic parameters with respect to pressure are studied to determine the sources of anisotropy. The anisotropy will be compared to that found in field studies in the area. V_P/V_S ratios will also be examined. Only representative data and figures are shown in this chapter in order to illustrate important results. A full reporting of the waveform, velocity, anisotropy, and elastic constant results are available in Appendix A.

5.1 Velocities

As outlined in Chapter 3, one P- and one S-wave velocity were measured in each of the directions perpendicular, 45°, and parallel to bedding. The travel time of the waveform was picked at the first peak or trough and a velocity was obtained from the quotient of the distance traveled and the travel time. Velocities were measured during both pressurization and depressurization. Each sample was taken up to a maximum confining pressure based on the depth that the core was retrieved from (Chapter 3). The velocities all increased with pressure but the velocity-pressure curves do not all show the same characteristics. The velocities in the shales and anhydrite are largely pressure

invariant, though pressure has a large effect of velocities in the two carbonate and sandstone samples.

In this section, certain velocities measured in the laboratory are presented as illustrative subsets of the samples. First, however, some discussion of the potential effects of consolidation on these samples is given.

5.1.1 Consolidation Tests

In the context of this study, consolidation refers to a permanent or irreversible change in the physical properties while the material is under pressure. This has long been a concern in laboratory measurements where many authors (e.g., Christensen & Wang, 1985; Christensen & Wang, 1986; Gardner, 1986) noted that the velocity of their rock samples subject to a constant pressure was time dependent. Unfortunately, most workers who measure ultrasonic velocities on rock samples do not discuss this issue.

To observe any irreversible consolidation that might occur, the 2nd White Specks sandstone was used as a test sample and measured twice. Figure 5.1 shows the average of the velocities parallel and perpendicular to bedding during pressurization and depressurization for both runs. Velocity anisotropy is seen as waves traveling parallel to bedding are notably faster than those traveling perpendicular to bedding for both P- and S-waves. Comparing the velocities between runs shows that the differences between all of the P- and S-wave velocities are approximately the magnitude of experimental error and there is no evidence that the sample has consolidated much. The average difference between the P-waves is 40 ± 34 m/s while the S-waves differ by 19 ± 19 m/s. Most of the samples tested were low porosity, relatively stiff, and they were not subjected to extreme

pressure conditions. There is no reason to believe that major consolidation occurred in any of these samples tested.

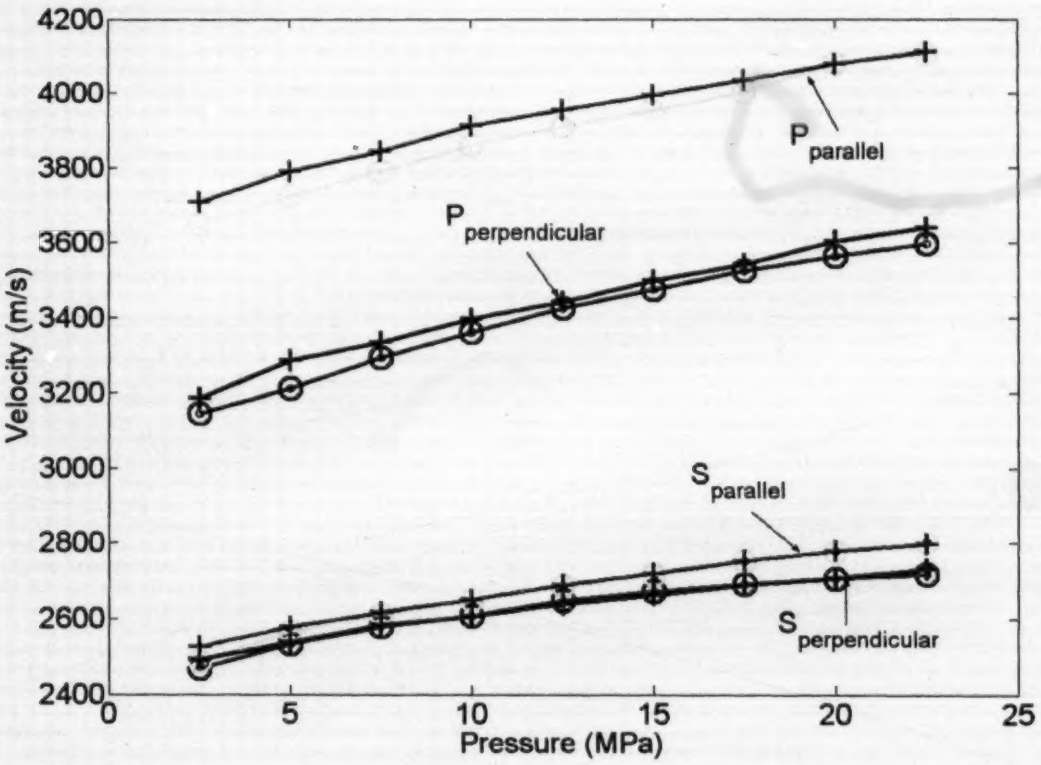

Figure 5.1 - Results of consolidation tests on the 2nd White Specks sandstone. The first test is represented by blue and green 'o' markers, while the second test is indicated by black and red '+' markers.

5.1.2 Sandstone Velocities

Figure 5.2 shows all six measured velocities versus pressure for the Bow Island sandstone. It is easy to see that the velocity not only depends on the current confining pressure, but on the pressure history of the sample. The velocity taken while the confining pressure is decreased is slightly higher than that while increasing the pressure. This effect is known as hysteresis (e.g., Gardner et al., 1965). Increasing pressure has the

effect of closing microcracks and other porosity. As the confining pressure is decreased the closed pores and microcracks begin to open. However, due to frictional forces, they open at a lower pressure than they initially closed which causes the velocity at the same pressure to be slightly higher during depressurization. The Bow Island sandstone shows hysteresis that is of the same magnitude for each of the three P-waves and for each of the three S-waves.

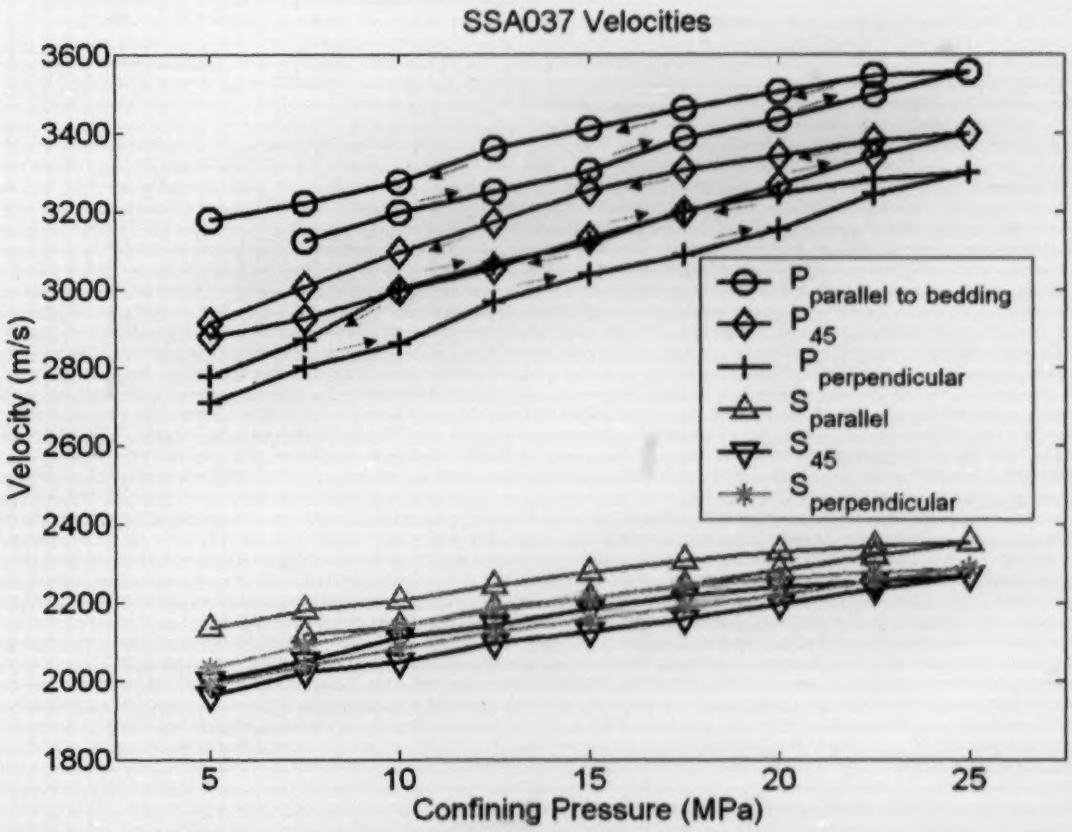

Figure 5.2 - Velocities of the Bow Island sandstone. Arrows on the P-waves indicate the progression of measurements. Arrows on the S-waves are omitted for clarity. Velocities are higher while decreasing pressure.

Velocity increase with pressure is often explained primarily by closing microcracks. Microcracks are caused by various sources such as stress relief during coring and are present in many rocks. Velocity increase due to microcracks is characterized by a rapid increase in velocity at low pressures followed by a low velocity gradient at higher pressures (e.g., He, 2006). Microcracks have low aspect ratios and consequently are more compliant than rounded pores. Thus, microcracks close at relatively low pressures. Due to this higher compliance, cracks affect the velocities more dramatically than rounded pores (Kuster & Toksöz, 1974). This is the cause of the unique velocity-pressure curve that characterizes the presence of cracks. Microcracks are open at low pressure but quickly begin to close as the pressure is increased.

A wave traveling through the sample reacts to the closure of microcracks. When cracks are open, the wave encounters more low-rigidity material (air) and high compliance cracks which decrease the velocity considerably. The cracks quickly close under pressure which increases the stiffness of the rock and causes the velocities to rapidly increase. Eventually, most of the microcracks are closed and the stiffness of the rock is the same as that of the uncracked rock. Once this point is reached the velocity becomes much less pressure dependent. Only a small amount of microcracks (< 1% porosity) are needed to significantly affect velocity (e.g., Kuster & Toksöz, 1974; Vernik, 1993).

Velocities of the Bow Island sandstone are moderate, P-waves range from 2700 – 3550 m/s and S-waves are between 1950 – 2350 m/s. The velocity increase of this sample is roughly linear and still increasing at the same rate at peak pressure. The

linearity of the velocity-pressure curve seems to indicate that microcracks play only a small role in the increase of the velocities. However, the pressure that this sample was subjected to was relatively low. In Section 5.1.3 we will see that microcracks play a large role on the velocities of the carbonate samples until pressures of roughly 40 MPa. This sample was only brought up to a peak confining pressure of 25.0 MPa. This is within the range that velocities are often still controlled by microcracks. It is likely the case that microcracks are largely causing the increase in velocities seen in this sample.

Though the velocities of the 2nd White Specks sandstone are slightly higher (Figure A.18), this sample exhibits behaviour similar to that of the Bow Island sandstone. There is a relatively linear velocity increase with a moderate velocity gradient and hysteresis. This is not surprising since the compositions are comparable. Again, the velocity increase appears relatively linear. This sample was brought up to only 22.5 MPa is within pressure range that microcracks are still actively controlling the velocity. Much like the Bow Island sandstone the increase in velocity is likely caused largely by closing microcracks, though we do not see the leveling out of the velocity with pressure due to the relatively low pressure that this sample was subjected to.

5.1.3 Carbonate Velocities

In contrast to the previous two samples, microcracks clearly play a major role on the velocities of the Mount Head carbonate. This sample shows a large velocity gradient at low pressures followed by a lower velocity gradient at high pressures (Figure 5.3). P-waves traveling perpendicular to bedding increase 1400 m/s from 5.0 – 30.0 MPa, but only increase by 400 m/s over the pressure range from 30.0 – 85.0 MPa. As described above, this is exactly the behaviour that is expected when microcracks are a dominant

control of velocity with pressure. Further, hysteresis effects are more pronounced in the wave traveling parallel to bedding which may be an indicator that the microcracks have some degree of orientation. The relative hysteresis in the P-wave traveling parallel to bedding is on average 67% larger than the hysteresis in the P-wave traveling perpendicular to bedding. The consequences of this orientation will be discussed in more detail in Section 5.2.

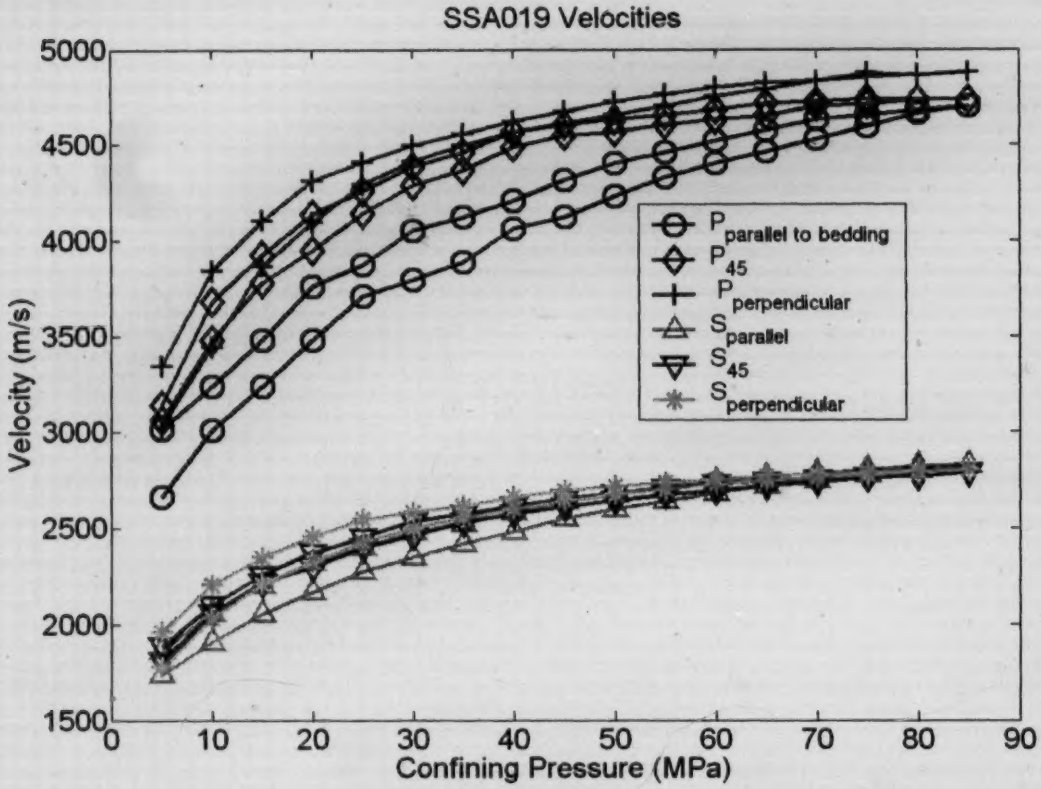

Figure 5.3 - Velocities of the Mount Head carbonate. Each velocity is measured for increasing and decreasing pressure. Velocities are higher for decreasing pressure.

The Wabamun carbonate is similar to the Mount head carbonate in the fact that microcracks control much of the velocity behaviour. The velocity gradient at low

pressures is larger than that at high pressures, indicative of microcracks. There is a large amount of hysteresis in the Wabamun carbonate, particularly in P-waves, and the differences between waves traveling parallel and perpendicular to bedding are very noticeable (Figure A.14). At low pressures, hysteresis is 75-100% larger perpendicular compared to parallel to bedding. This could be an indicator that porosity in the sample has a preferential orientation. This sample is different from the Mount Head carbonate in the fact that it is very low porosity, however, even a small amount of porosity from microcracks can have a large effect on velocities (e.g., Lo et al., 1986; Vernik, 1993). This low porosity makes the velocities in the Wabamun sample much faster than those of the Mount Head sample, despite the fact that both have dolomite as the chief constituent mineral. P-waves vary between 5200 – 6800 m/s, and S-waves are between 3400 – 4050 m/s. Based on the velocity-pressure curve and hysteresis effects, it is clear that microcracks are a major control on the velocities in this sample at pressures below approximately 40 - 50 MPa.

5.1.4 Shale & Anhydrite Velocities

The travel times and velocities of the Mannville shale 1 are relatively stable over the pressure range (Figure 5.4). Up to 75.0 MPa, P-wave speed traveling parallel to bedding increases by only 224 m/s. Waves traveling perpendicular to bedding increase more than this, almost 400 m/s. Since velocities will increase more traveling parallel to the crack normal, this may indicate that the porosity is aligned predominantly horizontally. Preferred orientation of clay minerals is seen in SEM images of this sample. This will cause differences between the velocities traveling perpendicular and parallel to bedding, and will be discussed further in section 5.2.

The Mannville shale 2 is similar in composition to that of the other shale sample and the velocity behaviour is also similar (Figure A.6). The effects of microcracks are minor since the velocities appear stable over the pressure range. The SH-wave velocity gradient is only 70 m/s over a pressure range 5.0 - 75.0 MPa. This sample is low porosity and the velocities do not change much over the pressure range. The velocities of this sample are slightly higher than those of the Mannville shale 1 at 4650 – 5000 m/s for P-waves and 3100 – 3270 m/s for S-waves. This is likely due to the fact that the Mannville shale 2 contains chlorite and dolomite, both of which have faster velocities than smectite (Wang et al., 2001) which is the main non-quartz mineral in the Mannville shale 1. As well, this sample has a relatively larger amount of quartz compared to clay, and a slightly smaller amount of porosity, which would increase the velocity.

The composition of the Big Valley anhydrite is different than that of the two shale samples, however the velocity behaviour is similar (Figure A.22). The velocity gradient is relatively small, increasing to a peak pressure of 45.0 MPa has only a minor effect on the velocities. Because of this, it is clear that there are not many microcracks, oriented or otherwise, in the sample.

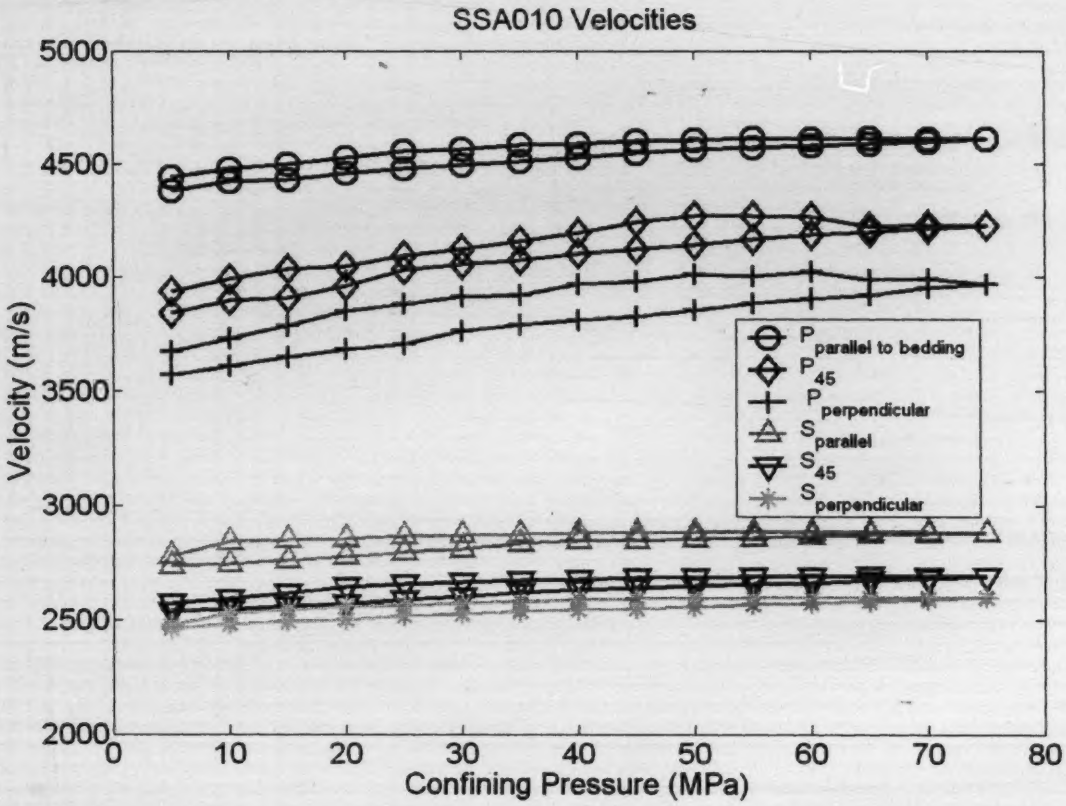

Figure 5.4 - Velocities of the Mannville shale 1. The velocities are relatively stable over the pressure range.

5.1.5 Empirical Velocity-Pressure Relation

Khaksar et al. (1999) developed an empirical equation modified from an earlier empirical equation (Eberhart-Phillips et al., 1989) in order to describe the dependence of velocity with pressure in cracked samples:

$$V = A - Be^{-DP} \tag{5.1}$$

where V is the velocity, P is the confining pressure, and A, B, and D are estimated best fit constants. A is the velocity of the uncracked rock, B is a measure of the relative

importance of crack closure, and D is a measure of the rate of crack closure. This equation was developed to describe sandstone samples whose velocity increase is controlled by microcracks and is thus nonlinear. By fitting the velocity curves with this equation we can predict velocity at pressures beyond what was measured, and by analyzing the constant B we may also attempt to observe the relative importance of cracks in each sample.

The velocities of each sample were attempted to be fit with Equation 5.1. The velocities of the Mount Head and Wabamun carbonates were fit well by this equation. The best fit parameters from these two samples are shown in Table 5.1. Most of the rest of the samples were not generally well fit using Equation 5.1. As explained above, the rest of the samples had relatively linear velocity increases over the pressure range encountered. The equation was developed for nonlinear velocity behaviour and this is the reason that suitable fits were not obtained.

The velocities of the two carbonate samples fit well with the curves produced from Equation 5.1 using a least-squares residual method. Figure 5.5 and Figure 5.6 show the fits of the velocities of the two samples as black lines. The fits were made on velocities averaged at the same confining pressure. The root-mean-square (rms) error of the fit on the three P-waves of the Mount Head carbonate was 27 ± 6 m/s. The rms error on the S-waves of the same sample was 12 ± 3 m/s. The curves fit the velocities of the Wabamun carbonate slightly better. P-waves were accurate to 19 ± 9 m/s and fits on the S-waves were very accurate, having only 5 ± 1 m/s rms error. Comparing the fit parameters of the carbonates we see that A is considerably larger in the Wabamun sample. This, of course, is expected because of the lower porosity and hence faster

velocity of this sample. The parameter *B* is more interesting. As mentioned earlier, *B* is a measure of the importance of crack closure. The Mount Head carbonate shows a larger, indeed generally considerably larger, *B* than the Wabamun sample. This indicates that microcracks are a more important velocity control in the Mount Head sample. This is not surprising, given that the Mount Head carbonate velocities appear much more nonlinear, although it is informative.

Sample	Wave	*A* (m/s)	*B* (m/s)	*D* (1/MPa)	R^2
Mount Head carbonate (SSA019)	$V_{P\,Par}$	4886	2344	0.02892	0.9983
	$V_{P\,45}$	4745	2118	0.05557	0.9978
	$V_{P\,Perp}$	4858	2167	0.05672	0.9951
	$V_{S\,Par}$	2909	1270	0.03133	0.9991
	$V_{S\,45}$	2793	1149	0.04545	0.9976
	$V_{S\,Perp}$	2800	1165	0.05100	0.9969
Wabamun carbonate (SSA025)	$V_{P\,Par}$	6882	1104	0.02938	0.9981
	$V_{P\,45}$	6793	1417	0.03613	0.9940
	$V_{P\,Perp}$	6884	1889	0.02481	0.9961
	$V_{S\,Par}$	4334	607	0.00929	0.9978
	$V_{S\,45}$	3870	450	0.02111	0.9964
	$V_{S\,Perp}$	3940	526	0.01758	0.9984

Table 5.1 - Parameters fit to velocities parallel, 45°, and perpendicular to bedding using Equation 5.1.

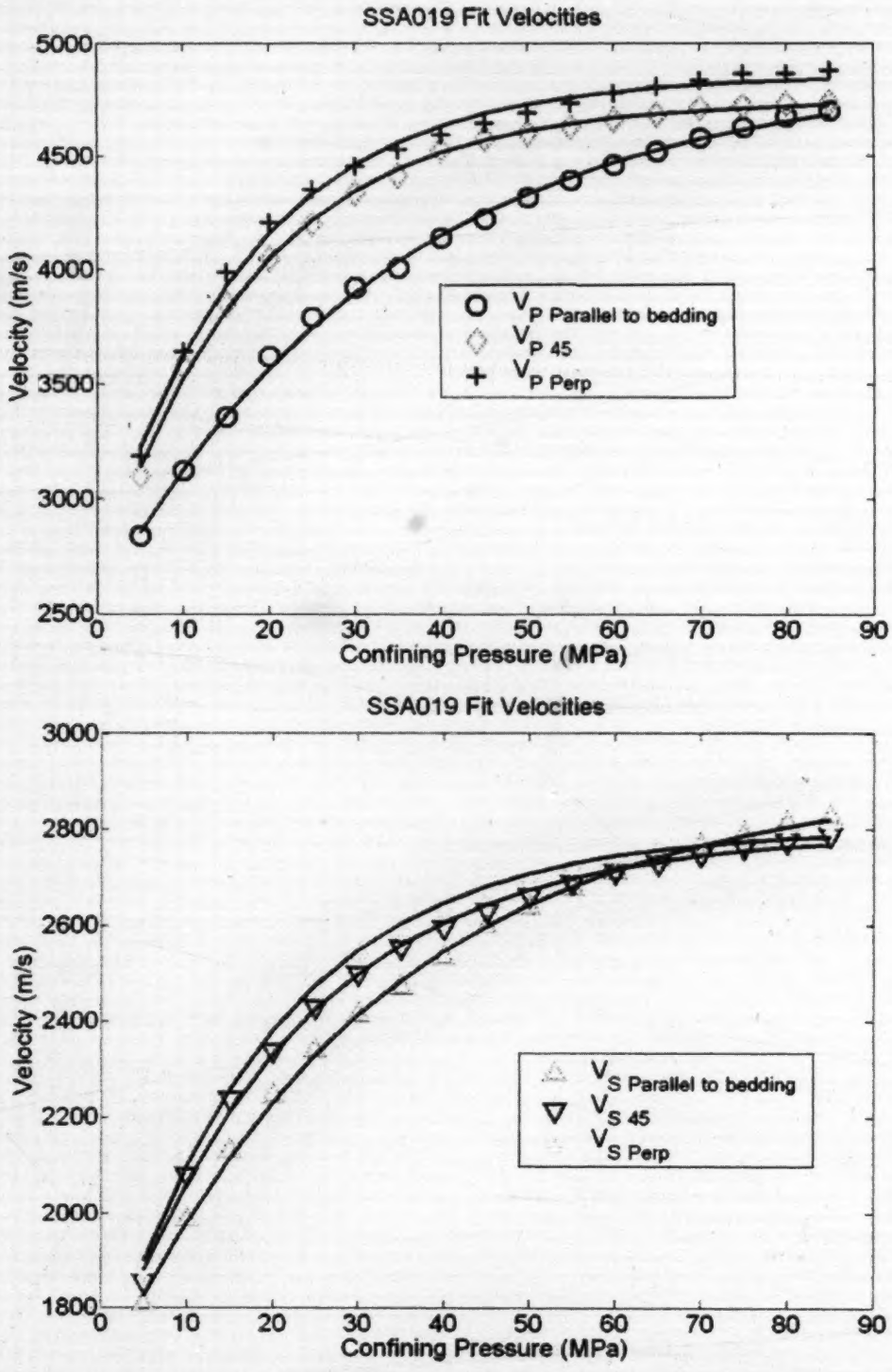

Figure 5.5 - Fits of the velocities of the Mount Head carbonate using Equation 5.1.

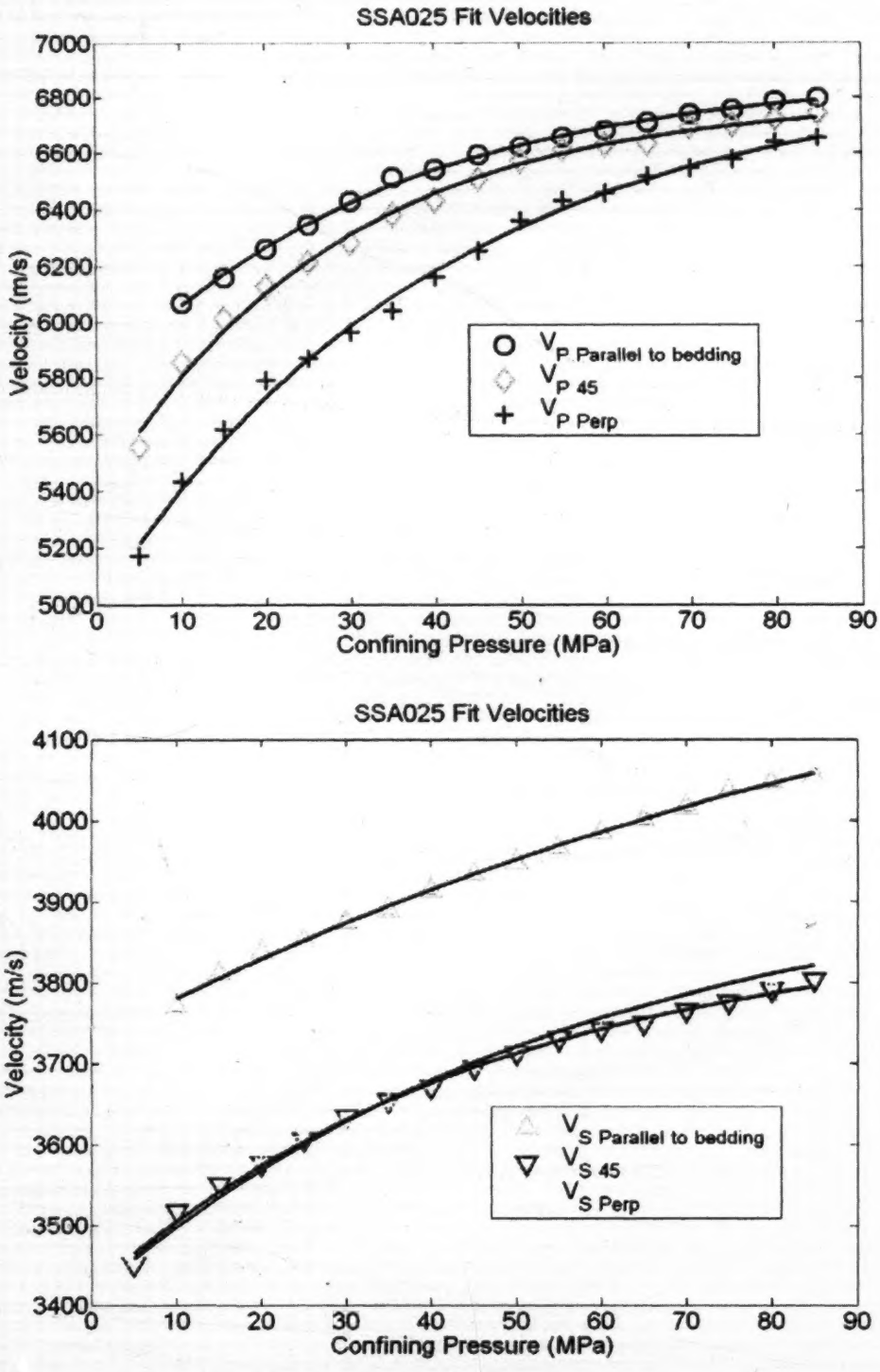

Figure 5.6 - Fits of the velocities of the Wabamun carbonate using Equation 5.1.

5.2 Sources of Anisotropy

All of the samples examined are at least slightly anisotropic. At peak pressure, the Mannville shale 1 exhibited the largest anisotropy at 17.4% (ε) and 11.5% (γ), while the Mannville shale 2 is almost isotropic with 1.4% and 1.4% for ε and γ, respectively (Table 5.2). The anisotropic parameters ε, γ, and δ, are defined mathematically in Equations 2.20 - 2.22. ε is a measure of P-wave anisotropy, while γ is a measure of SH-wave anisotropy. δ is an expression that relates to the curvature of the P-wavefront. The causes of anisotropy can qualitatively be determined using velocity-pressure curves in combination with characterization techniques. In these samples only the Mannville shale 1 showed discernable preferred orientation through examination of SEM images. There are more quantitative ways of determining the orientation of minerals (e.g., Valcke et al., 2006; Lonardelli et al., 2007; Wenk, 2007), although these techniques are beyond the scope of this exploratory work. These techniques may reveal a small amount of orientation not apparent through visual examination of SEM images. Thus, any of the samples studied here may have preferred orientation of minerals to some degree. However, because preferred orientation of minerals was not visible in SEM images nor readily apparent in the thin sections, the amount of orientation is probably minor and the overall effect on the anisotropy is probably small. The exception, of course, is the Mannville shale 1 which had clear orientation even through visual inspection of SEM images. From the behaviour of the velocities during pressurization, all of the samples show microcrack activity to some extent and this trend is also evident in the anisotropies.

We saw in Section 5.1 that velocities increased as microcracks and other porosity closed under pressure. Hysteresis anisotropy also provided some evidence of aligned

cracks. The samples studied here generally show decreasing anisotropy with increasing pressure. This is caused by aligned cracks closing. This effect is established in modeling (e.g., Agersborg et al., 2007) and in laboratory studies (e.g., Lo et al., 1986). Consider a set of cracks in an isotropic medium whose normals are oriented vertically. A P-wave traveling vertically is affected (i.e. the velocity would slow) much more than a P-wave traveling horizontally. Thus, as pressure is increased, the P-wave traveling vertically would increase more rapidly. This brings the velocity of the wave traveling vertically closer to the velocity of the wave traveling horizontally. So as pressure is increased, the anisotropy due to microcracks is decreased. Eventually, when all the cracks are closed, the two velocities will be the same and the sample is again isotropic. It is also useful to note that while anisotropy typically increases with depth due to increased alignment of minerals, the time scale of these studies does not allow for much, if any, mineral realignment. Thus, pressure increases in this study are not analogous to increasing depth in the Earth. Anisotropy generally decreases with pressure due to closing microcracks.

Typically, the decrease in anisotropy with pressure due to cracks in P-waves is larger than that for S-waves (e.g., Johnston & Christensen, 1995; Agersborg et al., 2007). The anisotropic parameters for all of the samples studied here are summarized at low, medium, and peak pressure in Table 5.2.

	Pressure (MPa)	Anisotropy (A) % P	S	ε	γ	δ
Mannville shale 1 (SSA010)	5.0	18.5	10.2	0.253 ± 0.021	0.120 ± 0.018	-0.002 ± 0.058
	40.0	16.0	10.5	0.208 ± 0.020	0.125 ± 0.018	0.092 ± 0.065
	75.0	13.9	9.8	0.174 ± 0.019	0.115 ± 0.017	0.079 ± 0.062

	Pressure (MPa)	Anisotropy (A) % P	S	ε	γ	δ
Mannville shale 2 (SSA011)	10.0	3.2	1.9	0.038 ± 0.015	0.028 ± 0.015	0.018 ± 0.051
	40.0	2.1	1.2	0.022 ± 0.015	0.012 ± 0.014	0.060 ± 0.055
	75.0	1.4	1.3	0.014 ± 0.015	0.014 ± 0.015	0.029 ± 0.051
Mount Head carbonate (SSA019)	5.0	-13.7	-2.3	-0.113 ± 0.011	-0.022 ± 0.014	0.170 ± 0.061
	45.0	-12.0	-3.6	-0.101 ± 0.011	-0.034 ± 0.013	0.039 ± 0.049
	85.0	-3.8	0.8	-0.036 ± 0.013	0.008 ± 0.014	-0.076 ± 0.039
Wabamun carbonate (SSA025)	10.0	12.0	8.4	0.146 ± 0.018	0.096 ± 0.017	0.235 ± 0.076
	45.0	7.0	6.0	0.078 ± 0.016	0.066 ± 0.016	0.163 ± 0.065
	85.0	2.1	5.6	0.022 ± 0.015	0.061 ± 0.016	0.032 ± 0.050
2nd White Specks sandstone (SSA034)	2.5	15.2	0.5	0.196 ± 0.020	0.006 ± 0.014	-0.133 ± 0.036
	12.5	13.3	1.3	0.166 ± 0.019	0.014 ± 0.015	0.046 ± 0.064
	22.5	12.4	3.1	0.152 ± 0.018	0.032 ± 0.015	-0.008 ± 0.054
Big Valley anhydrite (SSA035)	5.0	8.6	4.5	0.098 ± 0.017	0.049 ± 0.016	-0.001 ± 0.049
	25.0	6.3	6.5	0.070 ± 0.016	0.072 ± 0.016	0.015 ± 0.049
	45.0	5.6	6.8	0.061 ± 0.016	0.075 ± 0.016	-0.017 ± 0.049
Bow Island sandstone (SSA037)	7.5	10.4	3.7	0.123 ± 0.018	0.040 ± 0.015	0.049 ± 0.059
	15.0	8.0	2.5	0.090 ± 0.017	0.026 ± 0.015	0.026 ± 0.055
	25.0	7.2	2.8	0.081 ± 0.016	0.029 ± 0.015	0.039 ± 0.055

Table 5.2 - Anisotropies and Thomsen's anisotropic parameters at low, medium, and peak confining pressure.

5.2.1 Sandstone Anisotropy

The anisotropic parameters of the Bow Island sandstone are shown in Figure 5.7. Measurements made while increasing pressure are indicated by the upper curve and measurements made while decreasing pressure are the lower curve. Both P- and S-wave anisotropies decrease as the confining pressure increases. While the pressure is increased from 7.5 MPa to 25.0 MPa, the P-wave anisotropy decreases from 10.4 % to 7.2 % and the S-wave anisotropy decreases from 3.7 % to 2.8 % (Figure 5.7). As described above, the slight decrease in anisotropy is caused by cracks aligned roughly horizontal to bedding. At higher pressures, the effect of microcracks on anisotropy is lessened, and the remaining anisotropy is more of a result of intrinsic anisotropy; that is, layering and preferred orientation of minerals. Preferred orientation of minerals may play a small role, although no orientation could be identified from SEM images. This does not preclude any orientation in the sample, however, it does indicate that the contribution to anisotropy will likely be small. This sample was not brought up to high enough pressures to completely close the microcracks so the anisotropy at peak pressure will be mainly from a combination of microcracks and layering.

At a peak pressure of 22.5 MPa, the anisotropy of the 2nd White Specks sandstone is 15.2% (ε) and 3.2% (γ). This sample behaves much like the other sandstone sample. Over the pressure range, the P-wave anisotropy decreases slightly, however the S-wave anisotropy increases slightly (Figure A.20). The increase in S-wave anisotropy is 2.6%. γ seems relatively stable until 15.0 MPa, at which point it starts to increase slightly. The exact reason for the increase is not known. The SEM images did not observe any preferred orientation of minerals which suggests that this plays only a minor role in the

anisotropy. We must be careful in interpreting the anisotropy of this sample. The total anisotropy in this sample may not be true anisotropy. This sample appeared relatively heterogeneous and measurements for different directions were not taken on the same core. If the composition varies slightly for each core measured it is possible that wave speeds would be different due to the heterogeneity, rather than from intrinsic or crack-induced anisotropy. Densities found by measuring dimensions and weighing the three cores from this sample found densities ranging from 2.40 – 2.44 g/cm^3. This is not a large range, however the sample edges were heavily chipped and this method of measuring density is relatively imprecise. Unfortunately, there was not enough of this sample to take multiple cores for a heterogeneity test.

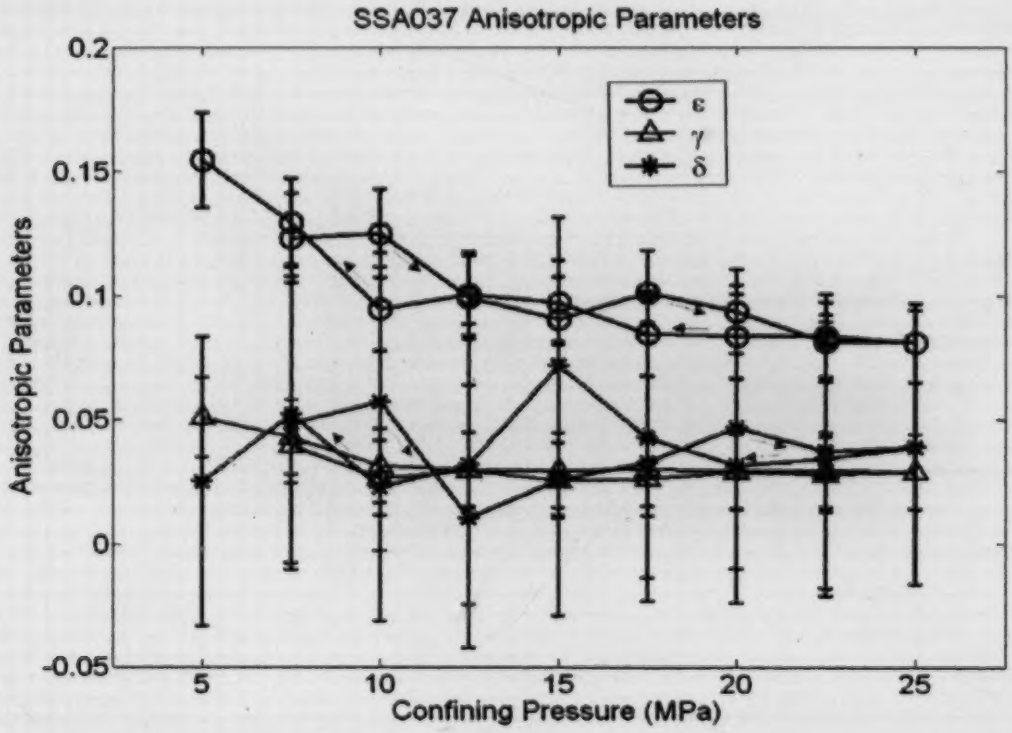

Figure 5.7 - Anisotropic parameters of the Bow Island sandstone. Measurements made while increasing pressure are the upper curves. Progression is marked by arrows.

5.2.2 Carbonate Anisotropy

As discussed above, velocities of the Mount Head carbonate with pressure are largely controlled by microcracks. The anisotropy is also largely controlled by microcracks. At low pressures the P-wave velocities differ by almost 20%. At peak pressure ε is less than -4% (± 1.3%). S-wave anisotropy decreases from almost -7% to +0.8% (± 1.4%), which is isotropic within error. As discussed, this large decrease in anisotropy is due to aligned microcracks.

The anisotropies of the Mount Head carbonate are anomalous to the rest of the samples in this data set in one respect. The velocities perpendicular to bedding are larger than those parallel to bedding, except for S-waves at high pressure. This causes ε and γ to be negative (Figure 5.8). This is curious since most rocks have velocities which are fastest within the bedding plane, indeed the basis of the measurements taken here was that the sample was TI with a vertical symmetry axis. This is a very homogenous sample so layering and preferred orientation of minerals will not be major sources of anisotropy. Microcracks are obviously the dominant control of the velocity change and of anisotropy. The fact that velocities are fastest perpendicular to bedding could possibly be caused by a set of cracks oriented orthogonal to bedding. This is not unreasonable because microcracks and fractures occur in many rocks due to stress relief while coring (e.g., Li & Schmitt, 1998). Depending on the initial state of stress there could possibly be a set of cracks oriented more vertically than horizontally.

A set of cracks oriented orthogonal to bedding is supported by the fact that much of the behaviour of the Mount Head carbonate is opposite to that of the other samples. Velocities traveling parallel to bedding increase more, and have more hysteresis, than

those traveling perpendicular to bedding. As further evidence, we will see later that the largest increase in the V_P/V_S ratio happens in the direction parallel to bedding. Another explanation may be that the sample has a symmetry that is different than TI with a vertical symmetry axis, although texturally there is no indication of this and the sample seems to approach isotropy at higher pressures. The anisotropy and velocities are clearly controlled in large part by microcracks, however, the alignment of the cracks and other mechanisms of velocity control are unknown.

The anisotropy of the Wabamun carbonate is also largely controlled by microcracks at low pressure. ε decreases from 14.6% to 2.2% (± 1.5%) over the pressure range. However, unlike the other carbonate sample, the Wabamun carbonate is layered and this is likely a cause of anisotropy at peak pressure. At peak pressure, the S-wave anisotropy is 6.1% (± 1.6%) and P-wave anisotropy is 2.2% (± 1.5%). ε, γ and δ all decrease with pressure.

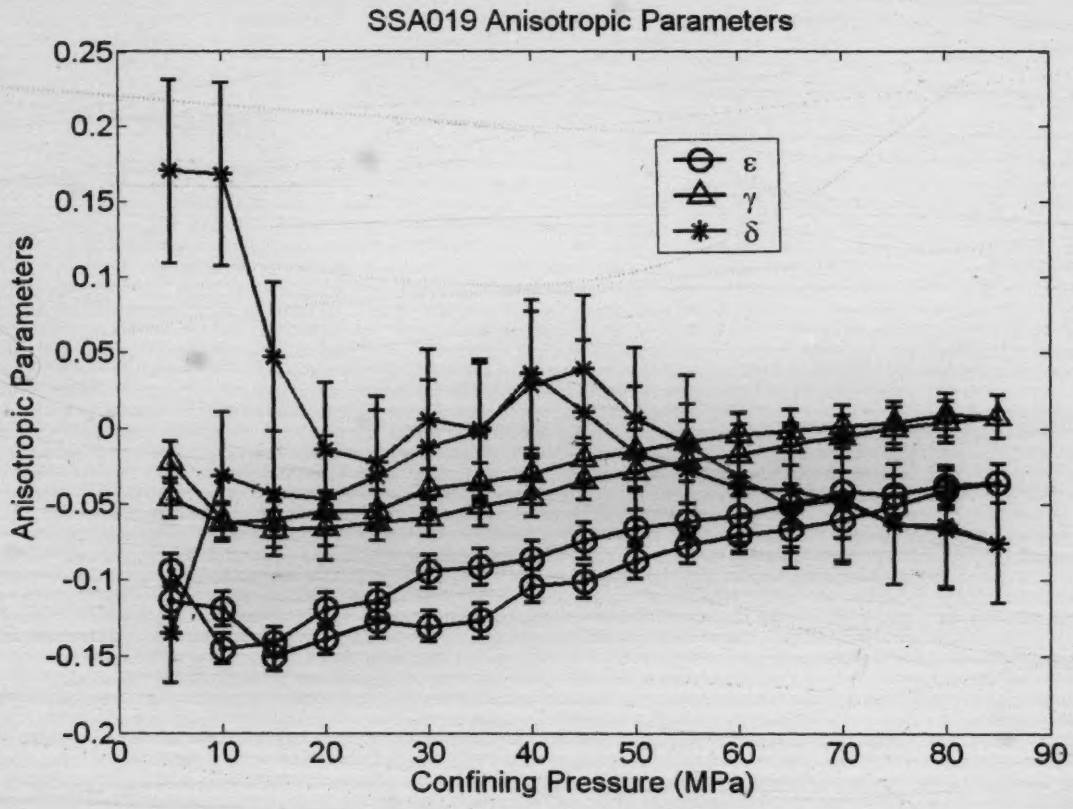

Figure 5.8 - Anisotropic parameters of the Mount Head carbonate.

5.2.3 Shale and Anhydrite Anisotropy

As mentioned earlier, the magnitude of anisotropy in the Mannville shale 1 was the largest of all the samples tested at 17.4% and 11.5% for ε and γ, respectively. This is not surprising given that it is the only sample that featured preferred orientation of clay minerals, which is a major cause of anisotropy. Figure 5.9 shows the anisotropic parameters with pressure of this sample. ε and γ decreases slightly with pressure due to the presence of a small amount of aligned microcracks. However, we saw that microcracks affected the velocities only slightly and it is the same for the anisotropy,

particularly at high pressure. Thus, the anisotropy in this sample is mostly due to layering and preferred orientation of minerals.

The Mannville shale 2 has much the same composition as the Mannville shale 1, though the clay minerals do not appear to be as aligned. The anisotropy of this sample changes with pressure, but only slightly. Both ε and γ decrease slightly with pressure. P-wave anisotropy decreases from 3.8% to 1.4% (± 1.5%), and S-wave anisotropy decreases from 2.8% to 1.4% (± 1.5%). This is again due to a small amount of aligned porosity closing. At peak pressure, this sample is isotropic within experimental error. There was no preferred orientation of minerals detectable in this sample. Any intrinsic anisotropy that exists in the Mannville shale 2 is largely due to layering.

The velocities in the Big Valley anhydrite did not change much with pressure, indicating that microcracks were not prevalent. The anisotropy also does not change much with pressure, P-wave anisotropy decreases by just 3.7%, and S-wave anisotropy increases slightly. Like the 2nd White Specks sandstone this increase is small, only 2.6%. This sample shows an initial increase in γ at low pressures and it seems to stabilize above approximately 20 – 25 MPa. The reason for this behaviour is not known. There is still noticeable anisotropy at peak pressure, P-wave and S-wave anisotropies are 6.1% and 7.5%, respectively.

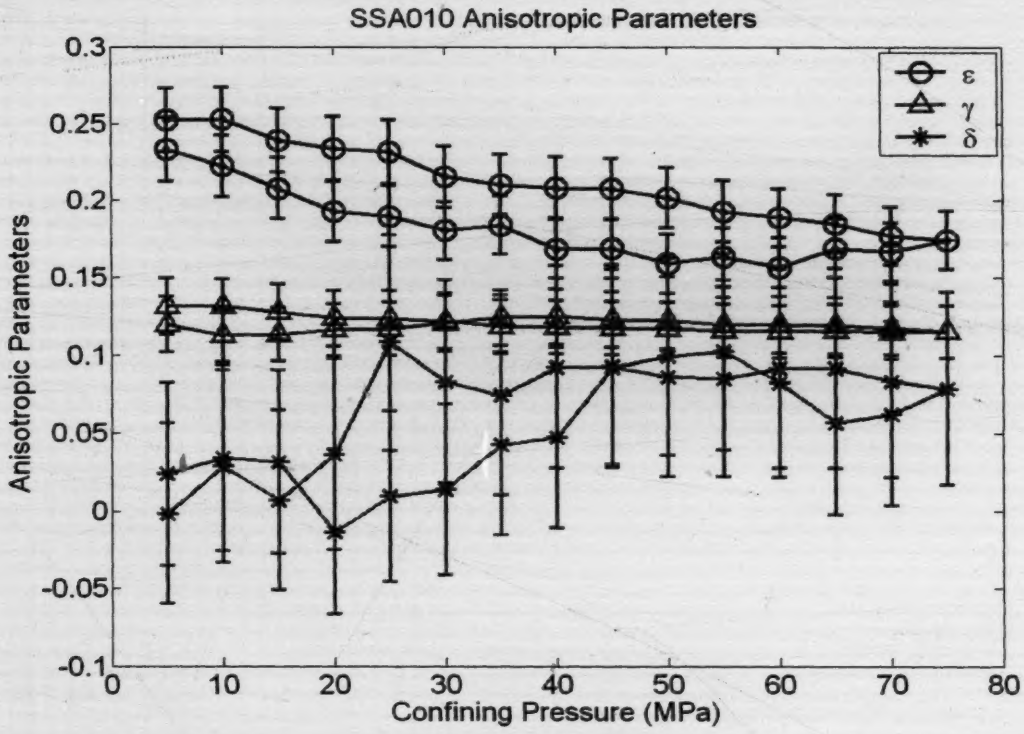

Figure 5.9 - Anisotropic parameters for the Mannville shale 1.

Table 5.2 provides an overview of the anisotropic parameters of the samples. As microcracks and other porosity closes ε and γ tend towards zero with increasing pressure. δ is much more variable with pressure, although it tends to be positive and small. Often it is difficult to confidently say what the trend δ has with pressure because of the error. The error in δ often greatly exceeds the value itself.

Although we do not have the proper tools to analyze exactly how much anisotropy comes from layering, preferred orientation of minerals, and microcracks, respectively, some general statements can be made. As mentioned, the Mannville shale 1 was the only sample that had discernable preferred orientation of minerals from SEM. Except for the sandstone samples which were not subjected to high pressures, at peak pressure the

anisotropic effect of microcracks is largely negated. This implies that the dominant source of anisotropy in most of the samples at peak pressure is layering. It bears repeating that this does not preclude any anisotropic contribution from the preferred orientation of minerals or cracks, just that the involvement is likely to be small. This is interesting because it shows that layering can perhaps constitute a fairly large portion of the overall anisotropy. In the anhydrite sample, for instance, microcracks did have much of a control on the anisotropies or the velocities, and no mineral orientation was seen, yet ε and γ are both over 6% at peak pressure. Detailed analyses such as those by Vernik (1993) and Wenk et al. (2007) are needed in order to determine the contribution of the different sources of anisotropy.

5.2.4 Comparison With Seismics in the Region

An important purpose of this research is to aid in the development of anisotropy models in Alberta. To that end, it is informative to compare typical values of ε and δ found from anisotropic depth migration in seismic experiments to ε and δ values found in this study. In field studies in this area typically $\varepsilon > \delta \geq 0$.

Leslie & Lawton (1999) collected data from P-wave refraction studies at Jumpingpound Creek, Alberta and Longview, Alberta, both located in the Rocky Mountain Foothills in Alberta. In both surveys, shales from the Wapiabi formation were studied. The Jumpingpound Creek survey found $\varepsilon = 0.14 \pm 0.05$ and $\delta = 0.00 \pm 0.08$, and the Longview study found $\varepsilon = 0.25 \pm 0.06$ and $\delta = 0.00 \pm 0.06$.

Robinson et al. (2006) performed anisotropic depth migration on a 3D seismic survey data set over an area of carbonate and shale near Stolberg, Alberta. They used an ε of 0.12 – 0.15 and a δ of 0.03 to produce their images.

Kirtland Grech et al. (2002) performed vertical seismic profiling in the Rocky Mountain Foothills of Alberta to examine dipping shale strata. They performed anisotropic prestack depth migration and found that values of $\varepsilon = 0.10 \pm 0.01$ and $\delta = 0.05 \pm 0.02$ gave them the best results.

Vestrum et al. (1999) investigated imaging and misposition problems in anisotropic media. Working with a data set from the southern Alberta Foothills consisting of shale-dominated clastics as well as carbonates, they found that the best images were produces using an $\varepsilon = 0.10$ and $\delta = 0.025$. These values are not independent as δ was set to be one-quarter of the value of ε.

Most of the studies mentioned above are performed over shale-rich areas. The Mannville shale 1 is the most anisotropic shale and has ε values ranging from approximately 0.16 – 0.25 and δ values of approximately 0 – 0.1. The values of ε for this sample are slightly higher than most of the values used in field studies, although they are comparable to those found by Leslie & Lawton (1999). The values of δ are within reason given the values of field studies, which vary between 0 – 0.05. Field studies will not test shales exclusively, however. Sandstone is another type of rock that is often present. At peak pressure, the values of ε in the 2nd White Specks sandstone and the Bow Island sandstone are 0.152 and 0.081, respectively, while the values of δ are -0.008 and 0.039. These values also compare well to values seen in the field.

5.3 Elastic Constants

There are five independent elastic stiffnesses C_{ij} in a transversely isotropic medium and their relations to phase velocity are given in Chapter 2 (Equations 2.14-2.18). The elastic constants of the Bow Island sandstone in relation to pressure are shown

in Figure 5.10. They increase with pressure linearly (Table 5.3), as expected from the behaviour of the velocities. The hysteresis in the elastic constants is also expected and is a result of the hysteresis in the velocities. In all of the samples except the Mount Head carbonate, $C_{11} > C_{33}$ and $C_{66} > C_{44}$. In the Mount Head carbonate the opposite is true. Full data sets for all of the samples are provided in Appendix A.

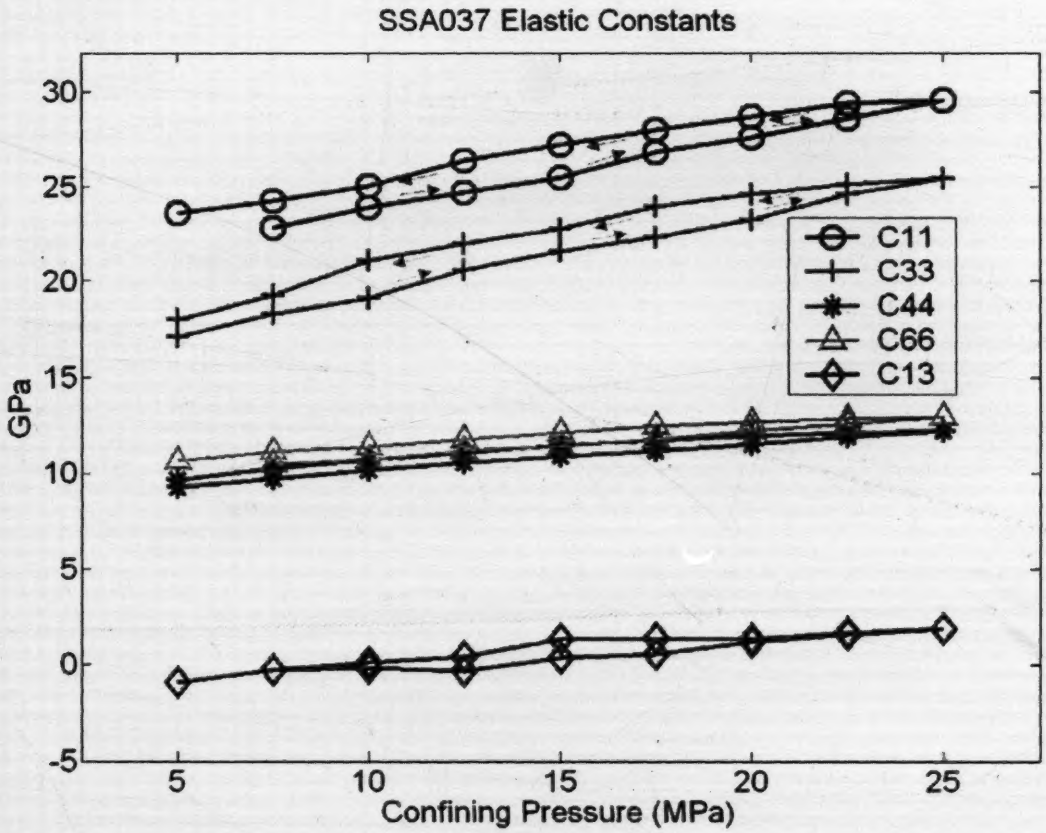

Figure 5.10 - Elastic constants for the Bow Island sandstone. Hysteresis effects cause the values to be higher during depressurization. Progression is indicated by arrows on C_{11} and C_{33}, and omitted on the other elastic constants for clarity.

The absolute values of the elastic constants vary significantly between samples. Table 5.3 gives the elastic constants for each sample at low, mid-range, and peak pressure. As expected, the elastic constants generally increase with increasing pressure. The only exception is the Mount Head carbonate, whose C_{13} starts decreasing slightly at approximately 45 MPa (Figure 5.11). The reason for this decrease is unknown, although it has been seen elsewhere. Domnesteanu et al. (2002) measured a shale under confining and pore pressure. While keeping the confining pressure constant they increased the pore pressure. This has the effect of decreasing the effective pressure and has similar effects to decreasing the confining pressure. As Domnesteanu et al. (2002) increased pore pressure in their sample they found that the C_{13} elastic constant increased. They claim that this is due to lower pore compliance and more coupling. Lo et al., (1986) found a similar trend with C_{13} to that found on the Mount Head carbonate in a preferentially cracked granite sample. C_{13} increased up to 30 MPa confining pressure and then abruptly became almost constant over the pressure range up to 100 MPa. In that same study a decreasing C_{13} was found with pressure in a Berea sandstone. The C_{13} in the Berea sandstone increased to 15 MPa confining pressure and then started decreasing. No explanation is given for this trend.

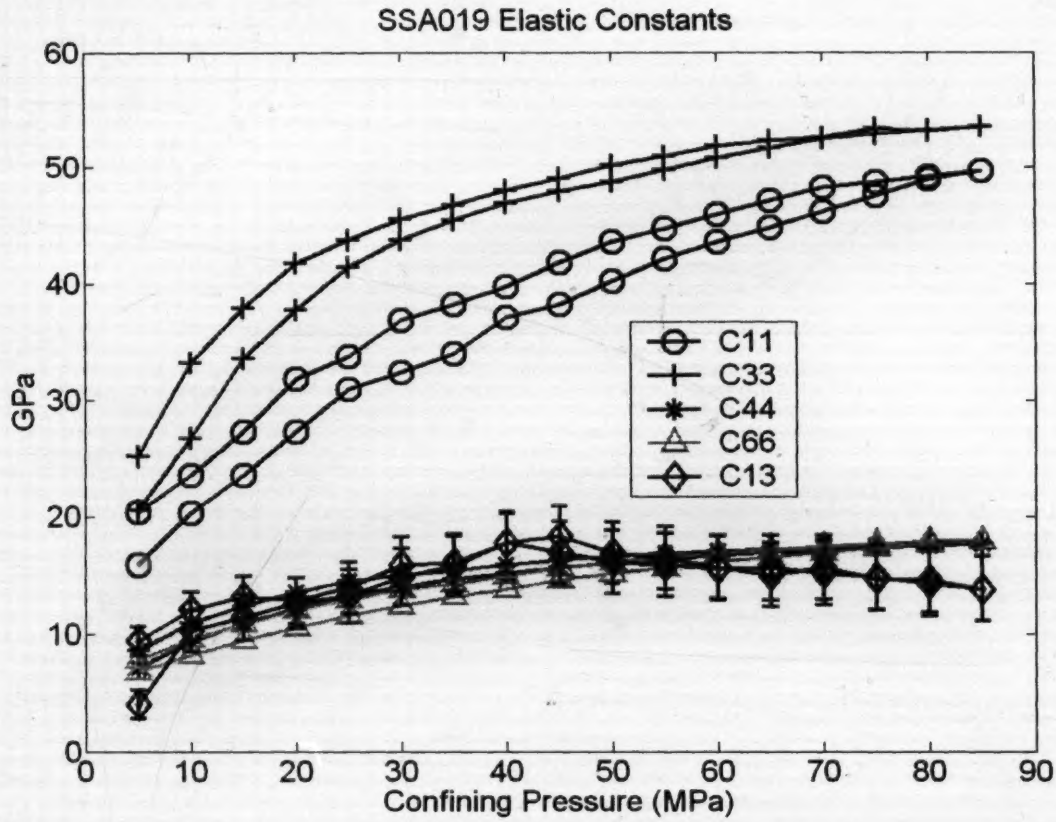

Figure 5.11 – Elastic constants for the Mount Head carbonate. Error bars are included for C_{13}.

Showing the elastic constants makes it simple to observe the symmetry of the sample and Table 5.3 can be used to see how 'isotropic' the sample is. If the sample is isotropic, it is expected that $C_{11} = C_{33}$, and $C_{44} = C_{66}$. We would also expect that $C_{13} = C_{12}$. Recall that $C_{12} = C_{11} - 2C_{66}$. All of the samples are somewhat anisotropic although the Mannville shale 2 becomes nearly isotropic at high pressure with both C_{11} and C_{33}, and C_{44} and C_{66} differing by less than 3%, which is within experimental limits. At peak pressure C_{12} = 9.8 GPa. This produces a 15% error with a C_{13} of 11.4 GPa at that

pressure. The error on C_{13} is ± 3.0 GPa, however, and these constants agree well within error. At peak pressure, the elastic constants of the Mount Head carbonate are also approaching isotropy, although C_{11} and C_{33} are not quite within error of one another. C_{12} has a value of 13.8 at peak pressure and is very close to C_{13}. In order to compare the elastic constants in Table 5.3, the bulk and shear modulus of the major minerals seen in these samples are shown in Table 5.4. There may also be other minerals in smaller amounts that influence the stiffness of the sample. For example, XRD identified fluorite in the Big Valley anhydrite. Fluorite has a high bulk and shear modulus (86.4 GPa and 41.8 GPa, respectively. Huffman & Norwood, 1960), so small amounts of this mineral could possibly influence the elastic constants. The elastic constants of the samples are reasonable when compared to the mineral values. Porosity also has a large affect; if there is more porosity the rock is less stiff.

	Pressure (MPa)	C_{11} (GPa)	C_{33} (GPa)	C_{44} (GPa)	C_{66} (GPa)	C_{13} (GPa)
Mannville shale 1 (SSA010)	5.0	50.0 ± 1.3	33.5 ± 0.8	15.8 ± 0.4	19.5 ± 0.5	1.6 ± 2.1
	40.0	53.4 ± 1.3	37.7 ± 0.9	16.9 ± 0.4	21.1 ± 0.5	7.1 ± 2.3
	75.0	55.2 ± 1.4	40.9 ± 1.0	17.6 ± 0.4	21.6 ± 0.5	8.8 ± 2.4
Mannville shale 2 (SSA011)	10.0	63.2 ± 1.4	58.8 ± 1.3	26.0 ± 0.6	27.5 ± 0.6	7.8 ± 2.7
	40.0	65.0 ± 1.5	62.3 ± 1.4	27.2 ± 0.6	27.9 ± 0.6	11.5 ± 2.9
	75.0	67.3 ± 1.5	65.5 ± 1.5	28.0± 0.6	28.7 ± 0.6	11.4 ± 3.0
Mount Head carbonate (SSA019)	5.0	15.9 ± 0.4	20.6 ± 0.6	7.2 ± 0.2	6.8 ± 0.2	9.4 ± 1.2
	45.0	38.2 ± 1.1	47.9 ± 1.3	15.7 ± 0.4	14.6 ± 0.4	18.3 ± 2.6
	85.0	49.7 ± 1.4	53.5 ± 1.5	17.7 ± 0.5	18.0 ± 0.5	13.9 ± 2.8
Wabamun carbonate (SSA025)	10.0	101.2 ± 2.5	78.3 ± 2.0	33.2 ± 0.8	39.6 ± 1.0	27.5 ± 4.7
	45.0	118.2 ± 3.0	102.3 ± 2.6	37.9 ± 1.0	42.8 ± 1.1	41.6 ± 5.7
	85.0	130.6 ± 3.3	125.2 ± 3.1	41.4 ± 1.0	46.5 ± 1.2	46.2 ± 6.4

	Pressure (MPa)	C_{11} (GPa)	C_{33} (GPa)	C_{44} (GPa)	C_{66} (GPa)	C_{13} (GPa)
2nd White Specks sandstone (SSA034)	2.5	32.9 ± 1.2	23.6 ± 0.9	14.8 ± 0.5	15.0 ± 0.5	-10.4 ± 2.5
	12.5	37.4 ± 1.4	28.1 ± 1.0	17.0 ± 0.6	17.5 ± 0.6	-4.7 ± 2.4
	22.5	41.8 ± 1.5	32.1 ± 1.2	18.3 ± 0.7	19.5 ± 0.7	-4.8 ± 2.7
Big Valley anhydrite (SSA035)	5.0	113.6 ± 2.8	95.0 ± 2.3	30.4 ± 0.7	33.4 ± 0.8	34.1 ± 4.9
	25.0	117.0 ± 2.9	102.7 ± 2.5	31.3 ± 0.8	35.8 ± 0.9	41.6 ± 5.3
	45.0	119.3 ± 2.9	106.3 ± 2.6	32.0 ± 0.8	36.8 ± 0.9	40.6 ± 5.3
Bow Island sandstone (SSA037)	7.5	22.8 ± 0.5	18.3 ± 0.4	9.7 ± 0.2	10.5 ± 0.2	-0.3 ± 0.9
	15.0	25.5 ± 0.6	21.6 ± 0.5	10.9 ± 0.2	11.5 ± 0.3	0.4 ± 1.0
	25.0	29.6 ± 0.7	25.4 ± 0.6	12.3 ± 0.3	13.0 ± 0.3	1.9 ± 1.2

Table 5.3 – Elastic constants at low, mid-range, and peak pressure for each sample.

Mineral	Bulk Modulus (GPa)	Shear Modulus (GPa)
Quartz[a]	36.6	45.0
Dolomite[b]	76.4	49.7
Dolomite[c]	94.9	45.0
Anhydrite[d]	62.1	33.6
Smectite[e]	9.3	6.9
Illite[e]	60.1	25.3

Table 5.4 - Bulk and shear modulus of selected minerals common in the samples in this work. [a] Koga et al., 1958. [b] Nur & Simmons, 1969. [c] Humbert & Plicque, 1972. [d] Rafavich et al., 1984. [e] Wang et al., 2001.

5.3.1 Calculation of C_{13} from V_{SV}

Although C_{13} is traditionally calculated from measurements of V_P in an off-axis direction, there is no reason why this elastic constant cannot be calculated using V_{SV}, or a combination of V_P and V_{SV} measurements. Table 5.5 shows the C_{13} elastic constant calculated at low, mid, and peak pressure using the equation:

$$C_{13} = -C_{44} + \sqrt{\frac{4\rho^2(V_P^2 - V_S^2)^2 - (C_{11} - C_{33})^2}{4}} \qquad (5.2)$$

where V_P and V_S are the velocities measured 45° to bedding. This expression is a result of manipulating Equations 2.11 and 2.12 at 45°. This equation uses both V_P and V_{SV}, which could reduce the influence of random errors in the resulting C_{13}. There have been, to our knowledge, only a handful of other workers who have used the shear velocity to assist in calculating C_{13}, typically using additional off axis measurements and an iterative procedure (Johnston & Christensen, 1995; Hornby, 1998).

The C_{13} elastic constant calculated using this method is generally close to the previously calculated C_{13} and they become more similar with increasing pressure. At peak pressure the average difference between the two calculations in all the samples is only 1.0 GPa. Equations 2.18 and 5.2 are both developed for TI media. Since similar values are obtained using either equation, this gives some confidence in the interpretation of the samples as TI. The behaviour of the new C_{13} with pressure is largely the same as previously. There are some slight differences however. The largest difference is seen in the Mount Head carbonate (Figure 5.12). Using only the V_P velocity at 45° we saw odd behaviour in C_{13} (Figure 5.11). Calculating the C_{13} with Equation 5.2 causes smooth, increasing trend with pressure, which is closer to the behaviour that is expected. Using an iterative procedure similar to that of Hornby (1998), the C_{13} values at peak pressure are close to those produced using Equation 5.2, differing by an average of only 0.3 GPa.

Sample	Pressure (MPa)	C_{13} from Equation 2.18 (GPa)	C_{13} from Equation 5.2 (GPa)
Mannville shale 1 (SSA010)	5.0	1.6 ± 2.1	4.1 ± 0.9
	40.0	7.1 ± 2.3	7.7 ± 1.0
	75.0	8.8 ± 2.4	9.1 ± 1.0

Sample	Pressure (MPa)	C_{13} from Equation 2.18 (GPa)	C_{13} from Equation 5.2 (GPa)
Mannville shale 2 (SSA011)	10.0	7.8 ± 2.7	8.5 ± 1.3
	40.0	11.5 ± 2.9	10.5 ± 1.4
	75.0	11.4 ± 3.0	11.1 ± 1.4
Mount Head carbonate (SSA019)	5.0	9.4 ± 1.2	6.3 ± 0.5
	45.0	18.3 ± 2.6	15.2 ± 1.0
	85.0	13.9 ± 2.8	15.3 ± 1.1
Wabamun carbonate (SSA025)	10.0	27.5 ± 4.7	24.3 ± 2.0
	45.0	41.6 ± 5.7	38.2 ± 2.4
	85.0	46.2 ± 6.4	46.2 ± 2.7
2nd White Specks sandstone (SSA034)	5.0	-10.9 ± 2.6	-6.3 ± 0.7
	12.5	-4.7 ± 2.4	-3.3 ± 0.8
	22.5	-4.8 ± 2.7	-3.4 ± 0.8
Big Valley anhydrite (SSA035)	5.0	34.1 ± 4.9	36.8 ± 2.1
	25.0	41.6 ± 5.3	42.5 ± 2.3
	45.0	40.6 ± 5.3	43.4 ± 2.3
Bow Island sandstone (SSA037)	7.5	-0.3 ± 0.9	0.5 ± 0.5
	15.0	0.4 ± 1.0	1.3 ± 0.5
	25.0	1.9 ± 1.2	2.6 ± 0.6

Table 5.5 - The difference in C_{13} calculations using Equation 2.18 and Equation 5.2.

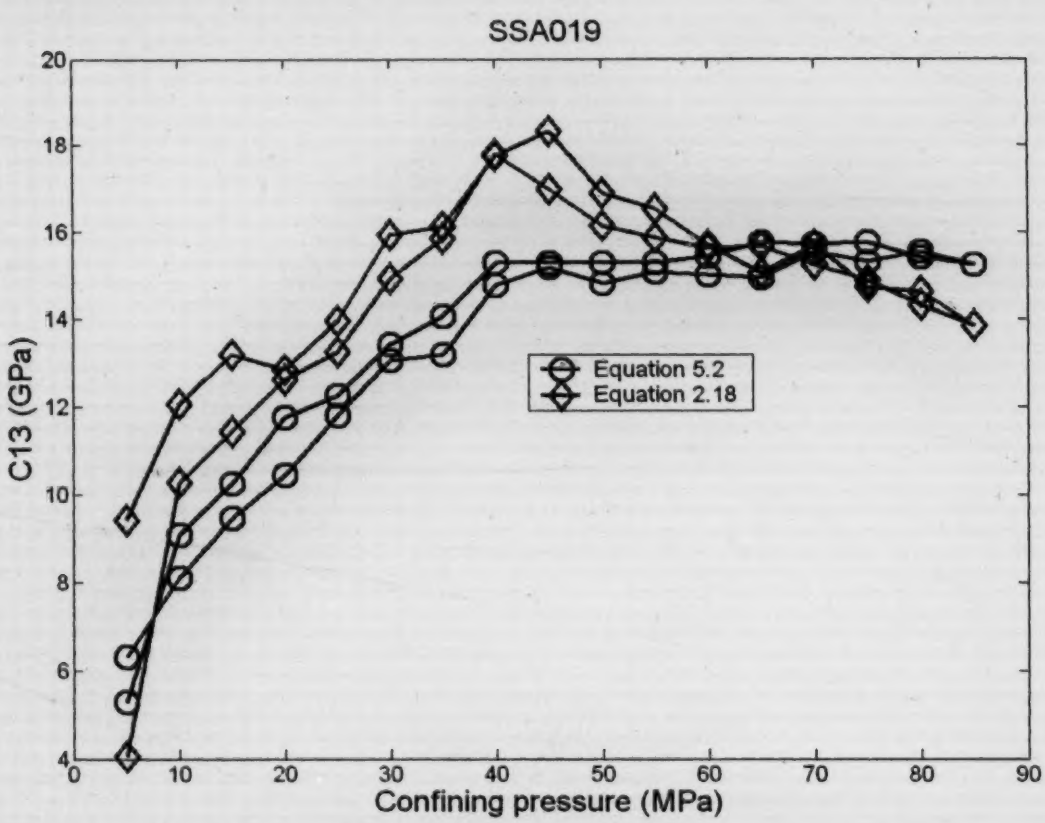

Figure 5.12 - C_{13} for the Mount Head carbonate calculated using Equation 2.18 and 5.2.

5.4 V_P/V_S Ratios

V_P/V_S ratios are controlled by many factors. Structure, pore fluid, saturation levels, stress conditions and many other properties can all change the ratio dramatically. The V_P/V_S ratio is used to identify lithology or fluid in amplitude versus offset (AVO) studies. Understanding how this ratio changes under various pressure or fluid conditions could lead to more accurate indicators.

The literature on V_P/V_S ratios in shales is relatively scarce, and meaningful comparisons are further complicated by varying experimental conditions. Some experiments are performed on dry samples (e.g., Lo et al., 1986; Johnston & Christensen,

1995), while others are performed saturated (e.g., Jones & Wang, 1981; Dewhurst & Siggins, 2006), with pore control (e.g., Domnesteanu et al., 2002) or drained to atmospheric pressure (Hornby, 1998). Further, some studies are performed using isotropic pressure (e.g., Johnston & Christensen, 1995), while others use various anisotropic stress conditions (Dewhurst & Siggins, 2006). Since experiments in this work were done with dry samples under isotropic pressure conditions, this section will focus on the pressure dependence of V_P/V_S ratios in dry shales.

V_P/V_S ratios for the seven samples tested here are between 1.27-1.83 and generally increase slightly with pressure (Figure 5.13). Both increases and decreases of this parameter in shales have been seen in the literature. Generally, however, for dry samples V_P/V_S increases with confining pressure. Johnston & Christensen (1994, 1995) measured seven shale samples under these conditions. The V_P/V_S ratios were between 1.46-1.79 and all increased or remained steady with pressure. None of the samples showed dramatic increases with pressure. The average increase in the ratio perpendicular to bedding was 0.09 which was three times the increase in the ratios parallel (V_P/V_{SH}) and 45° (V_P/V_{SV}) to bedding, where the average increase was only 0.03. In all cases the 45° ratio was the largest of the three. Lo et al. (1986) found similar results in a dry Chicopee shale. Increases in the V_P/V_S ratios traveling perpendicular, parallel, and 45° to bedding were 0.12, 0.04, and 0.01, respectively. The ratios were between 1.58 and 1.75, and the 45° ratio was the largest. Lo et al. (1986) state that these values show a lack of change with pressure because of a relative lack of microcracks in the sample.

There have also been studies with saturated shales. Hornby (1998) tested two shales under saturated conditions that were drained to atmosphere, and found varying

V_P/V_S behaviour. The ratios in these samples are typically larger (1.68-2.13) than those previously seen in dry samples. In the first shale V_P/V_S ratios all decrease. The ratio perpendicular to bedding changes the most, and unlike previous measurements on dry shales this ratio was the largest. The V_P/V_S ratio perpendicular to bedding in the second shale decreased by 0.02, while the ratio parallel to bedding increased by 0.05. Dewhurst & Siggins (2006) examined one fully saturated shale under isotropic stress conditions and found the V_P/V_S ratio to increase from ~2.32-2.58. They did not provide the propagation direction of this ratio.

The samples measured here generally increase or stay constant with pressure and the error in each is 0.02-0.03. The two Mannville shale samples best represent a clay rich shale. The V_P/V_S ratios of the Mannville shale 2 are relatively invariant with pressure. The ratio 45° to bedding is the largest. The largest increase is the ratio perpendicular to bedding which increases by 0.03. In the Mannville shale 1, the V_P/V_S ratios increase slightly more. Perpendicular and 45° to bedding the increase is 0.07 and 0.05, respectively, while the ratio parallel to bedding is steady at 1.60. The rest of the samples show similar behaviour. The two carbonate samples show the largest increases in V_P/V_S with pressure. The ratio perpendicular to bedding of the Wabamun carbonate increases by 0.20 over the pressure range and interestingly the ratio that shows the largest increase in the Mount Head carbonate is parallel to bedding. V_P/V_S ratios in the two sandstone samples increase or stay constant with pressure. The V_P/V_S ratios 45° and perpendicular to bedding increase in the Big Valley anhydrite, however, the ratio parallel to bedding decreases very slightly (0.03) with pressure.

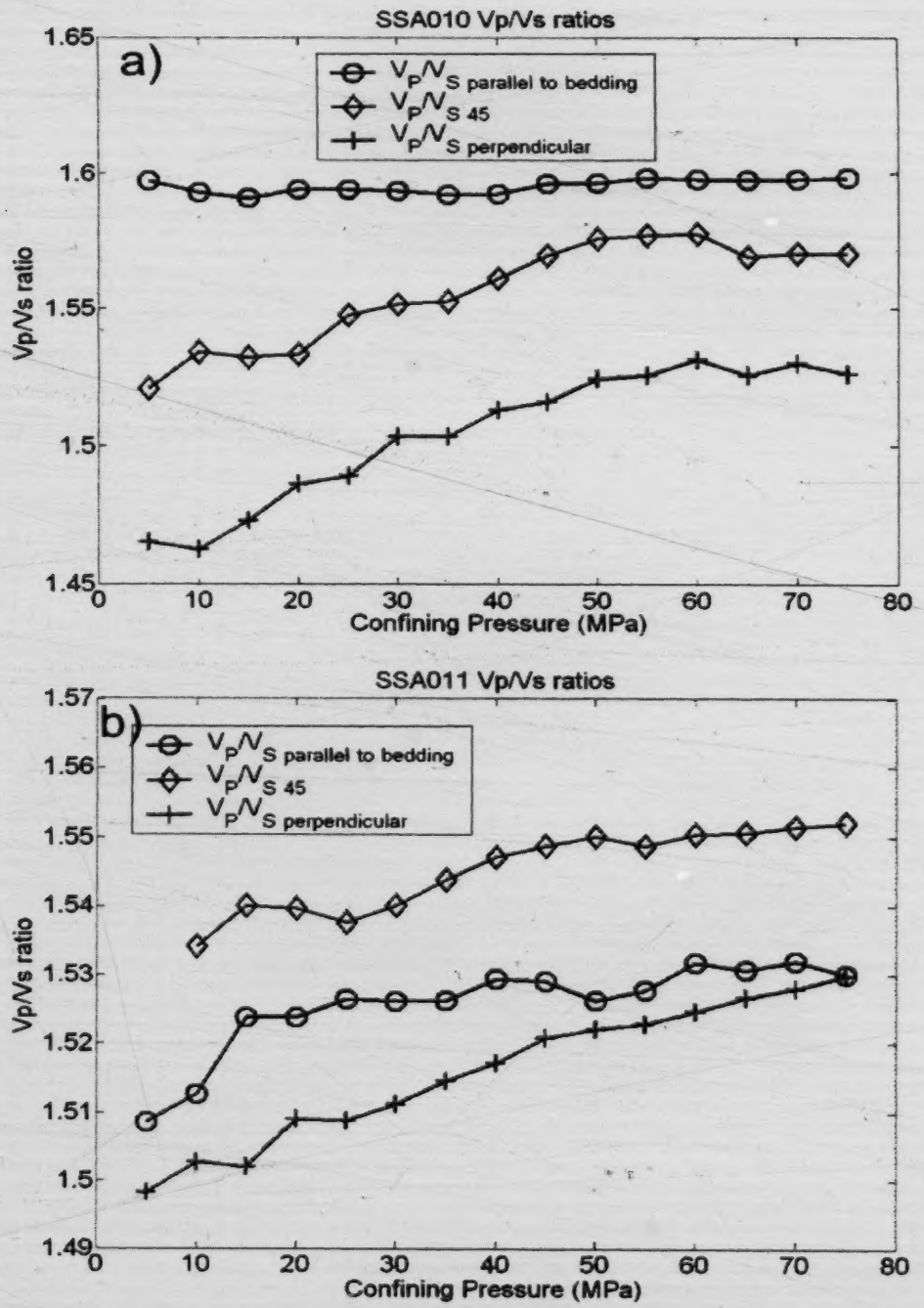

Figure 5.13 - V_P/V_S ratios for a) the Mannville shale 1 (SSA010) and b) the Mannville shale 2 (SSA011).

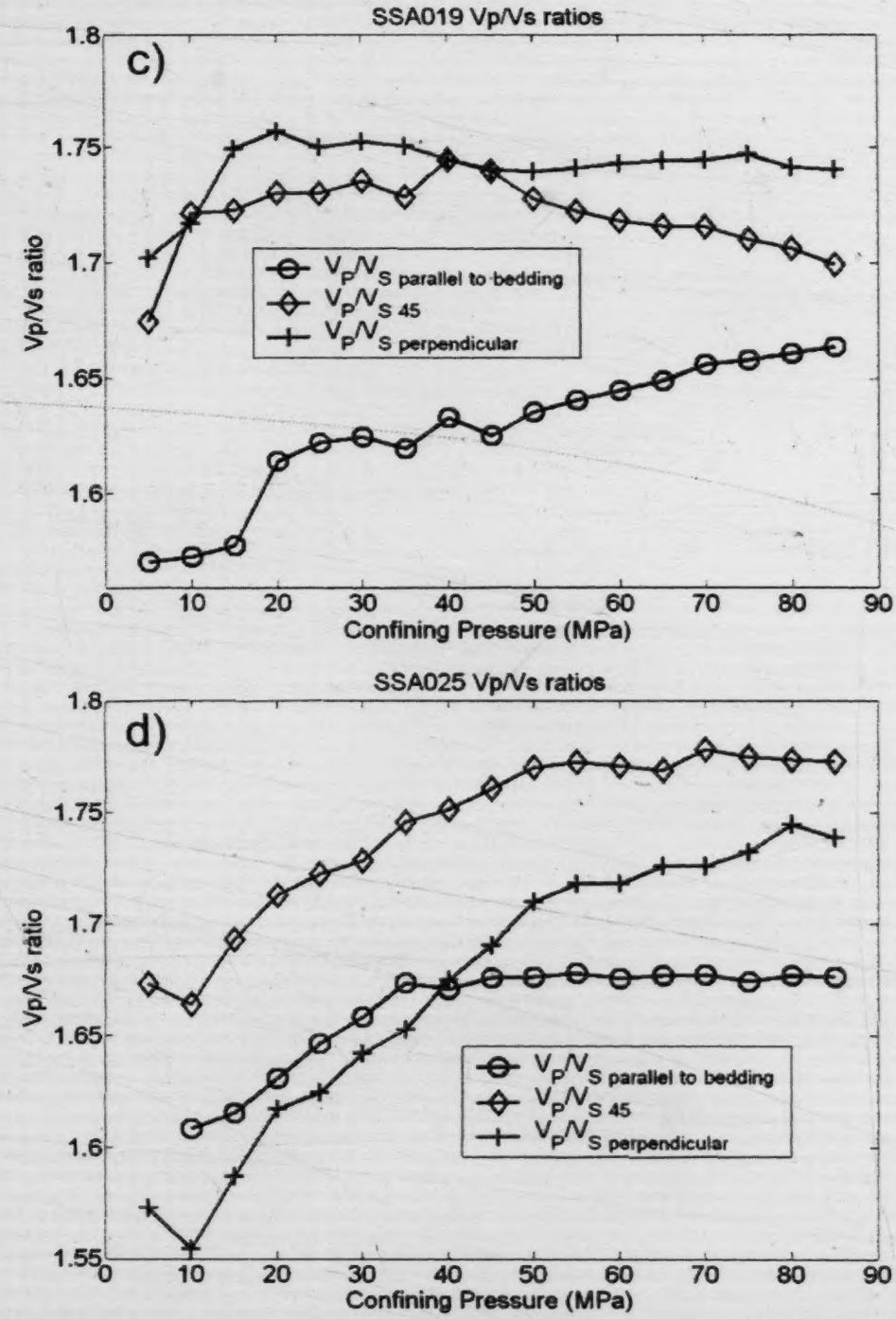

Figure 5.13 *(continued)* - V_P/V_S ratios for c) the Mount Head carbonate (SSA019) and d) the Wabamun carbonate (SSA025).

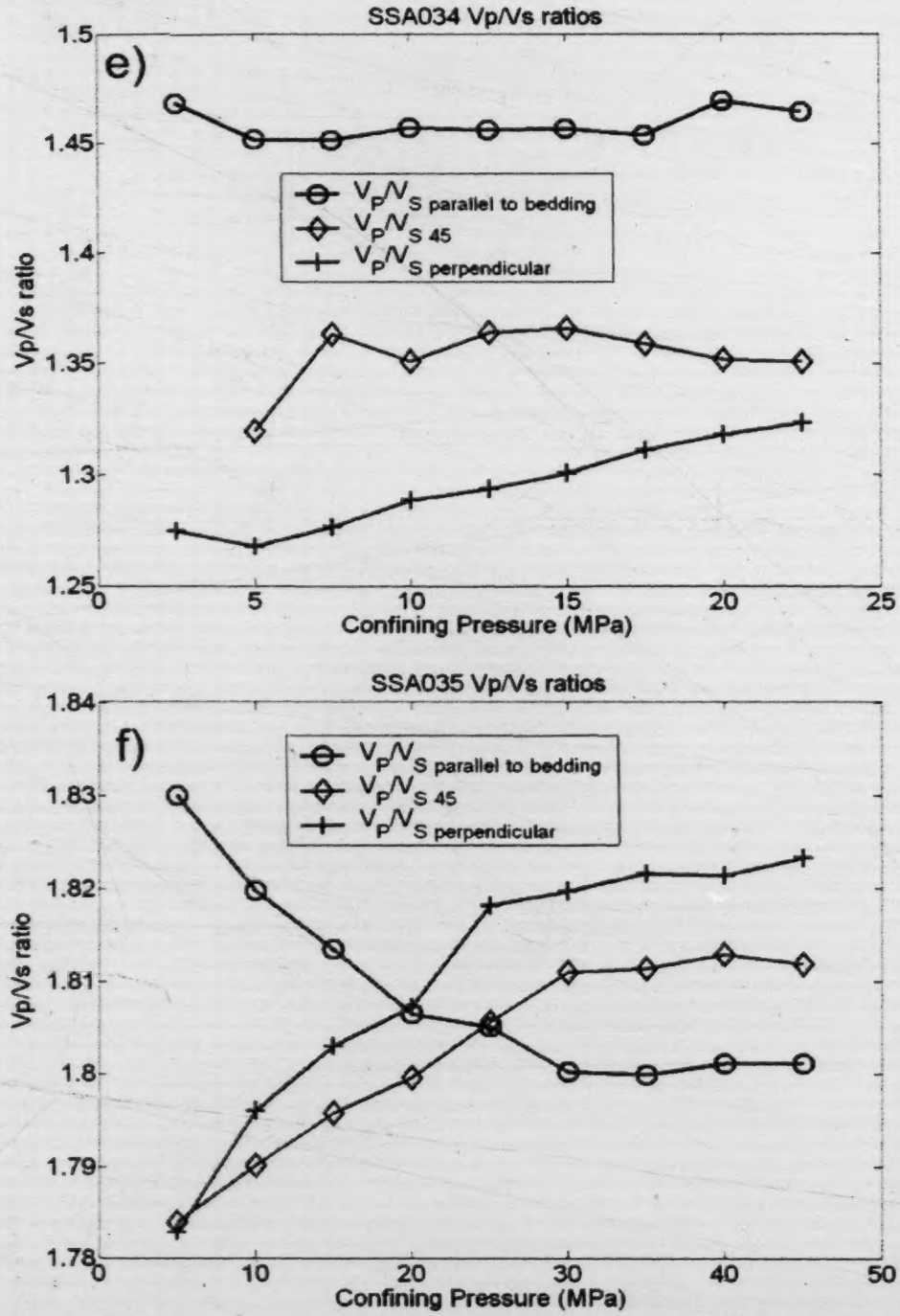

Figure 5.13 *(continued)* - V_P/V_S ratios for e) the 2nd White Specks sandstone (SSA034) and f) the Big Valley anhydrite (SSA035).

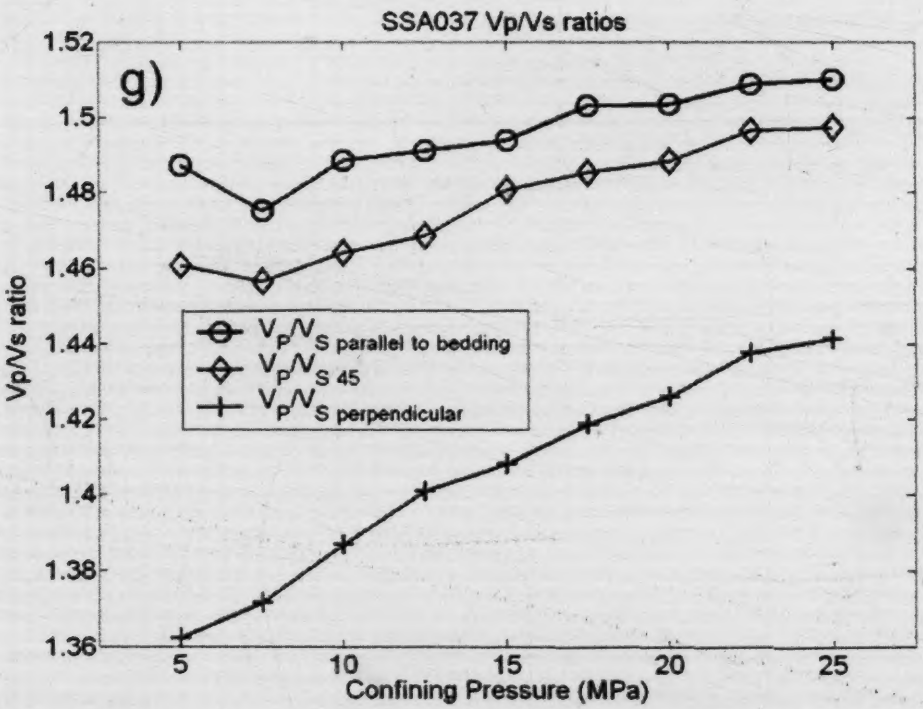

Figure 5.13 *(continued)* - V_P/V_S ratios for g) the Bow Island sandstone (SSA037).

Castagna et al. (1985) developed the so-called 'mudrock line', which relates P-wave velocity to S-wave velocity in water-saturated clay-rich clastic silicate rocks:

$$V_P = 1360 + 1.16V_S \qquad (5.3)$$

where V_P and V_S are given in m/s. Figure 5.14 shows the shale and sandstone samples as well as the mudrock line. The carbonate and anhydrite samples are not plotted because they are largely non-siliceous. Figure 5.14 shows that the shale and sandstone samples measured here all fall below the mudrock line. This indicates the V_P/V_S ratio is lower than is expected when measured water-saturated. In order to see how fluid saturation

might affect the V_P/V_S ratio in comparison to the mudrock line a Gassmann (1951) substitution was used to find the effective bulk modulus after water saturation:

$$K_{eff} = K_d + \frac{\left(1 - K_d/K_s\right)^2}{\frac{1 - \frac{K_d}{K_s} - \phi}{K_s} + \frac{\phi}{K_f}} \tag{5.4}$$

where K_{eff} is the bulk modulus after fluid saturation, K_d is the bulk modulus of the dry rock frame, K_s is the bulk modulus of the solid mineral material, K_f is the bulk modulus of the fluid, and φ is the porosity of the sample. Water was used as the pore fluid, and the velocities traveling parallel to bedding were used to calculated the bulk and shear moduli. No substitution was done on the Mannville shale 2 due to its very low porosity. Figure 5.14 shows that the new Gassmann substituted values are higher than the dry values in all cases. In the sandstone samples, the substituted values are much closer to the mudrock line. Previously, the values of the Mannville shale 1 were slightly below the mudrock line. After substitution, the values become slightly higher.

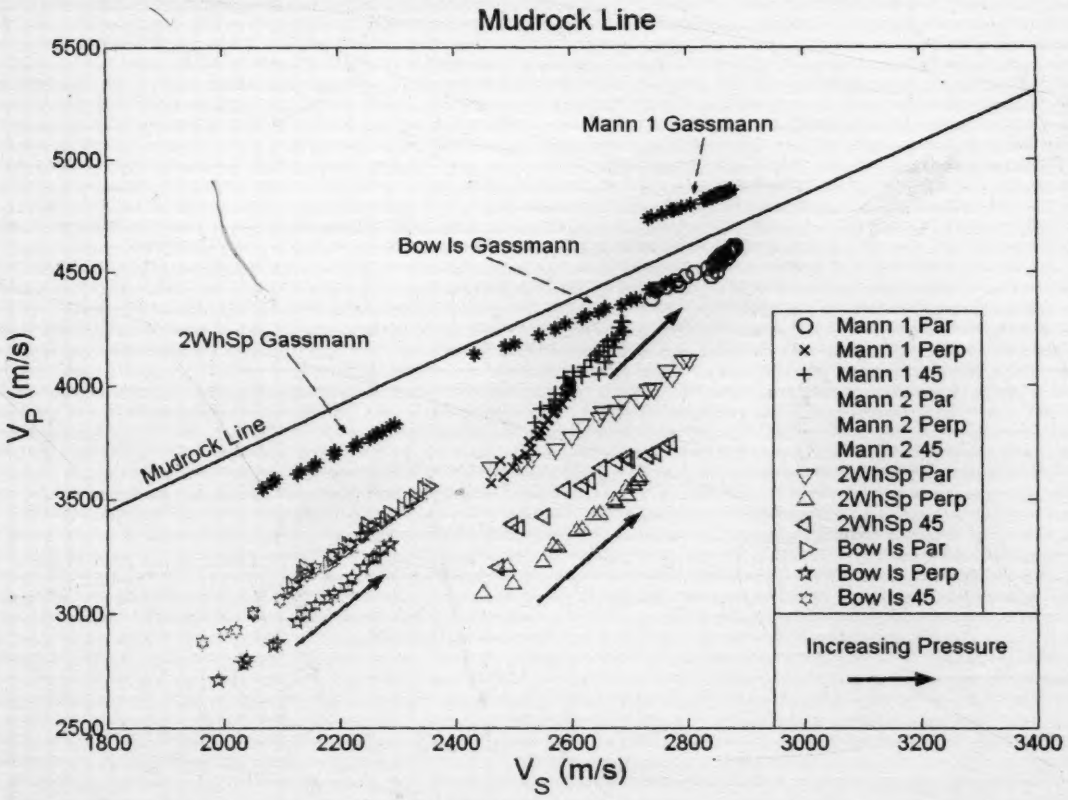

Figure 5.14 - V_P versus V_S for the shale and sandstone samples. The black line is the mudrock line defined by Castagna et al. (1985). The black asterisk symbols are the Gassmann substituted points using velocities parallel to bedding. No Gassmann substitution was performed on the Mannville shale 2 due to its very low porosity.

5.5 Discussion & Summary

Seven core samples from the Southern Alberta area were tested using a standard pulse transmission method. Under the assumption of transverse isotropy, ultrasonic P- and S-wave waveforms were found in the directions parallel, perpendicular, and 45° to bedding. Ultrasonic velocities were found as a function of pressure. The velocities of the samples all increased with pressure mainly due to the closure of microcracks. The

velocities of the two carbonate samples were clearly controlled by microcracks as the velocities increased sharply at low pressures and were followed by a more gradual increase at higher pressures. The rest of the samples exhibited largely linear velocity behaviour, though the total velocity increase was highly variable. The shale and anhydrite samples showed very little velocity increase while the two sandstones exhibited moderate increases.

Elastic constants and Thomsen's anisotropic parameters were also found as a function of pressure and revealed that all of the samples were at least slightly anisotropic, although at peak pressure one sample was isotropic within error. The anisotropy generally decreased with increasing pressure due to the closure of aligned microcracks. The anisotropies of the carbonates were very dependent on microcracks; the P-wave anisotropy of the Mount Head carbonate decreases from almost 20% to under 4%. The remainder of the samples showed only small amounts of anisotropy decrease with increasing pressure. The anisotropy of the Mannville shale 1 and the two sandstone samples were also compared to anisotropy found in typical field studies in the southern Alberta area. The values agreed well with representative values of ε and δ, where typically $\varepsilon > \delta \geq 0$.

At peak pressure, the Mannville shale 1 was the sample that had the largest anisotropy. This is in part due to the preferred orientation of clay minerals as suggested by the texture seen in the SEM micrographs. The main cause of anisotropy at peak pressure in most of the other samples was fine layering. The exceptions are the sandstone samples which were not subjected to high pressures. Many of the samples have anisotropies of 5% or more. This shows that layering can be a fairly significant, if not the

most important, source of anisotropy in these sedimentary rocks. V_P/V_S ratios range from 1.27 – 1.83 and generally increase with pressure. Most of the ratios increase only a small amount (< 0.1).

Chapter 6

Conclusions

6.1 Motivation for this Work

Anisotropic shales constitute a large portion of the material in sedimentary basins, and laboratory measurements give insights into the causes and magnitude of anisotropy in various rocks. Since anisotropy is prevalent to some degree in most geological structures it is important to understand this phenomenon. In the context of Alberta, there is a dearth of anisotropy measurements on core. This work was undertaken in order to study the effects of pressure on the elastic properties of transversely isotropic shale samples, to add to the scarce database of anisotropy measurements in cores from Alberta.

6.2 Summary

A pulse transmission method was performed on three cores from each sample to obtain the velocities necessary to fully elastically describe TI material. P- and S-wave transducers were stacked on top of one another in order to obtain simultaneous measurements of both types of waves. Phase velocities were determined to within 1% using this method. The samples were also extensively characterized to supplement velocity measurements in order to further study the anisotropy.

Although the original intent of this project was to study clay-rich shales, the end project contained several different types of samples. There were two shales, two carbonates, two sandstones, and one anhydrite. These samples were characterized

through density measurements, mercury porosimetry, X-ray diffraction, whole rock analysis, scanning electron microscope (SEM) and thin sections. Thin sections and SEM revealed that, except for the sandstones, the samples were all fine-grained, usually less than 100 μm, and most grains are less than 60 μm. Using SEM, we saw that the Mannville shale 1 was the only sample in which preferred orientation of clay minerals was obvious.

The velocity-pressure dependence was not the same for each sample. Both shale samples and the anhydrite sample showed very little dependence on pressure. The velocity increase in these three samples was small and largely linear, indicating that microcracks have only a small effect on the velocities. Microcracks did, however, have a large part in controlling the velocities of the two carbonate samples. The velocities in these two samples were highly nonlinear with pressure. The rate of velocity increase at low pressures is larger than it is at higher pressures because low aspect ratio microcracks tend to close at low pressure. Fitting the velocity curves indicated that microcracks had more of an effect on the velocities of the Mount Head carbonate as compared to the Wabamun carbonate. The velocity-pressure curves of the sandstone samples appeared to be linear with pressure; however, the peak pressure for these samples was only 22.5 - 25.0 MPa. Microcracks seemed to control the velocities of these samples, although the pressure was not increased enough to reach a point where most microcracks had closed and the velocity was relatively stable.

The anisotropy was also investigated as a function of pressure. Typically the anisotropy decreased in magnitude as the pressure increased due to aligned porosity. At peak pressure the Mannville shale 1 had the highest anisotropy and the Mannville shale 2

was the most isotropic. The effect of microcracks on the anisotropy was also evident by anisotropy-pressure curves. Much like the velocities, the two carbonate samples showed significant microcrack activity as their anisotropies decreased rapidly as pressure was increased; the P-wave anisotropy of the Mount Head carbonate decreased from almost 20% to under 4%. In most samples, at peak pressure, layering appeared to generally be a significant source of anisotropy.

The anisotropy of the Mannville shale 1 and the two sandstone samples were compared to measures of anisotropy in field data from southern Alberta. Studies performing depth migration on data from this area typically use ε and δ values of approximately 10 – 20% and 0 – 5%, respectively. The ε and δ values in the samples measured here were comparable to these values.

6.3 Contributions of this Work

There are several main contributions of this work. To our knowledge, this study is the first laboratory study on anisotropy in cores from Alberta. In the foothills of Alberta, for example, anisotropy is very prevalent and knowledge of the anisotropy is needed in order to construct more accurate seismic velocity models of the Earth. This study provides valuable information in this regard.

A large portion of this work was directed towards developing a method of measuring P- and S-waves simultaneously. A technique of stacking P- and S-wave transducers to measure ultrasonic waves is given in detail. This method gives reasonable signal on small diameter and attenuative core. Ultrasonic waves produced in this way can be measured to within 1%.

Another interesting finding of this work is the anisotropy seen in one sandstone sample. At a peak pressure of 22.5 MPa, ε is 15.2%. This anisotropy will inevitably decrease as pressure is increased, and there is some uncertainty to that value due to heterogeneity issues. Nonetheless, this value of ε is well above what would be expected for a typical sandstone and perhaps implies that more sandstones should be studied for anisotropy. Also in terms of the anisotropy, at peak pressure much of the anisotropy in the samples studied here seems to be due to layering. This is interesting and important as it shows that the most significant source of anisotropy in many samples may be due to layering. Detailed quantitative studies of anisotropy would help explore this issue.

6.4 Future Work

In this work we qualitatively determined the causes of anisotropy, and to some extent this study is exploratory. Our understanding of the anisotropy would be greatly improved by knowing more quantitatively what contributes to it. It is possible to determine the anisotropy due to cracks (e.g., Vernik, 1993), due to layering (Backus, 1962), and headway has been made determining the anisotropy due to the preferred orientation of minerals (e.g., Lonardelli et al., 2007; Wenk et al., 2007). This information would be very informative. Further, in the case of determining the anisotropy contributed from preferred orientation of minerals, ultrasonic measurements are needed in order to confirm and improve techniques currently used.

The main goal of this work was to study the elastic properties of clay rich shales under confining pressure as well as characterize them using various petrographic techniques. Limited success was achieved in choosing clay rich samples in this study; however, whole rock analysis was done on the entire suite of samples that were originally

chosen for this project (Table 4.6). This gives a good starting point for future samples to measure. Samples SSA017, SSA027, SSA031, SSA036, SSA039, and SSA042 all have Al_2O_3 levels above 10% and K_2O levels above 2%, which indicates that they are likely high in clay content. Several of these samples are too small to obtain three cores for anisotropy measurements and so a different approach, likely a multi-faced cube, may need to be applied. However, as noted earlier in the first parts of this research any approach that involves machining a sample into a specific shape is not so easily taken with such friable materials.

Another piece of information that would be very useful to have is the exact amount of clays found in the sample. Traditional X-ray diffraction (XRD) has trouble distinguishing between different types of clay minerals. The process to determine exact types and amount of clays is an involved process that uses data from different techniques including whole rock analysis and X-ray diffraction of oriented specimens using several pretreatments to control variables such as hydration and heat. If this data is obtained and anisotropy data is acquired on many shales, it might be possible to observe any effects cause by different types of clay.

6.5 Concluding Remarks

Anisotropy is an important subject in the field of oil and gas exploration. Large reserves are being depleted, and smaller reserves are increasingly becoming more economically viable to drill. As the targets in the Earth become smaller, room for error to locate them decreases, and anisotropy becomes even more critical to take into account. Anisotropy is studied in large-scale field experiments; however, there is some information available more directly from laboratory studies than in field studies. For

instance, depth migration algorithms in seismic processing use values of ε and δ to construct images of the subsurface. These parameters can be calculated in the laboratory using velocities not measurable in the field, such as those parallel to bedding. Studies such as the current one provide valuable information on anisotropy that can increase the chances of success when exploring the subsurface.

References

Agersborg, R., Jakobsen, M., Ruud, B. O., and Johansen , T. A., 2007, Effects of pore fluid pressure on the seismic response of a fractured carbonate reservoir: Stud. Geophys. Geod., **51**, 89-118.

Alkhalifah, T., and Tsvankin, I., 1995, Velocity analysis for transversely isotropic media: Geophysics, **60**, 1550-1566.

Assefa, S., McCann, C., and Sothcott, J., 2003, Velocities of compressional and shear waves in limestones: Geophysical Prospecting, **51**, 1-13.

Auld, B., A., 1973, Acoustic fields and waves in solids: John Wiley & Sons, Inc, New York.

Aussel, J. D., and Monchalin, J. P., 1989, Precision laser-ultrasonic velocity measurement and elastic constant determination: Ultrasonics, **27**, 165-177.

Backus, G. E., 1962, Long-wave elastic anisotropy produced by horizontal layering: J. Geophys. Res., **67**, 4427-4440.

Banik, N. C., 1984, Velocity anisotropy of shales and depth estimation in the North Sea basin: Geophysics, **49**, 1411-1419.

Best, A. I., and McCann, C., 1995, Seismic attenuation and pore-fluid viscosity in clay-rich reservoir sandstones: Geophysics, **60**, 1386-1397.

Birch, F., 1960, The velocity of compressional waves in rocks to 10 kilobars, Part 1: J. Geophys. Res., **65**, 1083-1102.

Birch, F., 1961, The velocity of compressional waves in rocks to 10 kilobars, Part 2: J. Geophys. Res., **66**, 2199-2224.

REFERENCES

Boggs, S., 2003, Petrology of sedimentary rocks: The Blackburn Press, Caldwell, New Jersey.

Carcione, J. M., Kosloff, D., and Behle, A., 1991, Long-wave anisotropy in stratified media: A numerical test: Geophysics, **56**, 245-254.

Castagna, J. P., Batzle, M. L., and Eastwood, R. L., 1985, Relationships between compressional-wave and shear-wave velocities in clastic silicate rocks: Geophysics, **50**, 571-581.

Castagnedède, B., Kim, K. Y., Sachse, W., and Thompson, M. O., 1991, Determination of the elastic constants of anisotropic materials using laser-generated ultrasonic signals: J. Appl. Phys., **70**, 150-157.

Cheadle, S. P., Brown, R. J., and Lawton, D. C., 1991, Orthorhombic anisotropy: A physical seismic modeling study: Geophysics, **56**, 1603-1613.

Cholach, P. Y., Molyneux, J. B., and Schmitt, D. R., 2005, Flin Flon belt seismic anisotropy: Elastic symmetry, heterogeneity, and shear wave splitting: Can. J. Earth Sci., **42**, 533-544.

Cholach, P. Y., and Schmitt, D. R., 2006, Intrinsic elasticity of a textured transversely isotropic muscovite aggregate: Comparisons to the seismic anisotropy of schists and shales: J. Geophys. Res., **111**, 410-427.

Christensen, N. I., and Wang, H. F., 1985, The influence of pore pressure and confining pressure on dynamic elastic properties of Berea sandstone: Geophysics, **50**, 207-213.

Christensen, N. I., and Wang, H. F., 1986, The influence of pore pressure and confining pressure on dynamic elastic properties of Berea sandstone – Discussion: Geophysics, **51**, 1016-1017.

REFERENCES

Chu, F., Lei, M., Maloy, S. A., Petrovic, J. J., and Mitchell, T. E., 1996, Elastic properties of C40 transition metal disilicides: Acta mater., **44**, 3035-3048.

Chu, Y. C., Degtyar, A. D., and Rokhlin, S. I., 1994, On determination of orthotropic material moduli from ultrasonic velocity data in nonsymmetry planes: J. Acoust. Soc. Am., **95**, 3191-3203.

Connell-Madore, S., and Katsube, T. J., 2006, Pore-size-distribution characteristics of Beaufort-Mackenzie Basin shale samples, Northwest Territories: Geological Survey of Canada.

Dellinger, J., and Vernik, L., 1994, Do traveltimes in pulse-transmission experiments yield anisotropic group or phase velocities?: Geophysics, **59**, 1774-1779.

Dewhurst, D. N., Aplin, A. C., Sarda, J. P., and Yang, Y, 1998, Compaction-driven evolution of porosity and permeability in natural mudstones: An experimental study: J. Geophys. Res., **103**, 651-661.

Dewhurst, D. N., Aplin, A. C., and Sarda, J. P., 1999, Influence of clay fraction on pore-scale properties and hydraulic conductivity of experimentally compacted mudstones: J. Geophys. Res., **104**, 29261-29274.

Dewhurst, D. N., and Siggins, A. F., 2006, Impact of fabric, microcracks and stress field on shale anisotropy: Geophys. J. Int., **165**, 135-148.

Dey-Barsukov, S., Dürrast, H., Rabbel, W., Seigesmund, S., and Wende, S., 2000, Aligned fractures in carbonate rocks: laboratory and in situ measurements of seismic anisotropy: Int. Journ. Earth Sciences, **88**, 829-839.

REFERENCES

Domnesteanu, P., McCann, C., and Sothcott, J., 2002, Velocity anisotropy and attenuation of shale in under- and overpressured conditions: Geophysical Prospecting, **50**, 487-503.

Eberhart-Phillips, D., Han, D-H., and Zoback, M. D., 1989, Empirical relationships among seismic velocity, effective pressure, porosity, and clay content in sandstone: Geophysics, **54**, 82-89.

Every, A. G., and Sachse, W., 1990, Determination of the elastic constants of anisotropic solids from acoustic-wave group-velocity measurements: Physical Review B, **42**, 8196-8207.

Gardner, G. H. F., 1986, The influence of pore pressure and confining pressure on dynamic elastic properties of Berea sandstone – Discussion: Geophysics, **51**, 1016-1016.

Gardner, G. H. F., Wyllie, M. R. J., and Droschak, D. M., 1965, Hysteresis in the velocity-pressure characteristics of rocks: Geophysics, **30**, 111-116.

Gassmann, F., 1951, Elasticity of porous media: Uber die Elastizitat poroser Medien: Vierteljahrsschrift der Naturforschenden Gesselschaft in Zurich, **96**, 1-23.

Gray, S. H., Etgen, J., Dellinger, J., and Whitmore, D., 2001, Seismic migration problems and solutions: Geophysics, **66**, 1622-1640.

Green, D. H., and Wang, H. F., 1994, Shear wave velocity and attenuation from pulse-echo studies of Berea sandstone: J. Geophys. Res., **99**, 11755-11763.

Hammecker, C., and Jeannette, D., 1994, Modelling the capillary imbibition kinetics in sedimentary rocks: Role of petrographical features: Transport in Porous Media, **17**, 285-303.

He, T., 2006, P- and S-wave velocity measurement and pressure sensitivity analysis of AVA response: M.Sc. thesis, University of Alberta.

Heiri, O., Lotter, A. F., and Lemcke, G., 2001, Loss on ignition as a method for estimating organic and carbonate content in sediments: reproducibility and comparibility of results: Journal of Paleolimnology, **25**, 101-110.

Hornby, B. E., 1998, Experimental laboratory determination of the dynamic elastic properties of wet, drained shales: J. Geophys. Res., **103**, 29945-29964.

Hornby, B. E., Schwartz, L. M., and Hudson, J. A., 1994, Anisotropic effective-medium modeling of the elastic properties of shales: Geophysics, **59**, 1570-1583.

Hovem, J. M., 1995, Acoustic waves in finely layered media: Geophysics, **60**, 1217-1221.

Huffman, D. F., and Norwood, M. H., 1960, Specific heat and elastic constants of calcium fluoride at low temperatures: Phys. Rev., **117**, 709-711.

Hughes, D. S., and Cross, J. H., 1951, Elastic wave velocities in rocks at high pressures and temperatures: Geophysics, **16**, 577-593.

Hughes, D. S., and Jones, H. J., 1951, Elastic wave velocities in sedimentary rocks: Trans. Am. Geophys. Union, **32**, 173-178.

Humbert, P., and Plicque, F., 1972, Proprietes elastiques de carbonate rhomboedriques monocristallins: calcite, magnesite, dolomie: Comptes rendus de l'academie des sciences, **275**, serie B, 391-394.

Isaac, J. H., and Lawton, D. C., 1999, Image mispositioning due to dipping TI media: A physical seismic modeling study: Geophysics, **64**, 1230-1238.

REFERENCES

Iwasawa, M., Mizutani, Y., Nishino, H., Takemoto, M., and Ono, K., 2002, Estimation of five elastic stiffness coefficients of unidirectional glass fiber reinforced plastic by laser generated ultrasonic: Adv. Composite Mater., **11**, 121-135.

Johnston, J. E., 1987, Physical properties of shale at temperature and pressure: Geophysics, **52**, 1391-1401.

Johnston, J. E., and Christensen, N. I., 1994, Elastic constants and velocity surfaces of indurated anisotropic shales: Surveys in Geophysics, **15**, 481-494.

Johnston, J. E., and Christensen, N. I., 1995, Seismic anisotropy of shales: J. Geophys. Res., **100**, 5991-6003.

Jones, S. M., McCann, C., Astin, T. R., and Sothcott, J., 1998, The effects of pore-fluid salinity on ultrasonic wave propagation in sandstones: Geophysics, **63**, 928-934.

Jones, E. A. L., and Wang, H. F., 1981, Ultrasonic velocities in Cretaceous shales from the Williston basin: Geophysics, **46**, 288-297.

Kaarsberg, E. A., 1959, Introductory studies of natural and artificial argillaceous aggregates by sound-propagation and X-ray diffraction methods: Journal of Geology, **67**, 447-472.

Katahara, K. W., 1996, Clay mineral elastic properties: 66th Ann. Internat. Mtg., Soc. Expl. Geophys., Expanded abstracts, 1691-1694.

Katsube, T. J., Mudford, B. S., and Best, M. E., 1991, Petrophysical characteristics of shales from the Scotian shelf: Geophysics, **56**, 1681-1689.

Kebaili, A., and Schmitt, D. R., 1996, Velocity anisotropy observed in wellbore seismic arrivals: Combined effects of intrinsic properties and layering: Geophysics, **61**, 12-20.

Kebaili, A., and Schmitt, D. R., 1997, Ultrasonic anisotropic phase velocity determination with the Radon transformation: J. Acoust. Soc. Am., **101**, 3278-3286.

Khaksar, A., Griffiths, C. M., and McCann, C., 1999, Compressional- and shear-wave velocities as a function of confining stress in dry sandstones: Geophysical Prospecting, **47**, 487-508.

Kim, J. W., Bryant, W. R., Watkins, J. S., and Tieh, T. T., 1999, Electron microscopic observations of shale diagenesis offshore Louisiana, USA, Gulf of Mexico: Geo-Marine Letters, **18**, 234-240.

Kirtland Grech, M. G., Lawton, D. C., and Gray S. H., 2002, A multioffset vertical seismic profiling experiment for anisotropy analysis and depth imaging: Geophysics, **67**, 348-354.

King, M. S., 1966, Wave velocities in rocks as a function of changes in overburden pressure and pore fluid saturants: Geophysics, **31**, 50-73.

Klimentos, T., 1991, The effects of porosity-permeability-clay content on the velocity of compressional waves: Geophysics, **56**, 1930-1939.

Klimentos, T., and McCann, C., 1990, Relationships among compressional wave attenuation, porosity, clay content, and permeability in sandstones: Geophysics, **55**, 998-1014.

Koga, I., Aruga, M., and Yoshinaka, Y., 1958, Theory of plane elastic waves in a piezoelectric crystalline medium and determination of elastic and piezoelectric constants of quartz: Phys. Rev., **109**, 1467-1473.

Koopman, M., Chawla, K. K., Coffin, C., Patterson, B. R., Deng, X., Patel, B. V., Fang, Z., and Lockwood, G., 2002, Determination of elastic constants in WC/Co metal

matrix composites by resonant ultrasound spectroscopy and impulse excitation: Adv. Eng. Mater., **4**, 37-42.

Kuster, G. T., and Toksöz, M. N., 1974, Velocity and attenuation seismic waves in two-phase media: Part 1. Theoretical formulations: Geophysics, **39**, 587-606.

Kwon, O., Kronenberg, A. K., Gangi, A. F., and Johnson, B., 2001, Permeability of Wilcox shale and its effective pressure law: J. Geophys. Res., **106**, 19339-19353.

Kwon, O., Kronenberg, A. K., Gangi, A. F., Johnson, B., and Herbert, B. E., 2004, Permeability of illite-bearing shale: 1. Anisotropy and effects of clay content and loading: J. Geophys. Res., **109**, B10205.

Leisure, R. G., and Willis, F. A., 1997, Resonant ultrasound spectroscopy: J. Phys.: Condens. Matter, **9**, 6001-6029.

Leisure, R. G., Foster, K., Hightower, J. E., and Agosta, D. S., 2004, Internal friction studies by resonant ultrasound spectroscopy: Materials Science and Engineering, **370**, 34-40.

Leslie, J. M., and Lawton, D. C., 1999, A refraction-seismic field study to determine the anisotropic parameters of shales: Geophysics, **64**, 1247-1252.

Li, Y., and Schmitt, D. R., 1998, Drilling-induced core fractures and in situ stress: J. Geophys. Res., **103**, 5225-5239.

Liu, Y., and Schmitt, D. R., 2006, The transition between the scale domains of ray and effective medium theory and anisotropy: numerical models: Pure and Applied Geophysics, **163**, 1327-1349.

Lo, T. W., Coyner, K. B., and Toksöz, M. N., 1986, Experimental determination of elastic anisotropy of Berea Sandstone, Chicopee Shale, and Chelmsford Granite: Geophysics, **51**, 164-171.

Lonardelli, I., Wenk, H. R., Lutterotti, L., and Goodwin, M., 2005, Texture analysis from synchrotron diffraction images with the Rietveld method: dinosaur tendon and salmon scale: Journal of Synchrotron Radiation, **12**, 354-360.

Lonardelli, I., Wenk, H. R., and Ren, Y., 2007, Preferred orientation and elastic anisotropy in shales: Geophysics, **72**, D33-D40.

Maeva, E., Severina, I., Bondarenko, S., Chapman, G., O'Neill, B., Severin, F., and Maev, R. G., 2004, Acoustical methods for the investigation of adhesively bonded structures: A review: Canadian Journal of Physics, **82**, 981-1025.

Mah, M., 2005, Determination of the elastic constants of orthorhombic and transversely isotropic materials: Experimental application to a kerogen rich rock: Ph.D. thesis, University of Alberta.

Mah, M., and Schmitt, D. R., 2001a, Experimental determination of the elastic coefficients of an orthorhombic material: Geophysics, **66**, 1217-1225.

Mah, M., and Schmitt, D. R., 2001b, Near point-source longitudinal and transverse mode ultrasonic arrays for material characterization: IEEE Transactions on Ultrasonics, Ferroelectrics, and Frequency Control, **48**, 691-698.

Mah, M., and Schmitt, D. R., 2003, Determination of the complete elastic stiffnesses from ultrasonic phase velocity measurements: J. Geophys. Res., **108**, 2016-2026.

Maltman, A., 1994, The geological deformation of sediments: Chapman and Hall, London.

Marion, D., Mukerji, T., and Mavko, G., 1994, Scale effects on velocity dispersion: From ray to effective medium theories in stratified media: Geophysics, **59**, 1613-1619.

Marion, D., Nur, A., Yin, H., and Han, D., 1992, Compressional velocity and porosity in sand-clay mixtures: Geophysics, **57**, 554-563.

Markham, M. F., 1957, Measurement of elastic constants by the ultrasonic pulse method: Brit. J. Appl. Phys., **6**, 56-63.

Mavko, G., Mukerji, T., and Dvorkin, J., 1998, The rock physics handbook: Cambridge University Press.

Melia, P. J., and Carlson, R. L., 1984, An experimental test of P-wave anisotropy in stratified media: Geophysics, **49**, 374-378.

Migliori, A., Sarrao, J. L., Visscher, W. M., Bell, T. M., Lei, M., Fisk, Z., and Leisure, R. G., 1993, Resonant ultrasound spectroscopic techniques for measurement of the elastic moduli of solids: Physica, **183**, 1-24.

Migliori, A., and Darling, T. W., 1996, Resonant ultrasound spectroscopy for materials studies and non-destructive testing: Ultrasonics, **34**, 473-476.

Musgrave, M. J. P., 1970, Crystal Acoustics: Holden-Day, Inc, San Francisco.

Nicholas, M. E., Joyner, P. A., Tessem, B. M., and Olson, M. D., 1961, The effect of various gases and vapors on the surface tension of mercury: Journal of Physical Chemistry, **65**, 1373-1375.

Nihei, K. T., Ball, G. J., Reverdy, F., Nakagawa, S., and Myer, L. R., 2006, Phased array compaction cell for measuring the anisotropic elastic properties of compacting clay-rich sediments: 12th International Workshop on Seismic Anisotropy, Expanded Abstracts, 21-22.

REFERENCES

Nur, A., and Simmons, G., 1969, The effect of viscosity of a fluid phase on velocity in low porosity rocks: Earth and Planetary Sci. Lett., **7**, 99-108.

Peselnick, L., and Robie, R. A., 1963, Elastic constants of calcite: Journal of Applied Physics, **34**, 2494-2495.

Pettijohn, F. J., 1975, Sedimentary rocks, Third Ed.: Harper and Row, New York.

Podio, A., L., Gregory, A., R., and Gray, K., E., 1968, Dynamic properties of dry and water-saturated Green River Shale under stress: Soc. Pet. Eng. J., **8**, 389-404.

Postma, G. W., 1955, Wave propagation in stratified media: Geophysics, **20**, 780-806.

Potter, P. E., Maynard, J. B., and Pryor, W. A., 1980, Sedimentology of Shale: Springer-Verlag, New York.

Rafavich, F., Kendall, C. H. St. C., and Todd, T. P., 1984, The relationship between acoustic properties and the petrographic character of carbonate rocks: Geophysics, **49**, 1622-1636.

Rai, C. S., and Hanson, K. E., 1988, Shear-wave velocity anisotropy in sedimentary rocks: A laboratory study: Geophysics, **53**, 800-806.

Reverdy, F., and Audoin, B., 2001, Elastic constants determination of anisotropic materials from phase velocities of acoustic waves generated and detected by lasers: J. Acoust. Soc. Am., **109**, 1965-1972.

Robinson, B., Alvarez, H., Krishnasamy, T., and Stevenson, M., 2006, Prestack depth migration at Stolberg, Alberta: 76th Ann. Internat. Mtg., Soc. Expl. Geophys., Expanded abstracts, 680-684.

Sayers, C. M., 1994, The elastic anisotropy of shales: J. Geophys. Res., **99**, 767-774.

Sayers, C. M., 2005, Seismic anisotropy of shales: Geophysical Prospecting, **53**, 667-676.

Sayers, C. M., and van Munster, J. G., 1991, Microcrack-induced seismic anisotropy of sedimentary rocks: J. Geophys. Res., **96**, 16529-16533.

Schwerdtner, W. M., Tou, J. C. –M., and Hertz, P. B., 1965, Elastic properties of single crystals of anhydrite: Canadian Journal of Earth Sciences, **2**, 673-683.

Sondergeld, C. H., and Rai, C. S., 1986, Laboratory observations of shear-wave propagation in anisotropic media: The Leading Edge, **11**, 38-43.

Takanashi, M., Nishizawa, O., Kanagawa, K., and Yasunaga, K., 2001, Laboratory measurements of elastic anisotropy parameters for the exposed crustal rocks from the Hidaka Metamorphic Belt, Central Hokkaido, Japan: Geophys. J. Int., **145**, 33-47.

Thomsen, L., 1986, Weak elastic anisotropy: Geophysics, **51**, 1954-1966.

Timur, A., 1977, Temperature dependence of compressional and shear wave velocities in rocks: Geophysics, **42**, 950-956.

Tsvankin, I., 1996, P-wave signatures and notation for transversely isotropic media: An overview: Geophysics, **61**, 467-483.

Uhrig, L. F., and Van Melle, F. A., 1955, Velocity anisotropy in stratified media: Geophysics, **20**, 774-779.

Ulrich, T. J., McCall, K. R., and Guyer, R. A., 2002, Determination of elastic moduli of rock samples using resonant ultrasound spectroscopy: J. Acoust. Soc. Am., **111**, 1667-1674.

Valcke, S. L. A., Casey, M., Lloyd, G. E., Kendall, J.-M., and Fisher, Q. J., 2006, Lattice preferred orientation and seismic anisotropy in sedimentary rocks: Geophys. J. Int., **166**, 652-666.

van Steveninck, J., 1967, Apparatus for simultaneous determination of longitudinal and shear wave velocities under pressure: J. Sci. Instrum., **44**, 379-381.

Vernik, L., 1993, Microcrack-induced versus intrinsic elastic anisotropy in mature HC-source shales: Geophysics, **58**, 1703-1706.

Vernik, L., and Liu, X., 1997, Velocity anisotropy in shales: A petrophysical study: Geophysics, **62**, 521-532.

Vernik, L., and Nur, A., 1992, Ultrasonic velocity and anisotropy of hydrocarbon source rocks: Geophysics, **57**, 727-735.

Vestrum, R. W., Lawton, D. C., and Schmid, R., 1999, Imaging structures below dipping TI media: Geophysics, **64**, 1239-1246.

Wang, Z., 2002a, Seismic anisotropy in sedimentary rocks, part 1: A single-plug laboratory method: Geophysics, **67**, 1415-1422.

Wang, Z., 2002b, Seismic anisotropy in sedimentary rocks, part 2: Laboratory data: Geophysics, **67**, 1423-1440.

Wang, Z., Wang, H., and Cates, M. E., 2001, Effective elastic properties of solid clays: Geophysics, **66**, 428-440.

Washburn, E. W., 1921, Note on a method of determining the distribution of pore sizes in a porous material: Proceedings of the National Academy of Sciences: **7**, 115-116.

Wenk, H. R., Lonardelli, I., Franz, H., Nihei, K., and Nakagawa, S., 2007, Preferred orientation and elastic anisotropy of illite-rich shale: Geophysics, **72**, E69-E75.

Winkler, K. W., 1979, The effects of pore fluids and frictional sliding on seismic attenuation: Ph.D. thesis, Stanford University.

Winkler, K. W., and Plona, T. J., 1982, Technique for measuring ultrasonic velocity and attenuation spectra in rocks under pressure: J. Geophys. Res., **87**, 776-780.

Wyllie, M. R. J., Gregory, A. R., and Gardner, L. W., 1956, Elastic wave velocities in heterogeneous and porous media: Geophysics, **21**, 41-70.

Wyllie, M. R. J., Gregory, A. R., and Gardner, G. H. F., 1958, An experimental investigation of factors affecting elastic wave velocities in porous media: Geophysics, **23**, 459-493.

Zadler, B. J., Le Rousseau, J. H. L., Scales, J. A., and Smith, M. L., 2004, Resonant ultrasound spectroscopy: theory and application: Geophys. J. Int., **156**, 154-169.

Appendix A

Experimental Data

A.1 Mannville Shale 1 (SSA010)

Location	Depth (m)	Grain Density (g/cm^3)	Bulk Density (g/cm^3)	Porosity (%)
Gulf Mohawk Blood 6-11-14-29W4	3021.0	2.63	2.58 ± 0.04	1.1 ± 1.5

Table A.1 - Geological parameters of the Mannville shale 1.

Direction relative to bedding	Length (cm)	Weight (g)
Parallel	2.558	33.4
45°	2.827	37.0
Perpendicular	2.140	28.1

Table A.2 - Properties of the cores used for velocity measurements of the Mannville shale 1.

Pressure (MPa)	$V_{P\,par}$	$V_{P\,45}$	$V_{P\,perp}$	$V_{SH\,par}$	$V_{SV\,45}$	$V_{S\,perp}$
5.0	4383	3838	3572	2740	2538	2462
10.0	4425	3897	3606	2747	2547	2482
15.0	4434	3908	3647	2764	2563	2497
20.0	4459	3960	3680	2781	2573	2505
25.0	4479	4031	3702	2799	2590	2520
30.0	4496	4056	3758	2814	2605	2526
35.0	4514	4074	3787	2838	2625	2540
40.0	4530	4105	3805	2847	2636	2547
45.0	4549	4125	3824	2850	2645	2553
50.0	4563	4143	3852	2857	2650	2561
55.0	4572	4166	3884	2861	2659	2571
60.0	4581	4186	3903	2867	2665	2575
65.0	4588	4200	3920	2874	2674	2583
70.0	4596	4216	3950	2878	2685	2591

Pressure (MPa)	$V_{P\ par}$	$V_{P\ 45}$	$V_{P\ perp}$	$V_{SH\ par}$	$V_{SV\ 45}$	$V_{S\ perp}$
75.0	4607	4228	3967	2882	2692	2599
70.0	4610	4232	3993	2883	2693	2600
65.0	4612	4225	3987	2884	2694	2599
60.0	4609	4269	4022	2884	2693	2600
55.0	4613	4274	4005	2885	2691	2599
50.0	4604	4272	4010	2884	2689	2596
45.0	4602	4245	3980	2882	2686	2594
40.0	4589	4196	3969	2879	2680	2590
35.0	4583	4158	3918	2875	2676	2584
30.0	4565	4124	3913	2872	2667	2575
25.0	4555	4095	3879	2868	2661	2569
20.0	4530	4047	3848	2858	2649	2559
15.0	4500	4034	3782	2852	2620	2546
10.0	4479	3993	3726	2843	2596	2530
5.0	4444	3937	3669	2786	2574	2479

Table A.3 - Velocities (m/s) for the Mannville shale 1. Directions are relative to bedding.

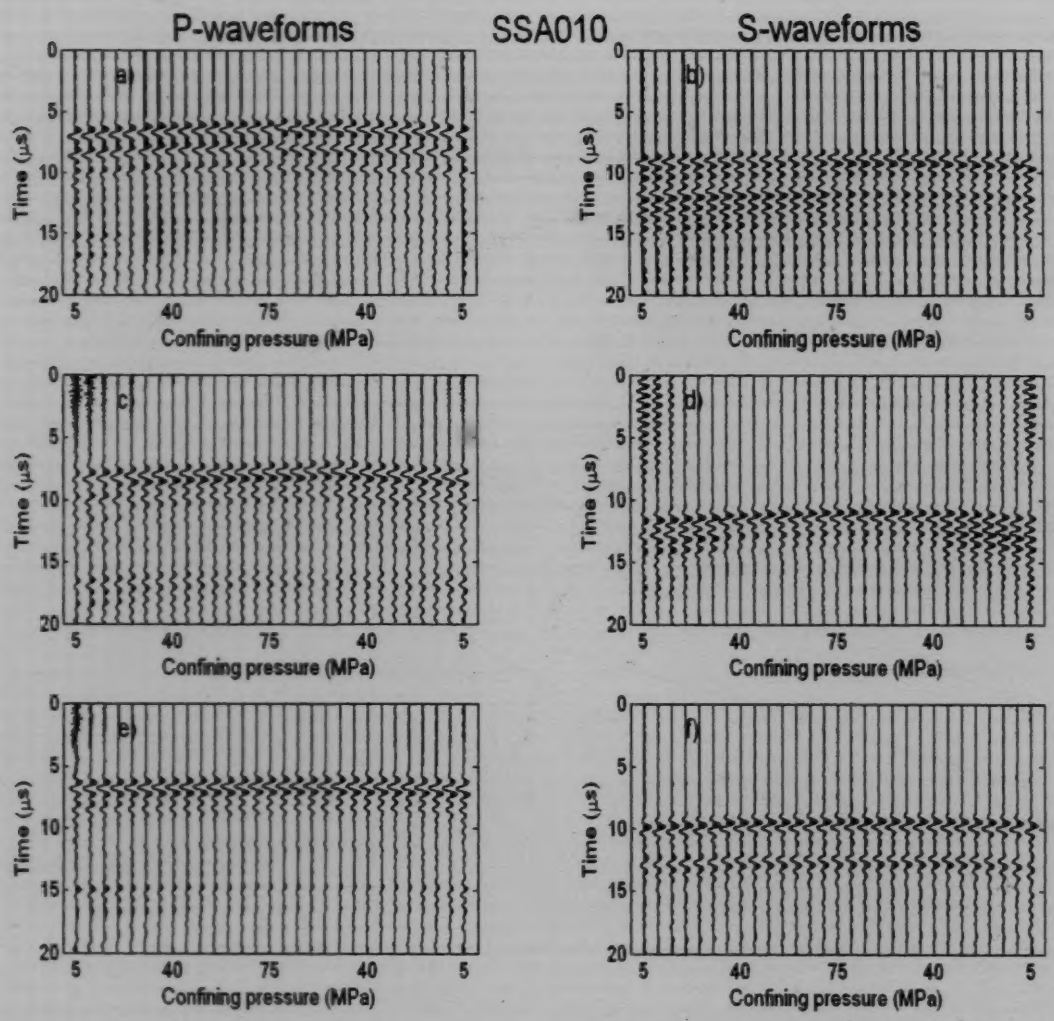

Figure A.1 – Complete suite of waveforms obtained for the Mannville shale 1. a) and b) show the P- and S-waves, respectively, traveling perpendicular to bedding. c) and d) show the waveforms traveling 45° to bedding, and e) and f) show the waveforms parallel to bedding.

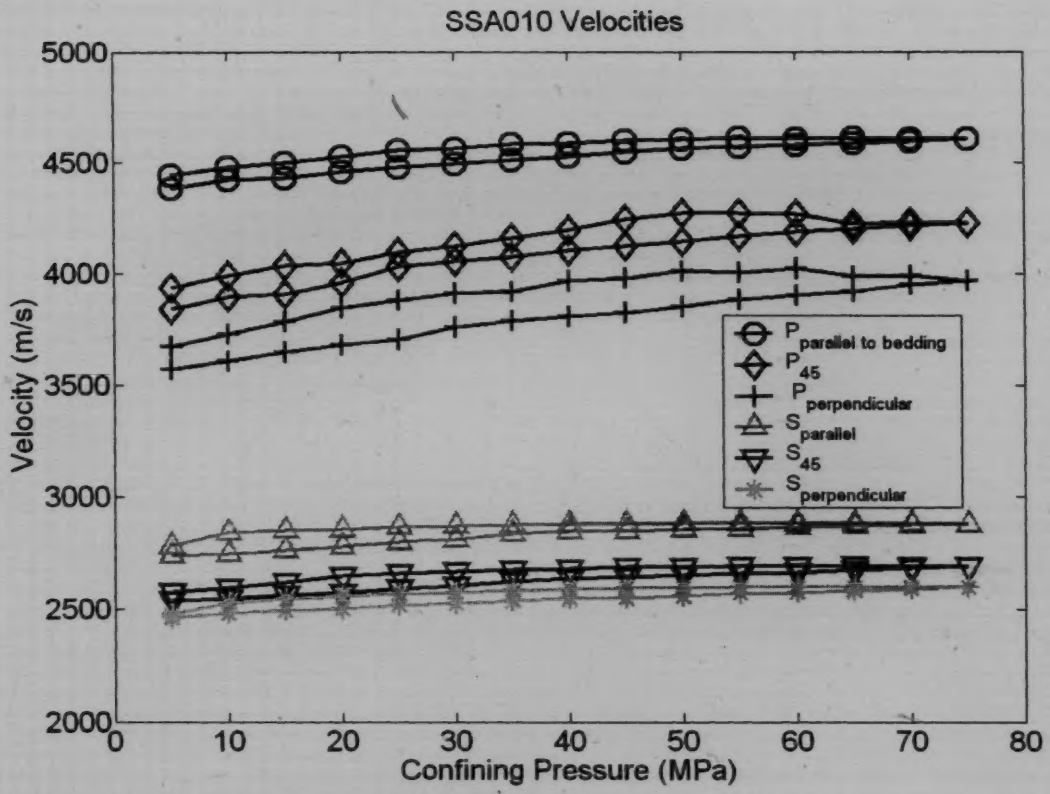

Figure A.2 - Velocities for the Mannville shale 1.

Pressure (MPa)	C_{11}	C_{33}	C_{44}	C_{66}	C_{13}	ε	γ	δ
5.0	49.96	33.19	15.76	19.53	1.62	0.253	0.120	-0.002
10.0	50.92	33.81	16.02	19.63	2.70	0.253	0.112	0.029
15.0	51.14	34.59	16.21	19.88	2.40	0.239	0.113	0.007
20.0	51.70	35.23	16.32	20.11	3.82	0.234	0.116	0.036
25.0	52.17	35.64	16.52	20.38	6.13	0.232	0.117	0.108
30.0	52.58	36.74	16.60	20.60	6.40	0.216	0.120	0.083
35.0	52.99	37.30	16.78	20.95	6.36	0.210	0.124	0.075
40.0	53.37	37.67	16.88	21.08	7.14	0.208	0.125	0.092
45.0	53.83	38.03	16.96	21.13	7.39	0.208	0.123	0.093
50.0	54.16	38.59	17.06	21.22	7.57	0.202	0.122	0.086
55.0	54.37	39.24	17.19	21.29	7.98	0.193	0.119	0.085
60.0	54.59	39.62	17.25	21.37	8.49	0.189	0.120	0.091
65.0	54.74	39.96	17.35	21.48	8.66	0.185	0.119	0.092
70.0	54.94	40.58	17.46	21.55	8.83	0.177	0.117	0.084

Pressure (MPa)	C_{11}	C_{33}	C_{44}	C_{66}	C_{13}	ε	γ	δ
75.0	55.20	40.94	17.56	21.60	8.84	0.174	0.115	0.079
70.0	55.27	41.47	17.58	21.62	8.76	0.166	0.115	0.062
65.0	55.33	41.36	17.56	21.63	8.47	0.169	0.116	0.057
60.0	55.26	42.08	17.58	21.63	10.18	0.157	0.115	0.083
55.0	55.35	41.73	17.57	21.65	10.53	0.163	0.116	0.102
50.0	55.12	41.83	17.53	21.63	10.60	0.159	0.117	0.099
45.0	55.08	41.19	17.50	21.61	9.74	0.169	0.117	0.092
40.0	54.76	40.97	17.45	21.56	7.92	0.168	0.118	0.047
35.0	54.62	39.93	17.37	21.49	6.84	0.184	0.119	0.043
30.0	54.19	39.83	17.24	21.45	5.88	0.180	0.122	0.014
25.0	53.97	39.13	17.16	21.40	5.17	0.190	0.123	0.009
20.0	53.37	38.51	17.04	21.25	3.91	0.193	0.124	-0.013
15.0	52.68	37.21	16.85	21.16	4.64	0.208	0.128	0.032
10.0	52.18	36.11	16.65	21.02	4.00	0.223	0.131	0.034
5.0	51.36	35.01	15.99	20.19	3.85	0.233	0.131	0.024

Table A.4 - Elastic constants (GPa) and anisotropic parameters for the Mannville shale 1.

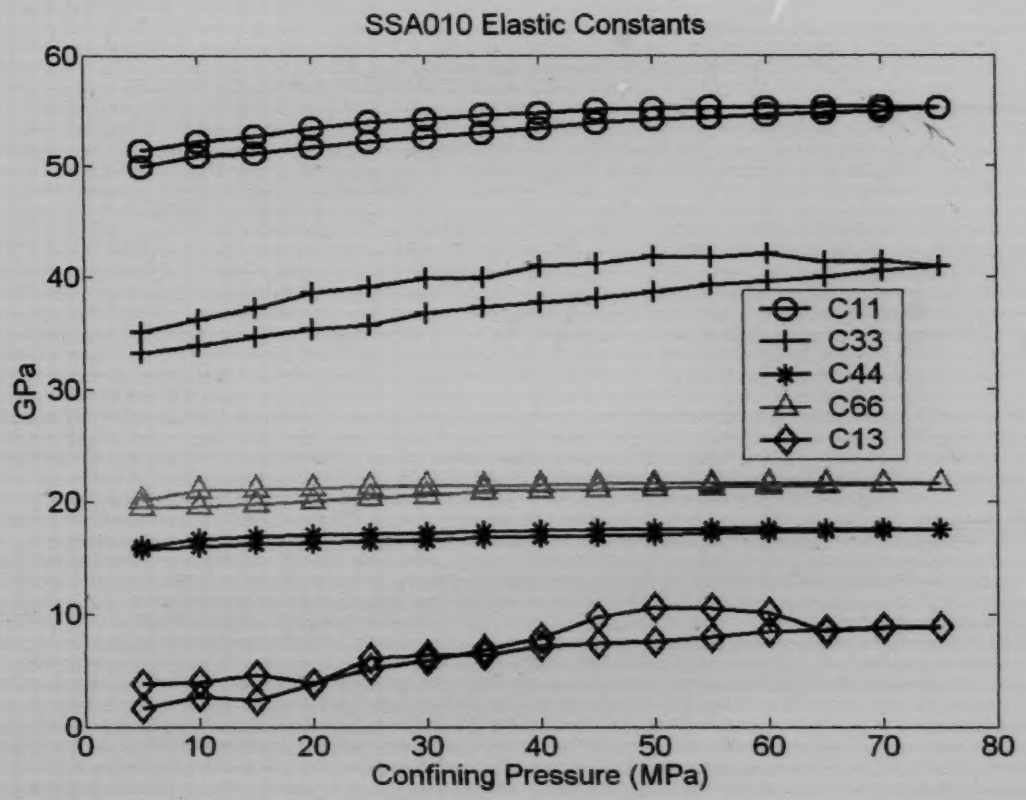

Figure A.3 - Elastic constants for the Mannville shale 1. Lower curve is increasing pressure and upper curve is decreasing pressure.

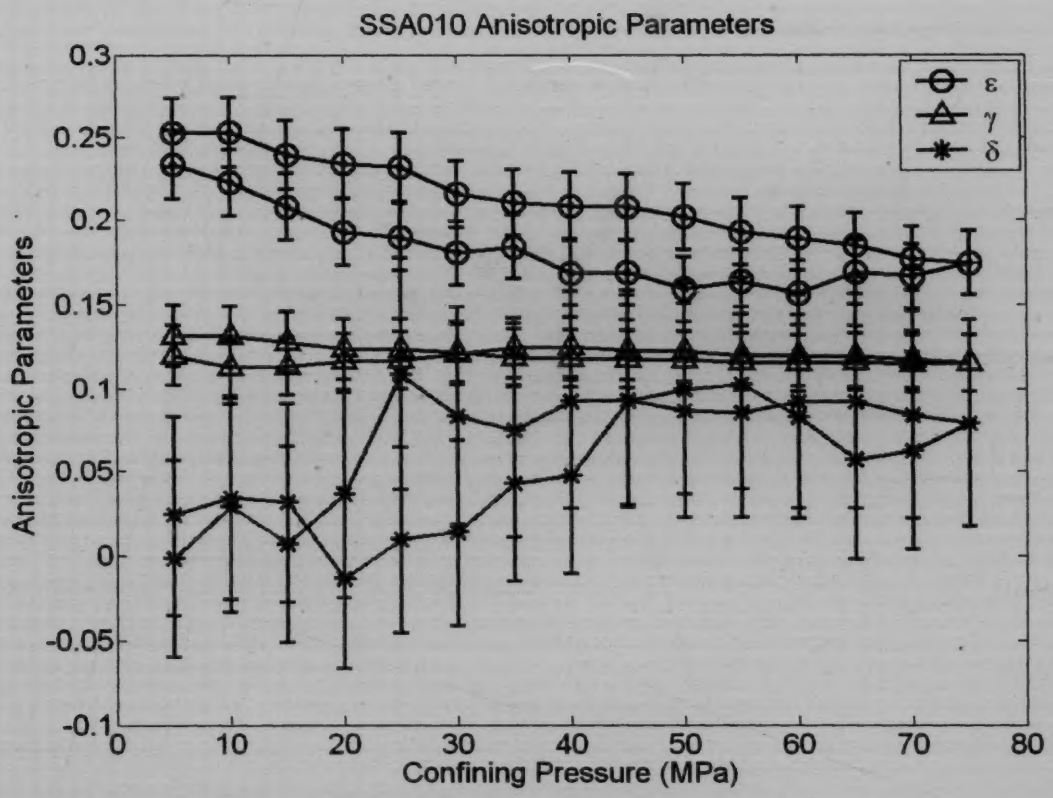

Figure A.4 - Anisotropic parameters of the Mannville shale 1.

A.2 Mannville Shale 2 (SSA011)

Location	Depth (m)	Grain Density (g/cm^3)	Bulk Density (g/cm^3)	Porosity (%)
Gulf Mohawk Blood 6-11-14-29W4	3078.9	2.64	2.69 ± 0.05	<< 1

Table A.5 - Geological parameters of the Mannville shale 2.

Direction relative to bedding	Length (cm)	Weight (g)
Parallel	4.539	59.58
45°	4.056	53.64
Perpendicular	4.628	63.90

Table A.6 - Properties of the cores used for velocity measurements of the Mannville shale 2.

Pressure (MPa)	$V_{P\ par}$	$V_{P\ 45}$	$V_{P\ perp}$	$V_{SH\ par}$	$V_{SV\ 45}$	$V_{S\ perp}$
5.0	---	---	4638	---	---	---
10.0	4847	4740	4674	3198	3098	3111
15.0	4859	4783	4702	3196	3113	3135
20.0	4864	4817	4722	3199	3141	3144
25.0	4872	4834	4741	3200	3150	3159
30.0	4884	4872	4764	3207	3157	3165
35.0	4895	4891	4788	3210	3164	3173
40.0	4915	4907	4812	3217	3170	3179
45.0	4927	4917	4841	3225	3174	3188
50.0	4938	4927	4853	3235	3180	3195
55.0	4953	4937	4867	3240	3190	3202
60.0	4965	4957	4880	3244	3197	3207
65.0	4974	4964	4900	3255	3204	3214
70.0	4988	4974	4912	3259	3206	3219
75.0	5000	4985	4932	3268	3212	3224
70.0	5003	4986	4934	3263	3214	3225
65.0	5001	4988	4930	3262	3214	3225
60.0	5000	4981	4920	3262	3213	3221
55.0	4991	4973	4911	3269	3209	3219
50.0	4981	4972	4903	3264	3206	3215
45.0	4975	4956	4887	3251	3201	3209
40.0	4966	4948	4875	3244	3200	3206
35.0	4957	4932	4858	3245	3199	3196
30.0	4953	4910	4836	3239	3195	3188
25.0	4946	4903	4817	3232	3183	3176
20.0	4929	4879	4795	3228	3157	3163
15.0	4907	4848	4743	3213	3141	3153
10.0	4885	4803	4719	3236	3123	3140
5.0	4862	---	4688	3223	---	3129

Table A.7 - Velocities (m/s) for the Mannville shale 2. Directions are relative to bedding.

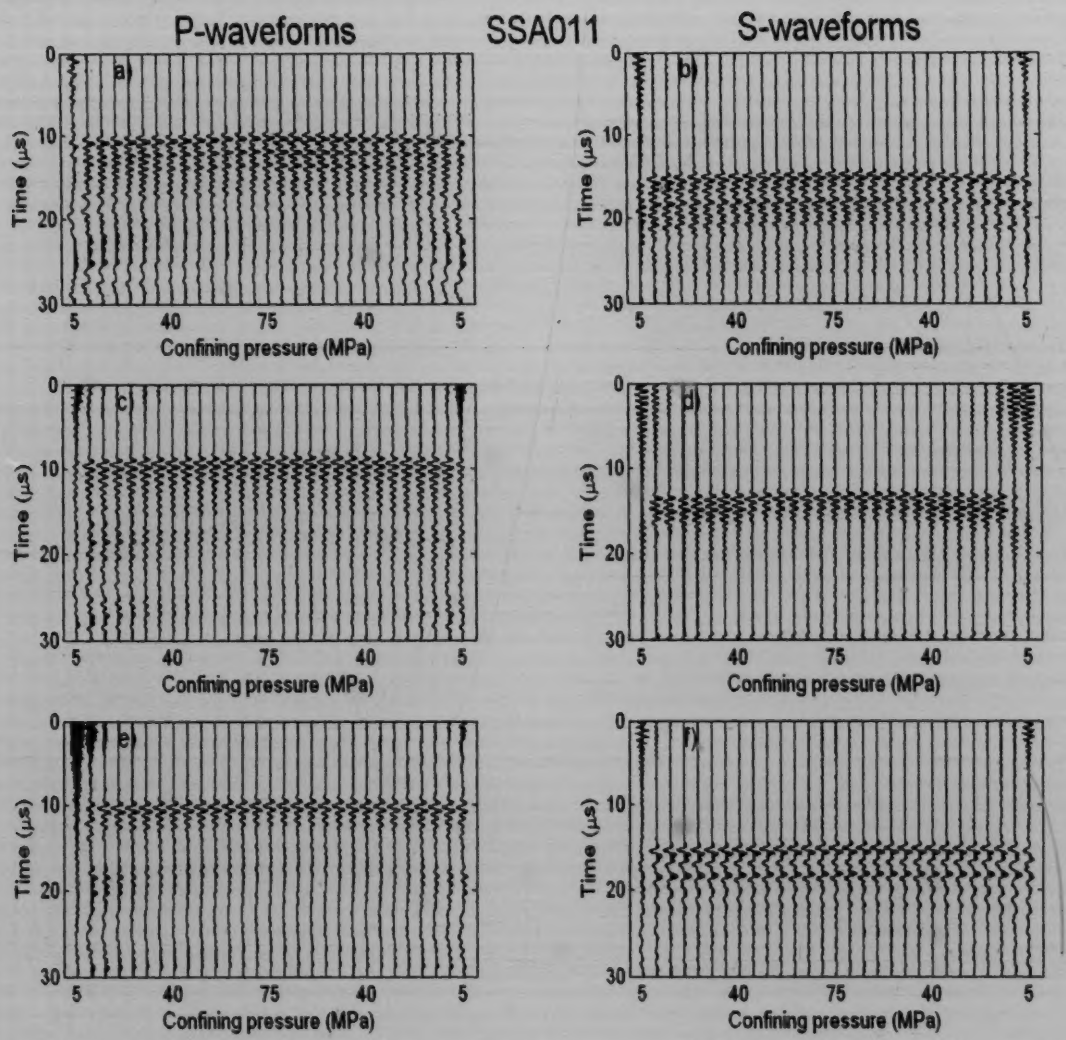

Figure A.5 – Complete suite of waveforms obtained for the Mannville shale 2. a) and b) show the P- and S-waves, respectively, traveling perpendicular to bedding. c) and d) show the waveforms traveling 45° to bedding, and e) and f) show the waveforms parallel to bedding.

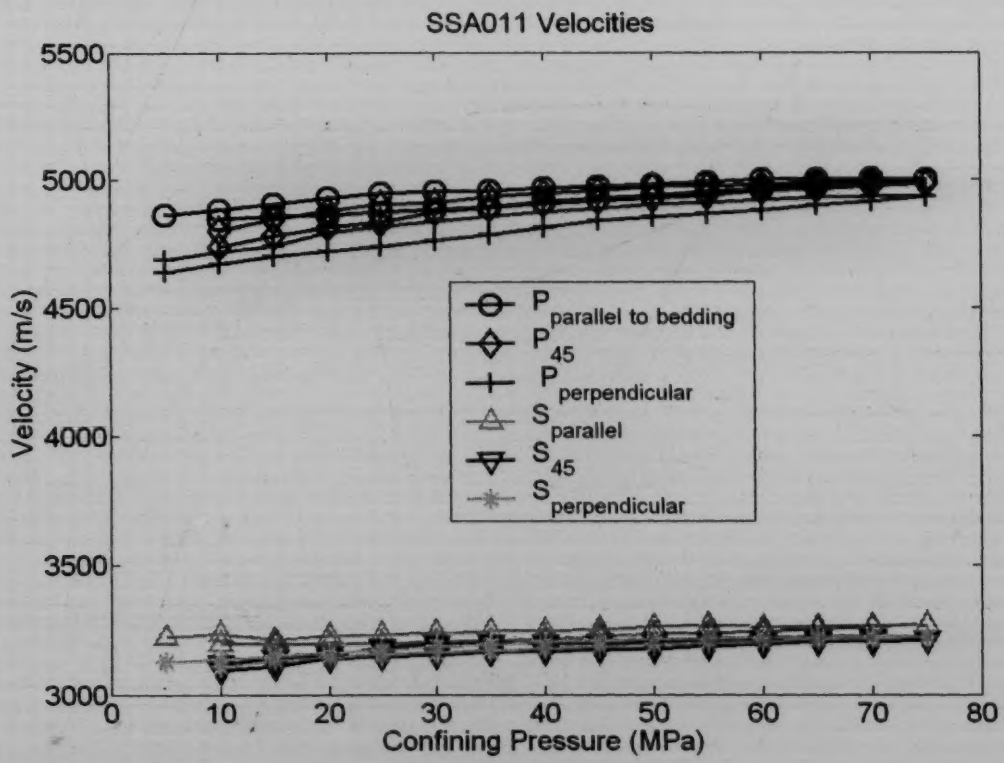

Figure A.6 - Velocities for the Mannville shale 2.

Pressure (MPa)	C_{11}	C_{33}	C_{44}	C_{66}	C_{13}	ε	γ	δ
5.0	---	57.90	---	---	---	---	---	---
10.0	63.22	58.79	26.04	27.52	7.75	0.038	0.028	0.018
15.0	63.53	59.50	26.45	27.49	8.65	0.034	0.020	0.036
20.0	63.68	60.01	26.60	27.54	9.81	0.031	0.018	0.052
25.0	63.89	60.48	26.85	27.56	9.85	0.028	0.013	0.053
30.0	64.18	61.08	26.96	27.68	11.14	0.025	0.013	0.069
35.0	64.49	61.69	27.09	27.73	11.43	0.023	0.012	0.067
40.0	65.00	62.31	27.20	27.85	11.49	0.022	0.012	0.060
45.0	65.32	63.07	27.36	27.99	11.18	0.018	0.012	0.047
50.0	65.62	63.38	27.47	28.16	11.20	0.018	0.013	0.045
55.0	66.01	63.75	27.58	28.25	11.12	0.018	0.012	0.041
60.0	66.32	64.09	27.68	28.31	11.64	0.017	0.011	0.047
65.0	66.57	64.61	27.79	28.51	11.42	0.015	0.013	0.038
70.0	66.96	64.94	27.89	28.58	11.41	0.016	0.012	0.036
75.0	67.28	65.46	27.97	28.73	11.40	0.014	0.014	0.029

Pressure (MPa)	C_{11}	C_{33}	C_{44}	C_{66}	C_{13}	ε	γ	δ
70.0	67.35	65.50	27.99	28.65	11.40	0.014	0.012	0.029
65.0	67.30	65.41	27.99	28.63	11.58	0.014	0.011	0.034
60.0	67.27	65.14	27.92	28.63	11.46	0.016	0.013	0.034
55.0	67.03	64.91	27.89	28.76	11.36	0.016	0.016	0.035
50.0	66.76	64.68	27.81	28.66	11.69	0.016	0.015	0.042
45.0	66.61	64.28	27.72	28.43	11.29	0.018	0.013	0.039
40.0	66.37	63.96	27.66	28.31	11.29	0.019	0.012	0.043
35.0	66.13	63.52	27.49	28.33	11.12	0.021	0.015	0.042
30.0	66.00	62.95	27.35	28.24	10.54	0.024	0.016	0.038
25.0	65.83	62.45	27.15	28.11	10.88	0.027	0.018	0.045
20.0	65.39	61.88	26.92	28.05	10.58	0.028	0.021	0.043
15.0	64.80	60.53	26.76	27.79	10.23	0.035	0.019	0.056
10.0	64.22	59.94	26.54	28.17	8.95	0.036	0.031	0.036
5.0	63.61	59.14	26.34	27.95	---	0.038	0.031	---

Table A.8 - Elastic constants (GPa) and anisotropic parameters of the Mannville shale 2.

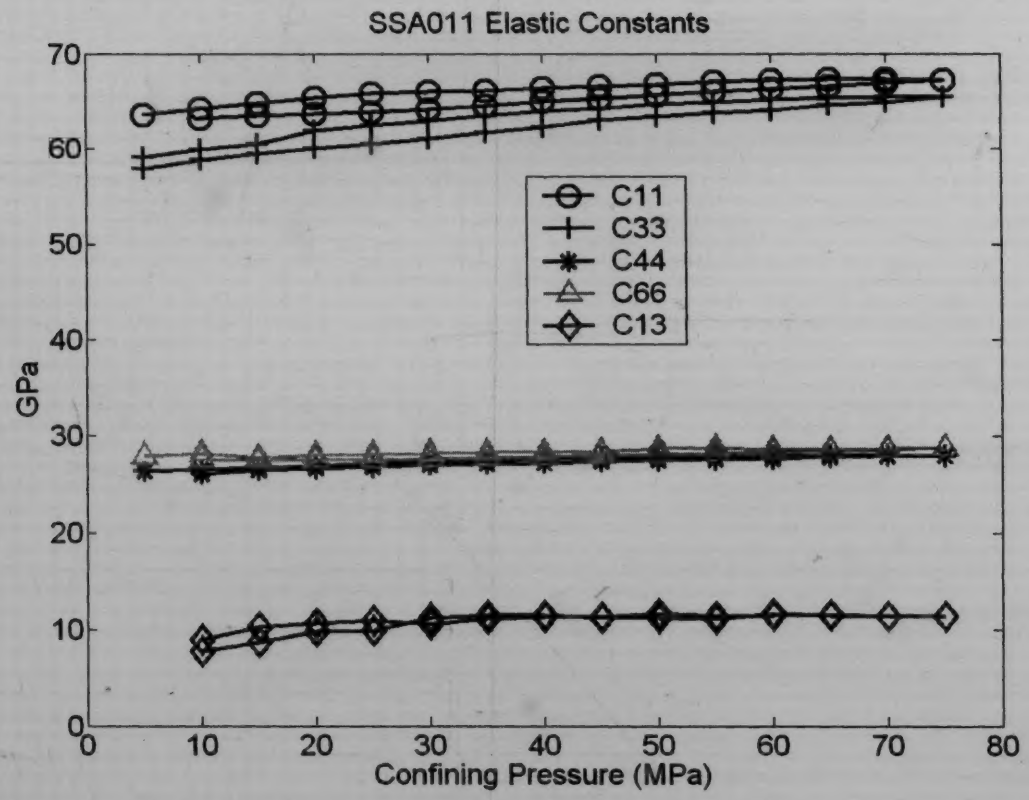

Figure A.7 - Elastic constants of the Mannville shale 2.

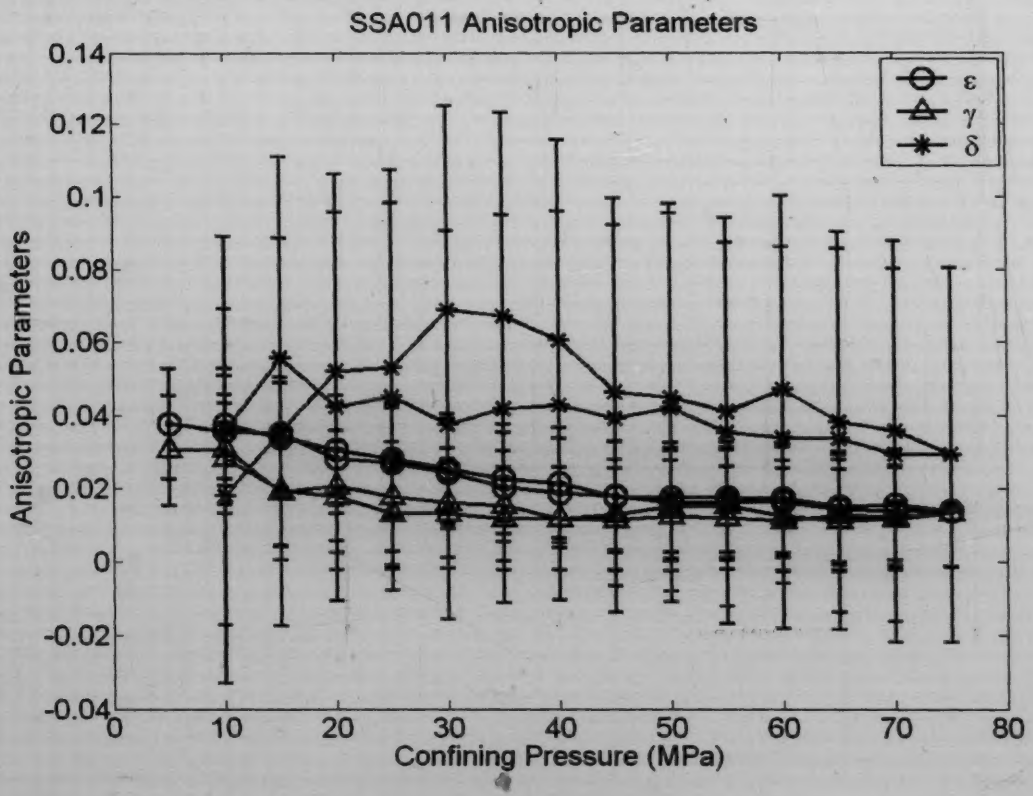

Figure A.8 - Anisotropic parameters of the Mannville shale 2.

A.3 Mount Head Carbonate (SSA019)

Location	Depth (m)	Grain Density (g/cm^3)	Bulk Density (g/cm^3)	Porosity (%)
Amoco Stimson Creek 14-12-16-2W5	3620	2.81	2.25 ± 0.05	20.1 ± 1.9

Table A.9 - Geological parameters of the Mount Head carbonate.

Direction relative to bedding	Length (cm)	Weight (g)
Parallel	3.475	38.72
45°	2.497	25.79
Perpendicular	2.347	24.51

Table A.10 - Properties of the cores used for velocity measurements of the Mount Head carbonate.

Pressure (MPa)	$V_{P\,par}$	$V_{qP\,45}$	$V_{P\,perp}$	$V_{SH\,par}$	$V_{qSV\,45}$	$V_{S\,perp}$
5.0	2661	3061	3026	1743	1814	1783
10.0	3008	3481	3446	1910	2059	2037
15.0	3236	3779	3866	2056	2218	2209
20.0	3482	3951	4095	2168	2299	2326
25.0	3709	4142	4292	2273	2402	2429
30.0	3793	4286	4411	2348	2460	2500
35.0	3887	4366	4497	2421	2530	2555
40.0	4063	4488	4566	2482	2573	2602
45.0	4122	4550	4616	2550	2609	2642
50.0	4229	4567	4656	2599	2642	2675
55.0	4328	4606	4704	2641	2671	2698
60.0	4404	4633	4753	2681	2695	2727
65.0	4465	4653	4794	2717	2719	2745
70.0	4531	4703	4832	2749	2739	2762
75.0	4596	4710	4852	2779	2760	2777
80.0	4666	4734	4865	2804	2772	2790
85.0	4702	4736	4879	2826	2787	2803
80.0	4679	4734	4864	2823	2776	2797
75.0	4658	4741	4875	2802	2766	2790
70.0	4631	4726	4835	2783	2756	2779
65.0	4577	4715	4824	2766	2740	2769
60.0	4519	4686	4801	2744	2728	2754
55.0	4459	4658	4762	2715	2707	2739
50.0	4404	4631	4725	2679	2681	2718
45.0	4314	4603	4673	2640	2652	2695
40.0	4206	4567	4621	2582	2617	2663
35.0	4122	4459	4559	2523	2575	2618
30.0	4051	4385	4498	2479	2536	2584
25.0	3875	4259	4410	2403	2453	2545
20.0	3761	4138	4309	2319	2375	2457
15.0	3481	3928	4105	2202	2255	2347
10.0	3237	3684	3840	2061	2102	2204
5.0	3015	3140	3345	1868	1890	1960

Table A.11– Velocities (m/s) for the Mount Head carbonate. Directions are relative to bedding.

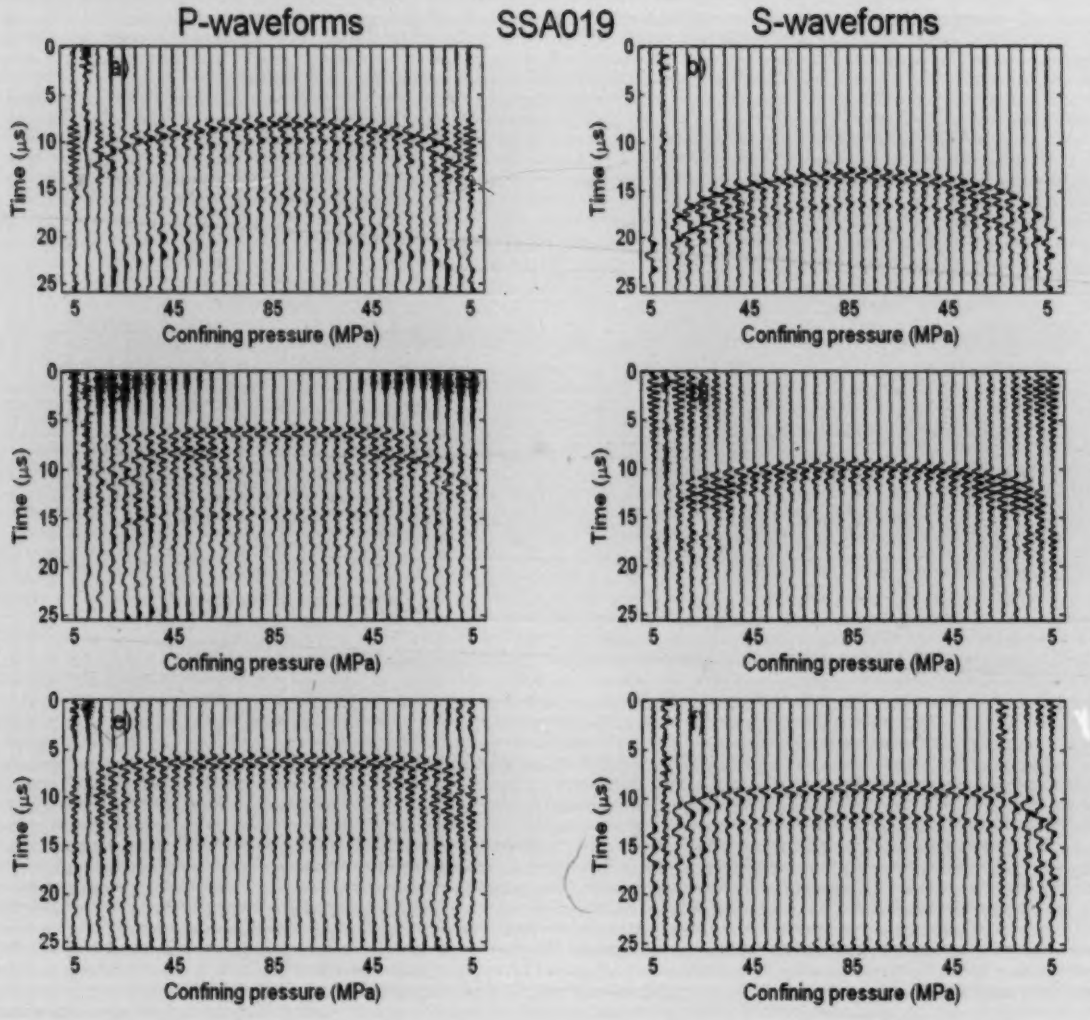

Figure A.9 – Complete suite of waveforms obtained for the Mount Head carbonate. a) and b) show the P- and S-waves, respectively, traveling perpendicular to bedding. c) and d) show the waveforms traveling 45° to bedding, and e) and f) show the waveforms parallel to bedding.

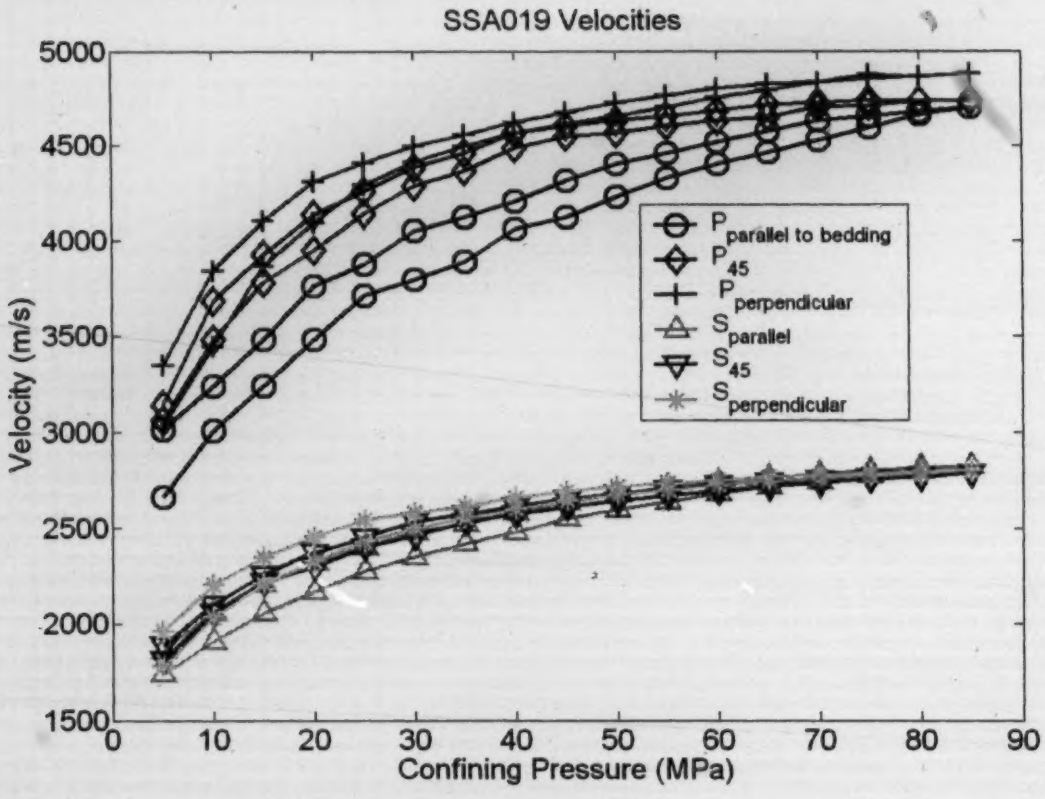

Figure A.10 - Velocities for the Mount Head carbonate.

Pressure (MPa)	C_{11}	C_{33}	C_{44}	C_{66}	C_{13}	ε	γ	δ
5.0	15.92	20.59	7.15	6.83	9.43	-0.113	-0.022	0.170
10.0	20.34	26.69	9.33	8.20	12.06	-0.119	-0.060	0.168
15.0	23.54	33.60	10.97	9.50	13.18	-0.150	-0.067	0.047
20.0	27.25	37.70	12.16	10.56	12.84	-0.139	-0.066	-0.014
25.0	30.92	41.41	13.26	11.61	13.96	-0.127	-0.062	-0.022
30.0	32.35	43.74	14.05	12.39	15.93	-0.130	-0.059	0.006
35.0	33.96	45.46	14.68	13.17	16.11	-0.127	-0.051	0.000
40.0	37.11	46.87	15.22	13.85	17.74	-0.104	-0.045	0.029
45.0	38.20	47.89	15.69	14.62	18.33	-0.101	-0.034	0.039
50.0	40.21	48.73	16.08	15.18	16.89	-0.087	-0.028	0.007
55.0	42.12	49.75	16.36	15.67	16.52	-0.077	-0.021	-0.010
60.0	43.61	50.78	16.72	16.16	15.69	-0.071	-0.017	-0.032
65.0	44.82	51.66	16.94	16.59	15.05	-0.066	-0.010	-0.051
70.0	46.16	52.49	17.15	16.99	15.68	-0.060	-0.005	-0.046

Pressure (MPa)	C_{11}	C_{33}	C_{44}	C_{66}	C_{13}	ε	γ	δ
75.0	47.49	52.92	17.34	17.36	14.73	-0.051	0.001	-0.063
80.0	48.94	53.20	17.50	17.67	14.61	-0.040	0.005	-0.064
85.0	49.71	53.52	17.67	17.95	13.86	-0.036	0.008	-0.076
80.0	49.21	53.18	17.58	17.92	14.33	-0.037	0.009	-0.066
75.0	48.77	53.42	17.50	17.65	14.88	-0.044	0.004	-0.063
70.0	48.22	52.55	17.36	17.42	15.23	-0.041	0.002	-0.048
65.0	47.10	52.31	17.24	17.19	15.66	-0.050	-0.001	-0.040
60.0	45.90	51.82	17.06	16.92	15.63	-0.057	-0.004	-0.039
55.0	44.70	50.98	16.86	16.57	15.86	-0.062	-0.009	-0.027
50.0	43.59	50.19	16.61	16.13	16.14	-0.066	-0.014	-0.016
45.0	41.83	49.08	16.32	15.67	16.97	-0.074	-0.020	0.011
40.0	39.76	47.99	15.94	14.98	17.78	-0.086	-0.030	0.036
35.0	38.20	46.73	15.41	14.31	15.83	-0.091	-0.036	-0.002
30.0	36.88	45.48	15.02	13.82	14.91	-0.095	-0.040	-0.012
25.0	33.76	43.73	14.55	12.98	13.25	-0.114	-0.054	-0.031
20.0	31.79	41.74	13.57	12.09	12.60	-0.119	-0.055	-0.046
15.0	27.24	37.89	12.39	10.90	11.44	-0.141	-0.060	-0.043
10.0	23.55	33.16	10.92	9.55	10.27	-0.145	-0.063	-0.031
5.0	20.44	25.16	8.64	7.84	4.05	-0.094	-0.046	-0.135

Table A.12 - Elastic constants (GPa) and anisotropic parameters of the Mount Head carbonate.

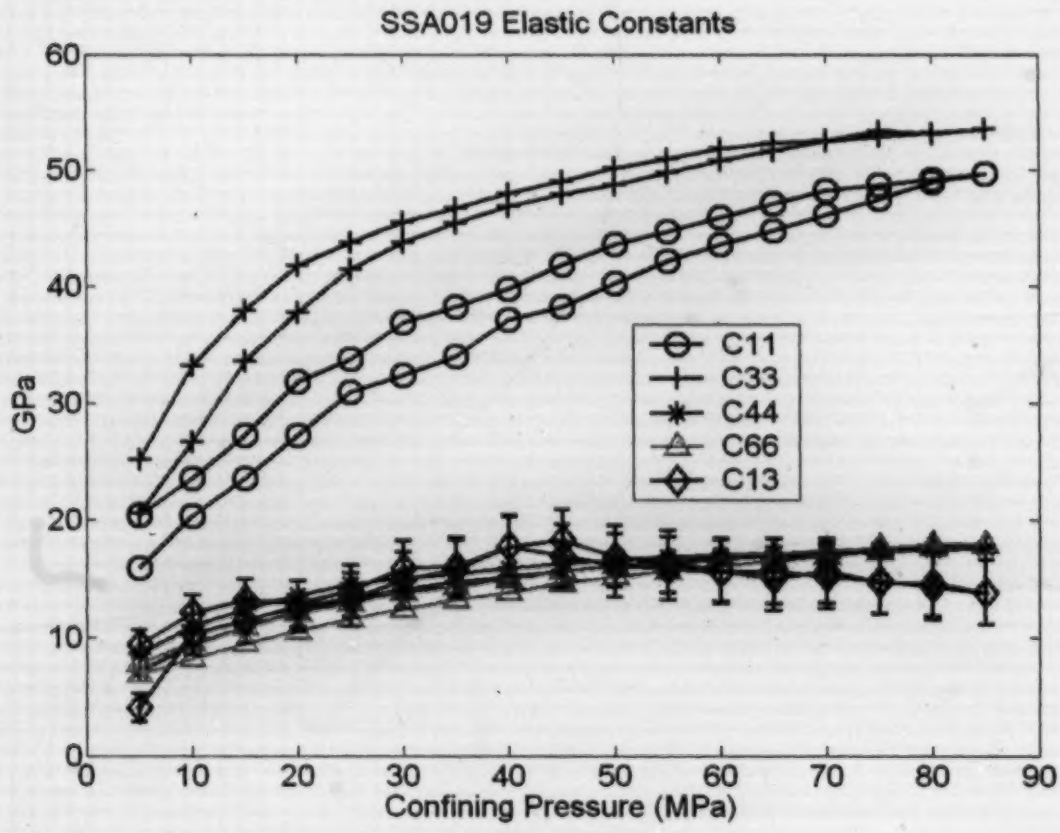

Figure A.11 - Elastic constants of the Mount Head carbonate.

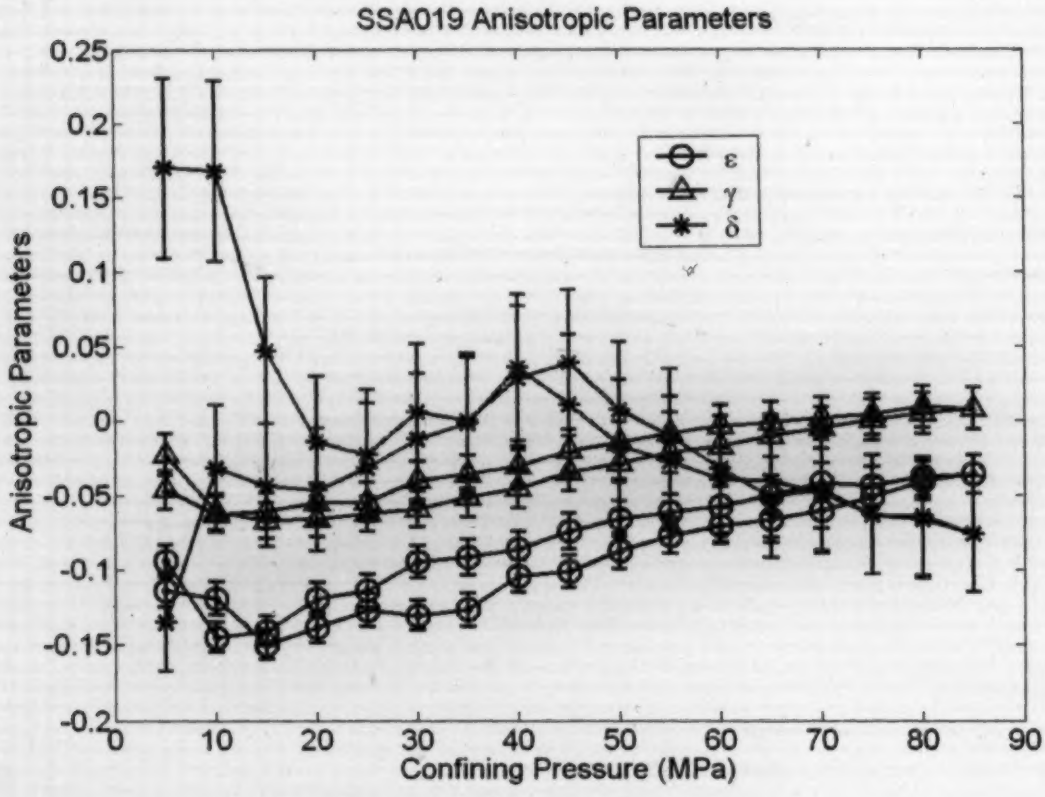

Figure A.12 - Anisotropic parameters of the Mount Head carbonate.

A.4 Wabamun Carbonate (SSA025)

Location	Depth (m)	Grain Density (g/cm^3)	Bulk Density (g/cm^3)	Porosity (%)
Shell et al Waterton 7-20-6-3W5	3643.9	2.82	2.83 ± 0.04	0 ± 1.3

Table A.13 - Geological parameters for the Wabamun carbonate.

Direction relative to bedding	Length (cm)	Weight (g)
Parallel	3.231	45.66
45°	3.754	53.11
Perpendicular	2.159	30.15

Table A.14 - Properties of the cores used for velocity measurements of the Wabamun carbonate.

Pressure (MPa)	$V_{P\ par}$	$V_{P\ 45}$	$V_{P\ perp}$	$V_{SH\ par}$	$V_{qSV\ 45}$	$V_{S\ perp}$
5.0	---	5555	5171	---	3393	3372
10.0	5982	5717	5264	3743	3454	3429
15.0	6029	5837	5360	3776	3490	3481
20.0	6111	5919	5528	3808	3517	3524
25.0	6206	5984	5605	3815	3542	3562
30.0	6282	6095	5699	3835	3573	3578
35.0	6375	6206	5764	3847	3591	3601
40.0	6410	6265	5927	3877	3610	3625
45.0	6465	6348	6015	3893	3639	3659
50.0	6501	6431	6157	3916	3661	3681
55.0	6561	6495	6270	3939	3688	3709
60.0	6590	6514	6331	3967	3707	3725
65.0	6647	6545	6431	3983	3721	3742
70.0	6698	6648	6487	4001	3746	3758
75.0	6735	6665	6512	4023	3763	3768
80.0	6780	6710	6618	4041	3783	3785
85.0	6797	6742	6655	4055	3803	3828
80.0	6794	6734	6660	4054	3798	3825
75.0	6777	6737	6641	4048	3789	3824
70.0	6778	6741	6601	4034	3784	3825
65.0	6772	6720	6600	4019	3779	3808
60.0	6769	6742	6582	4006	3778	3791
55.0	6753	6727	6586	3995	3771	3774
50.0	6742	6713	6561	3984	3764	3755
45.0	6721	6664	6492	3974	3750	3738
40.0	6675	6596	6393	3953	3732	3728
35.0	6649	6554	6312	3934	3717	3703
30.0	6575	6470	6224	3916	3696	3680
25.0	6484	6441	6130	3891	3670	3658
20.0	6410	6336	6050	3868	3635	3631
15.0	6289	6189	5871	3847	3613	3591
10.0	6153	5991	5599	3800	3581	3559
5.0	---	---	---	---	3508	3544

Table A.15 - Velocities (m/s) of the Wabamun carbonate. Directions are relative to bedding.

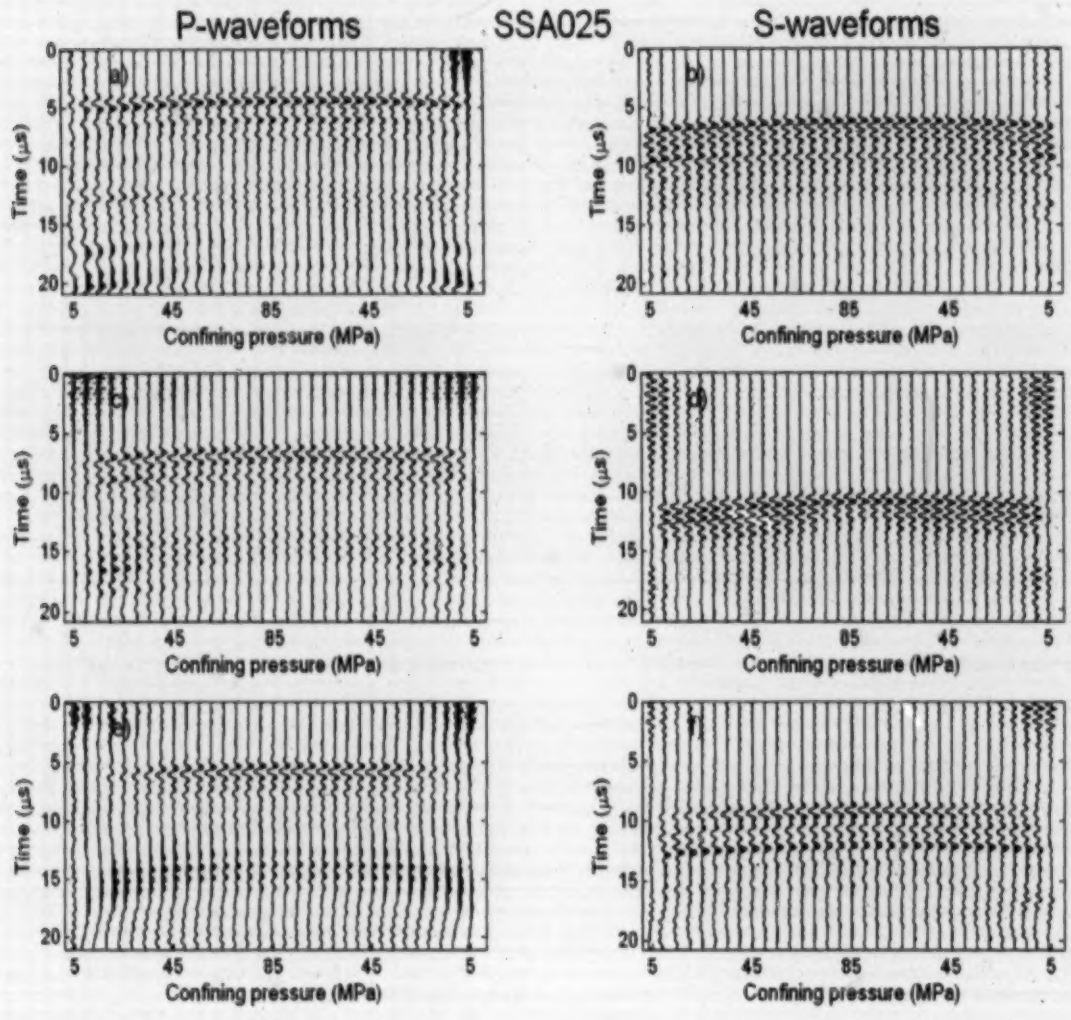

Figure A.13 – Complete suite of waveforms obtained for the Wabamun carbonate. a) and b) show the P- and S-waves, respectively, traveling perpendicular to bedding. c) and d) show the waveforms traveling 45° to bedding, and e) and f) show the waveforms parallel to bedding.

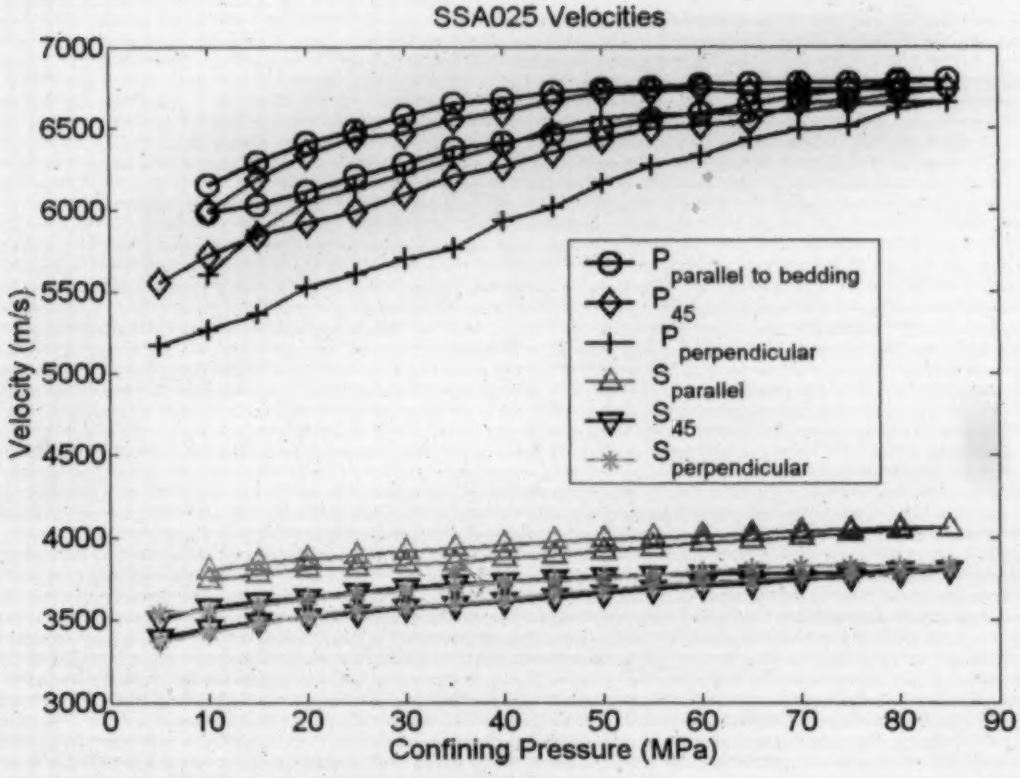

Figure A.14 - Velocities of the Wabamun carbonate.

Pressure (MPa)	C_{11}	C_{33}	C_{44}	C_{66}	C_{13}	ε	γ	δ
5.0	---	75.60	32.15	---	---	---	---	---
10.0	101.18	78.34	33.23	39.60	27.53	0.146	0.096	0.235
15.0	102.75	81.21	34.26	40.31	31.24	0.133	0.088	0.274
20.0	105.59	86.40	35.11	41.00	31.18	0.111	0.084	0.199
25.0	108.88	88.81	35.87	41.15	31.13	0.113	0.074	0.179
30.0	111.55	91.81	36.19	41.59	35.32	0.108	0.075	0.198
35.0	114.88	93.92	36.65	41.83	39.36	0.112	0.071	0.232
40.0	116.17	99.32	37.15	42.49	39.40	0.085	0.072	0.162
45.0	118.16	102.27	37.85	42.84	41.55	0.078	0.066	0.163
50.0	119.48	107.18	38.30	43.35	43.68	0.057	0.066	0.134
55.0	121.69	111.15	38.90	43.87	44.10	0.047	0.064	0.104
60.0	122.77	113.32	39.23	44.48	43.24	0.042	0.067	0.078
65.0	124.89	116.93	39.58	44.85	42.00	0.034	0.067	0.037
70.0	126.83	118.97	39.92	45.24	47.03	0.033	0.067	0.070
75.0	128.24	119.89	40.14	45.75	46.75	0.035	0.070	0.062

Pressure (MPa)	C_{11}	C_{33}	C_{44}	C_{66}	C_{13}	ε	γ	δ
80.0	129.95	123.83	40.49	46.17	46.62	0.025	0.070	0.031
85.0	130.60	125.19	41.43	46.49	46.23	0.022	0.061	0.032
80.0	130.50	125.39	41.36	46.47	45.68	0.020	0.062	0.024
75.0	129.85	124.69	41.35	46.33	46.64	0.021	0.060	0.038
70.0	129.87	123.18	41.35	46.01	47.62	0.027	0.056	0.061
65.0	129.65	123.15	40.99	45.67	46.91	0.026	0.057	0.048
60.0	129.55	122.49	40.63	45.36	49.65	0.029	0.058	0.072
55.0	128.92	122.62	40.27	45.12	49.52	0.026	0.060	0.063
50.0	128.49	121.67	39.85	44.86	49.95	0.028	0.063	0.069
45.0	127.69	119.13	39.50	44.65	48.54	0.036	0.065	0.074
40.0	125.96	115.53	39.29	44.17	46.47	0.045	0.062	0.088
35.0	124.99	112.62	38.76	43.76	46.31	0.055	0.065	0.107
30.0	122.23	109.50	38.29	43.35	44.00	0.058	0.066	0.109
25.0	118.84	106.23	37.84	42.80	46.15	0.059	0.066	0.164
20.0	116.14	103.47	37.27	42.29	42.36	0.061	0.067	0.143
15.0	111.80	97.46	36.46	41.84	38.69	0.074	0.074	0.162
10.0	107.03	88.61	35.80	40.82	32.93	0.104	0.070	0.207
5.0	---	---	35.51	---	---	---	---	---

Table A.16 - Elastic constants (GPa) and anisotropic parameters of the Wabamun carbonate.

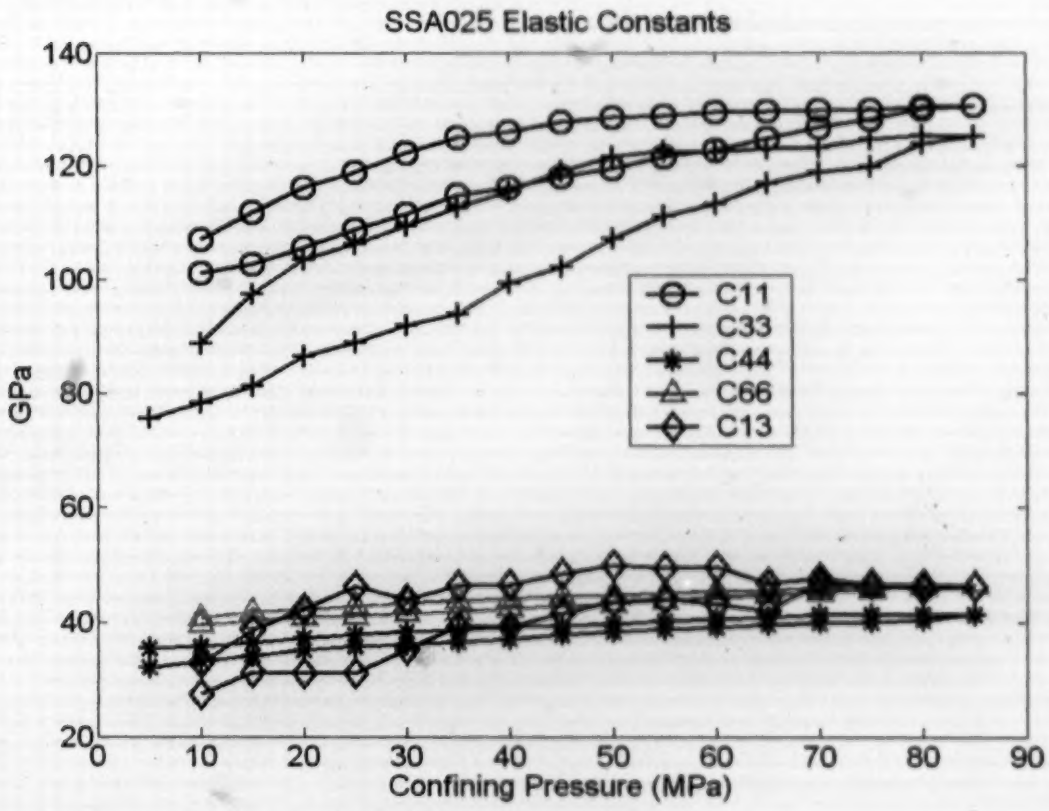

Figure A.15 - Elastic constants for the Wabamun carbonate.

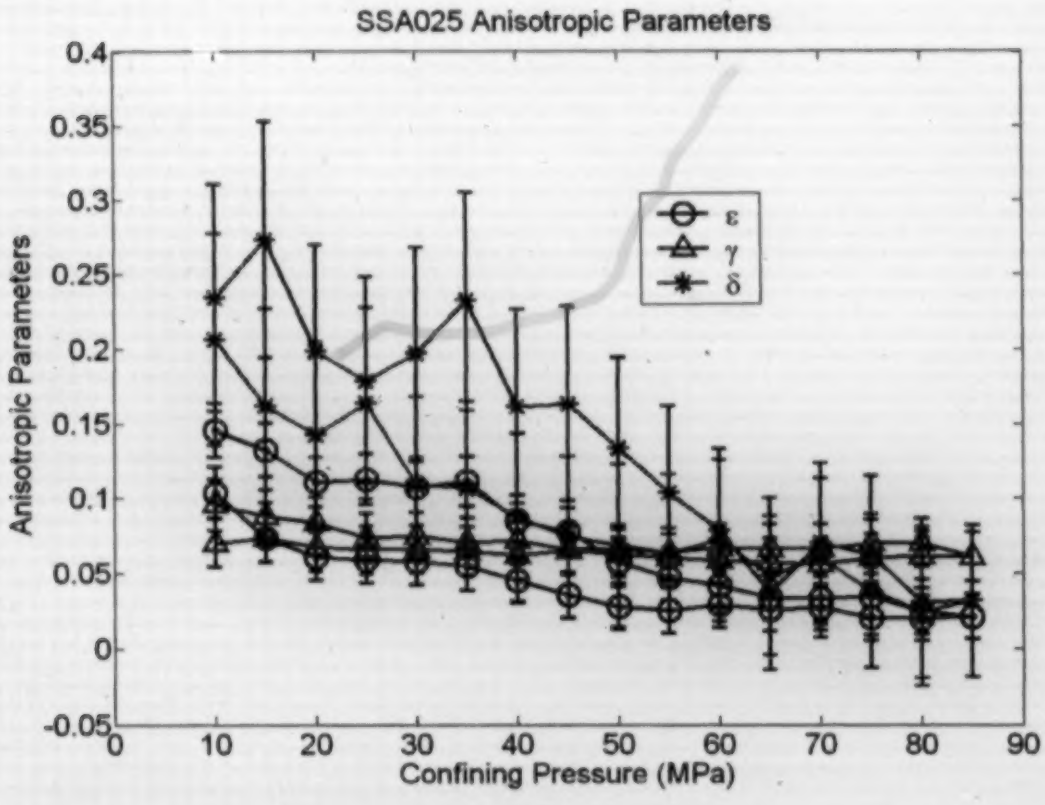

Figure A.16 - Anisotropic parameters for the Wabamun carbonate.

A.5 2nd White Specks Sandstone (SSA034)

Location	Depth (m)	Grain Density (g/cm^3)	Bulk Density (kg/m^3)	Porosity (%)
Gulf Mohawk Blood 6-16-6-22W4	970.0	2.62	2.48 ± 0.08	5.3 ± 2.9

Table A.17 - Geological parameters of the 2nd White Specks sandstone.

Direction relative to bedding	Length (cm)	Weight (g)
Parallel	4.577	56.8
45°	3.159	39.1
Perpendicular	2.359	28.8

Table A.18 - Properties of the cores used for velocity measurements of the 2nd White Specks sandstone.

Pressure (MPa)	$V_{P\,par}$	$V_{P\,45}$	$V_{P\,perp}$	$V_{SH\,par}$	$V_{qSV\,45}$	$V_{S\,perp}$
2.5	3643	3166	3087	2461	---	2447
5	3676	3203	3127	2530	2474	2498
7.5	3723	3392	3225	2573	2500	2550
10	3829	3426	3287	2619	2554	2576
12.5	3884	3561	3365	2654	2620	2618
15	3931	3641	3433	2688	2652	2649
17.5	3977	3687	3495	2733	2695	2673
20	4063	3695	3550	2766	2733	2694
22.5	4107	3747	3597	2804	2774	2718
20	4107	3733	3580	2794	2762	2716
17.5	4030	3706	3559	2776	2746	2707
15	3980	3671	3518	2743	2702	2696
12.5	3935	3666	3484	2717	2679	2676
10	3887	3580	3433	2677	2633	2638
7.5	3857	3546	3361	2649	2589	2608
5	3774	3375	3297	2601	2510	2569
2.5	3660	3151	3205	2514	---	2490

Table A.19 - Velocities (m/s) for the 2nd White specks sandstone. Direction is relative to bedding.

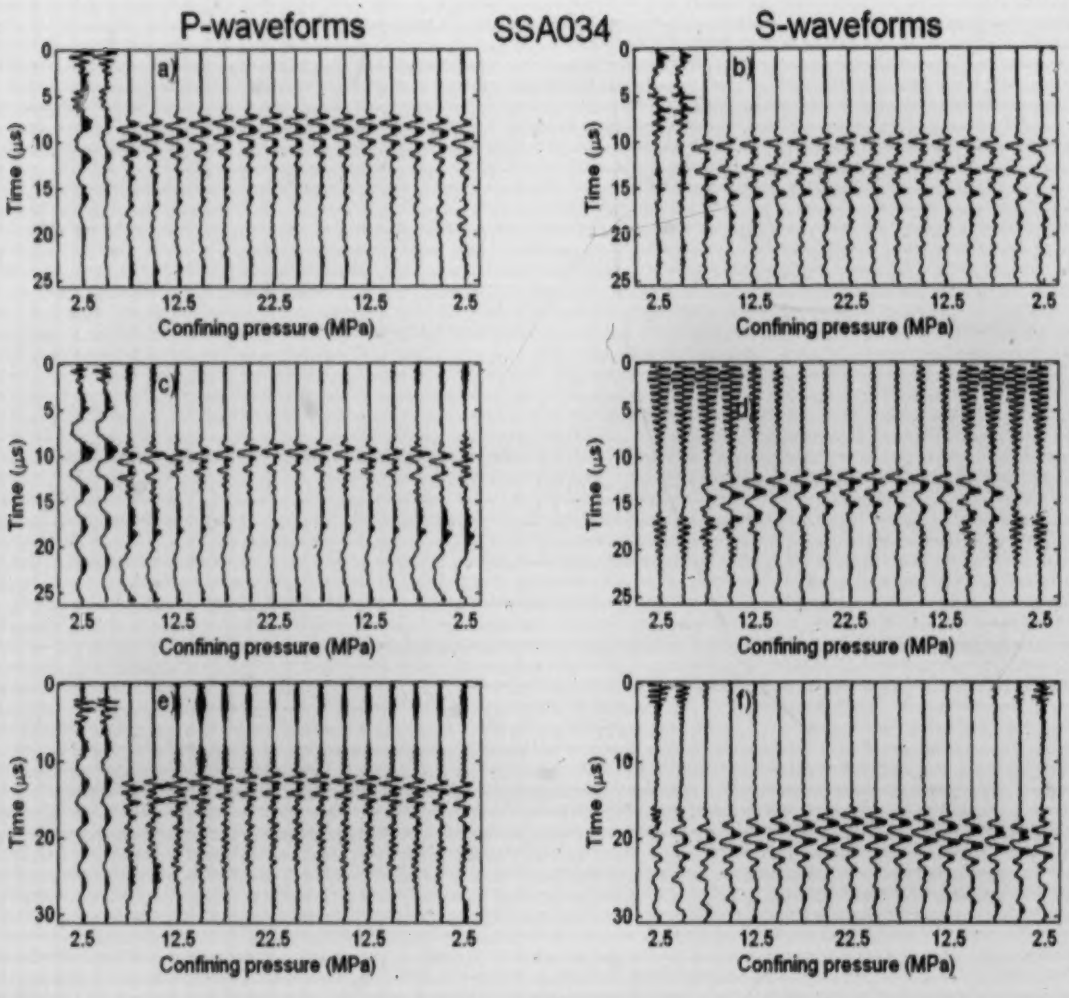

Figure A.17 – Complete suite of waveforms obtained for the 2nd White Specks sandstone. a) and b) show the P- and S-waves, respectively, traveling perpendicular to bedding. c) and d) show the waveforms traveling 45° to bedding, and e) and f) show the waveforms parallel to bedding.

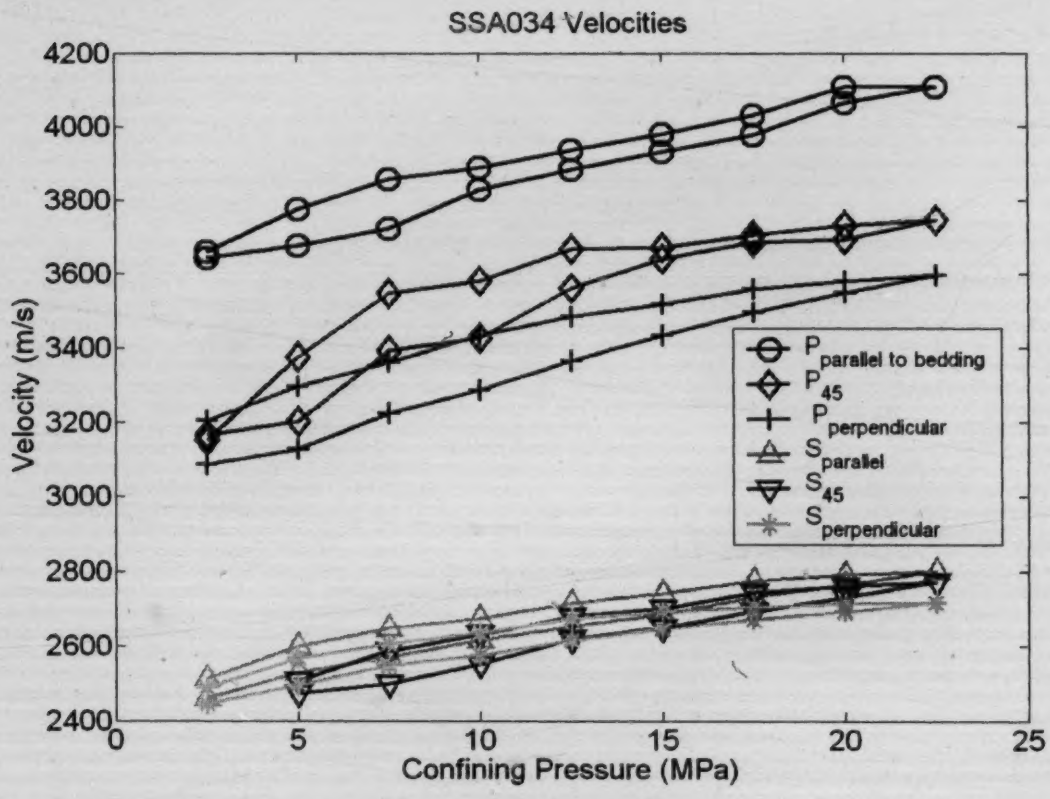

Figure A.18 - Velocities for the 2nd White Specks sandstone.

Pressure (MPa)	C_{11}	C_{33}	C_{44}	C_{66}	C_{13}	ε	γ	δ
2.5	32.88	23.62	14.84	15.00	-10.14	0.196	0.006	-0.133
5.0	33.49	24.23	15.47	15.87	-10.88	0.191	0.013	-0.131
7.5	34.34	25.77	16.12	16.41	-6.16	0.166	0.009	0.012
10.0	36.32	26.77	16.45	16.99	-7.46	0.178	0.017	-0.047
12.5	37.37	28.06	16.99	17.45	-4.69	0.166	0.014	0.046
15.0	38.30	29.20	17.38	17.91	-3.56	0.156	0.015	0.075
17.5	39.19	30.27	17.71	18.50	-3.48	0.147	0.022	0.059
20.0	40.91	31.23	17.98	18.96	-5.28	0.155	0.027	-0.017
22.5	41.79	32.06	18.31	19.48	-4.82	0.152	0.032	-0.008
20.0	41.80	31.75	18.28	19.35	-5.21	0.158	0.029	-0.013
17.5	40.24	31.39	18.16	19.09	-4.77	0.141	0.026	0.005
15.0	39.25	30.67	18.00	18.64	-4.86	0.140	0.018	0.016
12.5	38.38	30.08	17.75	18.29	-3.72	0.138	0.015	0.060
10.0	37.45	29.20	17.25	17.75	-4.98	0.141	0.015	0.011
7.5	36.86	28.00	16.86	17.38	-4.61	0.158	0.016	0.041

Pressure (MPa)	C_{11}	C_{33}	C_{44}	C_{66}	C_{13}	ε	γ	δ
5.0	35.30	26.94	16.36	16.77	-8.43	0.155	0.013	-0.086
2.5	33.20	25.46	15.36	15.66	-13.00	0.152	0.010	-0.187

Table A.20 - Elastic constants (GPa) and anisotropic parameters for the 2nd White Specks sandstone.

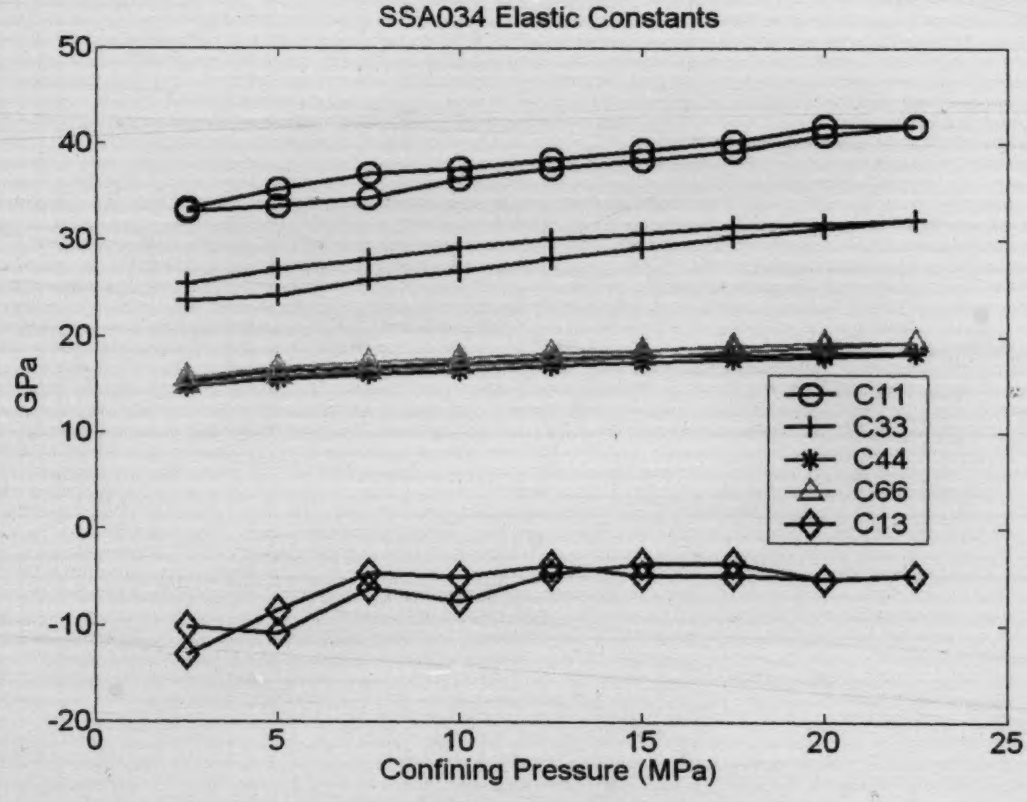

Figure A.19 - Elastic constants of the 2nd White Specks sandstone.

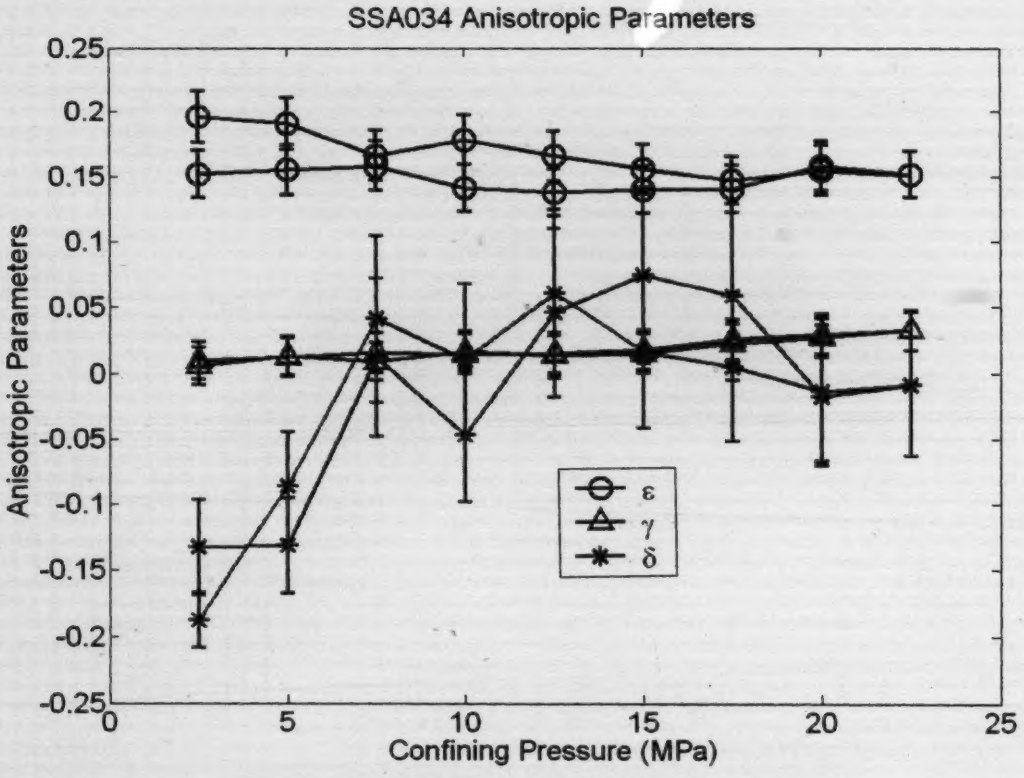

Figure A.20 – Anisotropic parameters for the 2nd White Specks sandstone.

A.6 Big Valley Anhydrite (SSA035)

Location	Depth (m)	Grain Density (g/cm^3)	Bulk Density (g/cm^3)	Porosity (%)
Gulf Mohawk Blood 6-16-6-22W4	1837.5	2.89	2.93 ± 0.04	<< 1

Table A.21 - Geological parameters of the Big Valley anhydrite.

Direction relative to bedding	Length (cm)	Weight (g)
Parallel	4.486	63.5
45°	5.751	82.5
Perpendicular	2.642	37.6

Table A.22 - Properties of the cores used for velocity measurements of the Big Valley anhydrite.

Pressure (MPa)	$V_{P\,par}$	$V_{P\,45}$	$V_{P\,perp}$	$V_{SH\,par}$	$V_{SV\,45}$	$V_{S\,perp}$
5.0	6228	5842	5696	3376	3310	3223
10.0	6257	5926	5767	3425	3343	3235
15.0	6292	5979	5809	3457	3352	3245
20.0	6303	6016	5852	3479	3357	3259
25.0	6322	6050	5921	3497	3358	3269
30.0	6342	6063	5964	3525	---	3279
35.0	6361	6074	5984	3534	3361	3286
40.0	6372	6085	5998	3537	3360	3298
45.0	6383	6096	6026	3544	3364	3305
40.0	6381	6102	6030	3544	3362	3306
35.0	6375	6106	6024	3542	3364	3306
30.0	6371	6091	6015	3537	3363	3304
25.0	6358	6085	6019	3528	3363	3298
20.0	6347	6076	5985	3524	3363	3291
15.0	6340	6068	5961	3509	3357	3283
10.0	6326	6055	5922	3490	3350	3273
5.0	6306	6024	5843	3474	3342	3249

Table A.23 - Velocities (m/s) for the Big Valley anhydrite. Directions are relative to bedding.

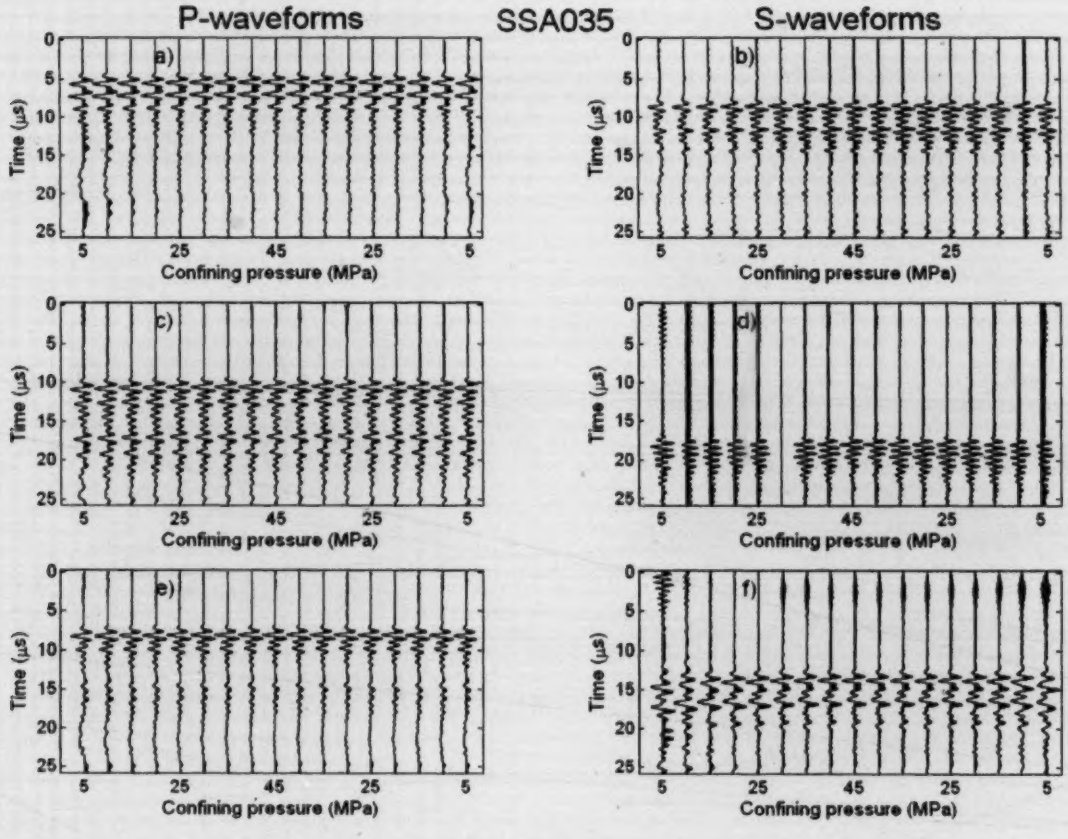

Figure A.21 – Complete suite of waveforms obtained for the Big Valley anhydrite. a) and b) show the P- and S-waves, respectively, traveling perpendicular to bedding. c) and d) show the waveforms traveling 45° to bedding, and e) and f) show the waveforms parallel to bedding.

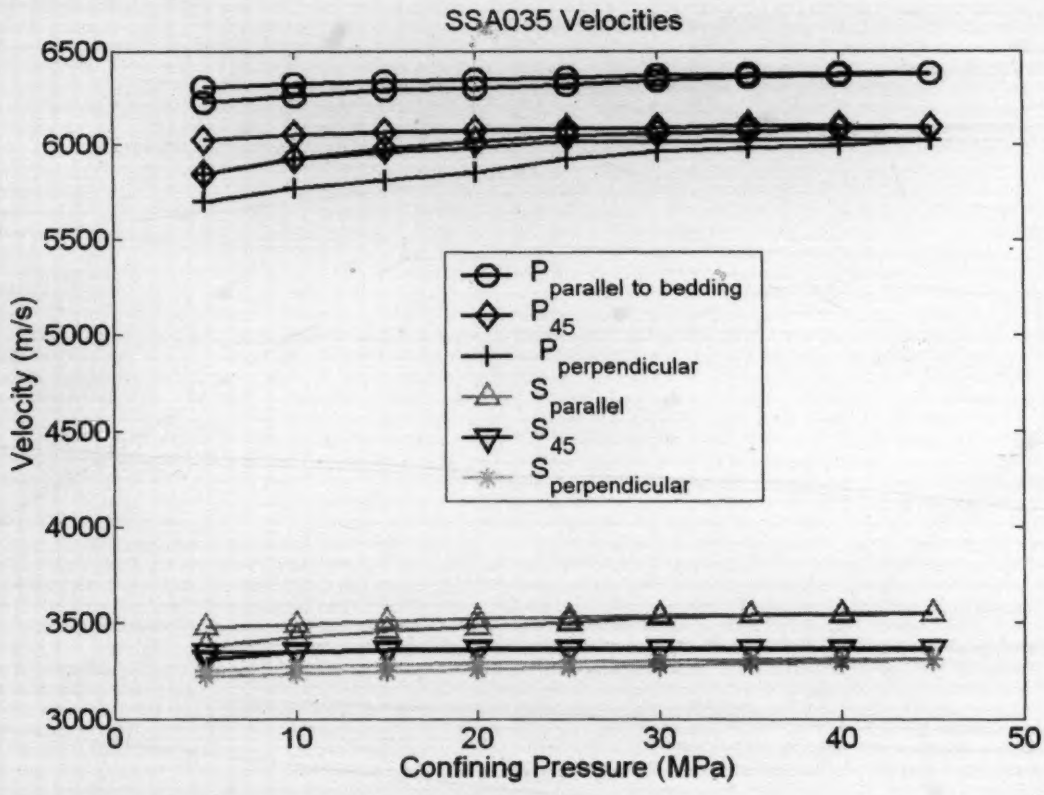

Figure A.22 - Velocities for the Big Valley anhydrite.

Pressure (MPa)	C_{11}	C_{33}	C_{44}	C_{66}	C_{13}	ε	γ	δ
5.0	113.59	94.98	30.42	33.37	34.08	0.098	0.049	-0.001
10.0	114.61	97.39	30.64	34.34	37.85	0.088	0.060	0.018
15.0	115.93	98.80	30.83	34.98	39.80	0.087	0.067	0.028
20.0	116.31	100.26	31.10	35.45	40.99	0.080	0.070	0.030
25.0	117.04	102.66	31.29	35.80	41.57	0.070	0.072	0.015
30.0	117.75	104.16	31.49	36.39	40.99	0.065	0.078	-0.002
35.0	118.48	104.83	31.62	36.57	40.79	0.065	0.078	-0.007
40.0	118.88	105.33	31.85	36.62	40.71	0.064	0.075	-0.009
45.0	119.28	106.34	31.98	36.78	40.56	0.061	0.075	-0.017
40.0	119.23	106.47	32.01	36.77	40.92	0.060	0.074	-0.014
35.0	119.01	106.27	32.01	36.74	41.41	0.060	0.074	-0.008
30.0	118.86	105.95	31.96	36.63	40.61	0.061	0.073	-0.013
25.0	118.36	106.07	31.84	36.45	40.70	0.058	0.072	-0.016
20.0	117.97	104.87	31.72	36.35	41.04	0.062	0.073	-0.004

Pressure (MPa)	C_{11}	C_{33}	C_{44}	C_{66}	C_{13}	ε	γ	δ
15.0	117.71	104.03	31.56	36.05	41.34	0.066	0.071	0.004
10.0	117.17	102.68	31.37	35.67	41.65	0.071	0.069	0.017
5.0	116.45	99.97	30.91	35.34	42.02	0.082	0.072	0.040

Table A.24 - Elastic constants (GPa) and anisotropic parameters for the Big Valley anhydrite.

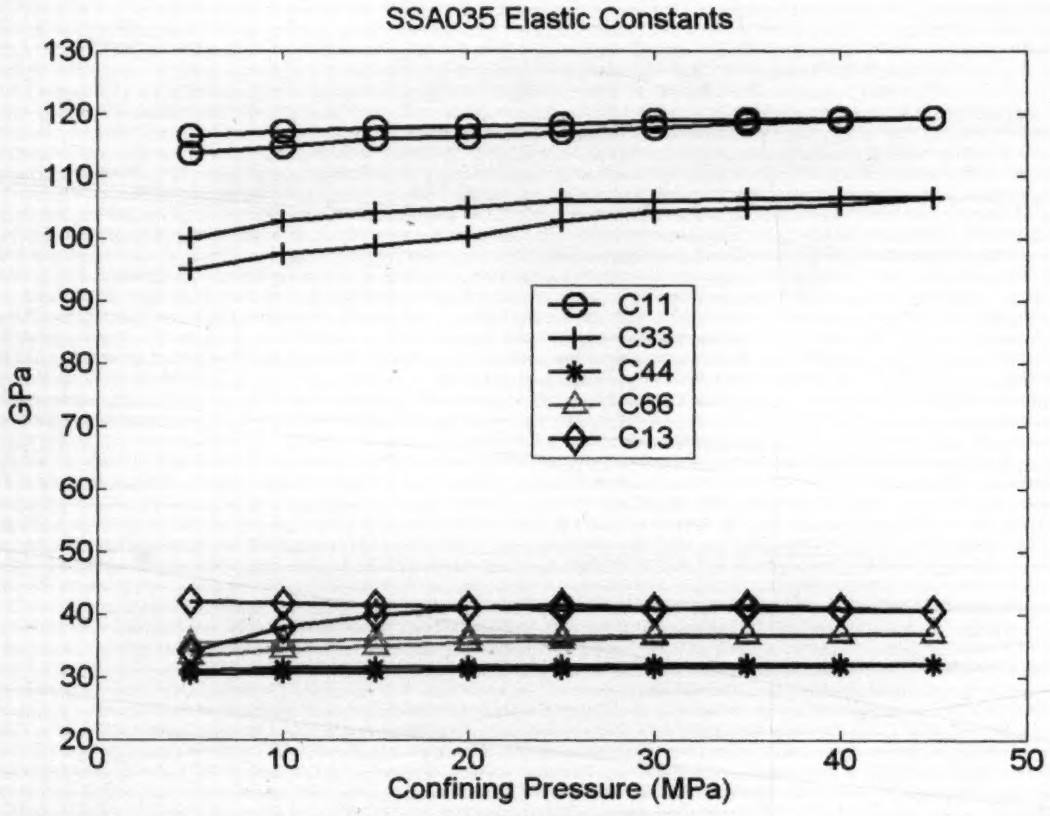

Figure A.23 - Elastic constants for the Big Valley anhydrite.

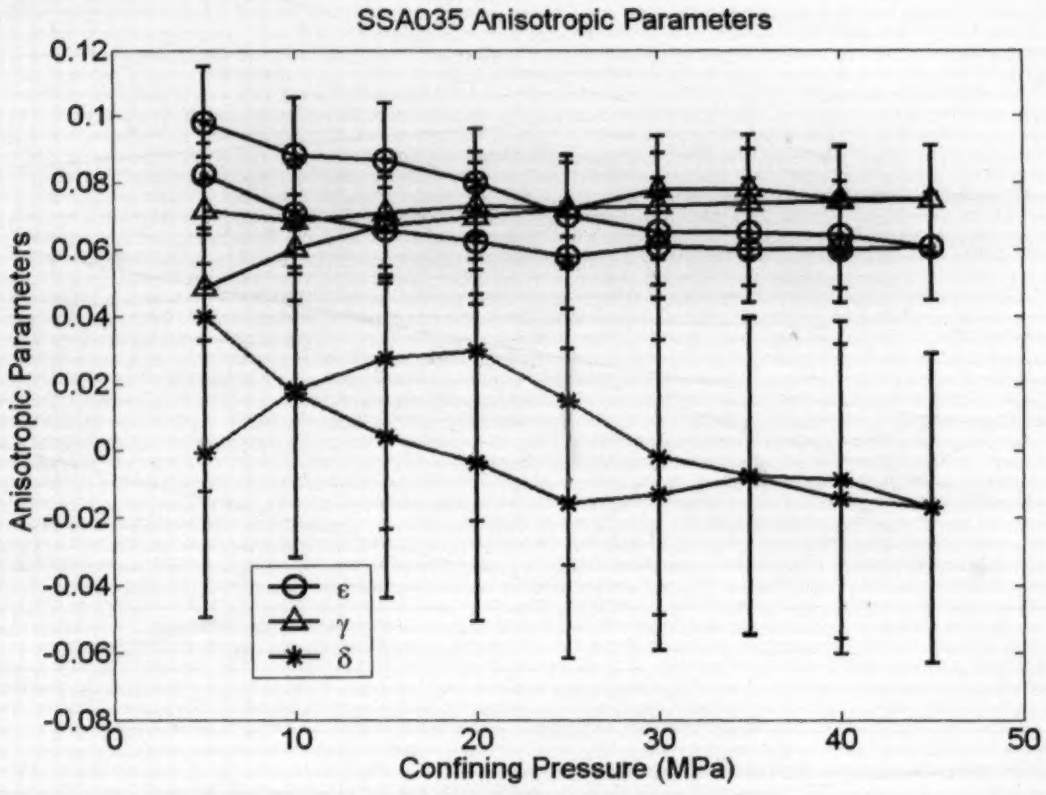

Figure A.24 - Anisotropic parameters for the Big Valley anhydrite.

A.7 Bow Island Sandstone (SSA037)

Location	Depth (m)	Grain Density (kg/m^3)	Bulk Density (kg/m^3)	Porosity (%)
Canhunter Keho 6-34-10-22W4	1044.7	2911	2338 ± 13	11.7 ± 0.5

Table A.25 - Geological parameters for the Bow Island sandstone.

Direction relative to bedding	Length (cm)	Weight (g)
Parallel	4.421	51.12
45°	3.675	42.28
Perpendicular	3.197	36.88

Table A.26 - Properties of the cores used for velocity measurements on the Bow Island sandstone.

Pressure (MPa)	$V_{P\ par}$	$V_{P\ 45}$	$V_{P\ perp}$	$V_{SH\ par}$	$V_{SV\ 45}$	$V_{S\ perp}$
5.0	---	2876	2708	---	1963	1991
7.5	3125	2926	2799	2119	2022	2040
10.0	3198	2996	2860	2141	2050	2086
12.5	3249	3056	2968	2188	2097	2126
15.0	3303	3132	3039	2214	2125	2159
17.5	3388	3198	3089	2247	2159	2191
20.0	3436	3267	3154	2286	2199	2222
22.5	3497	3342	3243	2321	2236	2259
25.0	3555	3400	3299	2354	2271	2289
22.5	3545	3381	3281	2346	2257	2279
20.0	3505	3341	3245	2331	2241	2266
17.5	3461	3305	3201	2310	2219	2243
15.0	3411	3253	3121	2280	2187	2216
12.5	3361	3173	3066	2245	2144	2181
10.0	3275	3096	3003	2208	2111	2141
7.5	3220	3006	2870	2181	2051	2093
5.0	3177	2914	2777	2136	2001	2035

Table A.27 – Velocities (m/s) for the Bow Island sandstone. Directions are relative to bedding.

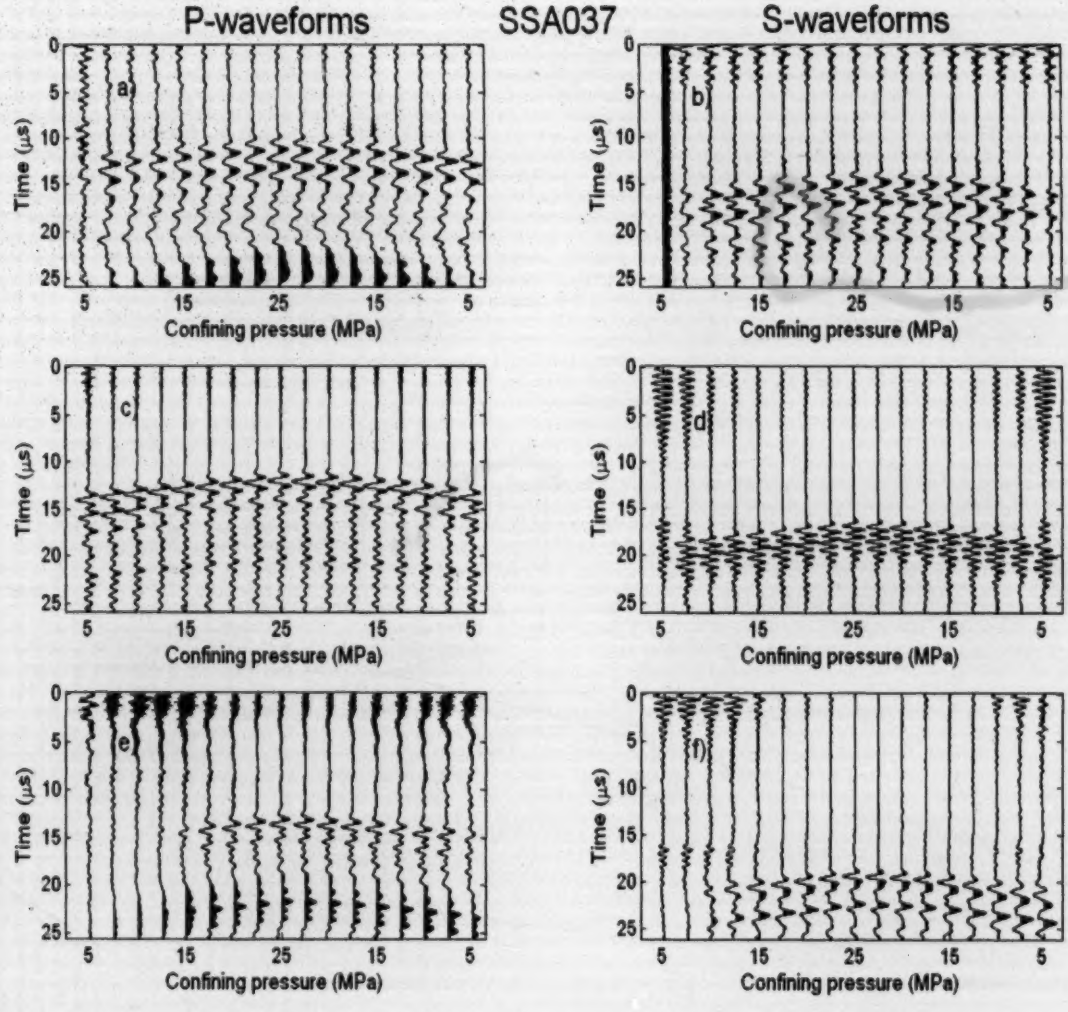

Figure A.25 – Complete suite of waveforms obtained for the Bow Island sandstone. a) and b) show the P- and S-waves, respectively, traveling perpendicular to bedding. c) and d) show the waveforms traveling 45° to bedding, and e) and f) show the waveforms parallel to bedding.

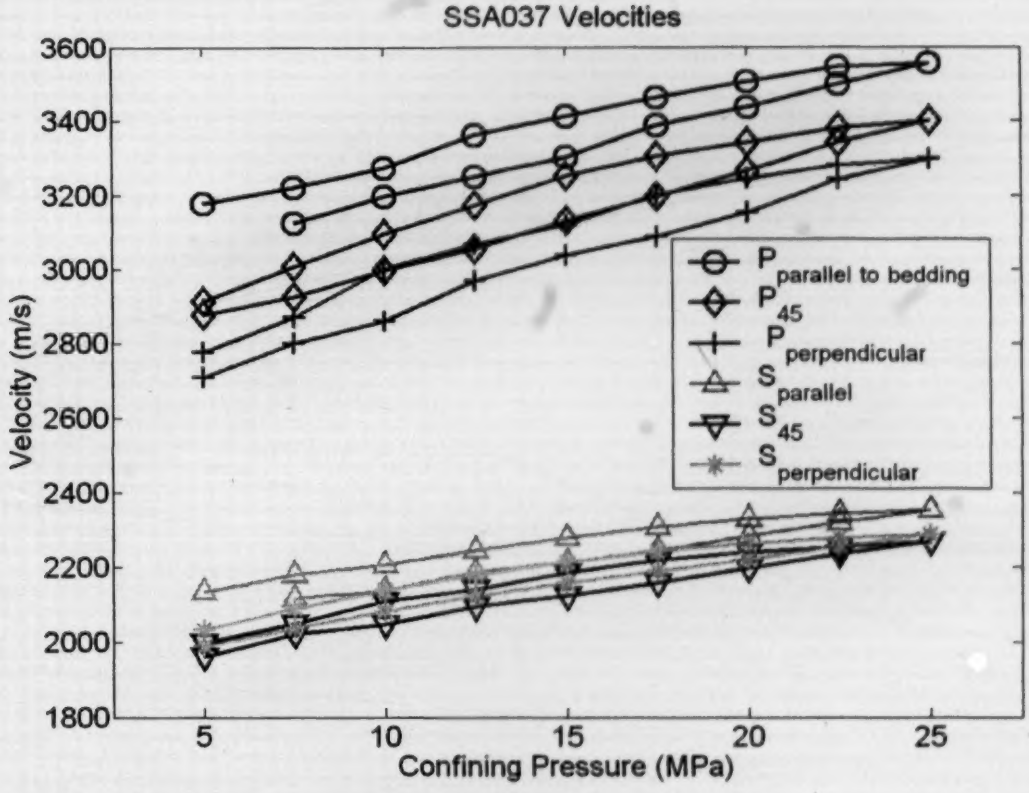

Figure A.26 - Velocities for the Bow Island sandstone.

Pressure (MPa)	C_{11}	C_{33}	C_{44}	C_{66}	C_{13}	ε	γ	δ
5.0	---	17.15	9.27	---	---	---	---	---
7.5	19.00	18.32	9.73	10.50	-0.29	0.123	0.040	0.049
10.0	22.84	19.13	10.18	10.72	-0.19	0.125	0.027	0.057
12.5	23.91	20.60	10.56	11.19	-0.31	0.099	0.030	0.011
15.0	24.69	21.60	10.90	11.46	0.35	0.090	0.026	0.026
17.5	25.51	22.31	11.22	11.81	0.59	0.101	0.026	0.033
20.0	26.83	23.25	11.55	12.22	1.21	0.094	0.029	0.047
22.5	27.60	24.59	11.93	12.60	1.63	0.081	0.028	0.037
25.0	28.59	25.44	12.25	12.96	1.91	0.081	0.029	0.039
22.5	29.55	25.17	12.15	12.87	1.71	0.084	0.030	0.034
20.0	29.38	24.61	12.00	12.71	1.37	0.084	0.029	0.032
17.5	28.72	23.95	11.76	12.47	1.41	0.085	0.030	0.043
15.0	28.01	22.77	11.48	12.16	1.35	0.097	0.030	0.072
12.5	27.21	21.98	11.12	11.79	0.42	0.101	0.030	0.032

Pressure (MPa)	C_{11}	C_{33}	C_{44}	C_{66}	C_{13}	ε	γ	δ
10.0	26.40	21.09	10.72	11.39	0.13	0.095	0.032	0.023
7.5	25.07	19.25	10.24	11.13	-0.28	0.130	0.043	0.053
5.0	24.24	18.02	9.68	10.67	-0.90	0.155	0.051	0.025

Table A.28 – Elastic constants (GPa) and anisotropic parameters for the Bow Island sandstone.

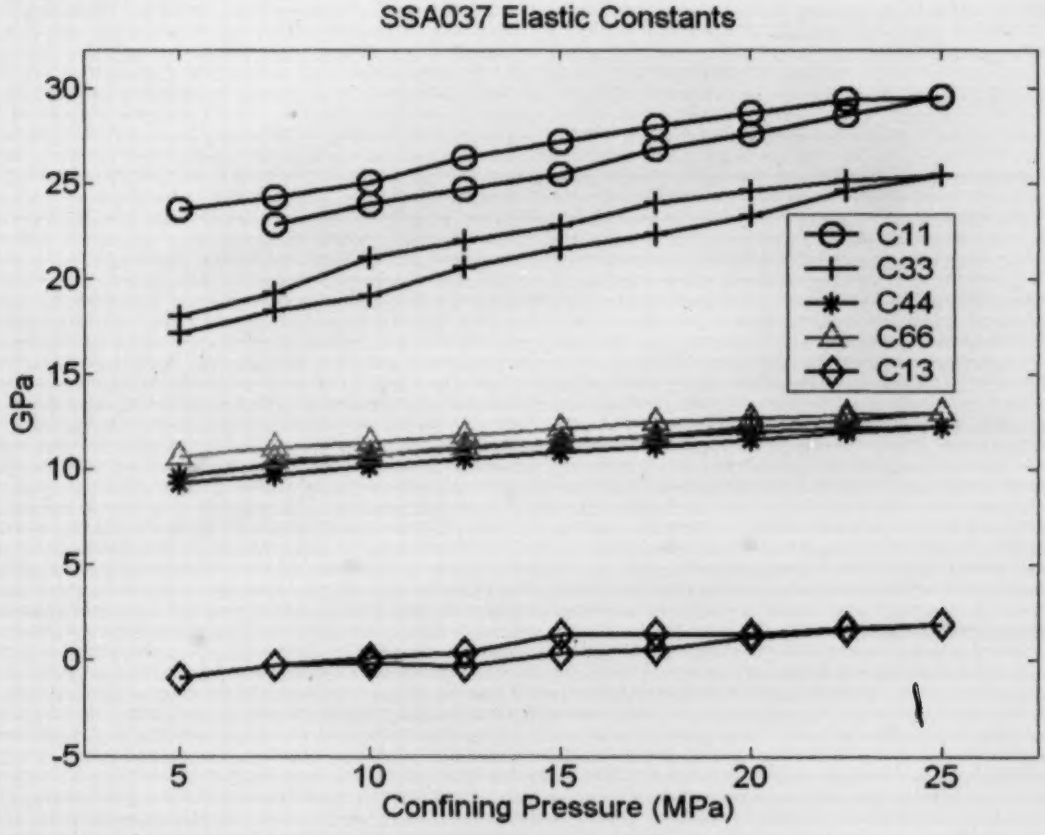

Figure A.27 - Elastic constants for the Bow Island sandstone.

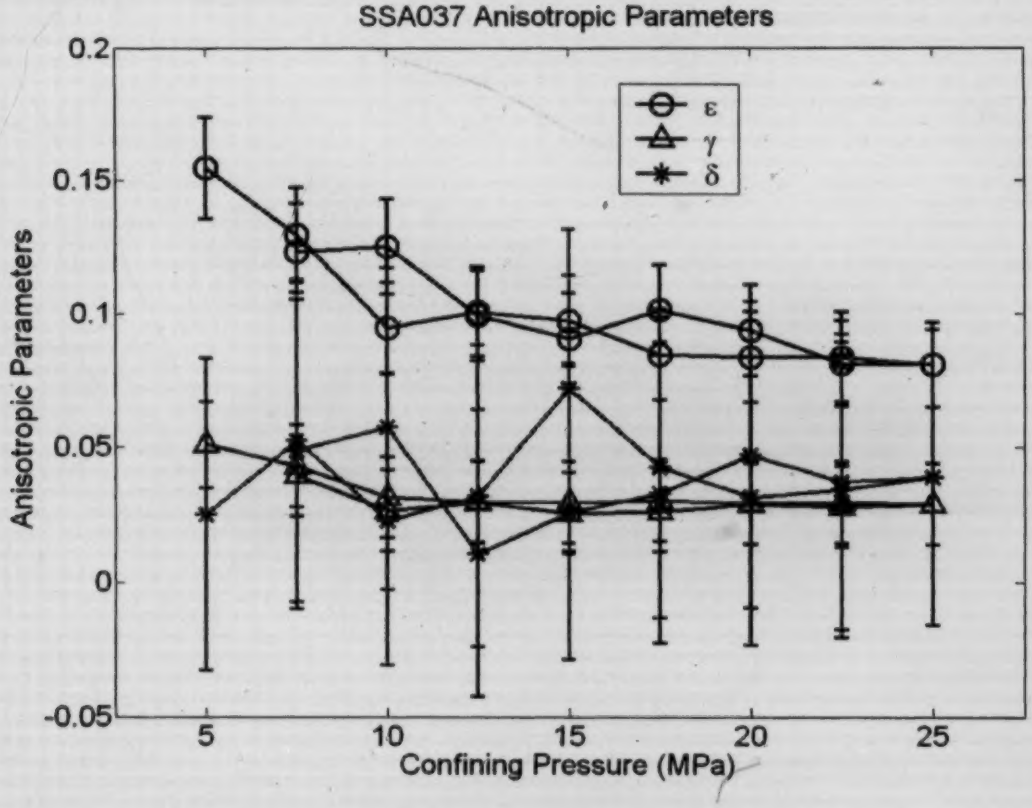

Figure A.28 - Anisotropic parameters of the Bow Island sandstone.